Josephson photonics : Statistics of photons emitted by inelastic Cooper pair tunneling

Alexander Grimm

UNIVERSITÉ DE GRENOBLE

THÈSE

Pour obtenir le grade de

DOCTEUR DE L'UNIVERSITÉ DE GRENOBLE

Spécialité : **Physique**

Arrêté ministériel : 7 août 2006

Présentée par

Alexander Grimm

Thèse encadrée par **Max Hofheinz**
et dirigée par **Olivier Buisson**

préparée au sein du **CEA Grenoble**
et de **l'école Doctorale de Physique**

Josephson photonics: Statistics of photons emitted by inelastic Cooper pair tunneling

Thèse soutenue publiquement le **2 octobre 2015**,
devant le jury composé de :

Dr. Jean-Michel Gérard
CEA Grenoble, Président
Prof. Dr. Joachim Ankerhold
Universität Ulm, Rapporteur
Prof. Dr. Andreas Wallraff
ETH Zürich, Rapporteur
Prof. Dr. Gerhard Kirchmair
Universität Innsbruck, Examinateur
Dr. Olivier Buisson
Institut Néel, Directeur de thèse
Dr. Max Hofheinz
CEA Grenoble, Encadrant de thèse

Acknowledgements

I would like to start by thanking Joachim Ankerhold, Gerhard Kirchmair, Jean-Michel Gérard and Andreas Wallraff for accepting to be part of my thesis jury. Thank you for the interest you have shown in my work and for all that I could learn from our conversations before, during and after my defense.

My sincere thanks to Göran Johansson from the university of Chalmers and Juha Leppäkangas from the Karlsruhe institute of technology for their theory support and their patient explanations on the dark magic of Keldysh contours.

Je dois également un grand merci à la Fondation Nanosciences, en particulier à Alain Fontaine, Marie-Anne Carré, Stéphanie Montfront et Feriel Kouiten, ainsi qu'à Jean-Pascal Brison et Marielle Perrier de l'INAC pour leurs efforts. Ils ont rendu cette thèse possible, et m'ont facilité la vie aussi bien tout au long de mon séjour au CEA que pendant les quelques mois de rédaction en dehors du centre.

Une thèse comme celle-ci, qui démarre sur un projet de recherche complètement nouveau, pose certaines conditions à la relation entre l'encadrant et le thésard. Il faut notamment une bonne mesure de complicité et de confiance entre les deux. En termes de complicité, je savais dès le premier jour de ma thèse que tout se passerait bien. Après tout, quoi de mieux pour forger une amitié que de chercher des fuites ensemble ? Et rares sont les thésards qui ont déjà joué dans un bac à sable avec leurs encadrants ! La confiance est quelque chose qui se construit sur les années, et là aussi je n'ai pas été déçu. En particulier, je ne me rappelle pas une seule occasion où je suis ressorti du bureau d'à côté sans les réponses à mes questions. Surtout au début, j'ai dû faire une dizaine d'allers-retours par jour, et à chaque fois j'étais accueilli avec la même patience et disponibilité. Tout cela a énormément contribué à me faire sentir qu'il était possible de mener à bien ce projet de thèse. C'est dans cet esprit que j'aimerais te remercier Max, non seulement pour ton excellent encadrement, mais encore et surtout pour ton amitié tout au long de ces dernières années.

D'autres personnes ont contribué de façon significative à ces travaux de thèse. Les premières d'entre elles sont les techniciens de notre laboratoire, Jean-Luc, Fred Gustavo et Poletti, Pierre (merci pour toutes ces idées de sorties !), Jean-Michel, Iulian et Michel.

Sans Frédéric Gustavo et Jean-Luc Thomassin, il m'aurait été beaucoup plus difficile de fabriquer toutes ces plaques pleines d'échantillons foireux ; mais sans eux je n'aurais surtout jamais réussi la fameuse plaque numéro 104, qui a donné les résultats présentés dans ce manuscrit de thèse. Merci pour vos leçons précieuses sur le dessin de masques de nano-fabrication et sur les tontons flingueurs ; merci aussi pour les séances de découpage de plaque de vraiment dernière minute et pour tous ces bons moments passés ensemble.

Deux autres combattants ont rejoint les rangs de notre petite équipe "circuits supra" au fil des années. C'est grâce à Salha et Dibyendu qu'après deux ans, je n'étais plus le seul non-permanent du bâtiment à se soucier d'impédances caractéristiques, d'inductances cinétiques, de résonateurs quart d'onde et autres incantations arcanes. Je vous remercie pour votre aide, pour vos encouragements et pour vos critiques, qui ont permis de nous faire avancer ensemble. Il ne me reste qu'à souhaiter bonne chance et de très bons facteurs de qualité à Florian, qui vient de commencer dans l'équipe.

J'aimerais également remercier tous les chercheurs permanents du bâtiment C1 pour m'avoir accueilli dans leur groupe. Merci à Marc, François, Claude, Xavier, Vincent, Silvano, Louis, Alexandre, Christophe, Bernard, Dai, Daniel et Georg. Les échanges avec vous lors des réunions de fabrication hebdomadaires (souvent agrémentées de gâteaux) et autour du café de dix heures et demi m'ont régulièrement fait oublier la qualité de ce dernier.

La vie de laboratoire ne serait pas la même sans les thésards et post-docs. J'ai eu la chance d'en connaître plusieurs générations. D'abord la "vieille garde", en commençant par mon collègue de bureau de deux ans, Andreas, dont la fine connaissance de la musique autrichienne me laissait souvent bouche bée ; puis Benoit, qui connaît la meilleure blague du monde, et Charlène, qui partage ma passion pour la Chartreuse (le massif, bien sûr). Il ne faut pas oublier Benoît (dit "l'optimiste"), Audrey (merci pour les cocazotes), Caroline, Driss, Tristan (daddy cool), Mathieu, Eduardo, Alexandra, Mounir, Natalia et Boris. Merci de m'avoir aidé à trouver le bon chemin dès le début de ma thèse. Après vient la nouvelle cuvée avec Eduard, Loïc, Andrea, Anaïs, Patrick, Toai, Paul, Jean-Eudes, Juan Carlos, Gaël (rends honneur à mes skis !), Jean-Pierre, Romain, Felipe, Dharmraj, Beilun et Adrien, qui ont su prendre le relais de façon excellente. Reste le thésard le plus illustre de France, Alexandre, que j'ai eu la chance de connaître quand il était encore seulement (mais éminemment) célèbre au "Carré". En passant, un grand merci à Carole pour toutes ces myrtes. Dans la même veine j'aimerais remercier Roman (le top chef) et la joyeuse bande des théoriciens Lars, Joseph, Vladimir, Elio, Kostia et Tania pour leur infatigable présence aux Pipotages, bières du vendredi soir, barbecues et autres activités communes.

Pour l'instant, je n'ai mentionné que le CEA, mais l'institut Néel a également été le théâtre de mes péripéties, surtout vers la fin de ma thèse. En premier lieu, je tiens à remercier mon directeur de thèse Olivier Buisson pour nos discussions pleines de questions

à l'allure innocente, mais qui ont toujours su taper là ou ça sonnait un peu creux. J'ai aussi beaucoup profité des échanges qui ont eu lieu lors de notre journal club commun, notamment avec Wiebke, Nico, Cécile, Yuriy, Bruno et Étienne. Surtout je n'oublierai pas la gentillesse avec laquelle Olivier, Nico, Julien et Étienne m'ont prêté tour à tour leurs bureaux climatisés pour la rédaction de ce manuscrit de thèse pendant la canicule des mois d'été 2015. Merci aussi à Arnaud, Jessica, Rémy, Javier et Kitti pour leur accueil pendant cet "exil".

Parmi les gens qui m'ont été les plus proches à Grenoble se trouvent beaucoup de compagnons de cordée. Nos sorties resteront gravées dans ma mémoire. Ainsi j'associe la Meije à Bruno, le Mont Aiguille à Erik, les arêtes de Rochefort à Christoph Groth, les Chourums du Grand Ferrand à Robert, l'arête des Papillons à Christoph Schenke, le Dôme de Neige à Ronni et Peter et les volcans d'Équateur à Pamela, à qui je dois bien plus, entre autres la décision de faire une thèse. Je les remercie pour ces escapades, qui m'ont toujours aidé à retrouver mon équilibre au cours de ces dernières années.

Mein besonderer Dank gilt meinen Eltern für ihre Unterstützung meiner Projekte und Träume, selbst wenn diese jahrelange Auslandsaufenthalte mit sich brachten. Ich danke meinem Vater Peter für den Rückhalt seiner ruhigen und sicheren Präsenz und meiner Mutter Barbara für ihre Begeisterungsfähigkeit und ihr Interesse an meiner Forschung. Danke für all die Wanderungen, Frankreichreisen und Kartenpartien. Danke auch dafür, dass ihr mich nie davon abgehalten habt dumme Fragen zu stellen. Das ist wohl der Grund, warum ich das auch heute noch mache.

Herzlichen Dank weiters meiner Tante Josefa und meinem Onkel Günther, die den weiten Weg bis nach Grenoble auf sich genommen haben, um meiner Verteidigung beizuwohnen. Es war mir eine Freude diesen Moment mit euch zu teilen.

Enfin, mes remerciements vont vers Emily, pour avoir été une vraie guerrière lors de nos "petites randos d'introduction" de douze heures, et pour son soutien infaillible pendant les moments les plus durs. Ce projet aurait été incroyablement plus difficile à mener à terme sans toi, merci beaucoup.

Meinen Eltern,
Barbara und Peter Grimm

Contents

Introduction and summary

In the work at hand, we study and control the statistics of microwave photons emitted by inelastic Cooper pair tunneling through a voltage biased Josephson junction. This sentence already indicates the two main components of the physics we have set out to investigate, namely charge tunneling and photonics in superconducting circuits. In this task, we can draw on the rich heritage of two different fields of condensed matter physics. On the one hand, there are Coulomb blockade phenomena, which are based on the interplay of the tunnel effect and the Coulomb interaction between charge carriers [1, 2]. The observation and study of these effects through electronic transport measurements has been long ongoing with the first experiments dating back over 50 years [3]. It is from this field that we derive the basic fundamental motivation for our experiments.
On the other hand, there is the younger field of circuit quantum electrodynamics (circuit QED) [4, 5], where artificial two-level systems (qubits) made of superconducting tunnel junctions [6] are coupled to microwave frequency photons. This approach allows for strong interactions between light and matter and has proven to be a formidable playground for quantum optics experiments in superconducting circuits [7–10]. The physical implementation of our devices is based on the concepts and techniques developed in circuit QED over the last 10 years.
This field at the intersection of inelastic Cooper pair tunneling and quantum microwaves has recently been dubbed Josephson photonics.

Scientific context and motivation

In the following section, we will situate our work in its scientific context by giving a brief overview of the precursory theoretical and experimental discoveries that have enabled us to ask the questions addressed in this PhD thesis. Moreover, we will point out some particularly original properties of the devices we have elaborated in order to provide additional motivation for our experiments.

Coulomb blockade and inelastic Cooper pair tunneling

Classical Coulomb blockade

Classical or orthodox Coulomb blockade (CB) is the phenomenon, where a charged particle tunneling onto a conductive island between two electrodes (Fig. 1) can inhibit

further addition of other charge carriers through Coulomb repulsion. This effect takes place when the overall charging energy of the island $E_C = q^2/(2C_{tot})$ is non-negligible compared to the energy qV conferred to the particle of charge q by the voltage difference V between the island and the neighboring electrode. It leads to the opening of a "Coulomb gap" in the current voltage characteristic of the system, meaning that current can flow through the island only from a finite voltage bias $V_b = q/C_{tot}$ on.
Naturally, for this effect to be observable, the total capacitance C_{tot} of the island has to be small enough, so that the charging effects are not washed out by thermal fluctuations. This leads to the restriction $E_C > k_B T$. Another condition is $R_T > R_K = h/q^2$, meaning that the tunnel resistance R_T of the junctions formed by the island and the electrodes has to be larger than the resistance quantum R_K, which is a measure for quantum fluctuations of the system.
Because of these constraints, the first observations of Coulomb blockade in the 1960s were limited to granular metallic films [3] and superconducting tunnel junctions with small conducting particles in their oxide barrier [11] (Fig. 1). However, with the advent of modern nano-fabrication techniques in the final quarter of the last century, such systems became more accessible and could be engineered at will, for instance by creating an artificial island between two tunnel junctions of very small surface [12]. Consequently, the theoretical and experimental understanding of CB progressed [1] and in the late 1980s new questions were asked.

Dynamical Coulomb blockade

Among these questions was the issue of Coulomb blockade effects in devices with only a single normal metal tunnel junction [13, 14]. More precisely, what was observed was a slight decrease of conductivity at low bias voltages (Fig. 2) instead of a full-blown gap as in the case of orthodox Coulomb blockade. Within the following years this phenomenon was successfully explained in the framework of the so-called "P(E)-theory" [2, 15–18]. It was found that a charge carrier, traversing a tunnel junction, could dissipate its energy qV_n by exciting modes of the electromagnetic environment seen by the junction. This opens additional conduction channels across a normal metal junction as shown in Fig. 3a. Because of the energy quantization of the electromagnetic field, a mode of frequency ω_0 can only be excited when $qV_n \geq \hbar\omega_0$. If the voltage bias is reduced, these channels are suppressed and one observes an effective drop in the differential conductance dI/dV of the junction, called dynamical Coulomb blockade (DCB).
To link this phenomenon to the concept of classical Coulomb blockade presented before, we can remark that these effects only happen when the impedance of the electromagnetic environment seen by the junction is comparable to the resistance quantum (the exact condition will be given later in chapter 5). On the samples where the effect was first observed (left panel of Fig. 2), the junction was for instance connected to resistive leads. Together with the junction capacitance this creates an RC element. For short times the tunneling electron charges the capacitor and effectively reduces the bias voltage, suppressing further tunneling during a time $\tau_c = RC$. This effect manifests itself more strongly at low bias voltages for the same reason as in the previous section. In this

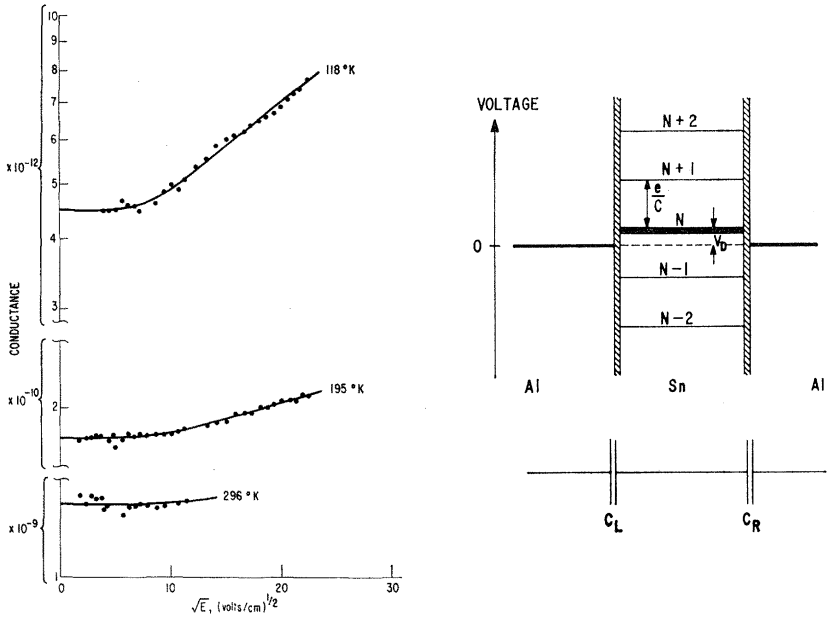

Figure (1): Left panel: The experimental observation by Neugebauer et al. [3] of a Coulomb gap in the conductance of a granular metallic thin film under an applied external field, given in $\sqrt{\mathrm{V/cm}}$. *Right panel: A sketch showing the interpretation of the effect by Zeller et al. [11]. Electrons can tunnel onto, and away from, a conducting island between two electrodes. The total capacitance of the island is* $C = C_\mathrm{L} + C_\mathrm{R}$. *The equilibrium voltage, indicated on the ordinate, leads to a charge of* N *electrons on the island. Adding more charges comes at an energy cost* $(N+1)^2e^2/(2C) - N^2e^2/(2C)$, *which is shown here as a voltage difference* e/C.

particular implementation it is easy to understand the role of the condition $R > R_\mathrm{K}$. The quantum fluctuations of energy on the RC-element are linked through the Heisenberg uncertainty principle to the discharging time-scale τ_c, as $\tau_\mathrm{c}\Delta E \geq \hbar/2$. When these fluctuations satisfy $\Delta E \ll E_\mathrm{C}$, which can be rewritten as $R_\mathrm{K}/(2\pi) \ll R$, the suppression is complete, and a Coulomb gap as in classical CB is observed.
Interestingly, already in 1988, Likharev *et al.* predicted an oscillatory current through such a system based on the periodic charging and discharging of the junction capacitance on the time-scale of τ_c. They dubbed this effect "Bloch oscillations" [1]. We will see later that our devices are based on a very similar concept.

Inelastic Cooper pair tunneling

In voltage biased superconducting tunnel junctions, however, dynamical Coulomb blockade manifests itself quite differently [19] (right panel of Fig. 2). Here, at temperatures small compared to the superconducting energy gap Δ, quasi-particle excitations are exponentially suppressed and for voltage biases $V_\mathrm{s} < 2\Delta/e$ the only charge carriers that

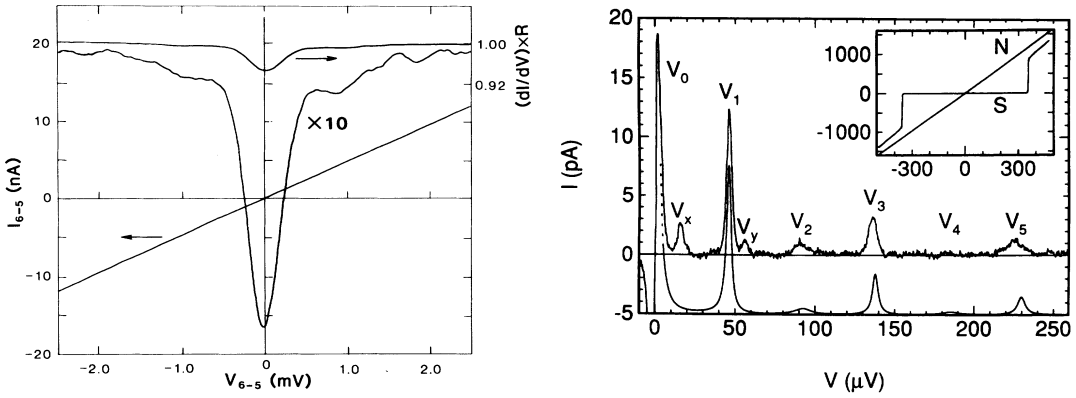

Figure (2): Left panel: The suppression of the conductance in the current voltage characteristic (straight line) of a single normal metal tunnel junction observed by Delsing et al. [14]. The normal scale conductance curve in the upper part of the figure is also shown ten times magnified for better visibility. Right panel: The first detailed spectroscopy of the electromagnetic environment of a superconducting tunnel junction, visible as peaks in the sub-gap current, by Holst et al. [19]. The fit of the data (offset for clarity) is given by the, at the time, recently developed P(E)-theory [2], while the inset shows the junction IV in the normal and superconducting state.

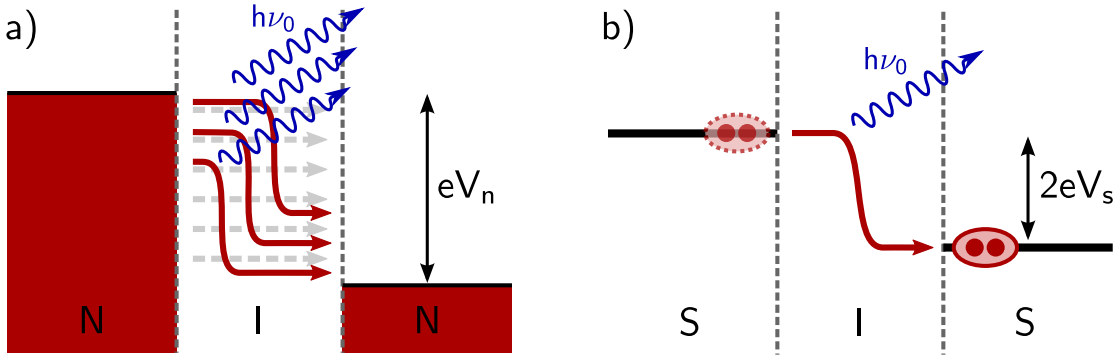

Figure (3): Dynamical coulomb blockade and inelastic Cooper pair tunneling. a) In a normal metal (NIN) tunnel junction at $k_BT \ll eV_n$. Due to the applied voltage difference V_n, electrons tunnel through the junction (faint gray arrows). Additional conduction channels are made available, because an electron can also inelastically tunnel while emitting a microwave photon of energy $h\nu_0$ into a mode of the electromagnetic environment (red and blue arrows). If the voltage bias is reduced, so that $eV_n < h\nu_0$, this process is suppressed and the overall conductivity is decreased (Fig. 2). b) In a Josephson junction (SIS) at $k_BT, 2eV_s \ll \Delta$. The voltage bias shifts the Cooper pair (CP) condensates by $2eV_s$ with respect to each other. A CP can only tunnel through the junction, if it can lose its surplus energy via emission of a photon. This leads to a finite current peak under the gap for $2eV_s = h\nu_0$. Multiple photon processes equally occur giving rise to peaks at respectively higher voltage biases (Figs. 2 and 4).

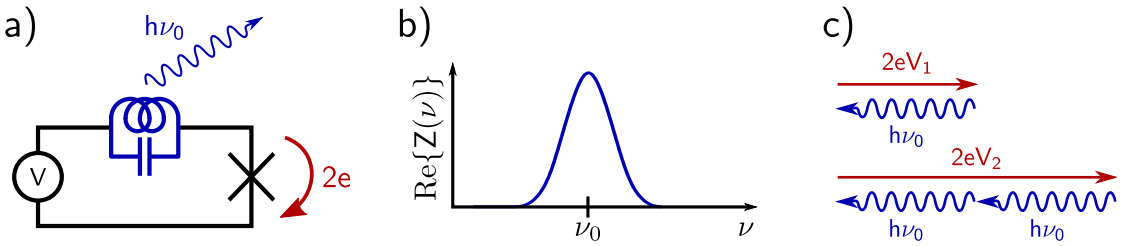

Figure (4): a) Schematic representation of a simple case of inelastic Cooper pair tunneling, where the electromagnetic environment of the voltage biased Josephson junction (marked by the cross) consists of a single LC resonator. b) The real part of the impedance is given by a single Lorentzian centered on the resonance frequency ν_0. c) The first two emission peaks occur at the voltages fulfilling the conditions $2eV_1 = h\nu_0$ and $2eV_2 = 2h\nu_0$, respectively corresponding to the emission of one and two photons by a tunneling Cooper pair.

have to be considered are Cooper pairs (CP). The CP-condensates on both sides of the junction are shifted by an energy $2eV_s$ with respect to each other and the only way for a CP to tunnel through the junction is to dissipate this surplus energy by exciting the modes of the electromagnetic environment as sketched in Fig. 3b. This environment can be described by an impedance $Z(\nu)$, giving the linear voltage response in the circuit to current fluctuations at the junction as a function of frequency ν. Since the case at hand involves dissipation into this environmental impedance, it is the real part of this quantity that has to be considered. The strength of the coupling to the environment at a specific frequency ν is proportional to the value of $\mathrm{Re}\{Z(\nu)\}$ [2, 15, 17].
In the simple example shown in Fig. 4, $\mathrm{Re}\{Z(\nu)\}$ is peaked at a frequency ν_0, due to a resonance mode in the electromagnetic environment seen by the junction. This leads to a peak in current at the resonance condition $2eV_1 = h\nu_0$, where the energy conferred to a CP by the voltage bias V_1 corresponds to one quantum of energy at the frequency of the environmental mode. Another peak appears at twice the voltage bias $V_2 = 2V_1$, when one tunneling Cooper pair can emit two photons, satisfying $2eV_2 = 2h\nu_0$.
Higher photon numbers and combined processes between different resonance peaks in the environment are equally possible (see results of Holst *et al.* in Fig. 2), but are exponentially suppressed according to their order, when the characteristic impedance of the associated peaks is smaller than the resistance quantum ($Z_0 \ll R_K$) [2]. Due to the enhancement, rather than suppression, of the current through a single voltage biased Josephson junction by dynamical Coulomb blockade we will refer to this effect as inelastic Cooper pair tunneling for the remainder of this work.

The photonic side of inelastic Cooper pair tunneling

After a good understanding of the current aspect of inelastic Cooper pair tunneling had been reached, the next step was taken by Hofheinz *et al.*, 20 years after the results of Holst *et al.* were published, by focusing on the photonic side of the problem [20].

For voltage biases well below the gap of a standard aluminum based Josephson junction ($\approx 200\,\mu$eV), the excitation quanta of the environment have frequencies in the microwave range ($\approx$ GHz). In their experiment they made use of the fact that in the last decades good microwave amplifiers and fast digitizers have become commercially available, while the impedance seen by the Josephson junction can readily be engineered at GHz-frequencies [21].
The left panel of Fig. 5 shows a diagram of their sample and measurement setup. A SQUID acting as a flux tunable Josephson junction (see Chs. 2 and 5) is coupled to a microwave resonator consisting of stacked transmission line segments with different parameters (see Ch. 2 and appendix B). The latter acts as an effective parallel LC resonator, creating a peak in the impedance seen by the SQUID. A bias tee separates the microwave photons leaking out of the resonator from the DC voltage bias. The CP current is determined via the voltage drop over a resistor in the DC bias line and the high frequency response is filtered and then integrated over the bandwidth of the resonator, giving the microwave output power. Schematically, their sample corresponds to the sketch presented in Fig. 4. As mentioned above, a Cooper pair can cross the junction when the tunneling conditions $2eV_1 = h\nu_0$ and $2eV_2 = 2h\nu_0$ are fulfilled. The results found by Hofheinz *et al.* show very good agreement between the CP tunneling current and the emitted microwave radiation (Fig. 5).

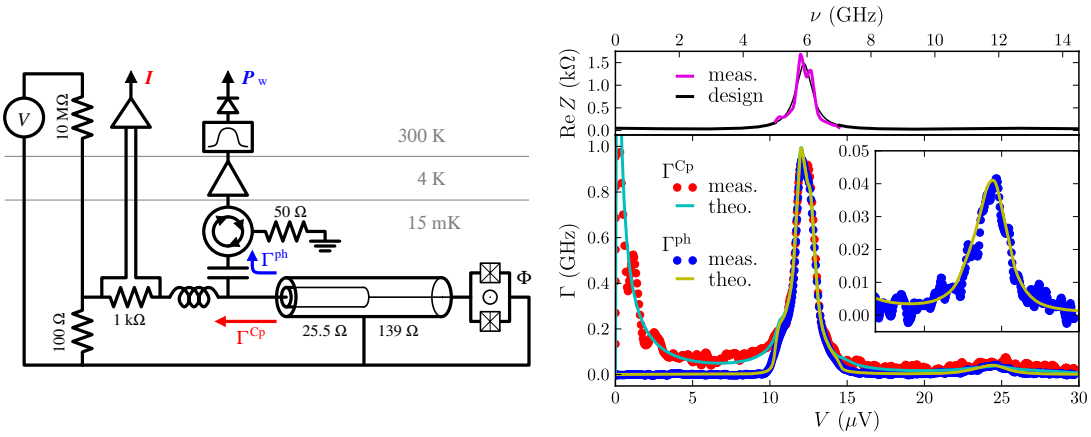

Figure (5): Left panel: The experimental setup of Hofheinz et al. [20]. In the lower right corner the two junctions forming the SQUID are depicted as crossed boxes and the transmission line resonator is represented as overlapping cylinders. The voltage bias and current measurement are separated from the high frequency part of the setup by a bias tee. The path of the DC current (microwave photons) is indicated by red (blue) arrows. Right panel: the upper part of the figure shows the real part of the designed (measured) impedance in black (magenta) as a function of frequency. The lower part gives the experimental results and theoretical prediction for the Cooper pair tunneling and photon emission rates (Γ^{Cp} and Γ^{ph}) depending on the voltage bias at the junction. The rates coincide very well for the first peak at $2eV_1 = h\nu_0$ around 12 µV. The second peak at twice that voltage bias ($2eV_2 = 2h\nu_0$) is shown magnified in the inset.

The significance of this work comes from its approach to the electromagnetic environment. It is no longer regarded as a simple model for dissipation, that can be traced out in calculations, but is instead actively monitored and its excitations considered as the output of the sample. While, at the same time, interest in the charge transport aspect of the effect was renewed, in particular to probe the environment seen by a Josephson junction [22, 23], it was this experiment that opened the door to further developments involving the photonic bright side of inelastic Cooper pair tunneling.

The objective of this thesis: Towards a bright microwave single photon source

The work presented in this PhD manuscript contributes to the investigation of this phenomenon by studying, not only the average photon emission rates, but also their statistics. This is made possible by new schemes for correlation measurements in the microwave regime that were recently developed [24]. Specifically, we aim to show that these statistics can be actively modified by carefully engineering the electromagnetic environment seen by the junction. In particular, we will demonstrate the generation of anti-bunched photons, an inherently quantum state of light, emitted at very high rates.

Working principle

Conceptually, a source capable of emitting such radiation is obtained from what is shown in Fig. 4a by simply adding a parallel RC-element to the circuit as depicted in Fig. 6a. This changes the energy balance of the system. Now a tunneling Cooper pair has to charge the island formed between the junction and the external capacitance at the additional energy cost of $E_\mathrm{C} = 4e^2/(2C)$. As a result, the only way to emit a photon into the mode at the resonance frequency of ν_0, is to provide a voltage bias V_1 fulfilling the equation:

$$2eV_1 = E_\mathrm{C} + h\nu_0 \tag{1}$$

Immediately after such an event, the next Cooper pair tunneling through the junction would have to pay a charging energy of $16e^2/(2C) - 4e^2/(2C) = 3E_\mathrm{C}$. This is prohibitive to another photon emission since $2eV_1 < 3E_\mathrm{C} + h\nu_0$ (Figs. 6c and d). Instead, one expects the time constant of the RC-element $\tau_\mathrm{c} = RC$ to regulate the timescale over which a new emission process can occur. This simple picture gives the basic principle of our devices, where we exploit the fact that anti-correlations in the Cooper pair tunnel current lead to anti-bunching in the emitted photons.
In order for this to be feasible the two quintessential conditions of Coulomb blockade have to be satisfied. As mentioned before, the first requirement is that $k_\mathrm{B}T \ll E_\mathrm{C}$, so that thermal fluctuations do not wash out the charging effects. At the typical base temperature of a dilution refrigerator of $\approx 15\,\mathrm{mK}$, this translates to a limit on the capacitance of $C \ll 250\,\mathrm{fF}$. Modern nano-fabrication techniques allow us to make junctions with shunting capacitances ($\approx 1\,\mathrm{fF}$) and on-chip resistors with stray capacitances ($\approx 10\,\mathrm{fF}$) completely negligible compared to this value (see Ch. 1) and so C can be engineered at will with an external capacitance to reach a good compromise between charging energy

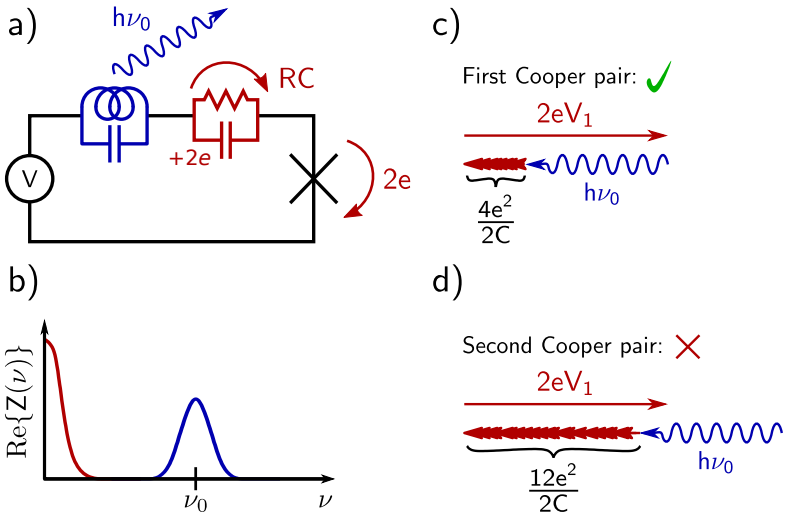

Figure (6): Working principle of a source of anti-bunched microwave photons. a) The modified circuit diagram and b) the real part of the impedance seen by the junction when adding an RC element to the circuit. c) A Cooper pair can tunnel through the junction, if the energy given to it by the voltage bias satisfies the relation: $2eV_1 = 4e^2/(2C) + h\nu_0$. *d) Immediately after a tunneling event the island is still charged and no new emission can occur, because* $2eV_1 < 12e^2/(2C) + h\nu_0$.

and RC time. The second condition is $R_Q \ll R$, where $R_Q = h/(4e^2) \approx 6.5\,\mathrm{k\Omega}$ is the superconducting resistance quantum. A value of R largely superior to this can be achieved with on-chip thin film resistors (see Ch. 2).

The THz frequency gap

So far, single photon sources have been limited either to the microwave frequency range of several tens of GHz [25–28] or to the optical range with the lowest accessible frequencies being on the order of $\approx 100\,\mathrm{THz}$ [29, 30].
The hard physical limit ν_{lim} to the emission frequency of our devices is fixed by the condition $h\nu_{\mathrm{lim}} < 2\Delta$, where Δ is the superconducting energy gap. If the produced photons were emitted at higher frequency they could be reabsorbed immediately and break up Cooper pairs. For this reason we use niobium nitride (NbN), with $2\Delta \approx 4.5\,\mathrm{meV}$ (see Ch. 1) resulting in a maximum frequency $\nu_{\mathrm{lim}} \approx 1.09\,\mathrm{THz}$. This possibility is an additional motivation for this work. Even though our devices operate at GHz frequencies at this stage to facilitate the measurements, we have developed our entire device fabrication and design with NbN-based Josephson junctions, paving the way for an extension of the operating frequency to the THz domain. The ability to emit anti-bunched light at these frequencies in a well controlled fashion can be useful to access excited states as well as for readout schemes in physical systems where the transition energies lie in the THz-regime, such as small semiconductor quantum dots or dopants in semiconductors [31].

Josephson photonics

In recent years several new theoretical descriptions dealing with the radiation emitted by inelastic Cooper pair tunneling in general, and its statistics in particular, were elaborated [32–35]. The developed theories cover a wide scope, from the perturbative limit of P(E)-theory [34] to the onset of classical dynamics due to strong coupling and back-action of the environment onto the tunneling process [33, 35]. Notably, Gramich *et al.* [33] and Leppäkangas *et al.* [34] predicted the possibility of non-classical radiation emitted by Josephson junctions coupled to suitable environments. Very recently, in view of the operating principle of our devices, an approach allowing predictions of the environment-induced correlations in the Cooper pair current has been developed. This has led to a collaborative publication with Leppäkangas *et al.* [36], predicting anti-bunching in the output radiation of the system described in this introduction.
In the meantime, further experiments based on the photonic side of inelastic Cooper pair tunneling have been conducted. Parlavecchio *et. al* [37] have shown the violation of a Cauchy-Schwarz inequality by amplitude squeezed radiation from a voltage biased Josephson junction coupled to an environmental impedance presenting a double peak. This effect was predicted by several recent theoretical works [34, 38, 39]. Chen *et al.* have investigated a strongly coupled system outside of the limits of P(E)-theory, where the high quality factor of the resonator leads to large photon occupation numbers and possible back-action on the tunnel process through the junction in the form of stimulated emission [40]. Another innovative approach, that has been touched upon in earlier works [19, 23], is to perform spectroscopy on the environment, by measuring the tunneling current as a function of voltage bias. This has been used to characterize transitions between Andreev states in a superconducting atomic contact by Bretheau *et al.* [41–44].
At the time of the redaction of this manuscript several other systems based on the emission or absorption of photons through inelastic Cooper pair tunneling are being elaborated, such as a source of entangled photon pairs [37] and a frequency converter as well as wide-band parametric amplifiers (see conclusion). The ongoing development of ideas for the application of these effects to practical devices, as well as the study of the fundamental physics behind them, is leading to the emergence of an active field of research dubbed "Josephson photonics" [38, 45]. This can be seen as a complementary development to classic circuit quantum electrodynamics with superconducting qubits, where coherent light sources are common, but emission rates are often limited. In Josephson photonics, devices generally have shorter coherence times due to the noise in the voltage bias (at least at the single photon level), but emission rates can be very fast.

Structure of this work

After the introduction and motivation presented here, we hope that the reader has a general idea of the experimental system we want to investigate. In chapter 1 we will proceed to give details on how we fabricate the different constituent elements of our samples. In the logic of this manuscript the next step after this is to describe how we

combine these elements on a chip to obtain our devices. This will be treated in chapter 2 dealing with sample design. With the finished devices ready to be measured, we then spend the next two chapters on our experimental setup. Chapter 3 illustrates the theory behind the particular scheme [24] we use for the determination of correlations between microwave photons, while chapter 4 gives details on the practical implementation of our measurement chain. The subsequent chapter 5, as a prelude to the experimental results, aims to cast the intuitive explanation of the physics behind our devices, which was established in this introduction, into a solid theoretical framework. Finally, chapter 6 will present and analyze the experimental results obtained during this PhD work. As an endpoint to this thesis, a conclusion and outlook will be given.
In the following we give a short summary of each chapter underlining the major points treated in an attempt to give the reader a quick guide to this manuscript.

Chapter 1: Fabrication

After quickly reiterating the reasons for our choice of material, chapter 1 describes the elaboration of the fabrication process for vertical Josephson junctions made from niobium nitride (NbN) and magnesium oxide, which was an essential part of this PhD work. We will equally give details on the characterization of the obtained junctions and resonators.

Chapter 2: Sample design

This chapter focuses on the practical implementations of the three main elements visible in the very schematic representation shown in Fig. 6. We describe how a superconducting quantum interference device is used as a flux-tunable Josephson junction, how coplanar waveguide (CPW) transmission lines are combined to give the high frequency impedance peak and how we realize the RC circuit using an on-chip thin film resistor. Some time is spent on a particular combination of CPWs playing the combined role of a beam splitter and a bias tee allowing us to realize these elements on-chip.

Chapter 3: Theory of photon correlation measurements

Here we pursue a twofold goal; on the one hand, we implicitly sketch how a microwave photon, emitted into a coplanar waveguide on the low temperature stage of a dilution refrigerator, becomes a voltage signal at the input port of the analog to digital converter of our measurement computer. On the other hand, we present a detailed analysis of all the different noise sources it encounters on this voyage and how their effect can be minimized by measuring cross-correlated quantities between the two channels of our experimental setup.

Chapter 4: Experimental setup

The experimental setup for our measurements was entirely created during this PhD work. It consists of two parts, namely the DC branch, which is used to apply a voltage bias to the junction and measure the current through it, and the high frequency branch, which

performs, amongst other things, the photon correlation measurements mentioned in the previous chapter. Both are described in this chapter, where we also give details on the different calibration setups and procedures we employ.

Chapter 5: Theory

In this part of the text, we present theoretical considerations for two different cases. The first system we study is based on samples without an RC-element akin to what is sketched in Fig. 4. In this, we focus on the photonic side of the effect, since the charge tunneling aspect has already been extensively studied and summarized in the literature [2]. The second system we deal with is naturally the device containing an RC-element (Fig. 6). Here, we quickly review the model used by Leppäkangas *et al.* in their description of this system, before giving an overview of their results, in particular pertaining to the expected second order correlations of the emitted photons [36].

Chapter 6: Experimental results

Following the same structural organization as the preceding chapter the results presented here are divided into devices without and with RC-element. For the first case, we show a detailed spectroscopy of the one ($2eV_1 = h\nu_0$) and two photon ($2eV_2 = 2h\nu_0$) processes in good agreement with the theoretical model, as well as an investigation of the associated correlations. In the latter case, we find a more complex behavior and a rich dependency of the emitted radiation on the main experimental parameters, namely the voltage bias at the SQUID and its Josephson energy. We provide a complete analysis of the observed effects and then go on to demonstrate the operation of a bright on-demand light source capable of emitting anti-bunched as well bunched microwave photons depending on only a single parameter.

Conclusion and outlook

Finally, we recall the content of this thesis and the obtained results, giving suggestions for the direction of future work.

Appendix A

Here we give details on the deposition and etch recipes developed during this PhD thesis.

Appendix B

This appendix provides a quick introduction to transmission line theory.

Appendix C

Here we develop in detail our calculation dealing with the noise sources in the photon correlation measurements presented in chapter 3.

Appendix D

This appendix regroups auxiliary calculations from different chapters.

Appendix E

Here we give the parameters of the devices discussed in chapter 6, including a figure reference for each sample.

Chapter 1

Fabrication of vertical NbN:MgO:NbN Josephson junctions

1.1 Introduction

Many superconducting circuits are based on aluminum, which oxidizes in a self-limiting and controllable way. Josephson junctions can then be fabricated employing the usual shadow mask evaporation (SME) techniques [46, 47]. In this work, however, we have chosen niobium nitride (NbN) as a superconductor. As previously mentioned, the physics governing our system puts a hard limit to the frequencies of our devices only at $2\Delta/h$. With NbN based samples, where $2\Delta/h \approx 1.1\,\mathrm{THz}$, it is possible to reach the THz frequency-regime. Moreover, this material presents a much higher kinetic inductance than aluminum. This is of particular interest to us, because of the proportionality of photon emission rates due to inelastic Cooper pair tunneling to the characteristic impedance $Z_c = \sqrt{L/C}$ of the resonators seen by the junction (see Ch. 5), which can be enhanced with the kinetic inductance. Lastly, the critical temperature of NbN is distinctly higher than 4.2 K enabling rapid sample tests with a dipstick in liquid Helium. These advantages are paid for with a considerably more complicated fabrication process. First and foremost, the native oxide of NbN is not fit for making reliable high quality tunnel barriers [48]. Then, while a sputtering device capable of depositing NbN and magnesium oxide (MgO) was available in our laboratory at the beginning of this work [49, 50], an SME approach was excluded by this deposition technique for two reasons: First, sputtering is too isotropic for SME and second, it heats the wafer and burns the resist thus contaminating the chamber. A fabrication process for vertical NbN:MgO:NbN Josephson junctions with surfaces of several tens of μm^2 equally existed in our group. Nevertheless, since having as small as possible shunting capacitances is essential to our sample, an entirely new process, including etch recipes, had to be developed allowing us to reduce the surface areas of our junctions to values as small as $0.02\,\mu m^2$. The elaboration of this nanofabrication method was an essential part of this PhD work and

will be described in more detail in this chapter. To begin with, the deposition of the NbN:MgO:NbN trilayers themselves will be sketched. Then, we will go on to describe the etch recipes we developed and go through the step-by-step process of fabricating a vertical NbN:MgO:NbN Josephson junction with self-aligned spacers. Finally, a brief overview of some relevant material properties of the deposited layers will be given and the tunneling characteristics of the fabricated Josephson junctions will be discussed.

1.2 NbN:MgO:NbN trilayer deposition

1.2.1 The Alcatel SCM 600

The device used for the deposition of the trilayers is an Alcatel SCM 600 DC and RF magnetron sputtering machine (Fig. 1.1). Its main chamber contains niobium (Nb) and MgO targets (respectively 150 mm and 125 mm in diameter), a rotatable substrate holder and an equally rotatable shutter in the form of a half-disk. It can be pumped down to a pressure of 7×10^{-8} mbar by a stepped pumping system comprising a primary and a cryogenic pump. If the main pumping valve is throttled, both argon (purity: 99.995 %) and nitrogen (purity: 99.995 %) can be flowed into the chamber, while regulating their partial pressures with a sensitivity of $\approx 10^{-4}$ mbar. The Nb target is connected to a DC power source, while the MgO target can be addressed by an RF power source with a frequency of 13.56 MHz and a maximum power of 1.2 kW. The substrate holder is connected to an RF source with a peak power of 300 W and can be water-cooled or heated up to 600 °C.

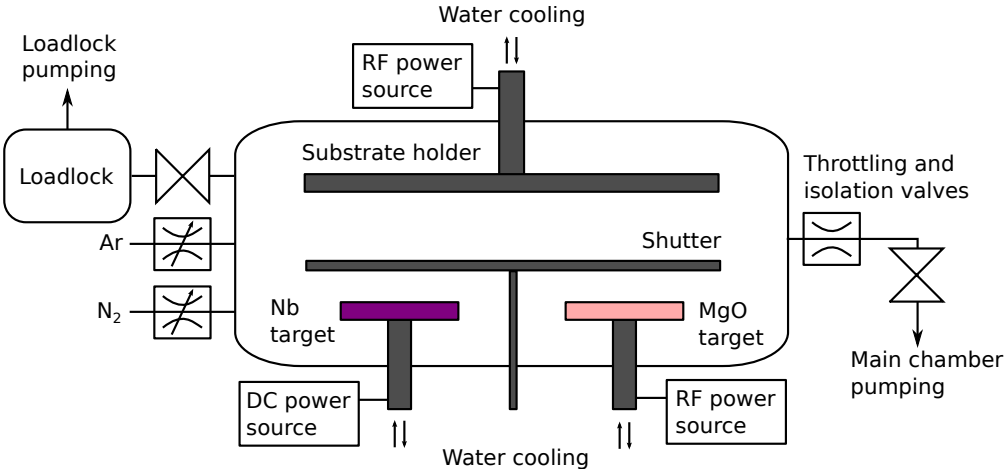

Figure (1.1): Schematics of the Alcatel SCM 600 sputtering device.

1.2.2 The sputtering process

When sputtering an electrically conductive material, a high DC electric field is applied between the target and a ground (usually a metallic ring around the target). The gas in the chamber (in our case argon) is ionized and the ions are accelerated towards the target. Upon impact, they eject atoms of the crucible that condense onto the substrate. When depositing NbN, one also introduces nitrogen (N_2) into the chamber. N_2 reacts with the Nb target forming NbN at its surface, which is constantly ejected by the ion bombardment. At first, the shutter is kept closed, while conditioning the target with a high N_2 flow, fully nitriding the surface. After some time the flow rate is reduced to the optimal value for the deposition of NbN and the shutter is opened. The partial pressures of both gases as well as the DC-bias power and the nitrogen flow-rate are parameters that have to be carefully calibrated in order to produce good quality films. In addition to that, after initially igniting the plasma, the optimal sputtering conditions have to be approached gradually before opening the shutter. These parameters and steps were developed by Villegier *et al.* [50] and could be further refined (e.g. to eliminate stress in the deposited layers) during this PhD work. A detailed account of the used parameters and deposition times for the different layers used in our fabrication process can be found in appendix A.
Our device also allows for RF magnetron sputtering and can thus be used to deposit insulating materials like MgO. When the crucible is insulating, charges cannot easily be evacuated and a simple DC bias is not able to uphold the sputtering process. Instead, an AC electrical field makes the electrons in the plasma oscillate. Some of them hit the target and charge it. Consequently, the ions are accelerated towards it and ablate the material, while neutralizing the added charges thus making the process sustainable. With the machine at hand, it is also possible to apply an inverse RF bias to the substrate holder enabling us to etch the substrate and thus clean it from contamination or surface oxide. This process is called backsputtering.

1.2.3 Deposition of the trilayer

The samples discussed in this work have been deposited on standard 4 in. (10.16 cm) Si(500 µm):SiO_2(500 nm) wafers with a resistivity between 1 and 100 Ω·cm. The wafers were systematically cleaned by backsputtering (5 min, 250 W) in the deposition chamber. To start with, a 20 nm MgO buffer layer was deposited. The good agreement between the lattice constants of this MgO base layer and of the sputtered NbN (lattice mismatch of 4 %), has been found to increase the critical temperature of the films by up to 2 K [50]. After this, the NbN(80 nm):MgO(4 nm):NbN(200 nm) trilayer was sputtered. The deposition rate for NbN was approximately 3.7 nm·s^{-1}. The produced NbN films are columnar with an average column diameter of ≈ 20 nm. The MgO barrier was deposited with the substrate holder rotating. This leads to a much slower deposition rate of approximately 0.04 nm·s^{-1}, because the substrate only spends ≈ 1/7 of the time above the target, allowing for a more precise control of the barrier thickness.

1.3 Fabrication of vertical Josephson junctions

1.3.1 Etch recipes

Several dry-etch recipes had to be developed on an Oxford ICP Plasmalab100 reactive ion etching machine for the fabrication of our samples. The involved NbN layers are several hundreds of nanometers thick, whereas the designed junction have side-lengths as small as 150 nm. The resulting aspect ratios call for very directional etch-processes. This was achieved through mixing different gases in the etching plasma. NbN is attacked both chemically, with SF_6 as well as mechanically, with Ar. A moderate forward bias accelerates the ions towards the sample and makes the etch more directional. Moreover, CH_2F_2 is added to the mixture, with the effect of polymerizing the exposed surface of the NbN film, making it less sensitive to the chemical etch. While in the vertical direction the Ar-bombardment constantly ablates the polymer film and leaves the surface exposed to the chemical etch; the sidewall of an etched step or trench stays protected. This permits the required aspect ratios for the etch (Fig. 1.2c). The MgO-barrier, on the other hand, is etched purely mechanically with a strongly biased argon plasma. It is worth mentioning that MgO is insensitive to the NbN etch described above. This allows us to use the MgO buffer and barrier tiers as stopping layers, meaning that we can let the NbN etch run longer to counteract inhomogeneities in etch speed over the entire wafer. Details on all the developed etch recipes can be found in appendix A.

1.3.2 Etching of the trilayer

Starting from the trilayer described in section 1.2.3, this first step is carried out with a combined optical lithography (OL) and electron beam lithography (EBL) process in order to be able to define small structures with high precision while keeping the processing times for bigger structures low. Again, entire 4 inch wafers are processed at a time. The following description will focus on the elaboration of one superconducting quantum interference device (SQUID) consisting of two Josephson junctions in a superconducting loop.
First, the wafer is coated in an EBL-sensitive resist (ZENON-ZEP520A) into which an EBL step and subsequent development define a rectangular hole. This shape is transferred to a Ti(10 nm):Pt(60 nm) hard-mask by evaporation and lift-off in a developer (AR-300-76). In the same step, the alignment markers for the remainder of the fabrication process are patterned. Then, a photosensitive resist (Clariant-AZ-1512-HS) is applied and the OL step is performed. As is shown on the scanning electron microscope (SEM) image Fig. 1.2b, the optical mask is designed in such a way that the EBL-defined rectangle is overlapping with an OL-patterned structure (the inner conductor of a transmission line). This allows for an unavoidable misalignment of several µm. After the trilayer is etched with a stepped dry-etch recipe, the hard-mask is removed with an argon plasma (see App. A). Finally, the wafer is sonicated in acetone and isopropanol for 10 minutes each to remove the photoresist. Throughout the process we systematically use a soft oxygen plasma to descum the wafer after the EBL steps and to clean it after resist removal.

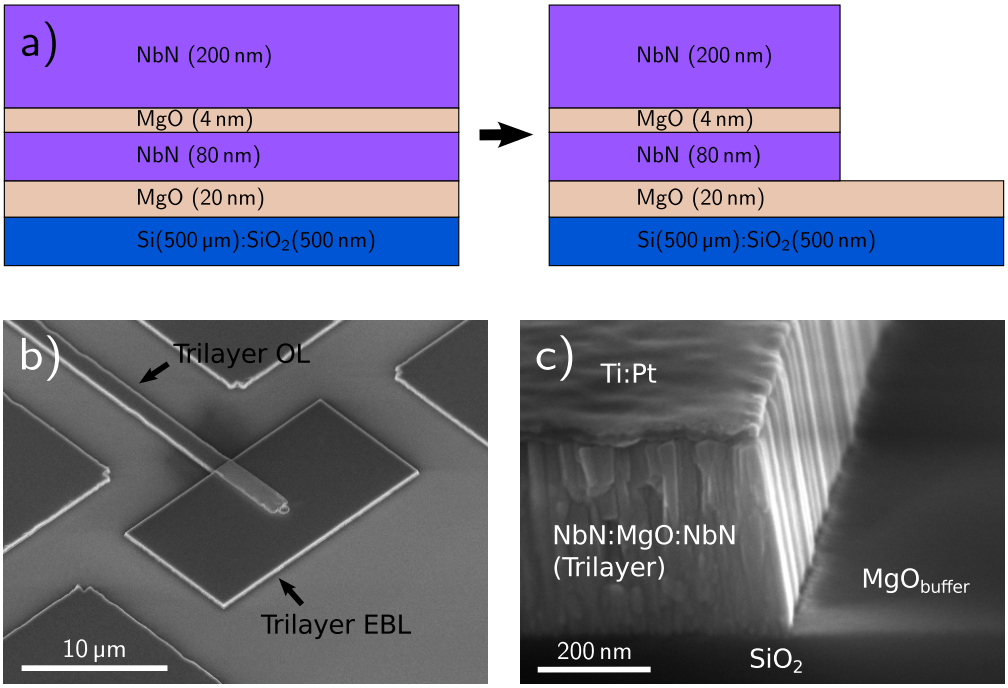

Figure (1.2): a) Representation of the NbN(80nm):MgO(4nm):NbN(200nm) stack (Trilayer) on top of the 20 nm MgO buffer layer and the substrate, before (left) and after (right) etching. b) Scanning electron microscope (SEM) micrograph of the structures etched in the first combined lithography step. The EBL-defined rectangle overlaps with an OL-defined structure coming in from the top left of the image. c) SEM micrograph of a step etched into a NbN:MgO:NbN trilayer using a Ti:Pt hardmask.

1.3.3 Self-aligned spacers

In this second step, the entire wafer is coated with a 500 nm thick film of Si_3N_4 by chemical vapor deposition (CVD). Then, a 10 nm thick layer of MgO is deposited on top of the SiN in order to protect it from overetching during subsequent fabrication steps. An optical lithography step is carried out defining regions where the dielectric will be etched. The entire SQUID lies in such an area. It should be noted that other structures, where the dielectric is etched away, include vias for mass-bridges over coplanar wave guides (see Sec. 2.3). In the structure at hand, the Si_3N_4 covers the step in the trilayer at the border of the rectangle defined by EBL earlier. After cracking the MgO with an argon milling step we perform an anisotropic dry-etch, similar to the one developed for NbN (see App. A). The vertical thickness of the dielectric at the step is considerably bigger than elsewhere. Hence, it can be etched away on all flat surfaces while leaving a self-aligned spacer clinging to the step (Fig. 1.3c).

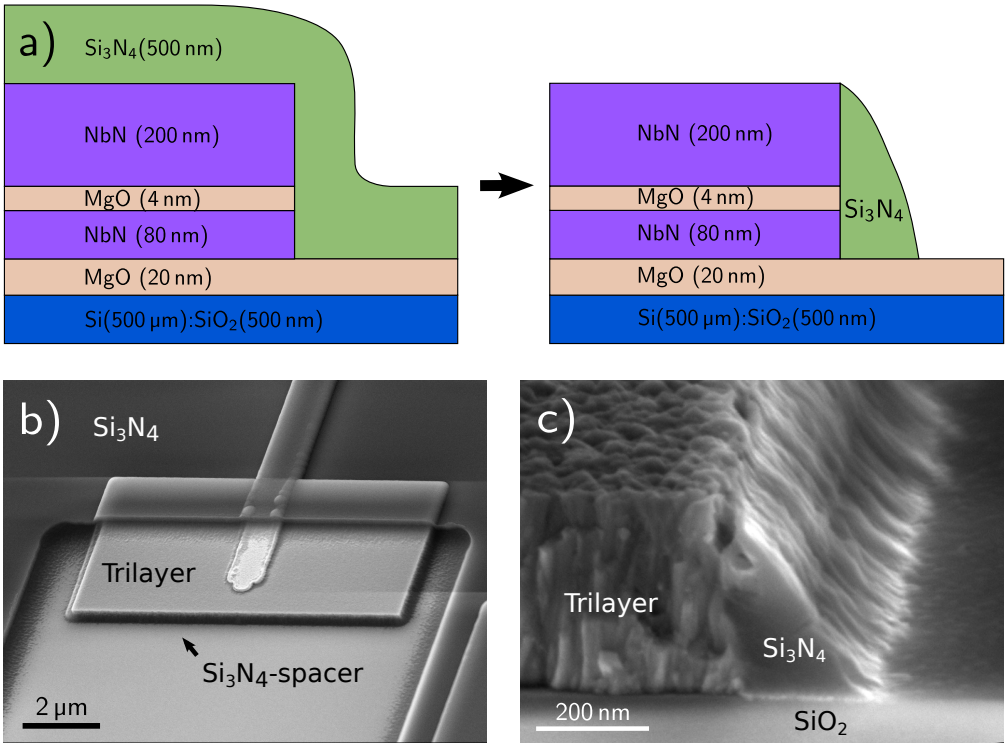

Figure (1.3): a) Representation of the trilayer covered by Si_3N_4 before (left) and after (right) etching. b) SEM micrograph of the SQUID after the second etch step. The areas where the dielectric is not etched away are darker. Note the self-aligned spacers surrounding the rectangle defined in the previous step. c) SEM micrograph of a Si_3N_4 spacer protecting a step in a trilayer.

1.3.4 Top-electrode

In the final major part of the fabrication process the wafer is once again taken back to the sputtering machine. After a brief back-sputtering step (10 min at 250 W) another layer of NbN (approximately 350 nm) is deposited. Then, another combined EBL (Ti(10 nm):Pt(60 nm) hardmask defined with PMMA and lift-off in acetone) and OL (AZ-1512-HS) step is carried out. In this etch step, the OL structures concern other areas of the waver. Two EBL-defined fingers overlap with the rectangle that has been etched into the trilayer. Once the unprotected areas are etched down all the way to the MgO tunneling barrier these fingers define the vertical Josephson junctions shown in Fig. 1.4c and the finished SQUID (Fig. 1.4b).

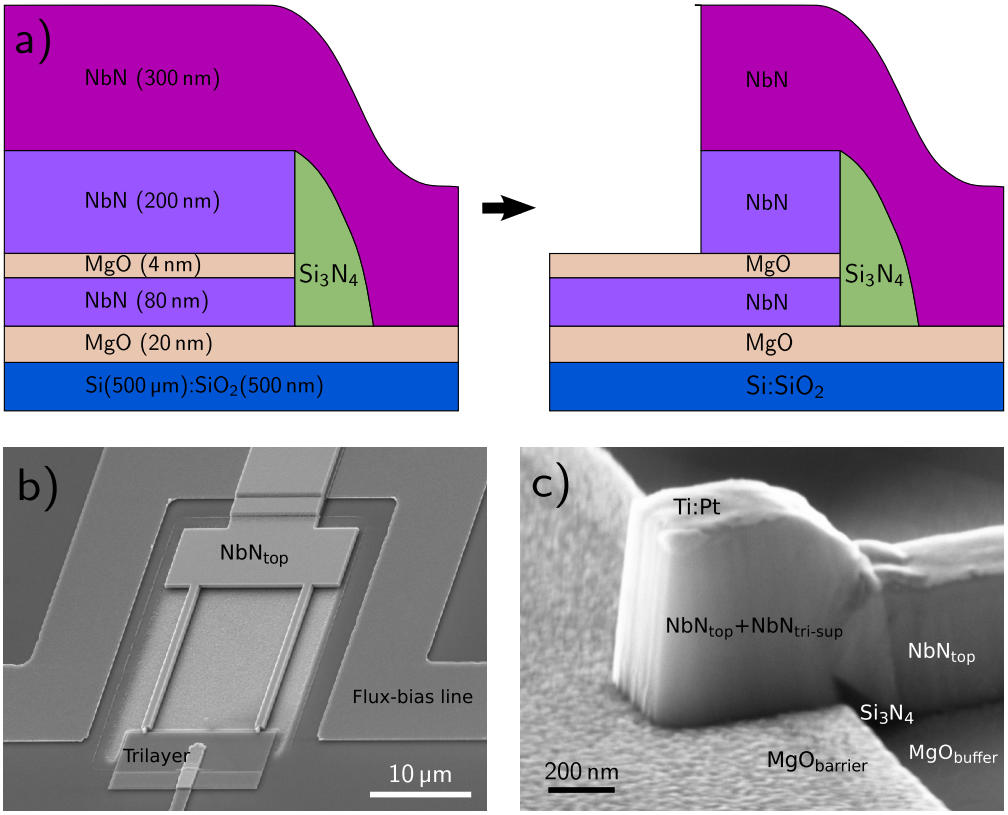

Figure (1.4): a) Representation of the step in the trilayer with self-aligned spacer covered by an NbN layer forming the top-electrode before (left) and after (right) etching. b) SEM micrograph of a finished SQUID. c) SEM micrograph of a Josephson junction. The Si_3N_4 spacer extends well beyond the lower NbN tier of the trilayer insulating it from the NbN top-electrode.

1.3.5 Chromium resistors

Some of our designs require resistive elements, which are realized on-chip with Cr films. In these structures the thin resistive sections (15 nm) alternate with much thicker cooling pads (100 nm). Both are deposited in the same fabrication step by using angle evaporation. An EBL step (ZENON-ZEP520A and AR-300-70) defines 300 nm wide trenches connecting bigger rectangles (Fig. 1.5). The thin lines are deposited by evaporating perpendicularly to the wafer into the narrow trenches. Afterwards, the direction of evaporation is tilted so that its angle with respect to the plane of the wafer is 35° and the angle between its projection onto the plane of the wafer and the trenches is 90°. In this configuration a 174 nm thick layer (vertical thickness: ≈ 100 nm) is deposited. Since the resist layer is > 300 nm thick, the Cr from this evaporation step does not go to the bottom of the trenches and is removed during the lift-off.

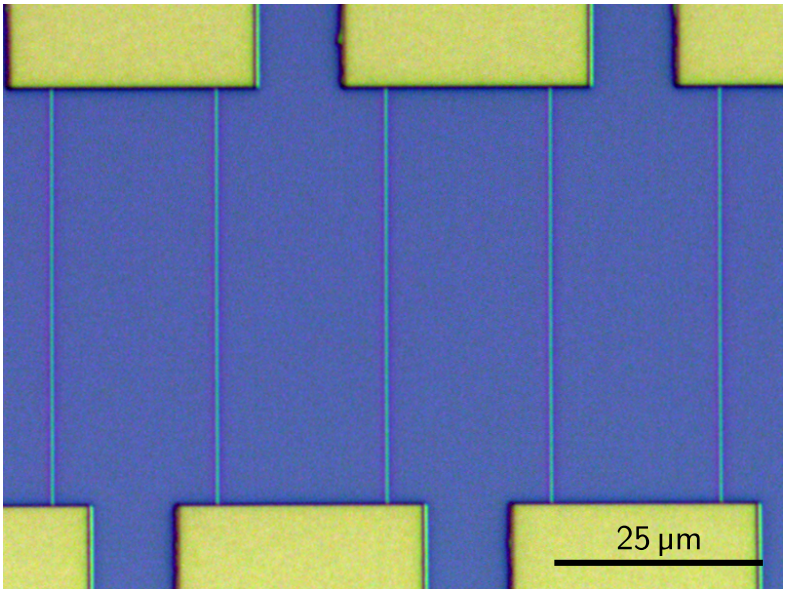

Figure (1.5): Optical micrograph of part of an on-chip Cr resistor showing thin resistive lines and thick cooling pads.

1.4 Characterization of the obtained Josephson junctions and trilayers

1.4.1 Properties of the NbN:MgO:NbN trilayers

Scanning electron microscope images show that the sputtered NbN films consist of columns with an average diameter of 20 nm. X-ray diffraction measurements confirm the polycrystalline structure and reveal that the films are of the cubic crystal phase of NbN. The superconducting transition temperature of the fabricated trilayers has been determined to be 14.8 K (Fig. 1.6) with a residual resistivity ratio of $R_{300\,\mathrm{K}}/R_{20\,\mathrm{K}} \approx 0.85$. These values were measured on a chip coming from the same wafer as the samples discussed in chapter 6. Columnar NbN thin films have a high upper critical field perpendicular to the film plane, with values reported in the literature ranging from 22 T [51, 52] to 40 T [53]. With the 9 T magnet available to us these values could not be directly confirmed, but the extrapolations of our curves fall into this range. The perpendicular lower critical field (the field at which vortices start to enter the film) has been shown to not exceed several tens of Gauss [54].
It is worth mentioning that in a different project, very thin (8 nm), textured, high-quality NbN films with a critical temperature of 13.2 K could be produced [55]. The conditions for the deposition of these films were slightly different and included heating the substrate to 300 °C.
Another important material property is the kinetic inductance per square $L_{\mathrm{kin},\square}$ of the films. L_{kin} of a superconducting wire is the reactive part of the impedance arising from

to the fact that an alternating current generates an oscillating magnetic field outside the wire, which enters the superconductor on the length scale of the penetration depth λ [56, 57] and works against the movement of the charge carriers. We calculate the value of $L_{\mathrm{kin},\square}$ from λ and the film thickness d according to the following formula:

$$L_{\mathrm{kin},\square} = \mu_0 \lambda \coth\left(\frac{d}{\lambda}\right) \tag{1.1}$$

Here, μ_0 is the permeability of free space. This expression can be derived from Maxwell's equations [57, 58] akin to the derivation of the skin effect in metals for a stripline-geometry transmission line, under the approximation that its width is much bigger than the thickness of the dielectric separating it from the ground plane. We calculate the penetration depth from the square resistance of the film $R_\square$ and the superconducting gap Δ:

$$\lambda = \sqrt{\frac{\hbar R_\square d}{\mu_0 \pi \Delta}} \tag{1.2}$$

This expression uses the results of Mattis and Bardeen for the complex conductivity of a superconductor [59, 60] in the limit where $\hbar\omega \ll 2\Delta$ and $k_\mathrm{B}T \ll \Delta$. It holds true in a local superconductor, where the coherence length ξ is much smaller than λ [57], meaning that the spatial extension of a Cooper pair is negligible compared to variations of the magnetic field inside the superconductor. Taking $R_\square \approx 7\,\Omega$, which is the value just before the superconducting transition on Fig. 1.6, and $\Delta \approx 2.07\,\mathrm{meV}$ (extracted in section 1.4.2) we find $\lambda \approx 400\,\mathrm{nm}$ and $L_{\mathrm{kin},\square} = 822\,\mathrm{fH}$. For $\lambda \gg d$, Eq. (1.1) can be approximated by $L_{\mathrm{kin},\square} \approx \mu_0 \lambda^2/d$. This simplified formula is often used. In our case, however, it gives $L_{\mathrm{kin},\square} = 709\,\mathrm{fH}$ leading to an error bigger than 16 %.

1.4.2 Properties of the fabricated Josephson junctions and superconducting resonators

A typical current-voltage characteristic of a junction with an area of $0.022\,\mu\mathrm{m}^2$ (150 nm side-length), measured at 4.2 K, is shown in Fig. 1.7. The gap voltage V_gap can be defined as the voltage at the steepest part of the curve, where $\mathrm{d}I/\mathrm{d}V$ is maximized [61]. Here, $V_\mathrm{gap} = 4.15\,\mathrm{mV}$ corresponding to a frequency of $\approx 1\,\mathrm{THz}$. A normal state resistance $R_N = V/I \approx 1.5\,\mathrm{M\Omega}$ can be extracted from the same curve far above V_gap at 7 mV. Together with the Ambegaokar-Baratoff formula at zero temperature $I_\mathrm{c}R_\mathrm{N} = \pi\Delta(0)/2e$ [56] and the relation $2\Delta = eV_\mathrm{gap}$ we find Eq. (1.3) and can evaluate the theoretical critical current at zero temperature to be $\approx 2.2\,\mathrm{nA}$.

$$I_\mathrm{c} = \frac{\pi V_\mathrm{gap}}{4R_\mathrm{N}} \tag{1.3}$$

The critical current density $J_\mathrm{c} = I_\mathrm{c}/A$, with A the surface of the Josephson junction, is $4.8\,\mathrm{A{\cdot}cm^{-2}}$. Note that our junctions are optimized for low critical current densities. J_c can easily be increased by several orders of magnitude. The current branch of the IV in Fig. 1.7

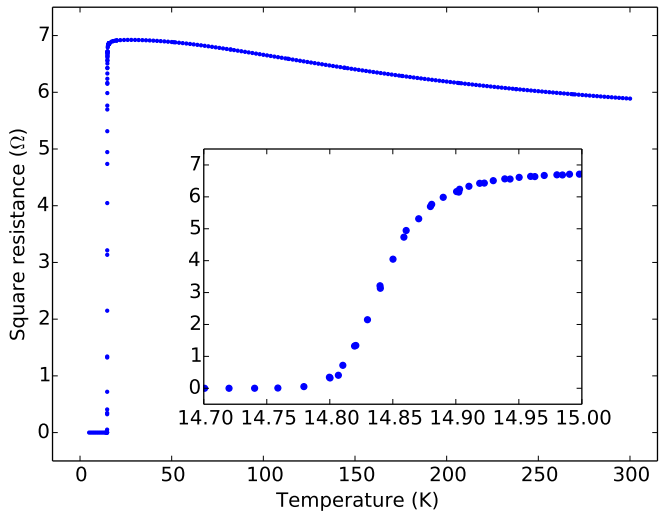

Figure (1.6): Square resistance in Ω against temperature curve showing the superconducting transition of the NbN:MgO:NbN trilayer. The inset is a zoom around the critical temperature.

is not visible, because the associated energy scale $E_J = \Phi_0 I_c/(2\pi) \approx 4.5\,\mu eV$ [56], where Φ_0 is the magnetic flux quantum, is much smaller than the thermal energy at 4.2 K ($k_B T \approx 362\,\mu eV$).

It is of particular importance to have as little leakage current under the gap as possible, for the physical effects we consider in this work to be feasible. In order to quantify the subgap leakage we compare the resistance under the gap (R_S) at 3 mV to R_N. A fit of the current voltage characteristic between −3 mV and 3 mV gives $R_S \approx 80\,M\Omega$ leading to $R_N/R_S < 0.019$. While the measured gap voltage on this specific sample is lower than the best values reported in the literature, the subgap resistance is comparable to the numbers achieved in other groups [61–63]. In particular, it should be pointed out that the smallest NbN:MgO:NbN tunnel junctions found in the literature have surface areas around $0.1\,\mu m^2$ [61, 64], several times bigger than the junction presented here, while showing considerably more subgap leakage.

Furthermore it is of interest to investigate the internal losses of a coplanar waveguide resonator fabricated from such a trilayer. The processed wafers systematically include samples with coplanar waveguide $\lambda/4$ resonators (see Ch. 2), which are capacitively coupled to a transmission line. This type of device shows a dip in its transmission measurement [21], from which the internal (Q_i) and external (Q_e) quality factors can be extracted. Here, we are interested in Q_i, which is limited by the internal losses of the material. Figure 1.8 shows the transmission S-parameters (ratio between transmitted and applied voltage signals [21]) of two such resonators. The samples were taken from the same wafer as the devices discussed in chapter 6. The data was taken at 12 mK and fitted

with an expression from reference [65] allowing us to extract Q_i and Q_e. The designed (fitted) external quality factors were 1000(1150) and 10000(8110) for the left and right panel respectively. The internal quality factors were found to be ≈ 6900 and ≈ 6700 and are probably limited by losses in the MgO buffer layer. With fast photon emission rates in mind, the resonators on the samples discussed in chapter 6 are coupled much more strongly to the outgoing waveguides leading to external quality factors of the order of 10 only. This means that the internal losses can safely be neglected by comparison.

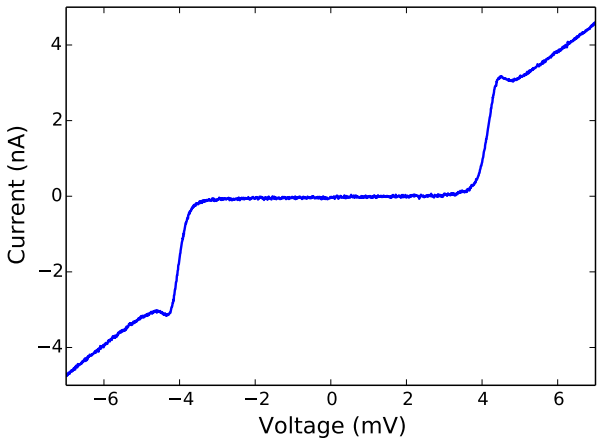

Figure (1.7): Typical current voltage characteristic of a SQUID consisting of two 150 nm × 150 nm *Josephson junctions in parallel.*

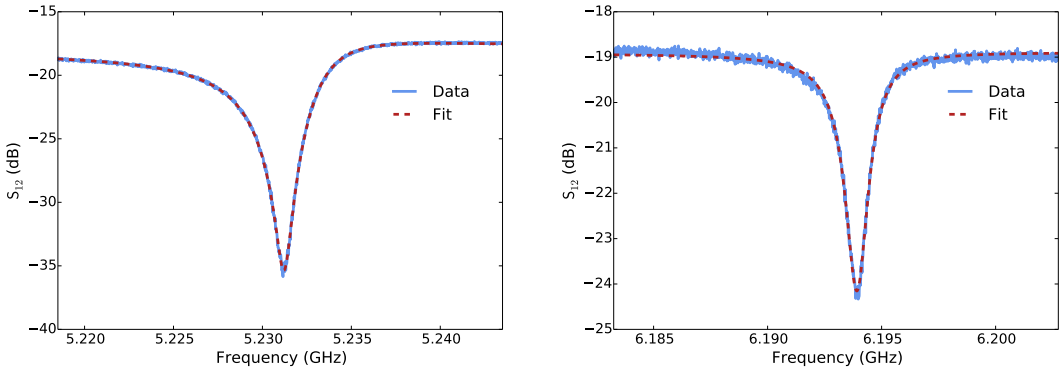

Figure (1.8): Transmission S-parameters of two side-coupled $\lambda/4$ resonators as a function of frequency. The blue solid lines are measurements and the red dashed lines are a fit used to extract the internal quality factors.

Chapter 2

Sample design

2.1 Introduction

As was mentioned in chapter 1, the nanofabrication process elaborated during this PhD work relies on the interplay between 3 electron beam lithography steps (EBL) and 3 optical lithography steps. The chromium masks for the latter are designed for 4 inch wafers. One wafer contains sixty-nine 10 mm × 10 mm chips. Global EBL alignment markers are present on the wafer and all individual chips, allowing us to process them separately if necessary. The 69 chips are subdivided into seven basic designs. The two main sample-types (Figs. 2.8 and 2.9) can be distinguished by the way how the emitted photons are coupled out to the measurement chain. The design of the first type is similar to the device measured in [20], while the second type makes use of an on-chip beam splitter and bias tee (see Sec. 2.5). In addition, the design contains samples with very high frequency or very high quality factor environments, chips with multiplexed coplanar waveguide resonators, as well as test chips to measure individual junctions, characterize sample holders and verify material parameters. The first two sample types are further partitioned by varying junction sizes, electromagnetic environments and the parameters of the RC circuit (see Sec. 2.6). The devices discussed in chapter 6 both contain on-chip beam splitters. In the following chapter an overview of the different parts of such a sample will be given. The basic concepts underlying each element will be touched upon and physical effects, as far as they pertain to the sample design, will be examined.

2.2 SQUID

A superconducting quantum interference device (SQUID) is a superconducting loop interrupted by two Josephson junctions in parallel. The critical current I_c^{Sq} of a SQUID depends on the critical currents of its constituent junctions and on the magnetic flux Φ threading its loop. When the SQUID is balanced, meaning that both junctions have the same critical current I_c, the expression of I_c^{Sq} takes the simple form (see App. D.5):

$$I_c^{Sq} = 2I_c \left| \cos\left(\frac{\pi\Phi}{\Phi_0}\right) \right| \tag{2.1}$$

Here, $\Phi_0 = h/(2e) \approx 2.068 \times 10^{-15}$ Wb is the magnetic flux quantum. The resulting effective Josephson energy is simply $E_J = \Phi_0 I_c^{Sq}/(2\pi)$ [56]. In the context of this work the SQUID will be treated as a Josephson junction with flux-tunable critical current and Josephson energy and the superscript Sq will be omitted from now on.
Figure 1.4 shows a superconducting line surrounding the SQUID on three sides. Its one end is connected to a current source via a 50 Ω matched transmission line, while the other merges into the ground plane of the chip. A current flowing through this line creates a magnetic field through the loop of the SQUID. The surface of the SQUID and its distance from this flux-bias line must be chosen so that it is easily possible to sweep at least one flux quantum through it without quenching the line. In order to verify our design parameters we can approximate the flux-bias line by a half circle. The magnetic field at the center of the SQUID is then just the half the field generated in the center of a loop of current carrying wire: $|\vec{\mathbf{B}}| = B_z = \mu_0 I/(4r)$. Here, μ_0 is the permeability of free space, I is the current through the wire and r is the radius of the half-circle. With $\Phi = |\vec{\mathbf{B}}|A$, where A is the inner surface of the SQUID, we get the expression of the minimum current necessary to sweep one flux-quantum through the loop:

$$I_{min} = \frac{4\Phi_0 r}{A\mu_0} \tag{2.2}$$

The radius of the flux-bias line is ≈ 20 µm and $A = 216\,\mu m^2$ giving $I_{min} \approx 610\,\mu A$, which should not lead to appreciable heating effects. In our measurements, NbN-lines with the same cross-section as the flux-line ($2.8\,\mu m^2$) have carried much higher critical currents of > 10 mA without quenching. In addition the entire area is surrounded by superconducting films, which should increase the local field density. Experimentally we indeed find a slightly smaller value of $I_{min} \approx 400\,\mu A$.
One last parameter of interest is the shunting capacitance of the SQUID. For a SQUID made of two 150 nm × 150 nm junctions with a MgO (relative permittivity $\epsilon_r = 9.9$) barrier thickness of ≈ 4 nm this capacitance is ≈ 1 fF and can be safely neglected at the working frequency of the device. Even at 1 THz it is small enough to not considerably limit the characteristic impedance (see following section and App. B) of the transmission line connected to it ($Z_0 = 1/(\omega_0 C) \approx 160\,\Omega$).

2.3 Superconducting coplanar waveguides

The microwave photons emitted by our system are electromagnetic wave-packets with frequencies in the GHz range. In this frequency regime, the wavelength of an electric signal in a conductor is of the order of millimeters and effects like reflection and superposition can occur even on the scale of a 10 mm × 10 mm chip [21]. Therefore, we have to use transmission lines, supporting radio frequency (RF) modes, to lead the produced signal away from its source.

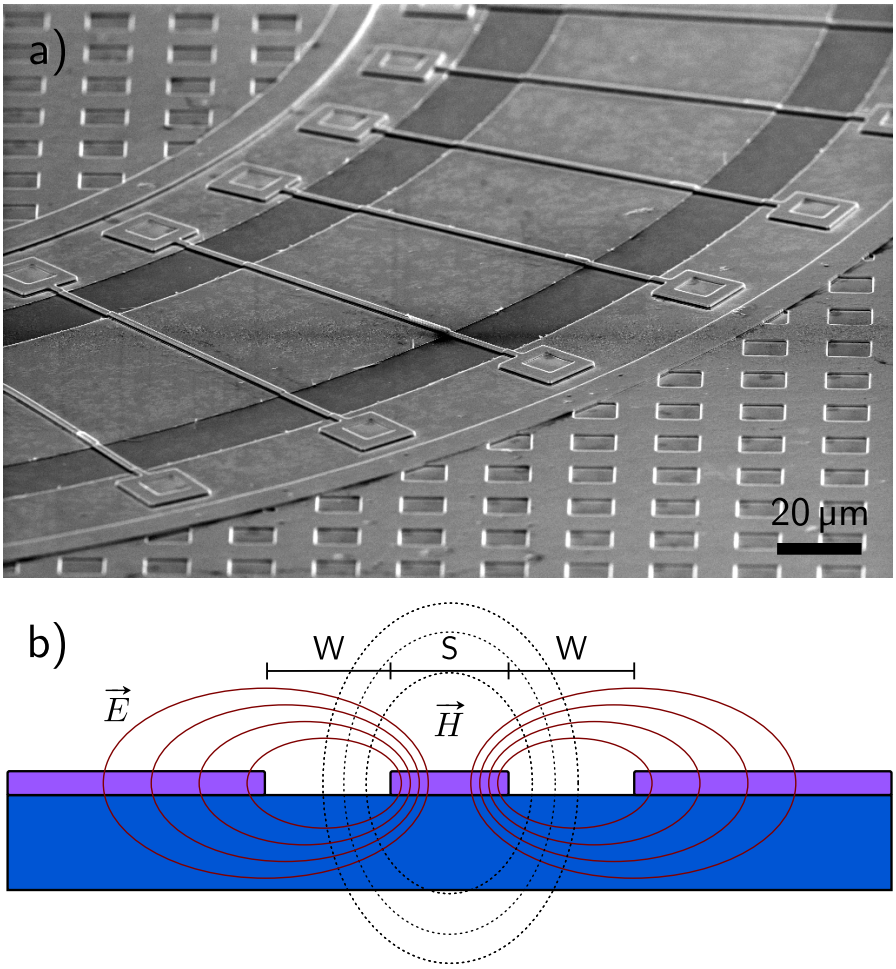

Figure (2.1): a) SEM micrograph of a coplanar waveguide with bridges connecting the ground planes on both sides of the inner conductor. b) Schematic section of a CPW with S and W being the widths of the center conductor and the gap. The electric and magnetic field lines are sketched. For clarity the magnetic field lines around the ground planes have been omitted.

A coplanar waveguide (CPW) transmission line consists of a center conductor and two lateral ground planes on a dielectric substrate (Fig. 2.1b). It resembles a coaxial cable in two dimensions and can carry a quasi-transverse electromagnetic (TEM) mode, where the electric and magnetic field are nearly perpendicular to the direction of wave-propagation [21]. A superconducting CPW is an almost perfectly lossless transmission line (TL) and is fully described by its shunting capacitance to ground C and series-inductance L. Both are distributed quantities and are usually given per unit length. More practically, these parameters are expressed in terms of the CPWs characteristic impedance $Z_0 = \sqrt{L/C}$ and phase velocity $v_\mathrm{p} = 1/\sqrt{LC}$. Z_0 is the ratio between voltage

and current amplitudes of the wave on the line. The theoretical model of such a TL is developed in more detail in appendix B, while here only the the main results will be used. When a CPW is connected to a load impedance or another CPW of different Z_0, the signals propagating on it are partially reflected at the interface and form standing waves. The voltage and current amplitudes of these standing waves vary as a function of the distance from the interface. Their ratio, the input impedance Z_{in}, is a function of the position along the line and the signal frequency (Fig. B.2). The input impedance seen when looking into a TL of characteristic impedance Z_0 at a distance l from a load impedance Z_{L} is given by the transmission line impedance equation (see App. B.2):

$$Z_{\text{in}} = \frac{Z_{\text{L}} + jZ_0 \tan(\beta l)}{Z_0 + jZ_{\text{L}} \tan(\beta l)} Z_0 \tag{2.3}$$

The propagation constant β depends on the wavelength λ or the angular frequency ω as $\beta = 2\pi/\lambda = \omega/v_{\text{p}}$. One important special case is the matched load $Z_{\text{L}} = Z_0$. Then, the equation simplifies and $Z_{\text{in}} = Z_{\text{L}}$ regardless of position or frequency. This is usually desirable in experimental setups when performing RF measurements, meaning that no signal will be lost to reflections. Another astonishing consequence of (2.3) is that the input impedance seen at a distance $\lambda/4$ from the load is:

$$Z_{\text{in}}(-\lambda/4) = \frac{Z_0^2}{Z_{\text{L}}} \tag{2.4}$$

The load impedance has been reversed to its opposite, turning, for instance, a short into an open and vice versa. In the following sections this effect will be used repeatedly as coplanar waveguides of length $l = \lambda/4$ with different characteristic impedances are the main building blocks of our design.

2.3.1 Implementation of CPWs with our fabrication process

The basic coplanar waveguide structures (center conductor and ground planes) are defined in the first optical lithography step and etched into the trilayer (see Sec. 1.3.2). At our operating frequencies, the wavelengths in the designed CPWs are around $\approx 10\,\text{mm}$. Several $\lambda/4$ elements will only fit on a chip, if they are folded to save space. This can lead to a host of problems due to the separated ground planes. When a signal propagates along a bend in the wave guide, it can give rise to charge imbalances between the grounds on either side and cause losses due to excitation of ground plane modes. Usually, these complications are circumvented by connecting both sides of the ground plane with wire bonds. A particularity of our multi-layered fabrication process is that we can easily make ground-bridges over our CPWs by opening up vias through the Si_3N_4 above the ground planes on either side of the center conductor and connecting them with the top NbN-layer (Fig. 2.1a). Both types of structures are defined using the respective optical lithography steps.

2.3.2 CPW parameters used in this work

In order to vary Z_0 of a CPW, one must change its capacitance and inductance. Making the width W of the gap smaller and the width S of the center conductor bigger, increases the capacitance to ground and reduces the inductance [66]. Aiming to keep CPW of different Z_0 interconnect-able, the total width $S + 2W$ was fixed to 100 µm or 20 µm, depending on the sample. We then used a Python-based finite surface element simulation program, written in our group, to compute C and L for different geometries. This program also takes into account the kinetic inductance of NbN, which we estimated from the results shown in section 1.4.1. When finally computing the L and C per unit length of a specific CPW geometry, we also had to consider the parts with ground-bridges over them. The capacitance to ground of these sections is greatly enhanced. We averaged the two types over the length of the line using effective widths for the bridges that take into account their lateral capacitance. This was done by approximating them to microstriplines across the central conductor and comparing the resulting capacitance to that of a parallel plate capacitor. Table 2.1 shows the main parameters for different types of CPW elements used in our design.

Z_0 (Ω)	C (pF·m^{-1})	L (nH·m^{-1})	L_{kin} (%)	S (µm)	W (µm)	d_{bridge} (µm)
146	64	1361	26	2	49	1000
50	262	643	10	18	41	50
31	472	459	8	40	30	50
22	704	349	9	64	18	50
14	1099	226	26	96	2	50
90	114	898	33	3	8.5	100
70	140	719	29	5	7.5	100
50	204	512	27	10	5	100

Table (2.1): Some relevant parameters of the CPW geometries used in this work. The definitions of S and W are shown in Fig. 2.1. The ground bridges have a width of 2 µm and the distance between the centers of two consecutive bridges on the line is given by d_{bridge}. All simulations have been carried out using the layers of materials and thicknesses specified in chapter 1. At a frequency of 6.7 GHz, the length of a $\lambda/4$ element is 2.4 mm to 4 mm depending on the parameters of the CPW.

2.4 CPW resonators

It has already been mentioned that combining CPW segments with different characteristic impedances can lead to standing waves in the voltage and current signals propagating on them. This effect makes it possible to build resonators out of transmission lines. A very intuitive example for this is the $\lambda/2$, or half-wave, resonator. It simply consists of a piece of transmission line of length l connected on both sides to lines with different Z_0. Just as in a Fabry-Perot cavity, reflections on both interfaces will create standing waves when the resonance condition $l = n\lambda/2$ (with $n \in \mathbb{N}$) is fulfilled.
In our case, we use $\lambda/4$, or quarter-wave, resonators. In that instance, the boundary conditions are not the same on both sides. If Z_0 is the characteristic impedance of the transmission line segment, then the load impedances connected to it on either side will be chosen such that e.g. $Z_{\text{left}} \gg Z_0 \gg Z_{\text{right}}$. Here, resonance occurs when $(2n+1)\lambda/4 = l$ (Fig. B.3).
In our design the resonator is connected to the SQUID on one side. In the GHz and THz ranges the impedance of the SQUID is many orders of magnitude higher than what can be reached with standard CPW geometries. In the context of this discussion it can therefore be treated as an open end (Z_{left}). Ideally, Z_{right} would then be a short, but we want to lead the photons in the resonator out towards an amplifier. Thus, we connect the right side to a low impedance line. Particularly low input impedances can be achieved by cascading several $\lambda/4$ sections. A detailed description of this approach and a derivation of the equivalence between this kind of resonator and a lumped element parallel LCR-resonator can be found in appendix B.3.

2.5 On-chip bias tee and beam splitter

2.5.1 Working principle

A key design element in many of our samples is a 4 port on-chip network of quarter-wave CPW segments fulfilling multiple purposes. On the one hand, it acts as a 50/50 beam splitter presenting two equal cascaded $\lambda/4$ resonators, each coupled to its own output port, to the SQUID, while isolating the ports from each other. On the other hand, it plays the role of a bias tee allowing to connect a third DC bias port to the SQUID, while decoupling it at high frequencies. Three different types of this device have been designed and used on our samples, the difference being the width in frequency of the resonator seen by the SQUID. The three versions have full widths at half maximum (FWHM) of 175 MHz, 350 MHz and 700 MHz and a common resonance frequency of 6.7 GHz. This leads to quality factors of $\approx 40, 20$ and 10 respectively.
Figure 2.2 gives a schematic representation of the device and Fig. 2.3 shows an optical micrograph of its central area. On the drawing, each purple line corresponds to a CPW. The respective characteristic impedances of each line are indicated and the 50 Ω-matched ports are marked by red circles, while the SQUID is represented by a cross. Each port is assigned a number to facilitate indexing for the quantitative analysis below. On the

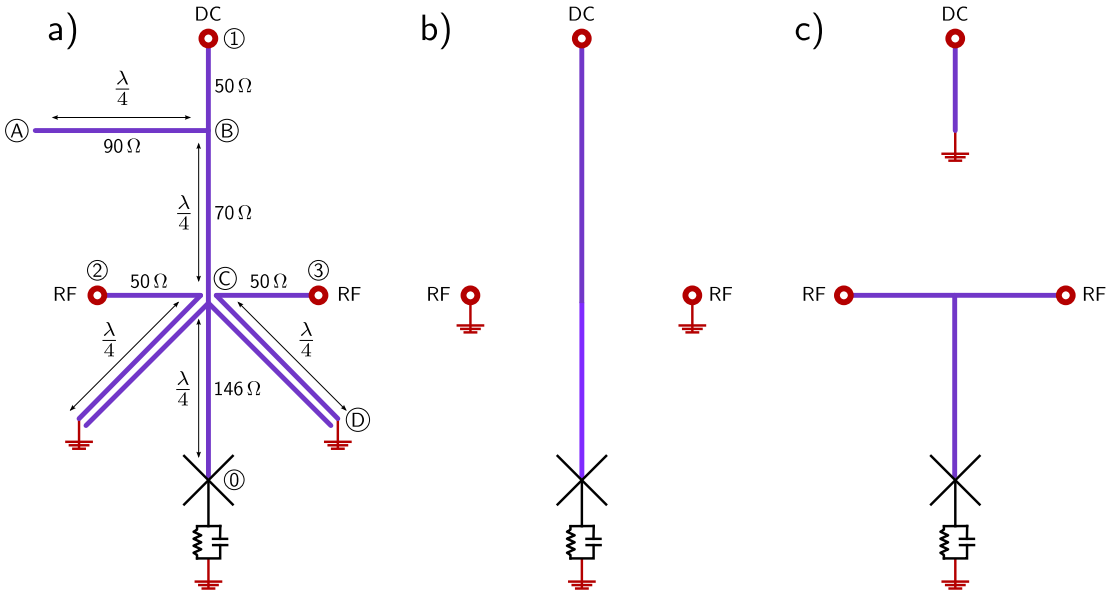

Figure (2.2): a) Schematic of the on-chip bias tee and beam splitter. Each simple purple line represents a CPW. The twin lines stand for a CPW with a double inner conductor. Characteristic impedances, ports and $\lambda/4$ segments are indicated. The SQUID is marked by a cross and is either grounded directly (not shown) or through an RC circuit. b) Schematic at low frequency. The two RF ports are grounded and the junction is directly connected to the DC bias port. c) Schematic at resonance frequency. The RF ports are connected to the junction and the DC port is grounded.

sample type depicted here, the SQUID is grounded through an RC circuit. Various quarter-wave segments are denoted by a $\lambda/4$. The two 45° double lines on the schematic are CPW-like lines with two inner conductors, which are coupled capacitively. The different ports and areas of interest highlighted by circled numbers and letters are also indicated in Fig. 2.8, which shows an entire chip with two samples.

Intuitively, the working principle of the device can be understood by considering separately what happens at the resonance frequency f_0 of the $\lambda/4$ segments and at zero frequency. In the latter case, the only port connected to the junction is the DC bias port, while the RF ports are grounded (Fig. 2.2b).

In contrast to that, at f_0 the open end of the stub at A transforms to a short at B and to an open again at C. This means that the RF ports and the SQUID are isolated from the DC port and that the impedance seen by the SQUID will be dominated by the RF ports. At the same time, this acts as a filter reflecting noise leaking down the DC measurement setup.

In a simplified picture, the double lines on either side can be seen as two capacitively coupled CPWs of impedance $Z_0 < 145\,\Omega$. Then, the line terminated in an open forms a stepped $\lambda/4$ resonator with the $146\,\Omega$ section next to the SQUID. Due to the symmetry of the impedance, a photon has a 50 % probability to be emitted either left or right. The

resonators capacitively couple to the RF ports through the other inner conductor letting the signal leak out towards the measurement setup.

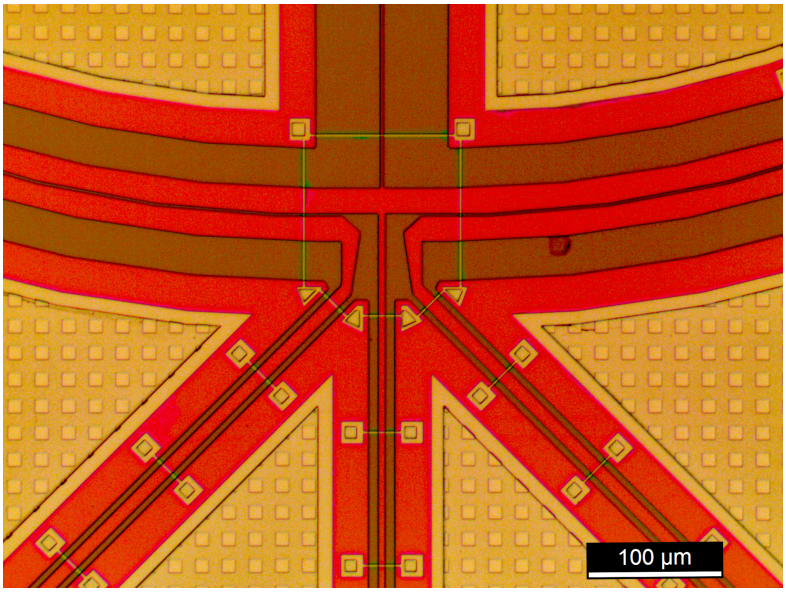

Figure (2.3): Optical micrograph showing the central area of the on-chip bias tee and beam splitter around point C from Fig. 2.2a. CPWs are visible as red lines separated by brown gaps from the red ground planes. Mass bridges appear in yellow. The continuous yellow regions are areas where the dielectric and the top-electrode are partially etched away to avoid macro-loading effects during the dry-etching. The CPWs leaving the image on the lower left and right are leading to the two RF ports. The line running straight down goes to the DC port. On the upper half of the picture the coplanar waveguides with double inner conductors are seen arching upwards. The line going straight up is the high-Z_0 CPW leading to the junction.

2.5.2 Simulation

A Python-based simulation program for linear networks was used to compute the frequency dependent response of the device. The simulator has been written in our group and computes the admittance matrix of a network defined by nodes, ports and circuit elements connecting them. The latter can be either lumped elements, regular transmission lines or multi-conductor TLs as the ones used in the beam splitter. Parameters such as the mutual capacitance between inner conductors are calculated with the finite surface element simulator mentioned before. This section will specifically focus on the 175 MHz version of the device, which is the one used on the samples discussed in chapter 6.
The first port to be analyzed is the SQUID. Here, the input impedance and the voltage response to a current through the SQUID port at the RF and DC ports are of interest. Figure 2.4 displays these quantities. The solid blue line shows the real part of the impedance seen by the SQUID when looking into the circuit. The other lines plot

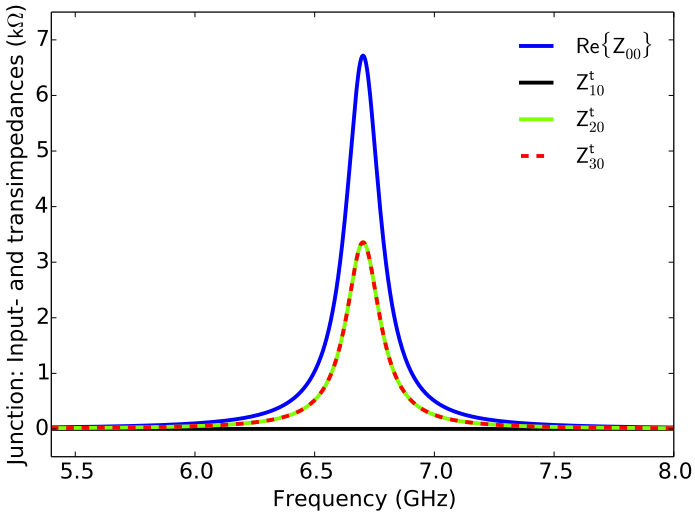

Figure (2.4): Solid blue line: Real part of the input impedance of the network seen by the SQUID. Solid green line and dashed red line: Magnitude of the voltage response at the RF ports to a current at the junction. Solid black line: The same quantity for the DC port.

quantities defined from the trans-impedances Z_{i0} as $Z^t_{i0} = |Z_{i0}|^2/50$. This is the part of the dissipation, i.e. $\mathrm{Re}\{Z_{00}\}$, due to the power emitted into the $50\,\Omega$ matched port i for unit current at the SQUID. It can be seen, that at resonance the signal is distributed only and evenly between the two high frequency ports (solid red line and dotted green line), while the DC port is isolated. This behavior is desirable, since we do not want any signal to leak into the low-frequency bias line, and is in good agreement with the intuitive description.

Further quantities of interest are the isolation between the DC and the RF ports and the filtering of the DC port against high frequency signals coming down the bias line (Fig. 2.5). At this point, it is advantageous to introduce the concept of S-parameters. Using the definitions for the complex voltage amplitudes from appendix B we can write: $S_{ij} = V_i^-/V_j^+$. Strictly speaking S_{ij} is the ratio between the complex voltage amplitude entering the network at port j and the outgoing voltage at port i, when all other ports are terminated with $50\,\Omega$ loads. The junction is not considered as a port, but simply as an open. Since none of the S-parameters shown in the following involve the junction this approach is justified. The S-parameters are given in units of decibel of power ratios as $20\log|S_{ij}|$. The first quantity to look at, is the reflection of incoming signals at the DC port $|S_{11}|$ (solid blue line). It is almost unity over a wide frequency range of several GHz around the resonance, meaning that high frequency noise on the DC bias line is reflected before reaching the sample. The solid green and dotted red lines show the transmission parameters from the RF ports to the DC port and for symmetry reasons also in the inverse direction. Isolation is generally rather good ($|S_{1i}| < -12\,\mathrm{dB}$) and

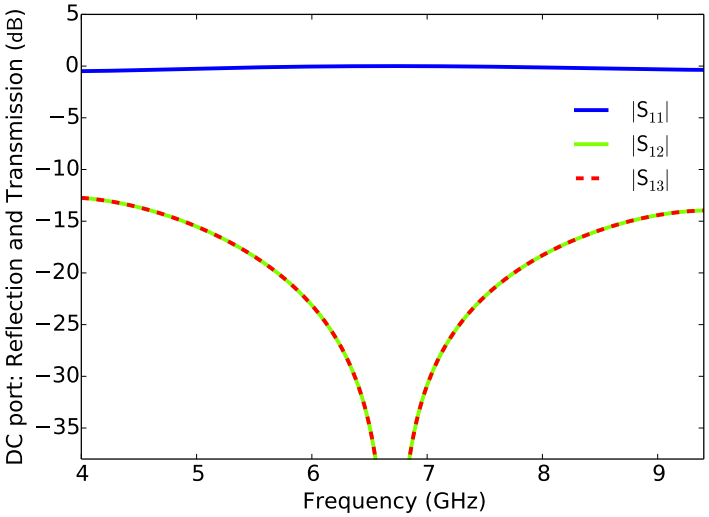

Figure (2.5): Isolation properties of the DC port. Solid blue line: Reflection S-parameter of the DC port. Solid green line and dashed red line: Transmission S-parameters between the RF ports and the DC port.

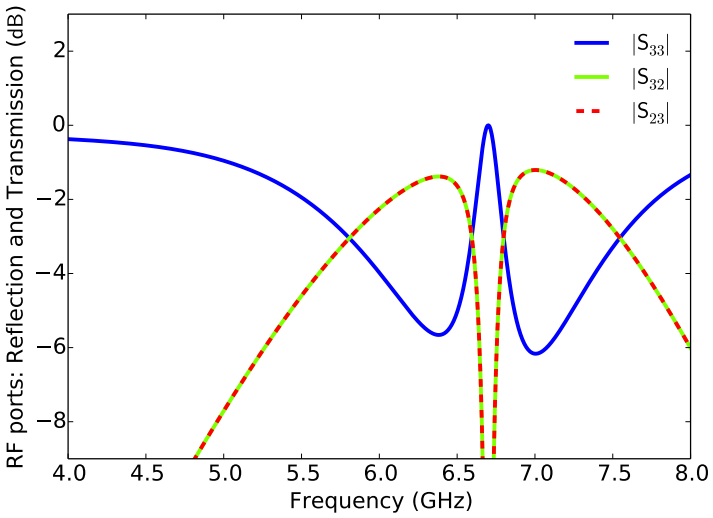

Figure (2.6): Isolation properties of the RF ports. Solid blue line : Reflection S-parameter of an RF port. Solid green line and dashed red line: Transmission between the two RF ports.

becomes excellent around resonance.
Figure 2.6 gives an overview of the different S-parameters concerning the RF ports. The abscissa was chosen corresponding to the frequency range of our cold amplifiers and circulators. Both, the reflection of incoming signals at the ports ($|S_{33}|$, solid blue line), and the transmission between the two ports ($|S_{32}|$ and $|S_{23}|$, solid green and dotted red lines) exhibit the behavior of a bandstop filter with a bandwidth of $\approx 200\,\mathrm{MHz}$ around $f_0 = 6.7\,\mathrm{GHz}$.

2.5.3 Spurious mode

Usually a beam splitter has four ports [21], which is not the case in our device seeing that the DC port is not part of the splitter but of the bias tee. The missing port acts like an open and leads to reflections and transmission between the RF ports. Nevertheless, this would also be the case for a four-port beam splitter, because the junction port is not matched. Comparing our structure to a 180° hybrid ring coupler one might say that we lack two more lines of length $\lambda/4$ and $3\lambda/4$ connecting the open ends at D to a fifth port (the Δ port) terminated with a cold $50\,\Omega$. However, this is an imperfect comparison, since it does not take into account the effect of the capacitively coupled inner conductors effectively connecting the RF-ports to point C on resonance. Additionally, in contrast to a 180° hybrid ring coupler, the last $\lambda/4$-element between the junction and point C (which would be the Σ port in this analogy) acts as a stub. It transforms the open at the junction to a short at C and leads to reflection of the incoming radiation from either RF port. This can be seen in Fig. 2.6, where the transmission between the two RF ports steadily rises when approaching the resonance frequency (the effect of the coupling through the double inner conductors), before it drops rapidly (the reflection due to the stub). As a result, the bandwidth of the isolation between the two RF ports is not very large, while still being sufficient to contain the resonator.

We have conducted a second simulation, where we eliminate the last $\lambda/4$ element between point C and the junction. The result is shown in Fig. 2.7 and confirms that without the stub no reflection occurs and the RF ports are coupled.
In order to be sure that the junction does not couple to a spurious $\lambda/2$ mode between the two RF branches of the device, we have run additional simulations, where we introduce asymmetries into the system. This is done by making one side of the beam splitter between points C and D shorter than the other. Then, in Z_{in}, the $\lambda/2$ resonance should detach from the peak of the $\lambda/4$ element. Nevertheless, we do not see another resonance appear, neither in our simulations nor during our experiments.

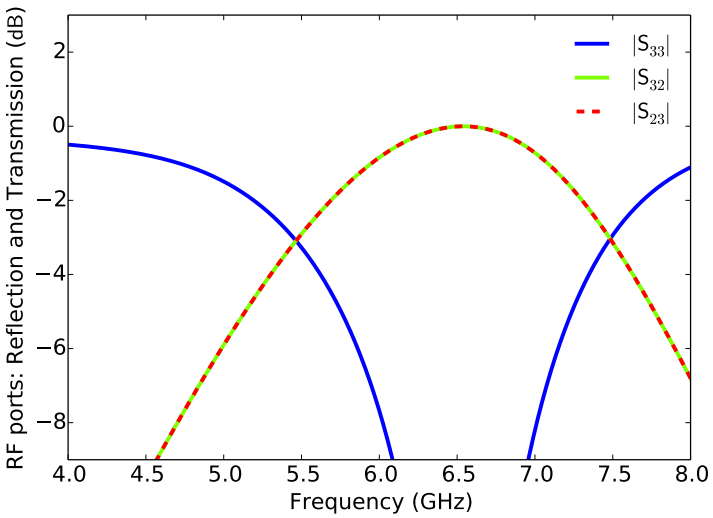

Figure (2.7): Isolation properties of the RF ports, when the $\lambda/4$ element between point C and the junction is removed. Solid blue line : Reflection S-parameter of an RF port. Solid green line and dashed red line: Transmission between the two RF ports.

2.6 On-chip resistor and capacitance to ground

Certain samples need a parallel RC-circuit connecting the SQUID to ground (see introduction and Secs. 5.3.2 and 6.3). The capacitive part of this element can be seen on the lower right-hand side image of Fig. 2.8. The top NbN electrode passes over the (grounded) flux-bias line, which is covered by Si_3N_4, and contacts the chromium resistor on the other side. This forms a parallel plate capacitor with a surface of 200 µm^2 and a dielectric thickness of 500 nm resulting in a capacitance to ground of $C \approx 25$ fF. This value is the same for all our samples. The resistive part is fabricated using chromium (see Sec. 1.3.5), which was chosen for its relatively high resistivity allowing us to limit stray capacitances by keeping the resistor short. It consists of thin (15 nm) resistive lines connected by much thicker (100 nm) cooling pads (right upper frame of the figure). Four different values of resistance were used in our sample designs: 11 kΩ, 21 kΩ, 43 kΩ, and 107 kΩ. These values were calculated from the number of squares on each sample and the square resistance of an independently deposited Cr film and are somewhat smaller than what was originally projected. This is partially due to an initial overestimation of the resistance of the Cr films. Even though far from ideal in terms of parameters, a sample with a 21 kΩ will be discussed in this section, because this type was measured first and has given the results of chapter 6. The values given in parentheses correspond to another designed resistor of 107 kΩ, giving longer RC times and more favorable heating conditions.

2.6.1 Heating and cooling effects in the resistors

Each resistor is deposited on the MgO buffer layer and is connected to superconducting leads on both sides. Here it will be described how the electron phonon coupling in the thick pads between the resistive lines helps to cool the electron temperature of the resistor below prohibitive values. Three suppositions will be made in this analysis:

1. The Joule heating in the resistor can be estimated using the average current given by the RC time. For a sample with $R = 21\,\mathrm{k\Omega}$ ($107\,\mathrm{k\Omega}$) the RC time is $\approx 0.5\,\mathrm{ns}$ ($2.7\,\mathrm{ns}$) and the resulting current is $I = 2e/RC = 0.6\,\mathrm{nA}$ ($0.12\,\mathrm{nA}$). This leads to a Joule heating power of $I^2R = 7.6\,\mathrm{fW}$ ($1.5\,\mathrm{fW}$).
   A second supposition is hidden in this one, namely that the temperature in the film is constant in time. This is the case, because the fluctuations in current on the timescale of RC are averaged out by the heat capacity of the electrons. The electronic heat capacity of a metal of volume V and conduction electron density n at a temperature T is [67]:

$$C_\mathrm{e} = \frac{\pi^2}{2} k_\mathrm{B} n V \frac{T}{T_\mathrm{F}} \tag{2.5}$$

   Here $k_\mathrm{B} \approx 1.38 \times 10^{-23}\,\mathrm{J{\cdot}K^{-1}}$ is the Boltzmann constant and $T_\mathrm{F} \approx 5 \times 10^4\,\mathrm{K}$ is the Fermi temperature. For one conduction electron per atom the electron density n evaluates as $n = \rho N_\mathrm{A}/A_\mathrm{r}$, with $N_\mathrm{A} \approx 6.02 \times 10^{23}\,\mathrm{mol^{-1}}$ the Avogadro constant, ρ the volumetric mass density and A_r the relative atomic mass.
   For Cr, $\rho \approx 7.19 \times 10^3\,\mathrm{kg{\cdot}m^{-3}}$ and $A_\mathrm{r} \approx 52 \times 10^{-3}\,\mathrm{kg{\cdot}mol^{-1}}$. The volume of the resistor is dominated by the cooling pads and is thus $V \approx 2000\,\mathrm{\mu m^3}$ regardless of the value of R. The energy needed to heat the structure up by $\Delta T = 1\,\mathrm{mK}$ is $C_\mathrm{e}\Delta T = 28.3\,\mathrm{eV}$. Comparing this to the Joule heating power yields a rise time: $\Delta t = C_\mathrm{e}\Delta T/P \approx 0.6\,\mathrm{ms}$. Fluctuations on the order of ns can safely be neglected.

2. The second assumption is that the Kapitza thermal resistance originating from the coupling of the phonon populations across the boundaries between the different layers of our substrate ($\mathrm{Si}(500\,\mathrm{\mu m}){:}\mathrm{SiO_2}(500\,\mathrm{nm}){:}\mathrm{MgO}(20\,\mathrm{nm})$) and the chromium pads is negligible. Following the reasoning of [68] we consider that a thin film cannot have an independent phonon population if its thickness is inferior to the wavelength of the most energetic phonons at a given temperature. Assuming that the Si base of the substrate is well thermalized with the copper sample holder, the combined thickness of the remaining films is $d = 620\,\mathrm{nm}$. For $T \ll T_\mathrm{D} = 460\,\mathrm{K}$, where T_D is the Debye temperature in Cr [67], only acoustic phonons are relevant, which have an energy $E_\mathrm{ph} = hv_\mathrm{c}/\lambda = k_\mathrm{B}T$ [67]. Here $v_\mathrm{c} = 5.9 \times 10^3\,\mathrm{m{\cdot}s^{-1}}$ is the speed of sound in chromium [69]. We make the above condition more stringent by requiring that even quarter-wave resonances can be excluded. The minimum temperature needed to excite phonons of $\lambda/4 = d$ is $\approx 114\,\mathrm{mK}$, a value clearly superior to the base temperature of our dilution refrigerator ($12\,\mathrm{mK}$).

3. Another premise is that there is no heat diffusion between the resistor and the superconducting contacts. The critical temperature of NbN being $\approx 15\,\mathrm{K}$, even hot electrons are far below the gap and the entire dissipated power has to be evacuated through electron-phonon coupling in the cooling pads.

With these three assumptions in mind, the electron temperature of a resistor with volume V, taking into account Joule heating and coupling to a phonon bath of temperature T_{ph}, is given by [68, 70]:

$$T_e = \sqrt[5]{T_{\mathrm{ph}}^5 + \frac{I^2 R}{\Sigma V}} \tag{2.6}$$

The electron phonon coupling constant Σ has values around $2 \times 10^9\,\mathrm{W{\cdot}m^{-3}{\cdot}K^{-5}}$ for good metals [70]. To work with a lower bound we will consider it to be $0.2 \times 10^9\,\mathrm{W{\cdot}m^{-3}{\cdot}K^{-5}}$ in our case [71]. The resistor at hand has 12 cooling pads connected by 12 thin resistive line of length 10 µm (50 µm) and width 0.3 µm each. For $T_{\mathrm{ph}} = 15\,\mathrm{mK}$, if there were no cooling pads, the electron temperature of the wire would be $\approx 150\,\mathrm{mK}$ (78 mK). Taking into account the volume of the pads the average electron temperature of the entire structure is $\approx 30\,\mathrm{mK}$ (22 mK). This statement relies heavily on assumption 3. It means that, while the entire heating is created in the lines, the entire cooling happens in the pads.
Another problem could arise in this context. Even though on average T_{e} is acceptable, the local electron temperature in the resistive lines could still be too high. Due to their small volume, electron-phonon coupling in the lines is negligible and they are in the hot electron interaction limit [72]. This can be confirmed by computing their electron phonon interaction length ($\approx 5.4\,\mathrm{mm}$) [70, 72]. The temperature profile along the wire in the normalized coordinate x is given by [70]:

$$T_{\mathrm{e}}(x) = \sqrt{T_{\mathrm{ph}}^2 + \frac{3}{\pi^2} x(1-x) \left(\frac{eRI}{k_{\mathrm{B}}}\right)^2} \tag{2.7}$$

The resulting temperature curve is very flat, with a difference between the T_{e} on the borders (electron temperature of the pads) and the maximum in the middle of the wire of only 0.7 % (1.2 %).
Finally, $k_{\mathrm{B}}T_{\mathrm{e}}$ should be compared to the smallest relevant energy scale in our system, the charging energy of the capacitor. With the calculated capacitance we find $E_{\mathrm{C}}/k_{\mathrm{B}} = 2e^2/(k_{\mathrm{B}}C) \approx 150\,\mathrm{mK}$. The difference between the two values, while satisfactory, could be further increased by reducing the capacitance and incrementing the resistance to keep constant RC times. With the current design, a resistor with 210 kΩ can be combined with a capacitor of 15 fF to give an RC time of 3.2 ns, an average electron temperature of 25 mK and a charging energy corresponding to 250 mK.

2.7 Complete samples

As was mentioned in the introduction of this chapter a multitude of samples is contained on each wafer. Nevertheless, this chapter focuses on two types only, namely chips with and without beam splitter. The first is relevant, because the majority of the results presented in this work have been achieved measuring samples of this kind, and the latter is mentioned for its relative simplicity and comprehensibility.
Figure 2.8 shows a 10 mm × 10 mm chip carrying two of the beam splitter samples and containing all the elements discussed in this chapter. Each of them is connected to four tapered 50 Ω bonding pads at the edges. Three of the CPWs coming from these pads end in the quarter-wave network. The fourth one going directly to the SQUID area, acts as the flux-bias line. Alignment crosses for optical and electron beam lithography are situated in the corners. The zoom on the general SQUID area (red frame) shows local EBL alignment markers and the RC element as well as the flux-bias line. The two samples on this chip differ by the sizes of the junctions making up the SQUID (300 nm × 300 nm and 150 nm × 150 nm).
The other chip shown in Fig. 2.9 holds four different samples differing by the characteristic impedances of the first segment (farther from the SQUID) in their cascaded quarter-wave resonators. The sketch to the right of the chip shows a schematic view of one sample where the combination is SQUID:146 Ω:22 Ω:50 Ω, which leads to a quality factor of $Q \approx 15$ (see App. B.4). The other samples have, instead of the 22 Ω segment, lines with 14 Ω ($Q \approx 37$), 31 Ω ($Q \approx 8$) and 50 Ω ($Q \approx 3$). As usual, all resonance frequencies are 6.7 GHz giving bandwidths ranging from 180 MHz to 2.2 GHz.

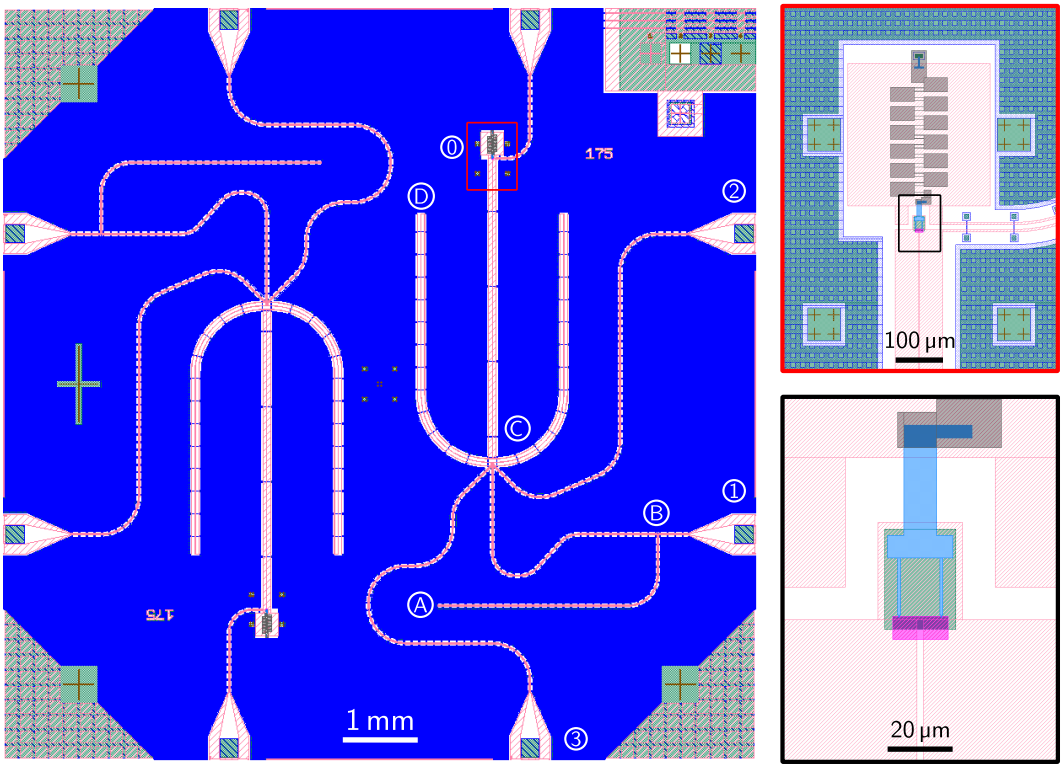

Figure (2.8): Layout of an entire chip with two beam splitter samples. For better visibility the color scheme is chosen differently than in the rest of this work. The holes in the trilayer are hatched light red, the holes in the Si_3N_4 are hatched green, the top NbN layer is blue and the chromium resistor is hatched grey. The circled numbers and letters indicate the same parts of the on-chip beam splitter and bias tee as in Fig. 2.2a. A zoom on the entire SQUID and RC area, indicated by the red frame, is shown in the top right corner. Another zoom (black frame) on only the SQUID is located in the bottom right corner. Here the EBL defined structures are colored differently (purple for the trilayer and light blue for the top NbN). Note that the purple rectangle and the white finger overlap and are in fact both representing structures etched into the trilayer (see Ch. 1).

.

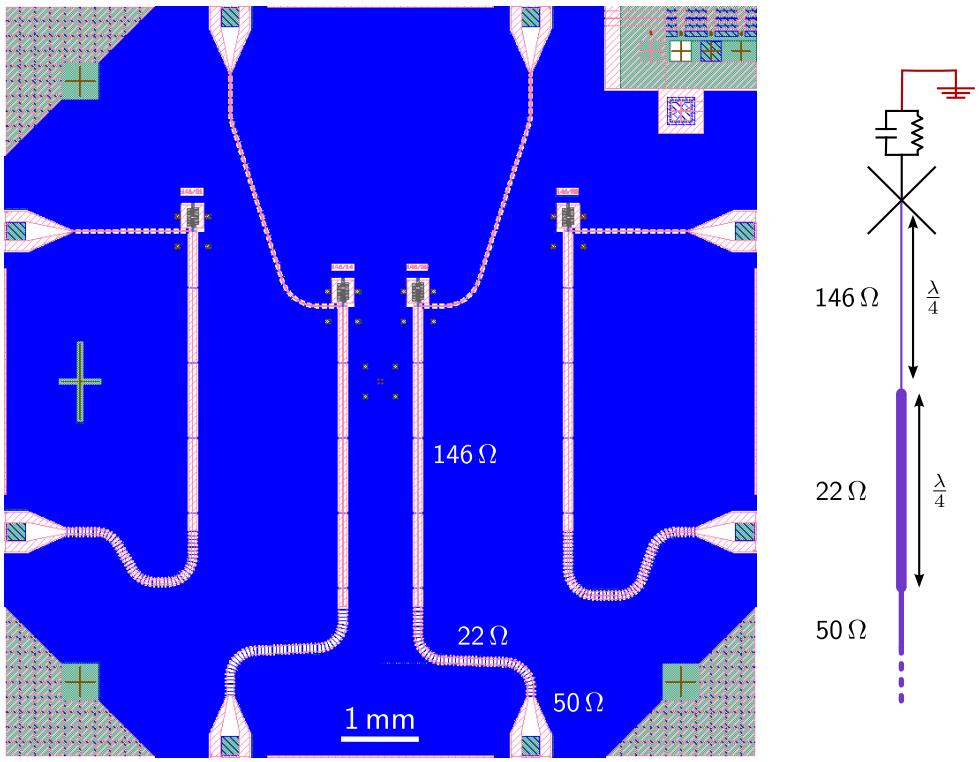

Figure (2.9): Layout image for a chip with four samples without beam splitters. The color code is the same as in Fig. 2.8. All four samples use different cascaded quarter-wave resonators. The schematic on the right side depicts the second sample from the right on the chip. CPW segments are again denoted by purple lines, characteristic impedances and lengths are given where relevant. The resonator on this sample corresponds to the one discussed in appendix B.4.

Chapter 3

Theory of photon correlation measurements at microwave frequencies

3.1 Introduction

In this chapter, we want to briefly address the question of what a microwave photon is and how it is linked to the voltages and currents in an LC resonator or on a transmission line. Then we will look at the different noise sources encountered by such a photon on its way from the light source on our chips to the input of our analog to digital converter card at room temperature. We want to show how we can calibrate out and subtract the majority of the spurious noise added to our signal. Finally, we will explain our data treatment protocols used to extract the different correlation functions presented in this work.

3.2 Microwave photons

In appendix B we show how an undamped transmission-line resonator can be described by a parallel LC circuit using effective values for capacitance and inductance, respectively C_{eff} and L_{eff}. Such a circuit can be quantized [73, 74], giving a Hamiltonian:

$$H = \frac{\hat{q}^2}{2C_{\text{eff}}} + \frac{\hat{\phi}^2}{2L_{\text{eff}}} = \hbar\omega_0 \left(\hat{a}^\dagger \hat{a} + \frac{1}{2}\right) \tag{3.1}$$

In this expression $\hat{q}$ is the operator representing the charge on the capacitor and $\hat{\phi}$ corresponds to the magnetic flux through the inductor. The right hand term is written in terms of quantized field amplitudes $\hat{a}$ and $\hat{a}^\dagger$, with $[\hat{a}, \hat{a}^\dagger] = 1$, emphasizing that the electromagnetic field in the resonator has excitation quanta of energy $\hbar\omega_0$, where $\omega_0 = 1/\sqrt{L_{\text{eff}} C_{\text{eff}}}$. At GHz frequencies, each quantum corresponds to a microwave-

photon [4, 7]. In the Heisenberg picture, the field amplitudes respect the following relation:

$$\hat{a}(t) = \sqrt{\frac{1}{2\hbar Z_c}}\hat{\phi}(t) + i\sqrt{\frac{Z_c}{2\hbar}}\hat{q}(t) \tag{3.2}$$

Here $Z_c = \sqrt{L_{\text{eff}}/C_{\text{eff}}}$. Noting that the voltage across the circuit is $\hat{V}(t) = \hat{q}(t)/C_{\text{eff}}$ and the current through the inductor is $\hat{I}_{\text{L}}(t) = \hat{\phi}(t)/L_{\text{eff}}$, this can be rewritten as:

$$\hat{a}(t) = \sqrt{\frac{L_{\text{eff}}}{2\hbar\omega_0}}\hat{I}_{\text{L}}(t) + i\sqrt{\frac{C_{\text{eff}}}{2\hbar\omega_0}}\hat{V}(t) \tag{3.3}$$

Since the current $\hat{I}_{\text{L}}(t)$ is lagging the voltage by a phase of $\pi/2$, we can express this in terms of in-phase and quadrature components of the voltage, generally with a random initial phase θ.

$$\hat{a}(t) = \sqrt{\frac{L_{\text{eff}}}{2\hbar\omega_0}}\frac{1}{Z_c}\hat{V}_\theta(t) + i\sqrt{\frac{C_{\text{eff}}}{2\hbar\omega_0}}\hat{V}_{\theta+\frac{\pi}{2}}(t) = \frac{1}{\sqrt{2}}\left(\hat{X}(t) + i\hat{P}(t)\right) \tag{3.4}$$

Each field quadrature $\hat{X}(t)$ or $\hat{P}(t)$ is proportional to a voltage quadrature and can be measured directly by down-converting the signal in frequency with an appropriate phase reference.
Similar derivations can be carried out for charge and phase densities in a transmission line resonator (giving spatial resolution) and can be extended to propagating modes on a TL, described by an infinite collection of LC-resonators [4, 75]. One notable difference in that case is that the quantized field amplitudes $\hat{a}(t)$ and $\hat{a}^\dagger(t)$ of the propagating modes are expressed in units of $\sqrt{\text{s}^{-1}}$ and the commutation relation becomes [76]:

$$\left[\hat{a}(t), \hat{a}^\dagger(t+\tau)\right] = \delta(\tau) \tag{3.5}$$

3.3 First and second order coherence functions

The statistics of the field produced by a light source can be investigated by means of measuring its coherence functions [76]. In this section we employ a notation that follows closely reference [24], which is at the basis of our measurement scheme. The first order coherence function is a measure for the capacity of a field to interfere with itself. It is usually determined with a Mach-Zehnder interferometer, where a light beam is separated into two and recombined after introducing a time difference τ. Interference effects lead to variations in the intensity of the resulting beam measured as a function of τ (Fig. 3.1a). This is equivalent to Young's double slit experiment where plane waves emitted by a light source, pass through two slits in a shutter effectively creating two line-shaped light sources. Their beams impinge on a detector plate after having traveled different distances. At a given point of the plate the intensity depends on the correlation between the field amplitudes at two times t and $t+\tau$, where the time lapse τ is due to the difference in path lengths. This effect is described by the first order correlation function:

$$G^{(1)}(t, t+\tau) = \left\langle \hat{a}^{\dagger}(t)\, \hat{a}(t+\tau) \right\rangle \tag{3.6}$$

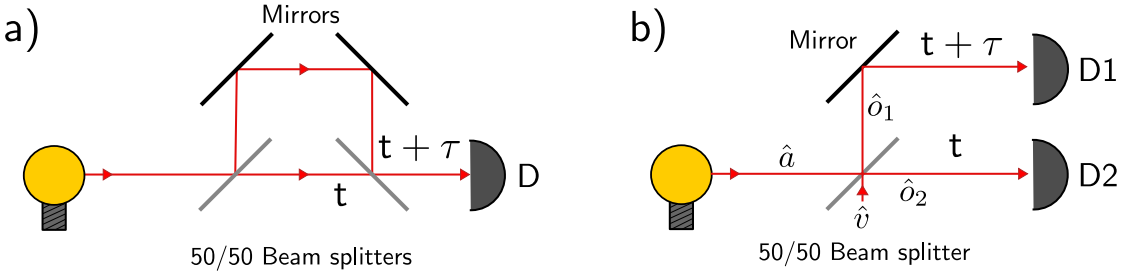

Figure (3.1): Sketches of a) Mach-Zehnder and b) Hanburry Brown and Twiss interferometers used for the determination of $G^{(1)}(t, t+\tau)$ and $G^{(2)}(t, t+\tau)$ respectively.

Averaging this quantity over the time coordinate and dividing it through the average of $G^{(1)}(t, t)$ gives a normalized expression that depends only on the time difference τ:

$$g^{(1)}(\tau) = \frac{G^{(1)}(\tau)}{G^{(1)}(0)} = \frac{\frac{1}{T}\int_T dt \left\langle \hat{a}^{\dagger}(t)\, \hat{a}(t+\tau) \right\rangle}{\frac{1}{T}\int_T dt \left\langle \hat{a}^{\dagger}(t)\, \hat{a}(t) \right\rangle} \tag{3.7}$$

In a similar way one can define a second order coherence or correlation function, as well as its normalized and time-averaged version:

$$G^{(2)}(t, t+\tau) = \left\langle \hat{a}^{\dagger}(t)\, \hat{a}^{\dagger}(t+\tau)\, \hat{a}(t+\tau)\, \hat{a}(t) \right\rangle \tag{3.8}$$

$$g^{(2)}(\tau) = \frac{G^{(2)}(\tau)}{G^{(1)}(0)^2} = \frac{\frac{1}{T}\int_T dt \left\langle \hat{a}^{\dagger}(t)\, \hat{a}^{\dagger}(t+\tau)\, \hat{a}(t+\tau)\, \hat{a}(t) \right\rangle}{\left(\frac{1}{T}\int_T dt \left\langle \hat{a}^{\dagger}(t)\, \hat{a}(t) \right\rangle\right)^2} \tag{3.9}$$

To understand this quantity, consider Fig. 3.1b showing a standard Hanburry-Brown and Twiss setup as it is used at optical frequencies to measure $g^{(2)}(\tau)$. The field passes through a 50/50 beam splitter and the two output beams are measured on two single photon detectors D1 and D2. In order to "split" the input beam $\hat{a}$ it has to be superposed with another input field $\hat{v}$, which commutes with $\hat{a}$:

$$\hat{o}_{1,2} = \frac{\hat{a} \pm \hat{v}}{\sqrt{2}} \tag{3.10}$$

This has to be the case so that the outputs $\hat{o}_{1,2}$ still respect the bosonic commutation relations. Here $\hat{v}$ is taken to be in the vacuum state; a more detailed analysis of what happens when this is not the case will be given later. We can write Eq. (3.9) using these outputs and reorder them to measure the number of photons in each beam $\langle \hat{n}_{1,2} \rangle = \langle \hat{o}^{\dagger}_{1,2} \hat{o}_{1,2} \rangle$. Since this operator is normally ordered, all terms containing the vacuum field $\hat{v}$ evaluate directly to zero and $\langle \hat{n}_{1,2} \rangle = \left\langle \hat{a}^{\dagger} \hat{a} \right\rangle / 2$. With this we can express (3.9) as:

$$g^{(2)}(\tau) = \frac{\frac{1}{T}\int_T dt \,\langle \hat{n}_1(t)\,\hat{n}_2(t+\tau)\rangle}{\frac{1}{T}\int_T dt \,\langle \hat{n}_1(t)\rangle \,\frac{1}{T}\int_T dt \,\langle \hat{n}_2(t)\rangle} \tag{3.11}$$

In this language of photon detection events we can thus describe $g^{(2)}(\tau)$ as a measure of the probability to get a photon on detector D2 after having measured a photon on detector D1 a time difference τ earlier. For time differences τ bigger than the correlation time of the light τ_c, the value of $g^{(2)}(\tau)$ always tends to 1, because $\hat{n}_1(t)$ and $\hat{n}_2(t+\tau)$ become independent [76]. Three different regimes are distinguishable in the special case where $\tau = 0$. They become evident when writing $g^{(2)}(0)$ in terms of the mean photon number $\bar{n} = \langle \hat{a}^\dagger \hat{a}\rangle$ and its variance $V(n) = \langle (\hat{a}^\dagger \hat{a})^2\rangle - \langle \hat{a}^\dagger \hat{a}\rangle^2$:

$$g^{(2)}(0) = \frac{\langle \hat{a}^\dagger \hat{a}^\dagger \hat{a}\hat{a}\rangle}{\langle \hat{a}^\dagger \hat{a}\rangle^2} = 1 + \frac{V(n) - \bar{n}}{\bar{n}^2} \tag{3.12}$$

This signifies that for a light source with independent emission events (i.e. underlying Poisson statistics), we get $g^{(2)}(0) = 1$, since the variance is equal to the mean. Thermal light has a values of $g^{(2)}(0) = 2$, because the intensity fluctuations in chaotic light are higher than those of a Poissonian light source [76]. This means that photons are more likely to arrive grouped. It is an example of *bunched* light, where $g^{(2)}(0) > 1$. The opposite case, $g^{(2)}(0) < 1$, is called *anti-bunching*. An ideal single photon source, for example, sends out one photon Fock states. The variance of such a light field is zero and the mean value $\bar{n} = 1$, giving $g^{(2)}(0) = 0$, necessarily leading to anti-bunching. Additionally, values of $g^{(2)}(0) < 1$ can not be achieved with purely classical light fields [76]. Therefore, the behavior of $g^{(2)}(\tau)$ close to $\tau = 0$ is an important benchmark for the quality of a single photon source and can be used to prove the quantum behavior of a light source.
As a closing remark for this section, it should be mentioned that standard single photon counters, readily available at optical frequencies [29], do not yet exist in the microwave domain. Instead, linear amplifiers, either in combination with square law detectors or with IQ mixers, are used to measure the in-phase and quadrature components of the voltage associated with the electromagnetic field of photons on a transmission line and the correlations of the corresponding field amplitudes are extracted from the data.

3.4 Cross correlation measurements

In this section we will explain, how we can extract the first and second order coherence functions from the time resolved measurement record of the quadratures of the voltage on the transmission line. The latter are, as we have seen above, directly proportional to the field quadratures. Following the argumentation presented in [24, 77] we will show that combining different quadrature measurements in an astute way enables us to minimize contributions arising from amplifier noise. Moreover, we will use a very general noise model to show that unwanted residual noise can be subtracted during data treatment through combinations of simple “On/Off” measurements.

3.4.1 Noise model of the measurement chain

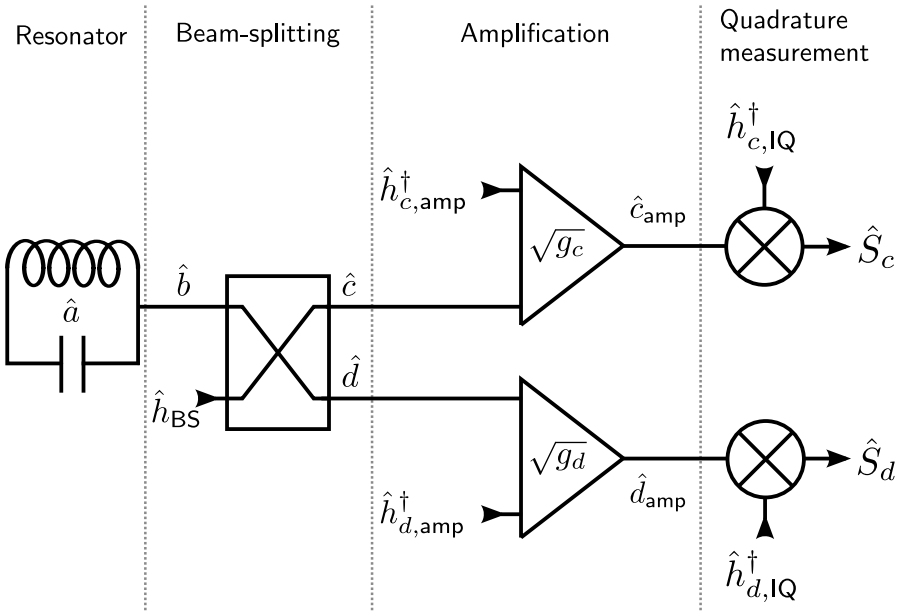

Figure (3.2): Schematic representation of the noise model of our measurement chain. The different symbols are explained in the text.

Of course, the input field of the quadrature measurement is not directly proportional to the output field of our light source, but has already undergone amplification and beam-splitting as shown in Fig. 3.2. The entire measurement process with the different noise sources is described step by step as follows:

1. Input-output theory states that the field leaking out of a cavity, such as a quarter-wave resonator coupled to a transmission line, is [76]:

$$\hat{b}(t) = \sqrt{\gamma}\hat{a}(t) - \hat{b}_{\mathrm{in}}(t) \tag{3.13}$$

   Where γ is the inverse cavity lifetime. At low enough temperatures ($k_{\mathrm{B}}T \ll \hbar\omega$) the input field $\hat{b}_{\mathrm{in}}$ can be considered to be in the vacuum state and will drop out in all normally ordered expectation values [24]. Consequently, we take the output field to be directly proportional to the field in the cavity. The constant of proportionality factorizes and simplifies in all normalized correlation functions and for the remainder of this discussion we will consider $\hat{b}$ to be the output of our sample.

2. The beam splitter necessarily mixes the field with another mode $\hat{h}_{\mathrm{BS}}$ in order for its two outputs to commute [78]. This mode can be taken to be in the vacuum state or treated as a noise source. Since our beam splitter does not have a fourth

port we will keep its description as general as possible including the possibility of correlation with noise leaking down from the amplification stage. It is reasonable, however, to take it as independent from the signal produced by our sample so that $[\hat{b}, \hat{h}_{bs}^\dagger] = 0$ and $\langle \hat{b}\hat{h}_{bs}^\dagger \rangle = \langle \hat{b} \rangle \langle \hat{h}_{bs}^\dagger \rangle = 0$. The latter relation also supposes that either the noise or the field do not have coherence terms in their density matrix. In our case, this is true for both, since the light source discussed here has no phase reference. The field operators $\hat{c}$ and $\hat{d}$, after the splitter, have the form:

$$\hat{c}(t) = \frac{\hat{b}(t) + \hat{h}_{\mathrm{BS}}(t)}{\sqrt{2}} \qquad \hat{d}(t) = \frac{\hat{b}(t) - \hat{h}_{\mathrm{BS}}(t)}{\sqrt{2}} \tag{3.14}$$

3. In the next step the signal is amplified, which adds more noise to it. With the power gains g_c and g_d and the noise modes $\hat{h}_{c,\mathrm{amp}}$ and $\hat{h}_{d,\mathrm{amp}}$, we can write the amplified signals on either chain as [79]:

$$\begin{aligned} \hat{c}_{\mathrm{amp}}(t) &= \sqrt{g_c}\hat{c}(t) + \sqrt{g_c - 1}\hat{h}_{c,\mathrm{amp}}^\dagger(t) \\ \hat{d}_{\mathrm{amp}}(t) &= \sqrt{g_d}\hat{d}(t) + \sqrt{g_d - 1}\hat{h}_{d,\mathrm{amp}}^\dagger(t) \end{aligned} \tag{3.15}$$

We take the noise on the amplifiers to be independent from their inputs giving $[\hat{c}, \hat{h}_{c,\mathrm{amp}}^\dagger] = [\hat{c}, \hat{h}_{d,\mathrm{amp}}^\dagger] = 0$ and $\langle \hat{c}\hat{h}_{c,\mathrm{amp}}^\dagger \rangle = \langle \hat{c}\hat{h}_{d,\mathrm{amp}}^\dagger \rangle = 0$. We suppose that the two noise modes commute, however, we do not consider them uncorrelated $\langle \hat{h}_{c,\mathrm{amp}}^\dagger \hat{h}_{d,\mathrm{amp}}^\dagger \rangle = G^{(1),\mathrm{nx}}(t, t+\tau)$ or independent from the noise of the beam splitter $\langle \hat{h}_{\mathrm{BS}}^\dagger \hat{h}_{c/d,\mathrm{amp}} \rangle \neq 0$ and $[\hat{h}_{\mathrm{BS}}, \hat{h}_{c/d,\mathrm{amp}}] \neq 0$. Here, and in the following calculation, no assumptions on the form of the noise cross-correlation are made.

4. Lastly, quadrature measurements are performed on both outputs. In practice, a quadrature measurement is carried out slightly differently at optical and microwave frequencies. Indiscriminately, any such measurement introduces noise, for instance through the mixing on an additional beam splitter. This is necessary to obtain two commuting modes, where one quadrature is measured on each (see App. C). One can define a complex envelope from the two quadratures, which is proportional to the input field and a noise mode [24]:

$$\begin{aligned} \hat{S}_c(t) &\equiv \hat{X}_c(t) + i\hat{P}_c(t) = \hat{c}_{\mathrm{amp}}(t) + \hat{h}_{c,\mathrm{IQ}}^\dagger(t) \\ \hat{S}_d(t) &\equiv \hat{X}_d(t) + i\hat{P}_d(t) = \hat{d}_{\mathrm{amp}}(t) + \hat{h}_{d,\mathrm{IQ}}^\dagger(t) \end{aligned} \tag{3.16}$$

These complex envelope operators are defined from the classical outputs of the quadrature measurements and fulfill the equality $\langle \hat{S}_i(t) \rangle = \langle S_i(t) \rangle$, where $S_i(t) = X_i(t) + iP_i(t)$ is a complex number. The modes $\hat{h}_{i,\mathrm{IQ}}(t)$ commute with the amplified fields and all the other modes except for the usual relation $[\hat{h}_{i,\mathrm{IQ}}(t), \hat{h}_{j,\mathrm{IQ}}^\dagger(t+\tau)] = \delta(\tau)\delta_{i,j}$. They can also have non-vanishing correlations.

The noise terms intervening after the first beam splitter can be condensed into one mode $\hat{h}_i$ per channel i. Even though the noise from mixing will most likely be negligible compared to the amplifier noise in an actual experimental setup, we keep it here for the sake of completeness.

$$\hat{h}_i^\dagger(t) = \sqrt{\frac{g_i - 1}{g_i}}\hat{h}_{i,\text{amp}}^\dagger(t) + \frac{1}{\sqrt{g_i}}\hat{h}_{i,\text{IQ}}^\dagger(t) \tag{3.17}$$

This operator still respects the commutation relations $[\hat{h}_i^\dagger(t), \hat{h}_j(t+\tau)] = \delta(\tau)\delta_{i,j}$ and the operators $\hat{S}_i$ take the form:

$$\hat{S}_i(t) = \sqrt{g_i}\left(\hat{i}(t) + \hat{h}_i^\dagger(t)\right) \tag{3.18}$$

Here the fields $\hat{i}$ are directly the outputs $\hat{c}$ and $\hat{d}$ of the beam splitter.

3.4.2 Correlations between complex envelopes

The complex amplitudes contain the original field $\hat{a}$ and can be combined in different ways to give the coherence (3.6). If we were just using one measurement channel (e.g. $\hat{c}$) the only option would be:

$$\begin{aligned}\Gamma^{(1)}_{\text{direct}}(t, t+\tau) &= \left\langle \hat{S}_c^\dagger(t)\, \hat{S}_c(t+\tau)\right\rangle \\ &= g_c\left[\frac{1}{2}G^{(1)}(t, t+\tau) + G^{(1)}_{c,\text{noise}}(t, t+\tau) + \delta(\tau)\right]\end{aligned} \tag{3.19}$$

The last equality is derived after some calculation taking into account the entire noise model mentioned above (see App. C). The first term in the last line is the desired correlation function, the second term corresponds to the summed direct correlations of all noise sources pertaining to this channel and the last term originates from the fact that we are measuring only on one output mode of the beam splitter. It comes from the commutator $[\hat{c}(t), \hat{c}^\dagger(t+\tau)] = \delta(\tau)$ and can be seen as the contribution of the vacuum fluctuations of the $\hat{c}$ mode. In a real experiment its divergence in time would be eliminated due to the necessarily finite measurement bandwidth [24].
An other, more astute, choice to extract the sought after correlation is:

$$\begin{aligned}\Gamma^{(1)}_{\text{cross}}(t, t+\tau) &= \left\langle \hat{S}_c^\dagger(t)\, \hat{S}_d(t+\tau)\right\rangle \\ &= \sqrt{g_c g_d}\left[\frac{1}{2}G^{(1)}(t, t+\tau) + G^{(1)}_{\text{x,noise}}(t, t+\tau)\right]\end{aligned} \tag{3.20}$$

The noise cross-correlation $G^{(1)}_{\text{x,noise}}(t, t+\tau)$ is taken between the noise sources on both channels and is intuitively and experimentally (Fig. 4.4) much smaller than $G^{(1)}_{c,\text{noise}}(t, t+\tau)$. Moreover, the delta function does not emerge, since $\hat{c}$ and $\hat{d}$ commute. The extraction of $G^{(1)}(t, t+\tau)$ is a simple matter of measuring $\Gamma^{(1)}_{\text{cross}}(t, t+\tau)$

with the sample in the "On" and "Off" state and then subtracting the results. Even disregarding the delta function, if such a subtraction was performed in the first case, the much larger noise signal would make the extraction very sensitive to any change between the "On" and "Off" measurements. The second case is therefore clearly preferable.
In a similar manner, one can define several combinations of complex envelopes to obtain the second order correlation function (3.8), and again, some will include delta functions and direct noise correlations, while others will not. Naturally, it is preferable to be in the latter case. A choice fulfilling this requirement is:

$$\begin{aligned}\Gamma^{(2)}_{\text{cross}}(t,t+\tau) &= \left\langle \hat{S}_c^{\dagger}(t)\,\hat{S}_c^{\dagger}(t+\tau)\,\hat{S}_d(t+\tau)\,\hat{S}_d(t)\right\rangle \\ &= \frac{g_c g_d}{2}\Big[\frac{1}{2}G^{(2)}(t,t+\tau)+G^{(1)}(t,t+\tau)G^{(1)}_{\text{x,noise}}(t,t+\tau) \\ &+G^{(1)}(t+\tau,t+\tau)\,G^{(1)}_{\text{x,noise}}(t,t)+G^{(1)}(t,t)\,G^{(1)}_{\text{x,noise}}(t+\tau,t+\tau) \\ &+G^{(1)}(t+\tau,t)\,G^{(1)}_{\text{x,noise}}(t+\tau,t)+G^{(2)}_{\text{x,noise}}(t,t+\tau)\Big]\end{aligned} \tag{3.21}$$

Again, the noise cross-correlation $G^{(2)}_{\text{x,noise}}(t,t+\tau)$ is the only term that remains when the sample is not active. All the other noise terms are known from the determination of $G^{(1)}(t,t+\tau)$ and can be subtracted off to find the correlation $G^{(2)}(t,t+\tau)$. If we would measure the direct second order correlation $\langle \hat{S}_c^{\dagger}(t)\,\hat{S}_d^{\dagger}(t+\tau)\,\hat{S}_d(t+\tau)\,\hat{S}_c(t)\rangle$, more terms depending on delta functions as in Eq. (3.19) would appear, making the simple noise subtraction scheme with "On/Off" measurements impossible.

3.4.3 Signal to noise ratio and averaging time

It has to be understood that this way of measuring does not provide instantaneous noise rejection, since during the entire derivation we have used the fact that the expectation values of modes in the vacuum state and of counter-rotating terms are zero. Naturally, this implies averaging.
From the preceding sections (Eqs. (3.4), (3.6) and (3.8)) we can see that the n$^{\text{th}}$-order correlation function $G^{(n)}$ is proportional to a product of $2n$ measured voltages $\prod_i^{2n} V_i$. We can write the variance of $G^{(n)}$:

$$\text{Var}(G^{(n)}) = \langle (G^{(n)})^2\rangle - \langle G^{(n)}\rangle^2 \propto \langle \prod_i^{2n} V_i^2\rangle - \langle \prod_i^{2n} V_i\rangle^2 \approx \prod_i^{2n}\langle V_{i,\text{noise}}^2\rangle - \langle \prod_i^{2n} V_{i,\text{sig}}\rangle^2 \tag{3.22}$$

In the last step we have split the voltage $V_i = (V_{i,\text{noise}} + V_{i,\text{sig}})$ into contributions from the noise and the signal. We have also supposed the different noise terms i to be uncorrelated and $\langle V^2_{\text{noise}}\rangle \gg \langle V^2_{\text{sig}}\rangle$. Introducing the average noise and signal photon numbers $N_{\text{noise}} \propto \langle V^2_{i,\text{noise}}\rangle$ and $N_{\text{sig}} \propto \langle V^2_{i,\text{sig}}\rangle$ we can write:

$$\mathrm{Var}(G^{(n)}) \propto N_{\mathrm{noise}}^{2n} + N_{\mathrm{sig}}^{2n} \approx N_{\mathrm{noise}}^{2n} \tag{3.23}$$

The term N_{sig}^{2n} is only an estimate of $\langle \prod_i^{2n} V_{\mathrm{sig}} \rangle^2$, but should in any case be negligible compared to N_{noise}^{2n}. Using the central limit theorem we write the variance of the average over R independent measurements as:

$$\mathrm{Var}\left(\overline{G^{(n)}}\right) = \frac{\mathrm{Var}(G^{(n)})}{R} = \frac{N_{\mathrm{noise}}^{2n}}{R} \tag{3.24}$$

The signal to noise ratio k is given by:

$$k = \frac{\langle G^{(n)} \rangle}{\sqrt{\mathrm{Var}\left(\overline{G^{(n)}}\right)}} = \frac{N_{\mathrm{sig}}^{n}\sqrt{R}}{N_{\mathrm{noise}}^{n}} \tag{3.25}$$

This means that for a specific desired value of k, the number of averages R has to be:

$$R = k^2 \left(\frac{N_{\mathrm{noise}}}{N_{\mathrm{sig}}}\right)^{2n} \tag{3.26}$$

The required measurement time depends on the noise raised to a power that scales as the order of the measured correlation function. In practice, this signifies that a *twofold* increase in noise leads to factor of *sixteen* in the measurement time of a second order correlator.

3.5 Data extraction

As mentioned before, we do not use IQ mixers to extract the quadratures, but a combination of heterodyne down-conversion and numerical demodulation. The reasons for this are mainly based on our choice of analog to digital converter enabling us to sample at high frequencies on two channels. Moreover, this helps us to avoid imperfections in the phase difference between the two channels of the IQ mixers, which otherwise have to be considered when measuring with such a large bandwidth. Finally, this way we can sample the signal in a window starting at higher frequencies (see Ch. 4), thus avoiding 1/f noise. This section describes the details of the resulting data extraction process.

3.5.1 Numerical extraction of the complex envelope

At the output of the amplifiers, before down-conversion, the signal on each channel has the form $S(t)e^{-i\omega_{\mathrm{RF}}t}$, where ω_{RF} is the carrier frequency (corresponding to the photon frequency) and $S(t)$ is the complex envelope described above, which can contain amplitude and phase modulation factors. A measurement of this complex mathematical quantity gives back only its real part so that the measured voltage is proportional to:

$$V(t) \propto \frac{1}{2}\left(S(t)e^{-i\omega_{\mathrm{RF}}t} + S^*(t)e^{i\omega_{\mathrm{RF}}t}\right) = X(t)\cos(\omega_{\mathrm{RF}}t) + P(t)\sin(\omega_{\mathrm{RF}}t) \tag{3.27}$$

In this expression $X(t)$ and $P(t)$ are defined by the relationship $S(t) = X(t) + iP(t)$. After frequency down-conversion through mixing with a local oscillator $V_{\mathrm{LO}}\cos(\omega_{\mathrm{LO}}t)$ and filtering (convolution with a filter function $\sqcap(t)$) the new signal is:

$$\begin{aligned} V_{\mathrm{IF}}(t) \propto [V(t)\cos(\omega_{\mathrm{LO}})] * \sqcap(t) = \frac{1}{2}\,[X(t)\cos\left((\omega_{\mathrm{RF}} - \omega_{\mathrm{LO}})t\right) \\ + P(t)\sin\left((\omega_{\mathrm{RF}} - \omega_{\mathrm{LO}})t\right)] * \sqcap(t) \end{aligned} \tag{3.28}$$

In frequency space the function $\sqcap(t)$ corresponds to a bandpass filter covering the second Nyquist band of our analog to digital converter:

$$\omega \in \left[\frac{\pi}{\Delta T}, \frac{2\pi}{\Delta T}\right] \tag{3.29}$$

The LO frequency is chosen so that the carrier wave is demodulated into the middle of this band (see also Ch. 4). This gives $\omega_{\mathrm{RF}} - \omega_{\mathrm{LO}} = \frac{3\pi}{2\Delta T}$, where ΔT is the sampling interval. We now assume that the bandwidth of $V(t)$ is narrower than $\sqcap$. Then $\sqcap$ has no effect on the down-converted signal, but removes the up-converted component and noise from other Nyquist bands. The sampled voltages are:

$$V_n = V_{IF}(n\Delta T) = \begin{cases} \frac{1}{2}X_n(-1)^{\frac{n}{2}} & \text{if } n \text{ is even} \\ \frac{1}{2}P_n(-1)^{\frac{n+1}{2}} & \text{if } n \text{ is odd} \end{cases} \tag{3.30}$$

Here X_n and P_n are the sampled quadratures. Now we can numerically demodulate the signal to zero frequency by calculating the factors $(-1)^{n/2}$ and $(-1)^{(n+1)/2}$. This comes with a caveat; the data points in both quadratures are not taken at the same time any more, but with a difference of one sampling step between two values and the two signals are sampled with half the original rate at intervals $2\Delta T$. Since the signal coming from the sample is bounded by the designed resonator, which is entirely contained in the bandpass filter, we have all the information needed to interpolate the quadrature signals. In our case we want to make them coincide in time to be able to extract the complex envelopes. The most straightforward approach to this is simply multiplying one quadrature in frequency space by a factor $e^{-i\omega\delta t}$, where δt the desired time shift. For now, we want to stay in the time domain, because we still want to multiply the complex envelopes from different channels with each other to calculate the correlators from the preceding section. The alternative would be to perform multiple fast Fourier transforms back and forth and the time gained by avoiding the convolution would be lost. Instead we can convolve the sampled values directly in time with the inverse Fourier transform of $e^{-i\omega\delta t}\sqcap(\omega)$, taking into account the width in frequency of the filtered signal with the window function $\sqcap(\omega)$. Because of the numerical down-mixing $\sqcap(\omega)$ now goes from $-\pi/(2\Delta T)$ to $\pi/(2\Delta T)$.

$$\begin{aligned} \mathrm{FT}^{-1}\left[e^{-i\omega\delta t}\sqcap(\omega)\right] &= \mathrm{FT}^{-1}\left[e^{-i\omega\delta t}\right] * \mathrm{FT}^{-1}\left[\sqcap(\omega)\right] \\ &= \delta(t-\delta t) * \int_{-\frac{\pi}{2\Delta T}}^{\frac{\pi}{2\Delta T}} e^{i\omega t}\mathrm{d}\omega \\ &= \frac{\pi}{\Delta T}\mathrm{sinc}\left(\frac{t-\delta t}{2\Delta T}\right) \end{aligned} \tag{3.31}$$

In the last expression the cardinal sine function is defined by $\mathrm{sinc}(x) = \sin(\pi x)/(\pi x)$ We can replace the t coordinate with the discrete sampling points $2m\Delta T$ with $m \in \mathbb{N}$, and the time shift δt with ΔT, giving:

$$\frac{1}{\Delta T}\frac{(-1)^{n+1}}{n-\frac{1}{2}} \tag{3.32}$$

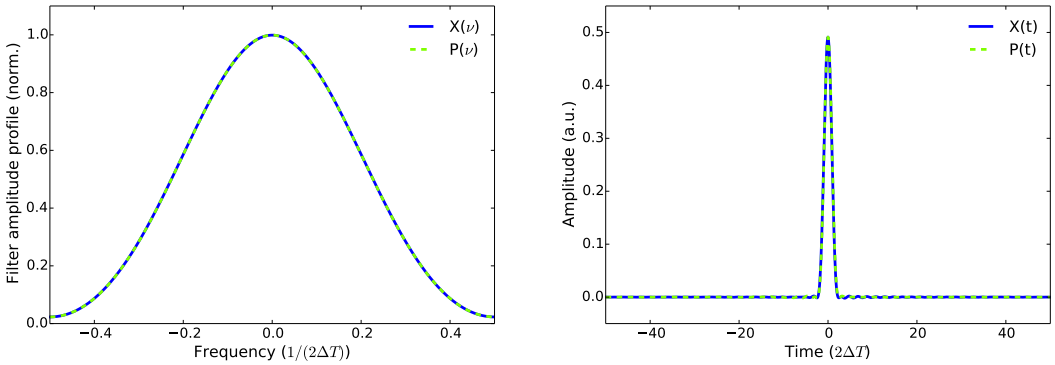

Figure (3.3): Benchmarking of the convolution kernel with a δ-impulse applied simultaneously on both quadratures. Left panel: The abscissa is given in units of the bandwidth $1/(2\Delta T)$. In frequency space the kernel corresponds to a Gaussian filter on both quadratures, which is contained entirely between $-1/(4\Delta T)$ and $1/(4\Delta T)$ and is thus narrower than the physical filter. Right panel: Result of the time domain benchmarking. Both (infinite bandwidth) quadratures are shifted to coincide in time, while minimizing the ringing resulting from the convolution with the narrower filter. Here the abscissa is in units of the sampling interval $2\Delta T$.

This discrete convolution kernel can shift one quadrature by a time ΔT to make it coincide with the other. Unfortunately, this approach has two considerable drawbacks. First, the kernel contains an arbitrary number of values and the resulting convolution is long and cumbersome to compute. Second, the sinc function emerging due to the abrupt cutoff of the filter leads to oscillations in the signal and can introduce spurious long-time correlations.

We chose to take a different approach by numerically finding a convolution kernel with a Gaussian frequency profile capable of shifting a quadrature by half of the original sampling interval ΔT. Then we can apply the same kernel in direct and reverse order to both quadratures and make them coincide. Figure 3.3 (left panel) shows the normalized frequency profile of the kernel. It is entirely contained within the bandwidth of the filter, which goes from $-1/(4\Delta T)$ to $1/(4\Delta T)$, thus eliminating its spurious oscillations in time. In order to verify that our kernel indeed shifts the two quadratures by the right amount, we use the following benchmark: We assume that the signals on Q and P have infinite bandwidth in frequency and are thus delta-functions in time. After applying the convolution with the kernel to both, they should coincide and show as little ringing as possible. Figure 3.3 (right panel) displays the results of this test. We can see that both quadratures coincide well in time and are slightly broadened due to the finite bandwidth of the Gaussian kernel. Here we have used a kernel with only five values, which considerably speeds up the convolution. This procedure allows us to measure both quadratures at the same time on each channel in order to combine them to the complex envelopes used in section 3.4.
Now the computation of the correlations $\Gamma^{(1)}(\tau)$ corresponds to performing a convolution product between blocks of the resulting complex envelope data vectors as shown in Fig. 3.4. This procedure follows three steps:

a) The reconstructed complex envelope vectors are cut into pieces $S_{c,N}$ and $S_{d,N}$ of duration $\tau_{\max}$, which is the maximum value of τ in the calculated correlators.

b) Each piece of $S_c(t)$ is convolved with its complex conjugated counterpart in $S_d(t)$ as well as the adjacent pieces following the convention $\int S_{c,N}(t)S^*_{d,M}(t+\tau)\mathrm{d}t$ where $M \in \{N-1, N, N+1\}$. To compute these convolution products efficiently we apply a fast Fourier transform (FFT) on each vector and calculate the element wise product in frequency space. For this to work we need to pad each block with the same amount of zeros to avoid wrap-arounds (Note that the FFT supposes periodic signals). We then average each of the three resulting products over all N before applying an inverse fast Fourier transform.

c) The three results are summed in order to have the same weight for each time difference τ. This is illustrated in Fig. 3.4c by considering the well known triangular result of a convolution of step functions. In the area of interest $\tau \in [-\tau_{\max}, \tau_{\max}]$ delimited by the dotted lines this sum gives equal weight to each time coordinate τ.

Extracting the functions $\Gamma^{(2)}(\tau)$ works in a similar manner by multiplying the two vectors to get $S_c(t)S^*_d(t)$ and then applying the same method to calculate numerical integrals of the type $\int [S_{c,N}(t)S^*_{d,N}(t)][S_{c,M}(t+\tau)S^*_{d,M}(t+\tau)]\mathrm{d}t$.
Finally, the values of $G^{(1)}(\tau)$ and $G^{(2)}(\tau)$ are calculated by subtraction as discussed in the previous section. In the very last step the normalized correlations are computed by dividing through $G^{(1)}(0)$ and $[G^{(1)}(0)]^2$ respectively. Note that, while measuring cross correlated quantities as defined in (3.20) and (3.21) can introduce additional phase terms

due to path length differences, these terms are efficiently eliminated by normalizing with likewise cross correlated quantities. Therefore $\Gamma^{(2)}_{\text{cross}}(\tau)$ will in general be complex valued, while the normalized $g^{(2)}_{\text{cross}}(\tau)$ is real.

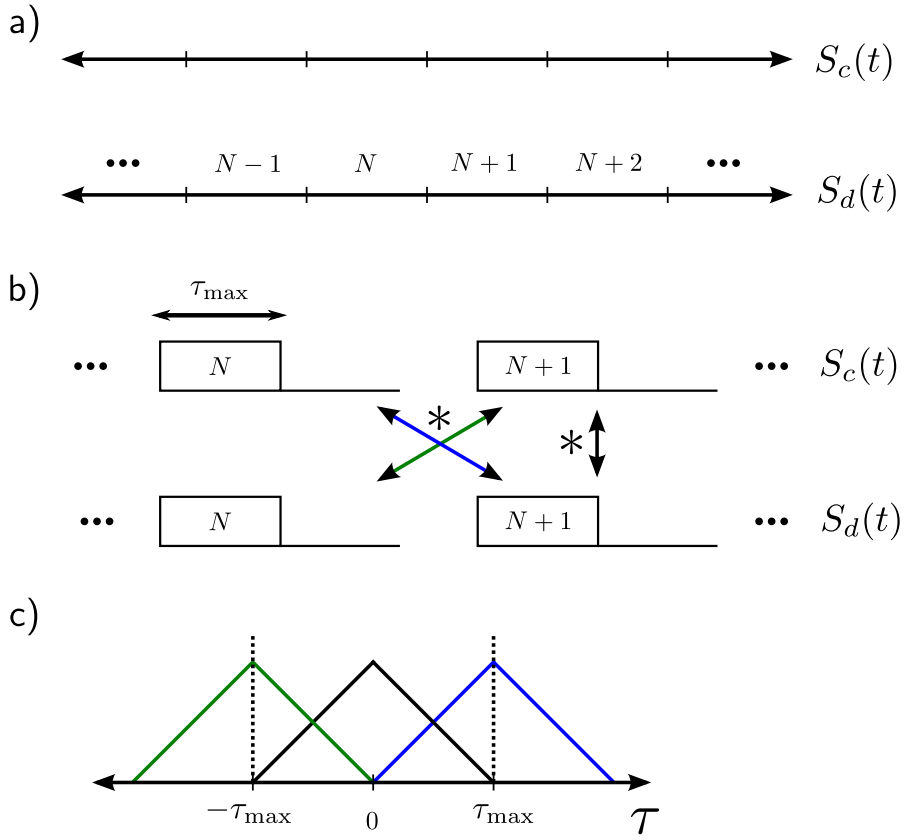

Figure (3.4): Schematic of the data treatment process. a) The two complex vectors with the sampled envelopes are divided into chunks of length $\tau_{\max}$. b) The way sections of both vectors are combined, with $*$ denoting the convolution product defined in the text. c) The three results of the convolution products shown in b) color coded to match the arrows. Here the simplest case where the chunks are constant window functions is considered for illustration purposes. Within the boundaries $\tau \in [-\tau_{\max}, \tau_{\max}]$ the sum of the three preserves equal weight for each time coordinate.

Chapter 4

Experimental setup

4.1 Introduction

In this chapter we aim to describe the measurement setup used in our experiments, which was completely built up during this PhD work, including the installation, testing and wiring of the dilution refrigerator as well as of the entire room temperature part.
The outline of this chapter is given in the form of a schematic representation of the entire measurement chain in Fig. 4.1. Only elements inside the refrigerator are described in detail. On the right side, the different temperature zones are marked. The lower two tiers are inside our Cryoconcept pulse tube refrigerator and correspond to the pulse tube head stage ($\approx 3.3\,\mathrm{K}$ operating temperature with a cooling power of $350\,\mathrm{mW}$ at $4.2\,\mathrm{K}$) and the base-stage ($12\,\mathrm{mK}$ operating temperature and $6\,\mu\mathrm{W}$ of cooling power at $20\,\mathrm{mK}$). Everything in the $12\,\mathrm{mK}$ area is either mounted directly on the baseplate of the dilution refrigerator or thermalized through annealed copper bands, unless indicated otherwise. The setup can be divided into the following regions:

1. **Sample area -** The yellow region is called the sample area, because the elements contained therein, namely the light-source, the flux bias line, a bias tee and a beam splitter are realized entirely on-chip on certain samples (Fig. 2.8). Other chips, however, do only hold the source itself (Fig. 2.9). In that case, external microwave components were used for the other parts, in particular a 180° hybrid coupler and a Maki (DPXN-M50) bias tee.

2. **RF side -** The high frequency branch of the chain comprises everything on the far side of the bias tee capacitor as seen from the sample. It is used to measure the microwave photons emitted by our source.

   (a) **Calibration -** The blue rectangle encompasses a Radiall (R591-763-600) six way switch on each channel allowing us to connect its output either to the sample or to three other options used for calibration. More detail is given in section 4.2.3.

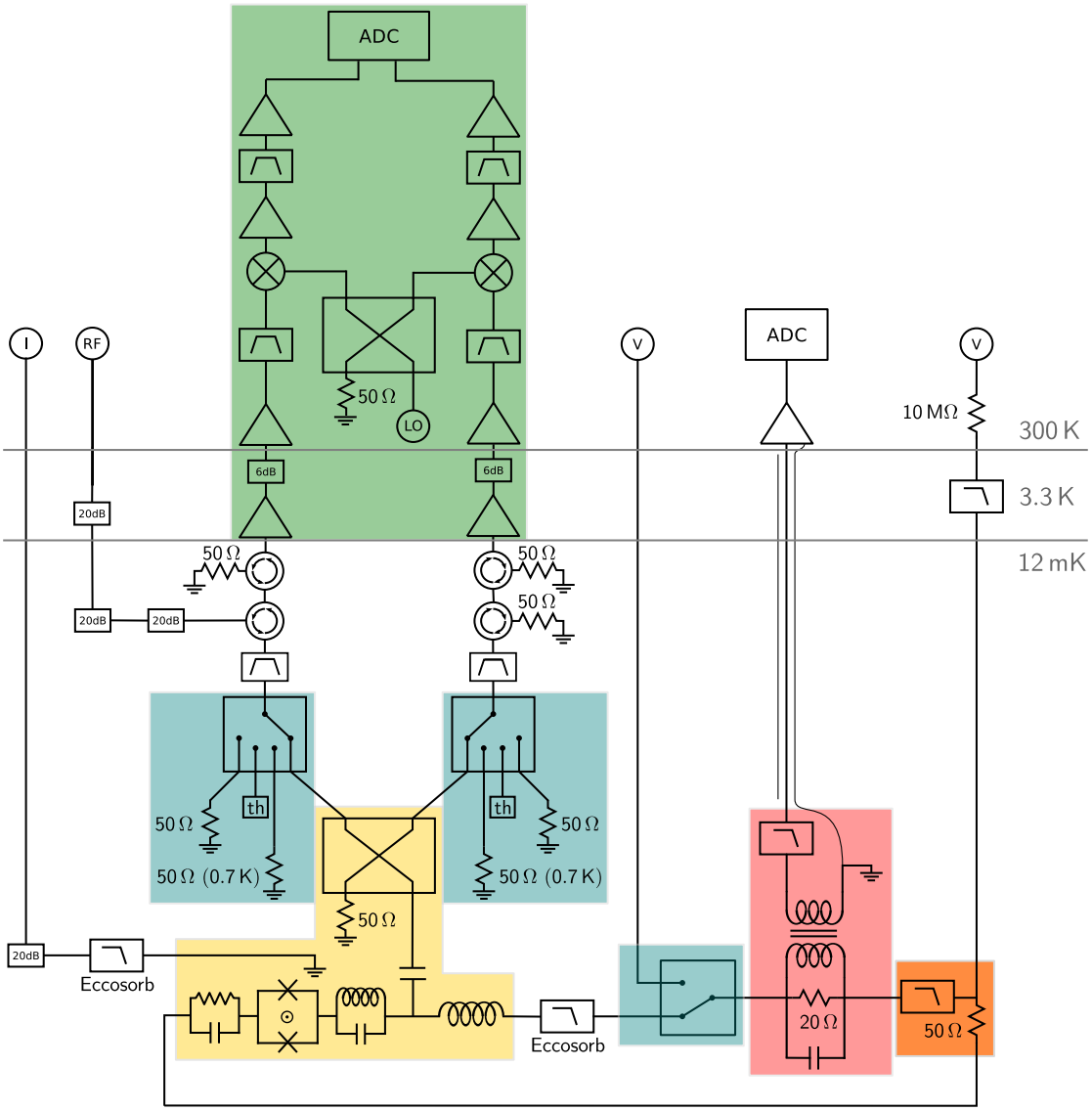

Figure (4.1): The entire measurement chain. Only elements inside the dilution refrigerator are represented in detail. The sample area (yellow) contains the light source, a bias tee and a beam splitter. RF (green) and DC (pink) measurement circuits are shown schematically and are described in the text. Blue regions indicate elements relevant to RF and DC calibration. The orange rectangle corresponds to the bias box described in the text. All resistors are thermalized at the temperatures corresponding to their area unless indicated otherwise.

(b) **Filtering and Isolation -** Next on each line are bandpass filters (Microtronics BPC50403, passband between 4 GHz and 8 GHz) and two successive circulators (Raditek RADC-4.0-8.0-Cryo-S21-qWR-M2-b) used as isolators by putting

a thermalized 50 Ω load at base temperature on the third port. They fulfill the purpose of protecting the sample from the amplifier noise leaking down the lines. The lower circulator on the left side is instead connected to an RF source via several thermalized 20 dB attenuators.

(c) **Amplification and measurement -** The remaining green section of the chain starts at the cold amplifiers mounted on the 3.3 K stage and ends at the analog to digital converter (ADC) of our measurement computer. It is described in section 4.2.1.

3. **DC side -** Everything beyond the inductor of the bias tee is the DC branch. It is used to apply a DC voltage bias to the sample and to measure a current through it.

   (a) **Eccosorb filter -** An element providing matched filtering beyond the working frequency of the bias tee (see Sec. 4.3.1).

   (b) **Calibration -** The blue rectangle highlights a two position switch allowing us to connect the DC measurement to a white noise source for calibration (see Sec. 4.3.2). Since the properties of the transformer do not change significantly over time this element was not present during most measurements.

   (c) **Transformer box -** The filtered box corresponding to the red area contains a transformer enabling us to measure the current by amplifying the voltage drop over a resistor on the DC bias line. Details can be found in section 4.3.2. Like the preceding component this was not part of the setup during all measurement campaigns.

   (d) **Bias box -** The orange square represents the base temperature part of a filtered voltage divider. This is used to voltage-bias the sample (see Sec. 4.3.3).

   (e) 3.3 K **filter -** Finally, the line is filtered at 3.3 K using a home-made element containing three series 10 kΩ resistors, with two 1 nF capacitances to ground between them.

4. **Flux bias line -** The flux bias line is visible at the very left side of the circuit diagram. As described in chapter 2, it is used to induce a magnetic flux inside the SQUID loop by making a current flow next to it. It consists of semi-rigid cupronickel coaxial cables (Coax Co., Ltd SC-219/50-CN-CN). At base temperature it is attenuated (thermalized 20 dB) and filtered (Eccosorb, cut-off frequency ≈ 1 GHz).

4.2 RF measurement setup

4.2.1 Overview

The main part of the high frequency measurement chain after the calibration stage and the isolators is indicated by the green box in Fig. 4.1. It has two independent channels starting with the first amplification stage consisting of two Low Noise Factory cryogenic amplifiers (LNF-LNC4-8A) working in the band between 4 GHz and 8 GHz. They are

mounted on 6 dB attenuators, which in turn are screwed directly on panel mount SMA connectors traversing the 3.3 K stage. The amplifiers themselves are thermalized to the stage with annealed copper bands. Their gain and noise temperature are indicated to be 44 dB and 2.2 K respectively. We have verified the latter values in a calibration measurement with as short as possible cables independent of the one presented later on. We use a LNF-PS2 power supply, with additional protection diodes at 300 K inside the refrigerator and filtered (1 nF) sub-d connectors at 3.3 K. As far as wiring is concerned, all RF base-stage connections as well as the lines leading up to room temperature from the cold amplifiers are semi-rigid cupronickel coaxial cables (Coax Co., Ltd SC-219/50-CN-CN), while the lines between the base-stage and the amplifiers are niobium titanium (SC-219/50-NbTi-NbTi).
Another amplification stage is set up at room temperature right on the outside of the refrigerator using Miteq amplifiers (AMF-5F-04000800-07-10P) with a gain of 50 dB and a noise temperature of ≈ 51 K , which is clearly dominated by the amplified noise of the first stage $T_{\mathrm{N,amp}} \approx 3500$ K (accounting for the attenuator and another 6 dB of cable attenuation).
After some additional filtering (Microtronics BPI 17594, bandpass between 4.25 GHz and 7.75 GHz) the signal is down converted using Marki (M1-0408LA) mixers with a conversion loss of 5.5 dB and a Rohde Schwarz SMF100A high frequency source as local oscillator, which is split on a AA-MCS power divider (AAMCS-PWD-2W-2G-18G-10W-Sf) to simultaneously act on both channels.
Then, the down-converted signal is further amplified (4 times Minicircuits ZX60-V62+, gain: 15 dB, $T_{\mathrm{N}} \approx 627$ K) and filtered (Microtronics BPM17596 1 GHz-1.7 GHz) before being digitized on an Innovative Integration analog to digital converter (X6-GSPS) with two channels (1.8 GS·s^{-1} and 12 bit). The latter was replaced after failure by an AlazarTech ATS9373 also set to 1.8 GS·s^{-1}.

4.2.2 Frequency down-conversion scheme

A few words should be said about our particular choice of sampling frequencies. Our signal is initially contained in a frequency band between approximately 4 GHz and 8 GHz, corresponding to the amplifier bandwidth. With our mixing setup we can down-convert this to a wide range of frequencies. Due to the Shannon-Nyquist sampling theorem, stating that the usable bandwidth is half the maximum sampling rate of our ADC, we can sample 900 MHz wide slices of this band. This can be done in the first Nyquist band going from 0 MHz to 900 MHz or in the second Nyquist band from 900 MHz to 1.8 GHz. In both cases, the other band has to be filtered out to avoid aliasing. Note that in the actual setup both the original and the down-mixed signal are filtered a bit narrower to avoid aliasing (see previous section). Nevertheless, we will carry out this discussion with the round values given above.
Figure 4.2a shows a power spectral density (PSD) map of the cold amplifier noise using the second band (the filtering used here: 0.9 GHz-1.8 GHz) to illustrate this. The IF frequency axis corresponds to the signal sampled on the ADC and the LO axis indicates the local oscillator frequencies used for down-mixing. The distortions due to the frequency

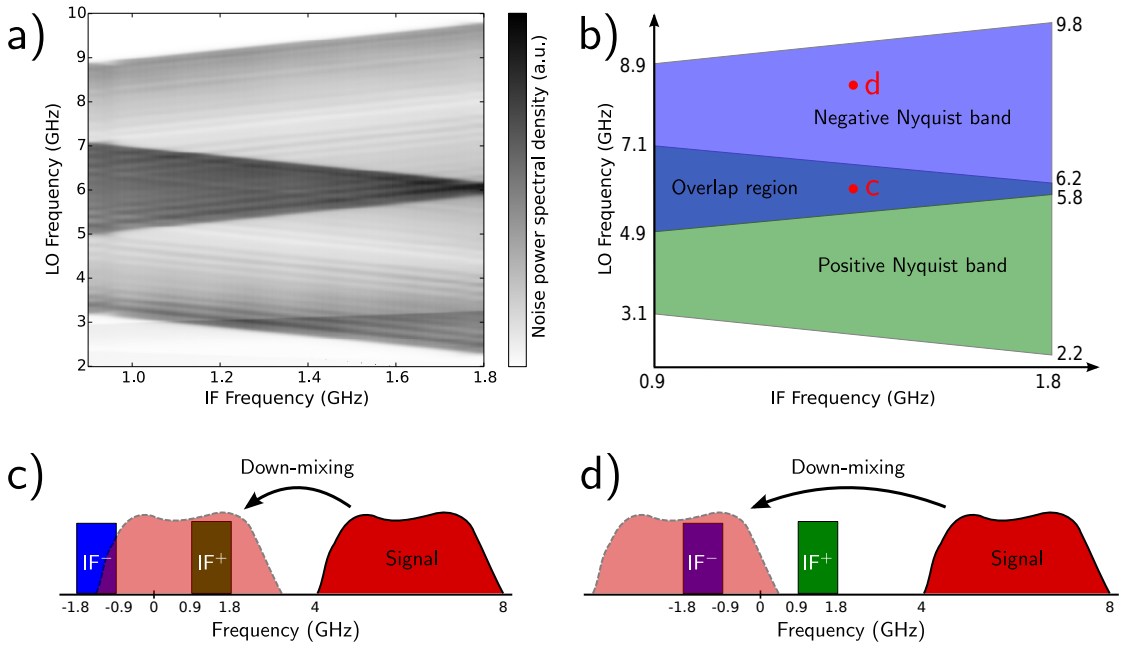

Figure (4.2): Down-mixing of the signal. a) The power spectral density (on one channel) of the noise on the cold amplifiers as a function of sampling frequency (IF) and local oscillator frequency (LO) in arbitrary units. b) Schematic representation of the data explaining where the different contributions come from. Green (blue) corresponds to mixing into the positive (negative) Nyquist band. The zone labeled "overlap region" is where both bands see parts of the signal and should be avoided when measuring. The letters c and d indicate where the examples given in the corresponding sub-figures are situated on this graph c) An illustration of the case when LO frequency is chosen badly and parts of the signal are mixed simultaneously into the positive (IF^+) and negative (IF^-) Nyquist bands. d) An example of mixing into the negative band with an LO frequency of $\approx 7.5\,\mathrm{GHz}$.

dependent gain of the measurement chain after the mixers have been calibrated out numerically. The gray scale is given in arbitrary units. Figure 4.2b aims to clarify the different zones, showing green (blue) regions where the signal has been mixed into the positive (negative) second Nyquist band. An overlap region where both positive and negative bands contribute to the measurement is visible in the middle. As an example for this consider the red point labeled "c", corresponding to the situation depicted in Fig. 4.2c. Here the signal (shown in red) is down-converted to the position on the frequency axis indicated by the light red form. Parts of it lie in either band and, since the ADC does not distinguish between positive and negative frequencies, are simply summed up in the final measurement result. This is why this region has a higher power spectral density in Fig. 4.2a. Naturally, this effect renders data extraction difficult and doubles the amplifier noise and should thus be avoided.

Figure 4.2d (red dot labeled "d" in Fig. 4.2b) shows a much more favorable situation. The signal is mixed down with an LO frequency of about 7.5 GHz and doesn't fall into the positive Nyquist band any more. The sampled slice corresponds directly to the original signal between 5.7 GHz and 6.6 GHz, which is centered on the emission frequency of one of the two devices discussed in this work. In a similar way we can use different local oscillator frequencies to directly and unambiguously sample the entire bandwidth of our cold amplifiers. Note that this would not be possible, if we were using the first Nyquist band. Then, the effect shown in Fig. 4.2c could not be avoided for some parts of the signal range.
Another discernible feature in Fig. 4.2a is the additional noise PSD at low LO frequencies reaching $\approx 3.3\,\mathrm{GHz}$ at the right edge. It originates from spurious down-mixing with the third harmonic of the LO signal into the negative Nyquist band. This effect is only detrimental to our measurements for signal frequencies below 4.2 GHz (requiring LOs $< 3.3\,\mathrm{GHz}$), but our samples typically operate between 6 and 7 GHz. To obtain a complete map of the PSD in the 4 GHz to 8 GHz range we use the following set of LO frequencies: 3.15 GHz, 3.6 GHz, 4.05 GHz, 4.5 GHz, 7.65 GHz, 8.1 GHz, 8.55 GHz and 9.0 GHz.

4.2.3 Calibration

Even though all correlation function measurements are self calibrated, because of the normalization and noise subtraction discussed in chapter 3, we still have to calibrate our measurement chain in order to be able to infer the average photon number emitted by our devices from power spectral density measurements.
The calibration part of the RF setup is indicated by the two blue boxes on the high frequency branch in Fig. 4.1. On each channel it consists of a 6-port Radiall switch connecting the input of the amplifiers to either the sample or the three calibration references. There are two $50\,\Omega$ loads thermalized at base temperature and at 0.7 K respectively and one output (labeled "th") of a 180° hybrid coupler splitting the signal coming from a $50\,\Omega$ load at 0.7 K (not shown). The 0.7 K loads are thermalized on the corresponding plate of the refrigerator with shared copper bands and their temperature is monitored with a dedicated thermometer. These loads are connected to the switch by means of short NbTi cables in order to insulate them thermally.
The noise power spectral density coming from a $50\,\Omega$ load on a matched line at temperature T is $S_{\mathrm{T}}^{(\mathrm{in})} = \hbar\omega \coth(\hbar\omega/2k_{\mathrm{B}}T)/2 \approx k_{\mathrm{B}}T$ for $k_{\mathrm{B}}T > \hbar\omega$. The total signal after amplification is:

$$S_{\mathrm{T}}^{(\mathrm{out})} = g\left(S_{\mathrm{T}}^{(\mathrm{in})} + k_{\mathrm{B}}T_{\mathrm{N}}\right) \tag{4.1}$$

Here g is the amplifier gain and T_{N} is the combined noise temperature of the amplifier and the cables leading up to it from the $50\,\Omega$ load. For this reason, it is important to put the switches as close to the sample as possible.
At base temperature ($T_{\mathrm{base}} \approx 12\,\mathrm{mK}$) the first term on the right side of Eq. (4.1) is negligible. By measuring the signal when switched to the 0.7 K load ($S_{0.7\,\mathrm{K}}^{(\mathrm{out})}$) as well

as the signal coming from the T_{base} load ($S_{\text{bT}}^{(\text{out})}$), we can extract both gain and noise temperature:

$$g = \frac{S_{0.7\,\text{K}}^{(\text{out})} - S_{\text{bT}}^{(\text{out})}}{S_{0.7\,\text{K}}^{(\text{in})}} \tag{4.2}$$

$$T_{\text{N}} = \frac{S_{\text{bT}}^{(\text{out})}}{g k_{\text{B}}} \tag{4.3}$$

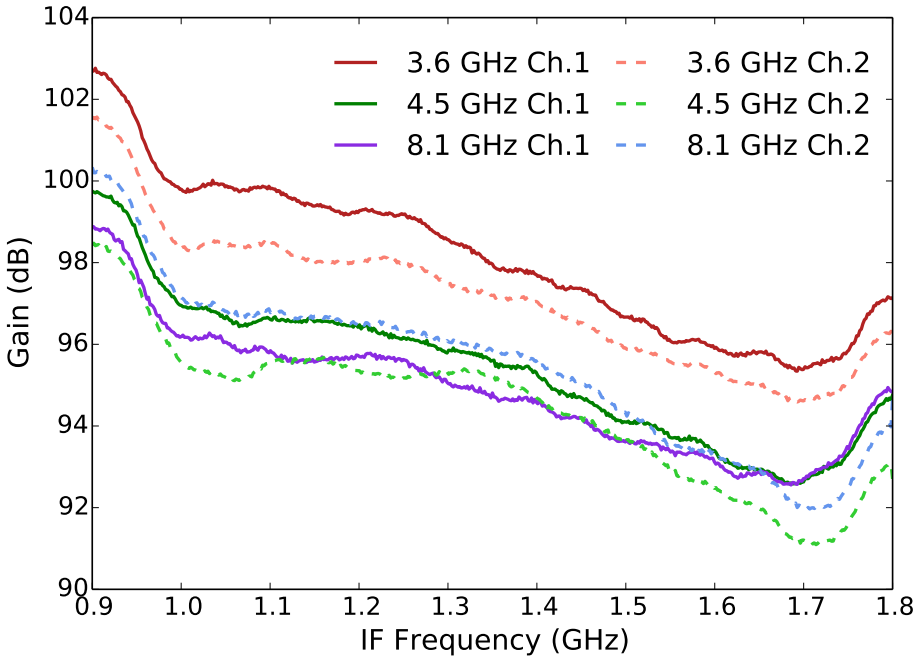

Figure (4.3): Gain of the entire measurement chain as a function of sampling frequency. The curves correspond to different values of the LO frequency on either channel (both given in the legend).

Since our measurement is spectrally resolved, this can be done for each frequency point and of course for each local oscillator on both channels thus fully calibrating the system.
Figure 4.3 shows the result of a gain calibration performed during the measurement campaign that gave the results described in chapter 6. Six curves are visible in the graph. The legend indicates which local oscillator frequency was used and on which channel the data was measured. The cross gain between both channels corresponds simply to the geometric average of the two individual gains.
The noise temperatures at the input of the first amplification stage for the same parameters are plotted in Fig. 4.4. The seventh curve around 5 mK in dark blue is magnified in the

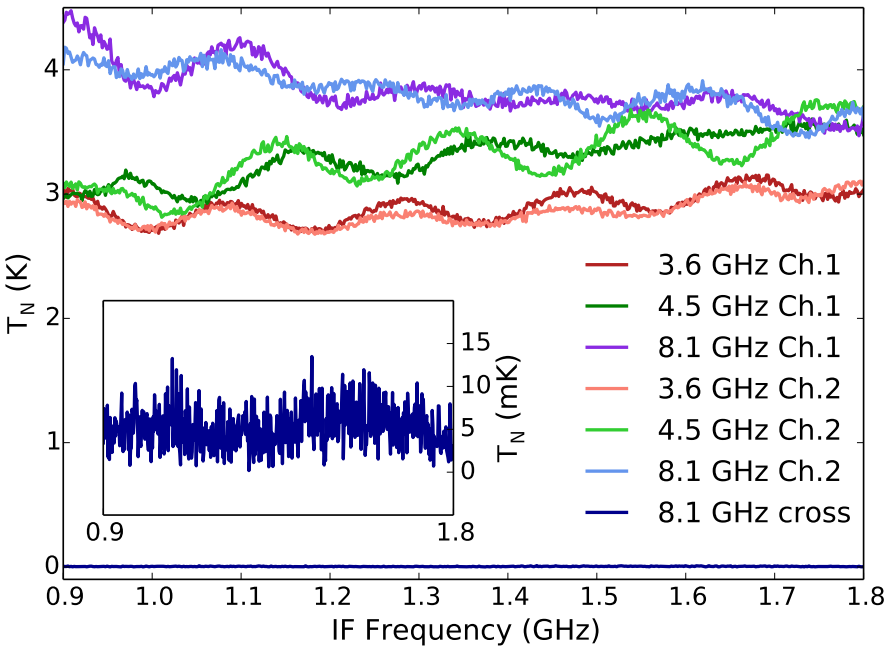

Figure (4.4): Noise temperature at the input of the cold amplifiers as a function of sampling frequency for three different local oscillator frequencies on either measurement channel. The dark blue line at the bottom of the graph is the noise temperature of the cross-noise between both channels and is shown magnified in the inset.

inset. It is of considerable interest, since it shows the cross noise temperature between both channels. All other local oscillators give similar values. This means that the cross noise power between both channels, which is directly proportional to $G^{(1)}_{\mathrm{x,noise}}(t,t)$, is indeed three orders of magnitude smaller than the direct noise power justifying the assumption made in section 3.4.2. Its main contribution comes from the digitizer itself. This calibration scheme naturally involves commuting the switches fixed to the base stage of our dilution refrigerator and cannot be repeated too often to avoid heating. Nevertheless, we can recalculate the gain for every single measurement while being connected to the sample and performing "On"/"Off" measurements. To do so we have to assume that the low temperature noise coming from the sample in the "Off" state (no voltage bias) is negligible compared to $k_{\mathrm{B}}T_{\mathrm{N}}$ and that T_{N} is stable on the timescale between calibrations (several days). Then the instantaneous gain is given by:

$$g_{\mathrm{inst}} = \frac{S_{\mathrm{off}}}{k_{\mathrm{B}}T_{\mathrm{N}}} \tag{4.4}$$

In this expression S_{off} is the measured signal when the sample is switched off. Thus, we can account for drifts in the gain of the entire chain as long as they are occurring on

timescales longer than a few seconds, which is the typical time of a measurement.
In Fig. 4.1 each switch has a fourth input called "th". It is coming from a 180° hybrid coupler splitting the noise emitted by a 50 Ω load at 0.7 K. Since at this temperature the load emits $\approx 2.2 \times 10^9$ photons·s^{-1} into the sampled bandwidth all noise sources can be neglected and the noise terms shown in Eq. (3.21) do not have to be subtracted. Nonetheless, we still have to correctly normalize the result since the second order correlations are given directly by:

$$g^{(2)}(\tau) = \frac{\Gamma^{(2)}_{\text{cross}}(\tau)}{\left[\Gamma^{(1)}_{\text{cross}}(0)\right]^2} \tag{4.5}$$

Here the $\Gamma(\tau)$ correspond to the complex envelope cross-correlators introduced in chapter 3. The outcome of this measurement is plotted in Fig. 4.5 displaying the expected bunching value of two at time difference $\tau = 0$. This signifies that all gain and phase factors are normalized out correctly, verifying the self calibration of the $g^{(2)}$ measurement and our data extraction protocols.

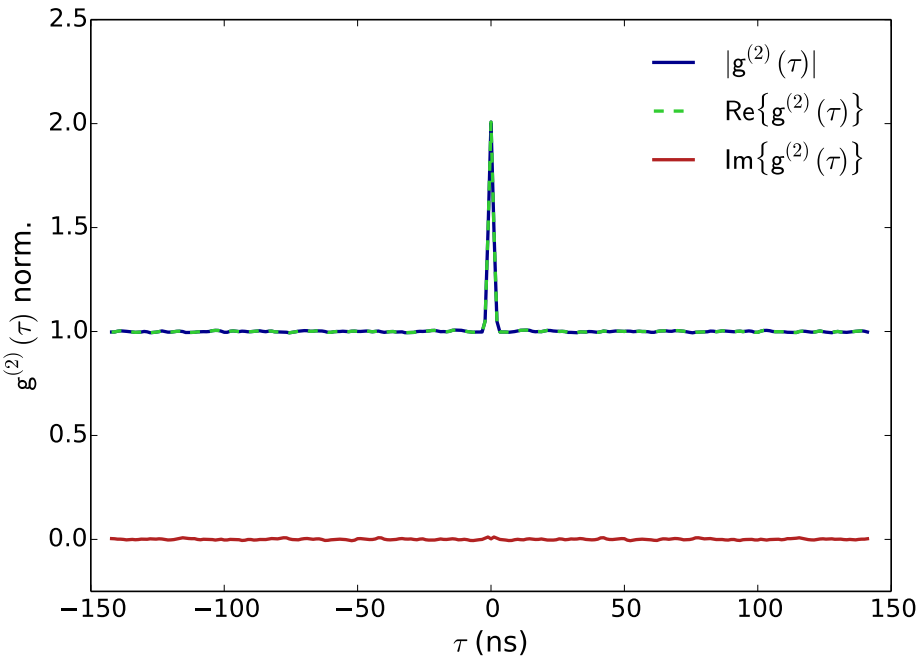

Figure (4.5): The normalized second order correlation function of a 50 Ω resistor at a temperature of 0.77 K emitting thermal radiation. As expected $g^{(2)}(0) = 2$ displaying thermal bunching. Then the correlation quickly drops to the long time limit of $g^{(2)}(\tau > 0) = 1$.

4.3 DC measurement setup

The purpose of the DC side of the measurement setup, shown in Fig. 4.1, is to measure the Cooper pair current passing through the sample. It should be decoupled from the high frequency side and, most importantly, it should not present a high impedance to the sample at any frequency in order to avoid emission of photons into this part of the measurement chain. The filtering properties of samples with an on-chip bias tee can be looked up in section 2.5. When measuring a sample of the type shown in Fig. 2.9 we use an external bias tee with a crossover frequency of 50 MHz. In both cases we add further filters as described below.
At the end of the DC branch is a Celians (EPC1-B) amplifier with a variable gain (40 dB, 60 dB or 80 dB) and a voltage noise of $\approx 0.7\,\mathrm{nV}\cdot\sqrt{\mathrm{Hz}}^{-1}$, which is connected to the transformer box by a Thermocoax cable. The shield of the cable is connected to ground on the base-stage and to the inverted input of the amplifier at 300 K to avoid ground loops. The amplifier is followed by a Measurement Computing (USB-1608GX-2AO) analog to digital converter, with a maximum sampling frequency of 500 kHz and 8 digital input/output ports. This device is also used to send a signal into the DC calibration setup.

4.3.1 Eccosorb filter

It has been shown that a stripline in a cavity surrounded by Emerson & Cumming Eccosorb dielectric acts as a low pass filter, which is absorptive in its stopband and thermalizes well at millikelvin temperatures. If its geometry is chosen appropriately, it acts as a 50 Ω matched load in its stopband [80]. We have made several versions of such filters using two different geometries. The first consists of an elongated rectangular box with a cylindrical hole as the outer, and a thin wire as the inner conductor. It has a ratio of 10 between the radii of inner and outer conductors, calculated from the data provided by the manufacturer, and a total length of 40 mm. The interstice was completely filled with Eccosorb (CRS 124). The S-parameters of the resulting element can be seen in Fig. 4.6a. The cutoff frequency was around 620 MHz and reflections are around −10 dB. We measured the response of the filter terminated with a 50 Ω load on a sampling oscilloscope and from the height of the reflection step we could calculate an optimized aspect ratio of ≈ 4.
Subfigures b) and c) show the characteristics of two filters made following a different design. We used a copper semi-rigid coaxial cable with an inner diameter of the outer conductor of 2.98 mm. The original inner conductor had a diameter of 0.91 mm and was taken out together with the original dielectric. Another copper wire with a diameter of 0.8 mm was used as new inner conductor and surrounded with Eccosorb. Finally, conical centering guides made from the original dielectric were introduced in the outer conductor tube at the ends, holding the wire in place, and SMA connectors were soldered on it. This procedure works well for short enough filter lengths, but causes imperfect matching for longer elements, when the inner conductor can bend inside the tube. An example of this can be seen in Fig. 4.6c at low frequencies, where a slight mismatch, caused by the

bending, leads to increased reflection. Since the cutoff frequency is inversely proportional to the length of the element, this fabrication method has a lower bound of a few hundred MHz. The characteristics of Fig. 4.6b on the other hand present a smooth rolloff around 1 GHz and low reflection (≈ -20 dB) over the entire frequency range.

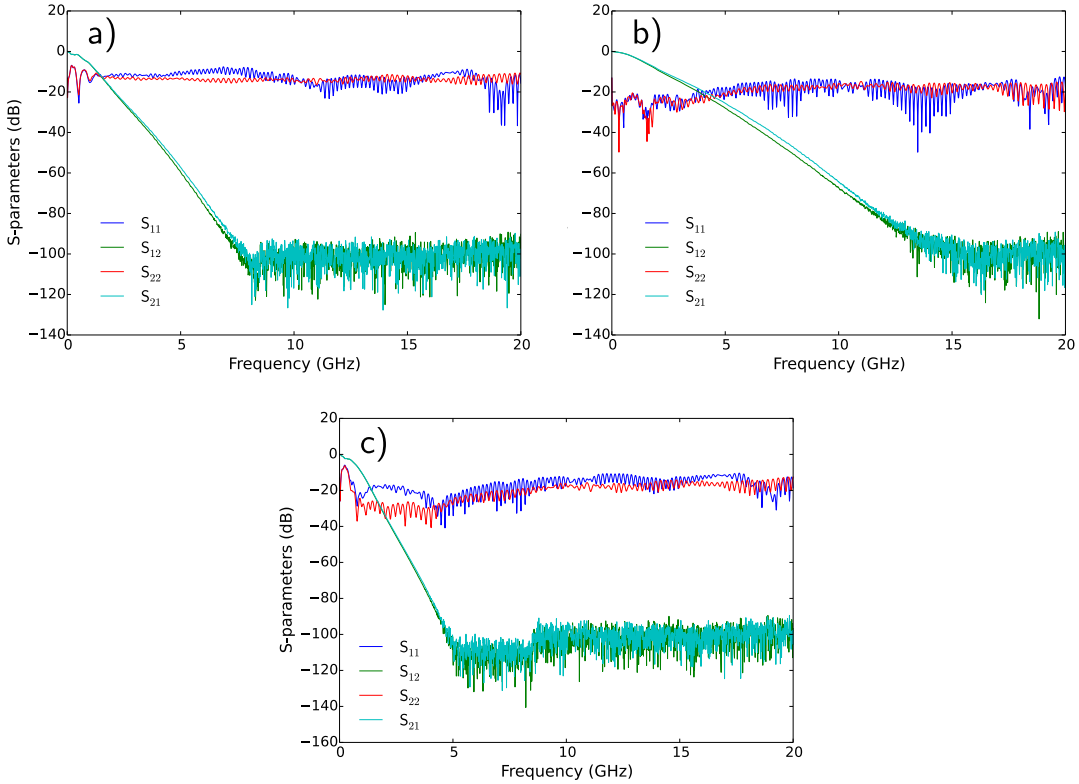

Figure (4.6): Transmission and reflection S-parameters of the Eccosorb filters. All measurements go from 300 kHz *to* 20 GHz *a) Filter of type 1 with a length of* 40 mm *and a* -3 dB *cutoff frequency of* 620 MHz. *b) Type 2 filter of length* $\approx$ 20 mm, *and cutoff at* 1 GHz *c) Type 2 filter of length* $\approx$ 70 mm *and cutoff at* 480 MHz. *The reflection properties at low frequencies are not as good as in b, probably due to a deformation of the inner conductor made possible through the increased filter length.*

4.3.2 Transformer box

The transformer box is the central element of the DC branch and is used to measure the current through the line leading to the sample via the voltage drop over a 20 Ω resistor. Its circuit diagram is represented in Fig. 4.7 with three ports indicating where the voltage source, the sample and the output towards the amplifier are connected.
All resistive elements are NiCr resistors (Sumusu RR1220P/Q-XXX-D) and have been tested at 4 K displaying a maximal change in their values of $< 2\,\%$. The capacitive

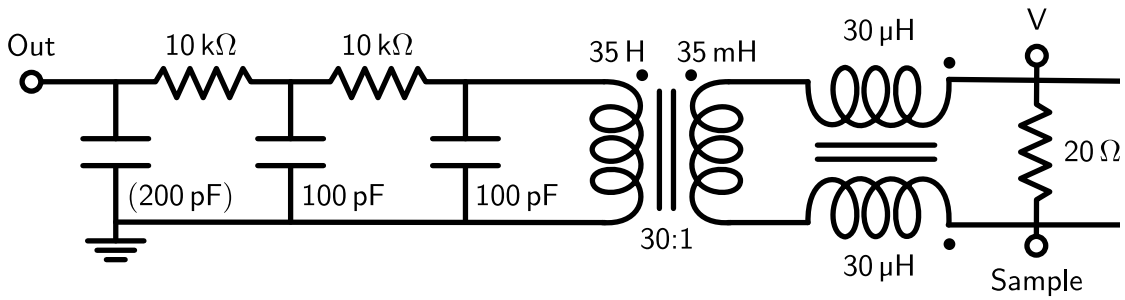

Figure (4.7): Circuit diagram of the transformer box. The 20 Ω resistor is in series with the bias line of our sample. A current traversing it causes a voltage drop which is amplified by the unbalanced transformer. The balanced transformer and the RC elements are added for filtering. Black dots indicate the polarization of the transformer windings. The value in brackets is our estimation of the capacitance of the cable leading to the amplifier.

elements are feed through capacitors. Together they make up the left side of the circuit diagram, which is responsible for filtering the output line.
The main element in the middle is a CMR-direct low temperature transformer (LTT-h) with a winding ratio of 30 : 1. It fulfills the triple purpose of filtering the signal, amplifying the voltage across the measurement resistor and up-converting its impedance by a factor of $\approx 10^3$ for better matching with the amplifier input impedance. Between both elements we have added another home-made transformer (a twisted pair wound around a ferrite bead) with a 1 : 1 winding ratio, which provides additional filtering of the common mode. The trans-impedance of this device and the part of the DC measurement chain beyond it has been calibrated as a function of frequency using the switch visible inside the blue box on the DC branch of Fig. 4.1. To do so, we commute the switch and send digitally created white current noise through the 20 Ω resistor. For this, we use the aforementioned Measurement Computing device with a 1 MΩ series resistor at 300 K. We then sample the response at the output of the amplifier and perform a Fourier transform. Dividing output voltage through input current directly yields the trans-impedance $Z_T = V_{out}/I_{in}$ of the DC setup including the amplifier gain, which is the desired calibration curve shown in Fig. 4.8.
In a running experiment the voltage bias on the sample is switched on and off alternately with a frequency of $\nu \approx 1$ kHz giving a rectangular signal $V_{in}\,\sqcap\!\_(t)$. In order to extract the measured current we first normalize the applied voltage to get the envelope $\sqcap\!\llcorner(t)$ and then calculate its Fourier transform (FT). This creates a reference signal. We also compute the FT of the measured signal $V_{out}(t)$ and compare its first Fourier component to the corresponding value of the reference. This gives the amplitude of the response in Volt from which we can get the current by dividing through $Z_T(\nu)$ at the frequency of the Fourier component:

$$|I| = \frac{\mathsf{FT}\left[V_{\mathrm{out}}(t)\right]}{\mathsf{FT}\left[\sqcap\!\!\llcorner(t)\right] Z_{\mathrm{T}}(\nu)} \tag{4.6}$$

As has been mentioned above, the transformer box along with the calibration were not part of all measurement campaigns.

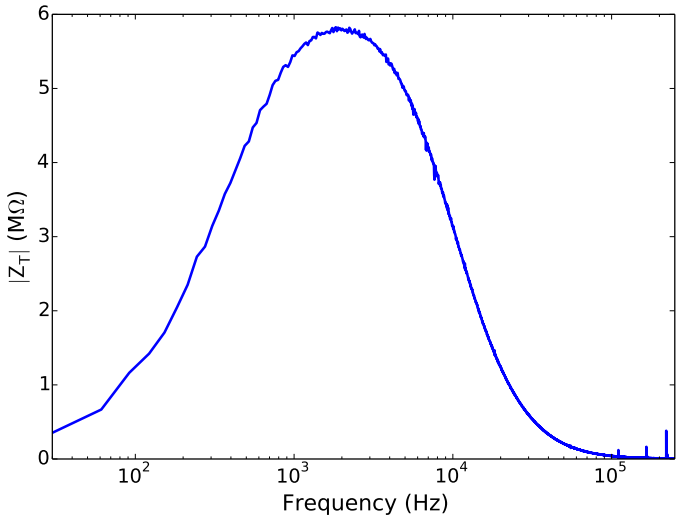

Figure (4.8): The trans-impedance of the DC measurement setup giving the gain conversion between a current through the 20 Ω *measurement resistor and the voltage measured on the ADC as a function of frequency. The maximum value of around* 6 MΩ *corresponds well to the expected value for a transformer winding ratio of 30:1 and an amplifier gain of* $\approx 10^4$*. The system acts as a bandpass filter between* 300 Hz *and* 11 kHz*.*

4.3.3 Bias box

This element is used for applying a voltage bias to the sample and as a first filtering stage against high frequency noise. A simplified circuit diagram of it is shown in the upper part of Fig. 4.9. The actual device is shielded inside a copper box. In general all values given in the following discussion and in the figure have been measured at 4.2 K. Codes given in brackets are Farnell references. All resistive elements are NiCr resistors as in section 4.3.2.

The resistor to ground at the input forms a voltage divider with another much bigger resistance at room temperature (usually 10 MΩ). Its value is either 25 Ω or 50 Ω depending on the version of the bias box. Three filtering tiers in separate cavities of the copper box are added in order to suppress noise leaking down the cables. Each capacitive element is realized by putting three different capacitors in parallel. We used two layered geometries, a 850 nF (2112915) and a 1 nF (1885457RL) as well as a 100 pF feed through capacitor in order to cover an as broad as possible frequency range. In addition, after soldering, each

cavity was partially filled with Eccosorb CRS 124 to eliminate high frequency modes. The series LR elements participate in the filtering and fulfill the purpose of matching the impedance to a value of several tens of Ω over a wider frequency range.

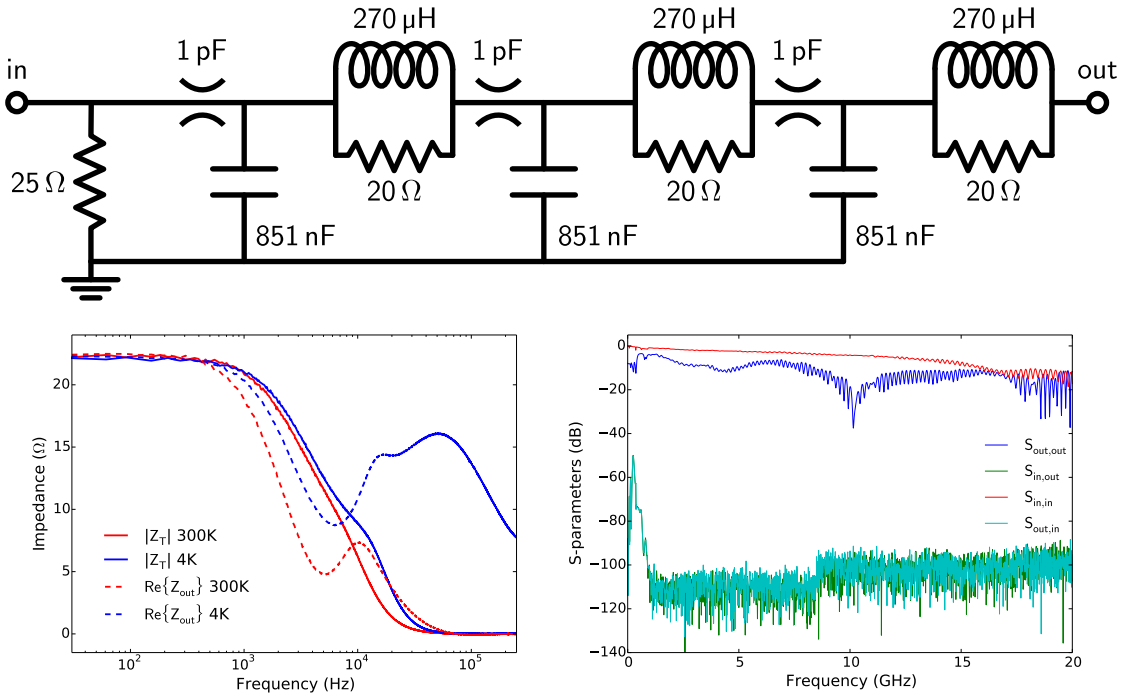

Figure (4.9): Top: Circuit diagram of the voltage bias box. Bottom left: Measured real part of the input impedance and absolute value of the trans-impedance of the device at both 300 K *and* 4 K *up to a frequency of* 250 kHz. *Bottom right: Transmission and reflection S-parameters from* 300 kHz *to* 20 GHz.

The lower left panel of Fig. 4.9 shows the input- and trans-impedance of the box as seen from the sample side (port labeled "out") in a frequency range going from 30 Hz to 250 kHz at room temperature and at 4 K. This characterization was performed in an analog manner to the calibration of the DC setup by measuring the frequency dependent voltage response to white current noise. Z_{out} is the voltage response on the "out" port to a current stimulus on the same side and Z_{T} is the response, if the current is injected on the "in" side. The output impedance drops to zero around 40 kHz at room temperature, but stays between 10 Ω and 25 Ω at 4 K, which is due to a decrease of the capacitances to the values marked in Fig. 4.9. Note that we plot the real part of Z_{out}, since this is the quantity that matters within the theoretical framework presented in chapter 5. The trans-impedance is a measure for how well high frequency noise at the input is filtered at the output and has a cutoff around 6.3 kHz at 4 K. The value at room temperature is slightly lower (5.3 kHz) for similar reasons as before.
Finally, the lower right panel of Fig. 4.9 shows the high frequency characteristics of the

device in the form of its S-parameters from 300 kHz to 20 GHz. The reflection values are of little consequence, since no efforts were made to match the impedance of the device at high frequencies and are only given for the sake of completeness. The transmission values show that noise is efficiently filtered over the entire studied frequency range.

4.4 The sample holder

The sample holders we use are copper and aluminium boxes fitted with eight SMA connectors, corresponding to the design of our chips (Fig. 2.8). The connector pins are soldered onto the inner conductors of coplanar waveguides (CPW) on a gold plated printed circuit board (PCB) with a rectangular hole of 1 cm^2 in its middle.
The chip is placed in this hole and clamped down as shown in Fig. 4.10. It rests on the lower part of the sample holder only at its corners, the volume underneath it being empty. This is done to remove the additional ground plane from the back of the sample. The coplanar waveguides of the sample are connected with Aluminum bonds to their counterparts on the PCB taking particular care to respect the distances between inner conductor and ground in order to preserve the 50 Ω matching. The ground planes of the PCB and the chip are connected at narrow intervals to eliminate resonances.
To avoid box modes we have lined the inner walls of the volume under the chip and the lid with Eccosorb.

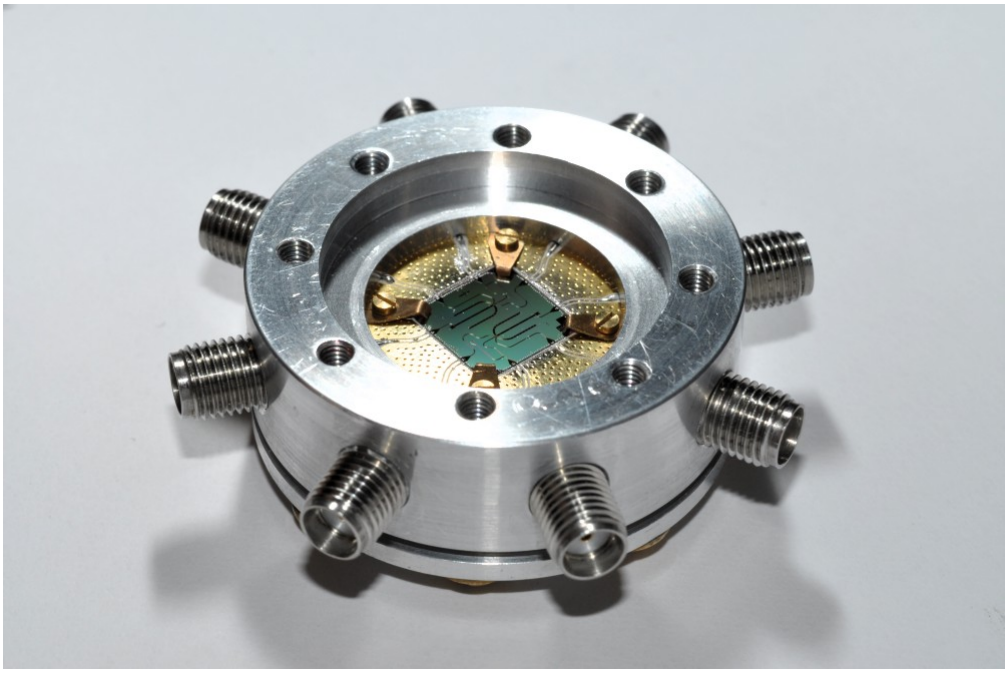

Figure (4.10): Photograph of the sample holder with a chip of the beam splitter type (Fig. 2.8) in place.

Chapter 5

Photon emission through ICPT: Theory

5.1 Introduction

The purpose of this chapter is to give an account of the theoretical framework, describing the emission of microwave photons through inelastic Cooper pair tunneling (ICPT). In this task we do not aim to be entirely exhaustive, since ICPT has solicited much theoretical and experimental work for several decades [2, 15, 18–20]. Instead, we discuss the basic concepts with a clear focus on the photonic side of the phenomenon. As part of this effort we will give a derivation for the photon emission rate as a function of relevant system parameters allowing us to efficiently describe some of the experimental results given in chapter 6. Recent theoretical developments concern not only emission rates but also statistics of the emitted radiation [32, 33, 35, 36, 81]. Again, in our overview of the latter, we will focus only on the results most relevant to our system. A particular emphasis will be placed on [36], which describes the exact implementation of our single photon source.

5.2 Photon emission rates as a function of the environmental impedance

In very general terms, the Hamiltonian of the system shown schematically in Fig. 5.1 can be described by taking into account the energy contributions of the Josephson junction and its electromagnetic environment:

$$H = H_{\mathrm{env}} + H_{\mathrm{J}} \tag{5.1}$$

5.2.1 Electromagnetic environment

The first term on the right hand side of (5.1) describes the electromagnetic environment of the junction. As previously mentioned (see Fig. 3b), a Cooper pair can tunnel inelastically

through a voltage biased Josephson junction by dissipating its surplus energy into the electromagnetic environment. Consequently, it is convenient to express H_{env} in a form that explicitly involves the real (dissipative) part of the input-impedance that is presented to the junction by its electromagnetic environment.

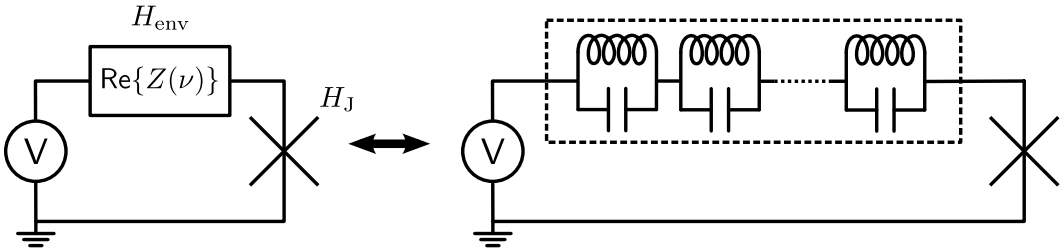

Figure (5.1): The schematic circuit diagram of the basic system consisting of a Josephson junction, marked by the cross, and its electromagnetic environment, represented by the real part of its impedance $Re\{Z(\nu)\}$. The right side illustrates the decomposition of $Re\{Z(\nu)\}$ in terms of parallel LC oscillators.

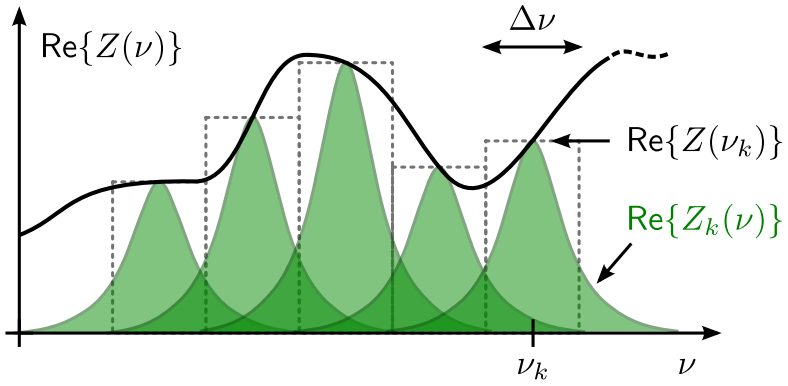

Figure (5.2): The decomposition of $Re\{Z(\nu)\}$ into a sum of LC oscillators. The combined surface of the oscillator impedances tends towards $Re\{Z(\nu)\}$ in the infinitesimal limit, if Eq. (5.4) is satisfied for each oscillator.

Figures 5.1 and 5.2 give a schematic illustration of how the real part of an arbitrary impedance $Z(\nu)$ can be described phenomenologically by a series collection of parallel LC oscillators with impedance $Z_k(\nu)$.

$$\sum_k \text{Re}\{Z_k(\nu)\} = \text{Re}\{Z(\nu)\} \tag{5.2}$$

To better understand this we can write the integral of $\text{Re}\{Z(\nu)\}$ as a Riemann sum:

$$\lim_{\Delta\nu\to 0} \sum_k \text{Re}\{Z(\nu_k)\}\Delta\nu \tag{5.3}$$

In order for a sum of infinitesimal LC oscillators to correspond to the above expression, the following condition has to be fulfilled for each oscillator:

$$\int_0^\infty \mathrm{d}\nu \mathrm{Re}\{Z_k(\nu)\} = \mathrm{Re}\{Z(\nu_k)\}\Delta\nu \tag{5.4}$$

The right-hand side of this equality describes the real part of the environmental impedance $Z(\nu)$ at frequency ν_k, while the left-hand side is proportional to the integral over the real part of the k$^{\text{th}}$ oscillator. The latter is found by integration in the complex plane over the real part of the expression for the impedance of a parallel RLC circuit. The resistance gives a finite width to the resonator, but drops out in the integral, giving:

$$\int_0^\infty \mathrm{Re}\{Z_k(\nu)\}\mathrm{d}\nu = \frac{\pi}{2}\nu_k Z_{\text{eff},k} \tag{5.5}$$

Together with (5.4) this leads to the condition:

$$Z_{\text{eff},k} = \frac{2}{\pi}\frac{\mathrm{Re}\{Z(\nu_k)\}\Delta\nu}{\nu_k} \tag{5.6}$$

Here, $Z_{\text{eff},k} = \sqrt{L_k/C_k}$ is the characteristic impedance of the k$^{\text{th}}$ oscillator. More details on this calculation are given in appendix D.2.
This result allows us to write the Hamiltonian of the environment in the following manner (using the usual quantization of the harmonic LC oscillator [73, 74]):

$$H_{\text{env}} = \sum_k \frac{\hat{q}_k^2}{2C_k} + \frac{1}{2L_k}\left(\frac{\hbar}{2e}\hat{\varphi}_k\right)^2 = \hbar\omega_k\left(\hat{a}_k^\dagger\hat{a}_k + \frac{1}{2}\right) \tag{5.7}$$

In this expression, $\hat{q}_k$, $\hat{\varphi}_k$, C_k and L_k are respectively the charge on the capacitor, the phase across the inductor, the value of the capacitance and the value of the inductance. The phase is defined from the flux Φ through the inductor as:

$$\hat{\varphi}_k = \Phi/(2\pi\Phi_0) = \sqrt{\pi\frac{Z_{\text{eff},k}}{R_{\text{Q}}}}(\hat{a}_k^\dagger + \hat{a}_k) \tag{5.8}$$

Where Φ_0 is the magnetic flux quantum and $R_{\text{Q}} = h/(4e^2)$ is the superconducting resistance quantum. The factor $\sqrt{\pi Z_{\text{eff},k}/R_{\text{Q}}}$ in the last term comes from the quantization of the LC-oscillator [73]. This definition is chosen to be in agreement with the AC Josephson relation [56]:

$$\varphi = \frac{2e}{\hbar}\int V\mathrm{d}t \tag{5.9}$$

This leads to a commutation relation between phase and charge operators of the form:

$$[\hat{\varphi}, \hat{q}] = 2ei \tag{5.10}$$

The information on the form of the real part of the environmental impedance given by condition (5.6) is contained in C_k and L_k and is still present in the right-hand side

of (5.7) as part of the normalization factors used to write charge and phase in terms of the creation and annihilation operators $\hat{a}_k$ and $\hat{a}_k^\dagger$ for each individual oscillator.

5.2.2 Josephson junction

The second term on the right hand side of (5.1) is the well known Josephson Hamiltonian[56]:

$$H_\mathrm{J} = -E_\mathrm{J}\cos(\hat{\varphi}) = -\frac{E_\mathrm{J}}{2}\left(e^{-i\hat{\varphi}} + e^{i\hat{\varphi}}\right) \tag{5.11}$$

Here, E_J is the Josephson energy of the junction and $\hat{\varphi}$ is the phase difference across it. The latter is not a completely independent variable, but is linked to the phase differences across all of the LC oscillators and to the constant external voltage bias.

$$\hat{\varphi} = \sum_k \hat{\varphi}_k + \frac{2e}{\hbar}Vt \tag{5.12}$$

In the context of our work, it is instructive to consider the form of H_J written on the right-hand side of (5.11). From the commutation relation (5.10), we can see that each of the two exponential functions corresponds to a translation operator for the charge difference between both sides of the junction. In other words, applying $e^{-i\hat{\varphi}}$ to a state of the system, makes a charge of $2e$, one Cooper pair, tunnel through the Josephson junction. Additionally, since $\hat{\varphi}$ is related to the phases over all the resonators, this operator contains combinations of the operators $\hat{a}_k$ and $\hat{a}_k^\dagger$ to all orders (see Eq. (5.8)). It will therefore also induce transitions between the states of the environment. This is discussed in the next section.

5.2.3 Tunneling probability and photon spectral density

The probability for a Cooper pair to tunnel through the junction inelastically can be computed with Fermi's golden rule using the Josephson Hamiltonian as a perturbation of the system consisting of all the environmental modes. This approach is the starting point for the so-called P(E)-theory of dynamical Coulomb blockade. An excellent overview of this calculation is given in reference [2], where the environmental degrees of freedom are traced out, leading to a result depending on correlations between the phase fluctuations at the junction. These are related to the real part of the impedance seen by the junction via the fluctuation-dissipation theorem, and in the end give an expression for the Cooper pair tunneling rate into the direction of the voltage bias:

$$\Gamma = \frac{\pi}{2\hbar}E_\mathrm{J}^2\mathrm{P}(2eV) \tag{5.13}$$

The function $\mathrm{P}(E)$ gives the probability for a Cooper pair to tunnel through the junction, while dissipating its energy E into the environment. Here, E is $2eV$, the energy given to the CP through the voltage bias. This function obeys the following normalization and detailed balance relations:

$$\int_{-\infty}^{\infty} \mathrm{P}(E)\mathrm{d}E = 1$$
$$\mathrm{P}(-E) = e^{-\frac{E}{k_\mathrm{B}T}}\mathrm{P}(E) \tag{5.14}$$

The second equation signifies that $\mathrm{P}(-E)$ vanishes for low temperatures. This happens, because at negative energies the Cooper pair tunnels against the voltage bias, thus drawing its energy from the thermal excitations of the electromagnetic environment. At zero temperature $\mathrm{P}(E)$ is given by the integral equation [2, 82]:

$$\mathrm{P}(E) = \frac{2}{E}\int_0^E \mathrm{d}E' \frac{\mathrm{Re}\{Z\,(E'/\hbar)\}}{R_Q}\mathrm{P}(E-E') \tag{5.15}$$

This form, called the Minnhagen equation (see Sec. D.3), depends only on the real part of the environmental impedance and the superconducting resistance quantum $R_\mathrm{Q} = h/(4e^2) \approx 6.5\,\mathrm{k\Omega}$, making it possible to calculate $\mathrm{P}(E)$ numerically from an arbitrary starting value with subsequent normalization.
Another integral equation for $\mathrm{P}(E)$ at finite temperature, well adapted to numerical calculation, has been developed in reference [18] and is used for temperature dependent theoretical predictions in chapter 6.
As pointed out before, the aim of this chapter is clearly not to review the extensive literature developed on the topic of dynamical Coulomb blockade. Instead, we would like to concentrate, as in our experiments, on the photonic side of the effect. In all of the calculations mentioned so far, the states of the environment have been traced out and the detailed information on their excitations has been lost. Here we want to focus on another idea, allowing us to make frequency dependent predictions on the photon emission rate [20]. This approach equally enables us to extract the exact form of $\mathrm{Re}\{Z(\nu)\}$ from the recorded emission spectrum.
The first step towards this, is to write down Fermi's golden rule for the forward tunneling rate as is done in the derivation of P(E)-theory [2], where the tunneling operator induces transitions between the initial state $|i\rangle$ of the environment and its final state $|f\rangle$:

$$\Gamma = \frac{\pi}{2\hbar}E_\mathrm{J}^2 \left|\langle f|\, e^{-i\sum_l \hat{\varphi}_l}\,|i\rangle\right|^2 \delta(2eV + E_i - E_f) \tag{5.16}$$

The phase factor $e^{-i2eVt/\hbar}$ has dropped out, but energy conservation is taken care of by the delta function retaining only the terms where the sum of initial energy of the environment E_i and the energy conferred to the Cooper pair through the voltage bias $2eV$ is equal to the final energy E_f. We can make the states of the environment appear explicitly:

$$\Gamma = \frac{\pi}{2\hbar}E_\mathrm{J}^2 \sum_{\vec{n},\vec{m}} p_{\vec{n}} \left|\langle \vec{n}+\vec{m}|\, e^{-i\sum_l \hat{\varphi}_l}\,|\vec{n}\rangle\right|^2 \delta(2eV - h\vec{m}\cdot\vec{\nu}) \tag{5.17}$$

Here we use a vector notation to indicate that each state is the tensor product of an infinite number of modes $|\vec{n}\rangle = |n_0, n_1, n_2, \ldots\rangle$. A vector $\vec{n}$ describes one possible

combination of the occupation numbers of all the modes and occurs with a probability $p_{\vec{n}}$. This means that the initial state is given by a statistical mixture without coherences as described by the density matrix:

$$\rho_i = \sum_{\vec{n}} p_{\vec{n}} \left|\vec{n}\right\rangle \left\langle\vec{n}\right| \tag{5.18}$$

We also sum over all the possible numbers of photons added to each mode via the vector $\vec{m}$. For each term in this sum, the difference between final and initial energies of the environment is $E_f - E_i = h\vec{m}\cdot\vec{\nu}$, where $\vec{\nu}$ is a vector containing all the mode-frequencies under the same convention.
Since the phase operators commute, we can rewrite the tunneling operator as:

$$e^{-i\sum_l \hat{\varphi}_l} = \prod_l e^{-i\hat{\varphi}_l} \tag{5.19}$$

Using that $\hat{\varphi}_l$ only acts on the mode l, we can exchange the sum over the initial states and the product:

$$\Gamma = \frac{\pi}{2\hbar} E_\mathrm{J}^2 \sum_{\vec{m}} \prod_l \left[\sum_n p_{l,n} \left| \left\langle n + m_l \right|_l e^{-i\hat{\varphi}_l} \left| n \right\rangle_l \right|^2 \right] \delta(2eV - h\vec{m}\cdot\vec{\nu}) \tag{5.20}$$

Note that the sum over all the added photon numbers $\vec{m}$ still has to remain outside of the product, because the condition on energy conservation given by the delta function links different modes. The quantity m_l giving the number of photons added to mode l can formally be written as $\vec{m}\cdot\vec{e}_l$, where $\vec{e}_l$ is the unit vector of this mode.
We recall that part of the above equation can be identified as $\mathrm{P}(2eV)$ by comparison with (5.13):

$$\mathrm{P}(2eV) \equiv \sum_{\vec{m}} \prod_l \left[\sum_n p_{l,n} \left| \left\langle n + m_l \right|_l e^{-i\hat{\varphi}_l} \left| n \right\rangle_l \right|^2 \right] \delta(2eV - h\vec{m}\cdot\vec{\nu}) \tag{5.21}$$

In the next step we will focus only on the processes where m_k photons are emitted into one specific mode k. Note that this can coincide with the emission of any number of photons into the other modes. In this case, each term in the remainder of the sum over $\vec{m}$ will contain a factor describing just mode k:

$$\sum_{n=\max\{0,-m_k\}} p_{k,n} \left| \left\langle n + m_k \right|_k e^{-i\hat{\varphi}_k} \left| n \right\rangle_k \right|^2 \tag{5.22}$$

In this summation we have taken into account that the Cooper pair tunneling process can also absorb photons, meaning that m_k can be negative. We can now factorize this mode and condense all the others into a modified function $\mathrm{P}'(2eV - m_k h\nu_k)$.

$$\Gamma_m = \frac{\pi}{2\hbar} E_\mathrm{J}^2 \sum_{n=\max\{0,-m_k\}} p_{n,k} \left| \langle n+m_k|_k \, e^{-i\hat{\varphi}_k} \, |n\rangle_k \right|^2 \mathrm{P}'(2eV - m_k h\nu_k) \tag{5.23}$$

As indicated in Eq. (5.8) the phase $\hat{\varphi}_k$ can be written as:

$$\hat{\varphi}_k = \sqrt{\frac{\pi Z_k}{R_\mathrm{Q}}} \left(\hat{a}_k^\dagger + \hat{a}_k\right) = \sqrt{2r(\nu_k)\frac{\Delta\nu}{\nu_k}} \left(\hat{a}_k^\dagger + \hat{a}_k\right) \tag{5.24}$$

In the last equality we have used (5.6) and introduced the dimensionless resistance $r(\nu_k) = \mathrm{Re}\{Z(\nu_k)\}/R_\mathrm{Q}$. In the infinitesimal limit $\Delta\nu \ll 1$, we can develop the tunneling operator from Eq. (5.20) in orders of $\Delta\nu$, restricting ourselves to the first two terms. This means that m only takes the values $\{0, \pm 1\}$. We will now focus on the case where $m = +1$ (emission of one photon during the tunneling process) and $p_{0,k} = 1$, meaning that mode k is initially in the ground state. This is a valid approximation in our experiments, where we work at a frequency of 6.5 GHz corresponding to ≈ 312 mK, whereas the temperature is ≈ 12 mK. We get:

$$\Gamma_{+1} = \frac{\pi}{2\hbar} E_\mathrm{J}^2 \left| \langle 1| \, 1 - i\sqrt{2r(\nu_k)\frac{\Delta\nu}{\nu_k}} \left(\hat{a}_k^\dagger + \hat{a}_k\right) + \mathcal{O}(\Delta\nu) \, |0\rangle \right|^2 \mathrm{P}'(2eV - h\nu_k) \tag{5.25}$$

After evaluation of the expectation value the above equation can be brought into the form:

$$\frac{\Gamma_{+1}}{\Delta\nu} = \frac{\pi}{\hbar} E_\mathrm{J}^2 \frac{r(\nu_k)}{\nu k} \mathrm{P}'(2eV - h\nu_k) \tag{5.26}$$

Finally, we can perform the limit $\Delta\nu \to \mathrm{d}\nu$, which leads to $\mathrm{P}'(E) \to \mathrm{P}(E)$, because the one missing mode acquires zero weight due to its infinitesimal width. This gives a photon emission rate density:

$$\frac{\mathrm{d}\Gamma}{\mathrm{d}\nu} = \frac{\pi}{\hbar} E_\mathrm{J}^2 \frac{r(\nu)}{\nu} \mathrm{P}(2eV - h\nu) \tag{5.27}$$

It is very important to note that this expression remains valid for tunneling processes involving any number of photons, since the function $\mathrm{P}(2eV - h\nu)$ contains the information on the Cooper pair tunneling rate due to emission into all the other modes. Going from Eq. (5.27) to the power spectral density at a given frequency ν simply implies multiplication with $h\nu$.

The emission rate is directly proportional to the factor $E_\mathrm{J}^2 r(\nu)/\nu$. It can be tuned by changing the Josephson energy as discussed in previous chapters. From the definition of the dimensionless resistance $r(\nu)$, we can see that $\mathrm{Re}\{Z(\nu)\}$ should not be negligible compared to the superconducting resistance quantum. This underlines the importance of trying to engineer peaks in $\mathrm{Re}\{Z(\nu)\}$ at the operating frequency of our devices in order to maximize emission rates.

It is clear form the Taylor expansion in (5.23), that higher order processes, corresponding to the emission of multiple photons by one tunnel event, are suppressed exponentially by gaining a factor $\sqrt{2r(\nu_k)\Delta\nu/\nu_k}$ with each emitted photon. Naturally, the semi-analytical expression (5.23) can also be computed numerically using other states than the ground state as input. One last remark on the form of (5.27) should be made: Even though this expression takes on very large values for a finite low-frequency impedance due its $1/\nu$-dependence, the power spectral density does not diverge because of its multiplication with $h\nu$. The full $\mathrm{P}(E)$-function, and consequently the Cooper pair current, has a pronounced peak around $\nu = 0$ which will dominate all other peaks as long as their associated characteristic impedances are smaller than the resistance quantum $\pi Z_0 \ll R_\mathrm{Q}$ [2]. This can be seen from the results of references [19, 20] shown in the right panels of Figs. 2 and 5.

5.2.4 Extraction of the environmental impedance

In this section, we will apply the formalism developed above to the special case, where the electromagnetic environment of the junction is given by a resonance of finite width (in practice: smaller than our measurement bandwidth), but arbitrary form, centered at a frequency ν_0. This will be used in chapter 6 to extract the real part of the impedance seen by the junction from the measured power spectral density curves.
The first two emission peaks are linked to the resonance conditions $2eV = h\nu_0$ and $2eV = 2h\nu_0$. With our measurement setup we have access to the power spectral density $\mathrm{PSD}(\nu, V)$ of the photon emission as a function of the applied voltage bias in a frequency bandwidth covering the entire resonance peak. As mentioned in the previous section the power spectral density for the one photon resonance is given by:

$$\mathrm{PSD}(\nu, V) = h\nu \frac{\mathrm{d}\Gamma(\nu, V)}{\mathrm{d}\nu}\bigg|_{V_{1\mathrm{ph}}} \tag{5.28}$$

Here the notation $V_{1\mathrm{ph}}$ signifies that the voltages are taken in the entire area encompassing the one photon peak. We can integrate over the voltage bias and find:

$$\int_{V_{1\mathrm{ph}}} \mathrm{PSD}(\nu, V)\mathrm{d}V = \frac{\pi^2}{e} E_\mathrm{J}^2 r(\nu) = \alpha(\nu) \tag{5.29}$$

Here we have used that at the given voltages (around the resonance $2eV \approx h\nu_0$) the argument of $\mathrm{P}(2eV - h\nu_0)$ becomes zero and the integration is effectively carried out over the peak in the $\mathrm{P}(E)$ function around $E = 0$. As discussed at the end of the previous section this part usually dominates all the other peaks. Using the normalization properties (5.14) we find $\int_{V_{1\mathrm{ph}}} \mathrm{P}(2eV - h\nu)\mathrm{d}(2eV) \approx 1$.
The power spectral density for a voltage bias sweeping over the two photon resonance is given by:

$$\mathrm{PSD}(\nu, V) = h\nu \frac{\mathrm{d}\Gamma(\nu, V)}{\mathrm{d}\nu}\bigg|_{V_{2\mathrm{ph}}} = \pi^2 E_\mathrm{J}^2 r(\nu)\mathrm{P}(2eV - h\nu) \tag{5.30}$$

With the temperature dependent form of the Minnhagen equation (D.19) we can rewrite this as:

$$\mathrm{PSD}(\nu, V) = \pi^2 E_\mathrm{J}^2 r(\nu) \frac{2h}{2eV - h\nu} \int_{-\infty}^{\infty} \mathrm{d}\nu' \frac{r(\nu')}{1 - e^{-\frac{h\nu'}{k_\mathrm{B}T}}} \mathrm{P}(2eV - h\nu - h\nu') \tag{5.31}$$

After bringing the factor $2eV - h\nu$ to the other side of the equation, this can again be integrated over the voltage. This time, since we are situated on the two photon peak the voltage sweeps the area around $2eV = 2h\nu_0$. If the entire peak is encompassed in the voltage sweep we can again use $\int_{V_{2\mathrm{ph}}} \mathrm{P}(2eV - 2h\nu)\mathrm{d}(2eV) \approx 1$ giving:

$$\int_{V_{2\mathrm{ph}}} \mathrm{PSD}(\nu, V)(2eV - h\nu)\mathrm{d}V = \pi^2 E_\mathrm{J}^2 \frac{h}{e} r(\nu) \int_0^{\infty} \mathrm{d}\nu' r(\nu') = \beta(\nu) \tag{5.32}$$

In the first step we have used that the Bose-factor tends towards the Heaviside step function for $k_\mathrm{B}T \ll h\nu$, thus effectively capping the lower limit of the integral at $\nu = 0$. The ratio between (5.32) and (5.29) yields an expression, which depends only on fundamental constants and the frequency integral over the real part of the impedance:

$$c(\nu) = \frac{\beta(\nu)}{\alpha(\nu)} = \frac{2h}{R_\mathrm{Q}} \int_0^{\infty} \mathrm{d}\nu' \mathrm{Re}\{Z(\nu')\} \tag{5.33}$$

In our experiment E_J is a tunable parameter. Since this entire theoretical development relies on a perturbative treatment in the Josephson energy it can not become too large. In order be able to eliminate E_J in Eq. (5.33) we have to perform both measurements at the same value of E_J resulting in a rather weak signal on the PSD of the two photon process. In other words, the absolute value of $\beta(\nu)$ is much smaller than $\alpha(\nu)$, giving a clearly worse signal to noise ratio. On the other hand, Eq. (5.33) should give the same ratio for each frequency point. Consequently, we can calculate $\bar{c}$, the frequency-averaged value of $c(\nu)$.
Finally, we can extract the frequency resolved expression of $\mathrm{Re}\{Z(\nu)\}$ by computing:

$$\mathrm{Re}\{Z(\nu)\} = \frac{\alpha(\nu)}{\int_\mathrm{BW} \mathrm{d}\nu \alpha(\nu)} \bar{c} \frac{1}{8e^2} \tag{5.34}$$

Here the integral is taken around ν_0 over the bandwidth of the sampled data, which is always significantly wider than the resonance in $\mathrm{Re}\{Z(\nu)\}$ around ν_0 (see Chs. 2 and 4). Implicitly we have assumed that the integral in (5.33) can be approximated by $\int_0^{\infty} \mathrm{d}\nu \mathrm{Re}\{Z(\nu)\} \approx \int_\mathrm{BW} \mathrm{d}\nu \mathrm{Re}\{Z(\nu)\}$. This is a valid assumption, since in both cases (one and two photon emission), the only impedance involved is the one around $\mathrm{Re}\{Z(\nu_0)\}$.

5.3 Photon statistics

So far we have only investigated the average photon emission rate. However, in order to correctly describe our experiments, it is necessary to gain information on the statistics

of the photons. The problem of predicting the statistics of the radiation emitted by a voltage biased Josephson junction in a specific electromagnetic environment has recently attracted some attention and several theoretical descriptions have been developed [32–35, 83].

5.3.1 Independent Cooper pair tunneling

First, we would like to treat the simple case of independent tunneling events giving one or two photons each. In the context of this work, this assumption applies to a device without RC circuit (like the one shown in Fig. 4) and with sufficiently low emission rates to avoid stimulated emission. In this case, the statistics of the Cooper pair current are governed by a Poisson distribution and the statistics of the photons emitted on the first resonance $2eV = h\nu_0$ can not be expected to deviate from this.
The next resonance condition at $2eV = 2h\nu_0$ however, should result in bunched light, since each tunneling CP now emits two photons.
To examine this, we can write down a rate equation for the occupation probabilities of the resonator. We will use the names P_0, P_1 and P_2 for the probability to find respectively zero, one and two photons in the resonator. We assume that its average photon number $\langle n \rangle \ll 1$, meaning that $P_0 \approx 1$. Using that, at the given bias voltage, the tunneling process never emits only one photon, the steady state equation for P_1 is simply:

$$\frac{\mathrm{d}P_1}{\mathrm{d}t} = 0 = -\Gamma_{1\to0}P_1 + \Gamma_{2\to1}P_2 \tag{5.35}$$

Here $\Gamma_{1\to0}$ is the transition rate from the one to the zero photon state and $\Gamma_{2\to1}$ is the rate between the two and one photon states. If the transitions are induced by coupling to a linear environment without back-action, these two rates are related as $\Gamma_{2\to1} = 2\Gamma_{1\to0}$ [78]. In this case we see from (5.35) that $P_1 = 2P_2$. With this, $\langle n \rangle = 4P_2$. Now we can evaluate expression (3.12) for the normalized second order correlation function at $\tau = 0$:

$$g^{(2)}(0) = \frac{\langle \hat{a}^\dagger \hat{a}^\dagger \hat{a}\hat{a} \rangle}{\langle \hat{a}^\dagger \hat{a} \rangle^2} = \frac{2P_2}{(4P_2)^2} = \frac{1}{2\langle n \rangle} \tag{5.36}$$

From the right-hand side of (5.36) we expect to get arbitrarily large bunching if $\langle n \rangle \to 0$. This is confirmed by the results of Gramich *et al.* in reference [33], which uses an effective Hamiltonian for a Josephson junction coupled to a superconducting resonator subjected to dissipation within a Lindblad master equation approach [76]. In the limit $\langle n \rangle \to 0$ they derive an analytical result similar to our phenomenological description, confirming, together with their numerical calculation, the arbitrary large bunching values achievable in the two photon process.

5.3.2 Correlated Cooper pair tunneling

It is notable, that Gramich *et al.* also predict short-time anti-bunching on the one photon peak in the emitted radiation, when the characteristic impedance of the resonator becomes

comparable to the superconducting resistance quantum. Characteristic impedances of that order could, in principle, be achieved with Josephson junction array meta-materials [84] or by exploiting the high kinetic inductance of certain superconductors, such as NbN. In our samples, we have chosen to take another approach by adding a low frequency contribution to the electromagnetic environment of the junction. This choice is based on the straightforward fabrication of very high on-chip impedances, at relatively low frequencies, using thin resistive films (see Sec. 2.6).
As mentioned in the introduction (see Fig. 6), we can give an intuitive explanation for the working principle of our single photon source by considering the charging effects on the island between the junction and the resistor. Together with an additional capacitance to ground the resistor forms an RC circuit. This sets a time scale for the discharging of the superconducting island between the RC and the junction. The applied voltage corresponds to the optimal bias point for charging the capacitor and emitting a photon into the resonator at $2eV_1 = 4e^2/(2C) + h\nu_0$. Immediately after the tunnel event, the capacitor is charged and the energy cost of adding another Cooper pair is increased from $2e^2/C$ to $6e^2/C$ inhibiting further photon emission for a time RC.
The second order correlations in the output field produced by this system have so far eluded a fully analytical description, but could be calculated numerically using input-output theory and the Keldysh formalism [36] with an effective model for the circuit (Fig. 5.3a). Within this theoretical approach [34, 81] a quantized flux field $\hat{\Phi}(x,t)$ [4, 85] is defined from propagating modes on a semi-infinite transmission line (TL).

$$\hat{\Phi}(x,t) = \sqrt{\frac{\hbar Z_0}{4\pi}} \int_0^\infty \frac{\mathrm{d}\omega}{\sqrt{\omega}} [\hat{a}_{\mathrm{in}}(\omega) e^{-i(k_\omega x + \omega t)} + \hat{a}_{\mathrm{out}}(\omega) e^{-i(-k_\omega x + \omega t)} + \mathrm{H.c.}] \tag{5.37}$$

In this expression $Z_0 = \sqrt{L/C}$ is the characteristic impedance of the transmission line, $k_\omega = \omega\sqrt{CL}$ is the wave number, while $\hat{a}_{\mathrm{in}}(\omega)$ $[\hat{a}^\dagger_{\mathrm{in}}(\omega)]$ and $\hat{a}_{\mathrm{out}}(\omega)$ $[\hat{a}^\dagger_{\mathrm{out}}(\omega)]$ are the annihilation (creation) operators for the incoming and outgoing propagating field on the line. They respect the usual commutator $[\hat{a}_{\mathrm{in}}(\omega), \hat{a}^\dagger_{\mathrm{in}}(\omega')] = \delta(\omega - \omega')$.
Current conservation at the Josephson junction sets the boundary condition linking incoming and outgoing radiation fields:

$$C_J \ddot{\hat{\Phi}}(0,t) - \frac{1}{L} \frac{\partial \hat{\Phi}(x,t)}{\partial x}\Big|_{x=0} = I_{\mathrm{c}} \sin\left(\frac{2eVt}{\hbar} - \frac{2\pi\hat{\Phi}(0,t)}{\Phi_0}\right) \tag{5.38}$$

The first term on the left hand side is the current through the shunting capacitance of the junction, while the second term stems from the incoming current through the inductance of the transmission line. The right-hand side is given by the well-known Josephson relation for the current through a superconducting tunnel junction [56]. This last part introduces a non-linear time dependent coupling between the voltage bias and incoming as well outgoing fields through the flux operator at the junction.
Generally, the solutions for the outgoing field $\hat{a}_{\mathrm{out}}(\omega)$ can be found as expansions in the critical current, but have to be evaluated numerically [36]. Since $I_{\mathrm{c}} \propto E_{\mathrm{J}}$ this

corresponds again to a perturbative treatment in the Josephson energy, but a controlled expansion to higher orders in E_J can be made. However, this approach presents a number of advantages, namely its input-output theory form [76] giving access to the outgoing photon flux and its correlations. Moreover, steps in the characteristic impedance of the transmission line can be introduced (Fig. 5.3), shaping the impedance seen by the junction similar to what is done in an actual experiment [20] (see Ch. 2) and temperature dependence can be taken care off by using a thermal input field.

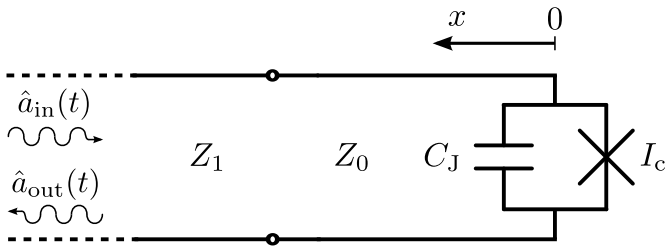

Figure (5.3): Simplified schematic representation of the model developed in reference [81]. A semi-infinite transmission line of characteristic impedance Z_1 is connected to the Josephson junction. The latter is modeled by its shunt capacitance C_J and the Josephson element with critical current I_c. The TL can have a segment of different characteristic impedance Z_0 next to the junction effectively creating a resonator as in appendix B.

Our particular system is described in this framework as shown in Fig. 5.4a. A voltage biased Josephson junction with its shunting capacitance C_J is connected to a transmission line segment of characteristic impedance Z_0 followed by a semi-infinite TL with very high characteristic impedance $R > R_Q \gg Z_0$ leading to a peak in the impedance around zero frequency. Another peak appears at the resonance frequency of the $\lambda/2$ resonator formed by the Z_0 segment. Figure 5.4c shows the two contributions to the input impedance seen by the junction in red and blue respectively. The version of the circuit presented in Fig. 5.4a is theoretically easier to describe, but experimentally difficult to implement. The version in Fig. 5.4b produces almost the same $\text{Re}\{Z(\nu)\}$ and corresponds to our actual implementation, where the resistor is realized on-chip on the other side of the junction and the resonator is a quarter-wave segment followed by a $50\,\Omega$ matched setup with a bias tee separating the DC voltage bias from the high frequency response. In our case the effective capacitance is dominated by the capacitor going over the flux-bias line (see Sec. 2.6).
The correlations between consecutive tunneling events induced by classical Coulomb blockade in this system can be computed numerically by going to the fourth order in E_J using the approach described above [36]. Only this order gives access to current-current correlations, since the second order perturbation in E_J is already necessary to compute the average current (see Eq. (5.16)).
The resulting normalized second order coherence function of the emitted photons $g^{(2)}(\tau)$ as a function of the time difference τ in units of RC is shown in Fig. 5.5. The dotted lines

correspond to a semi-analytical approximation using a phenomenological effective voltage $v(t) = V - \frac{2e}{C}e^{-\frac{t}{RC}}$. At $\tau = 0$ the bias voltage is diminished by the voltage drop $2e/C$ due to the charging of the capacitance after a tunnel event and goes back to its normal value with a time-constant RC. Intuitively, $g^{(2)}(\tau \approx 0)$ can be found by considering the ratio between the emitted power immediately after a tunnel event and the average power:

$$g^{(2)}(\tau) = \frac{\int_{\mathrm{BW}} \mathrm{Re}[Z(\nu)]\mathrm{P}(2ev(\tau) - h\nu)}{\int_{\mathrm{BW}} \mathrm{Re}[Z(\nu)]\mathrm{P}(2eV - h\nu)} \tag{5.39}$$

The integral is carried out over the entire measurement bandwidth, taking into account a filter function (described below). The numerator is in fact a measure for the conditional probability of emitting one photon, if another photon has been emitted a time τ earlier, while the denominator takes care of the normalization. This expression qualitatively shows anti-bunching and reproduces the long-time behavior of the full numerical calculation. The results of the latter are represented in Fig. 5.5 by solid lines of different colors for various temperatures (legend in the inset). In this simulation, the outgoing fields were filtered using a Gaussian function with a full width at half maximum of 1 GHz centered around the first resonator mode $\nu_0 = 5\,\mathrm{GHz}$. The system parameters were $R = 4R_\mathrm{Q} \approx 25.8\,\mathrm{k\Omega}$, $Z_0 = R/10$, and $C = 50\,\mathrm{fF}$. Note that the value of Z_0 does not correspond to an actual design parameter. It is chosen to give a resonance peak in the impedance of the model system (Fig. 5.4a) that is similar to the peak we get in the impedance on our samples (Fig. 5.4b). The capacitive value is superior to the designed capacitance of our samples (25 fF) and makes the simulated system more sensitive to temperature because of the smaller charging energy $E_\mathrm{C}/k_\mathrm{B} = 2e^2/(k_\mathrm{B}C) \approx 74\,\mathrm{mK}$. Nevertheless, anti-bunching survives up to temperatures of 40 mK.

The inset shows the corresponding $\mathrm{P}(E)$ function at different temperatures as a function of the voltage bias in units of GHz. The first peak is due to CP tunneling through the junction by solely exciting the RC circuit and is given by the $\mathrm{P}(E)$ function for a high ohmic environment [2], which has a Gaussian form:

$$P_\mathrm{CB}(E) \approx \frac{1}{\sigma\sqrt{2\pi}} e^{-\frac{\left(E-2e^2/C\right)^2}{2\sigma^2}} \tag{5.40}$$

Here, the broadening in energy is given by the thermal voltage fluctuations on the resistor via $\sigma/\sqrt{2\pi} = e\sqrt{4k_\mathrm{B}TR\Delta\nu}$ within a bandwidth $\Delta\nu = 1/(2\pi RC)$. This holds true as long as $\hbar/RC < k_\mathrm{B}T$, meaning that the thermal noise is white in the bandwidth given by the cutoff frequency of the RC-element. Using this, the expression for the total broadening in energy can be written independently of R as $\sigma = \sqrt{2E_\mathrm{C}k_\mathrm{B}T}$, with $E_\mathrm{C} = 2e^2/C$ the charging energy necessary to add another Cooper pair onto the capacitance.
The second peak corresponds to the combined process of charging the capacitance and emitting one photon ($E_\mathrm{C} + h\nu_0$). Its width in voltage is again dominated by the thermal fluctuations (for 50 fF and 30 mK, $\sigma/h \approx 1.4\,\mathrm{GHz}$), making it a smaller reproduction of the first peak shifted by $h\nu_0$. The total $\mathrm{P}(E)$ function is then given by

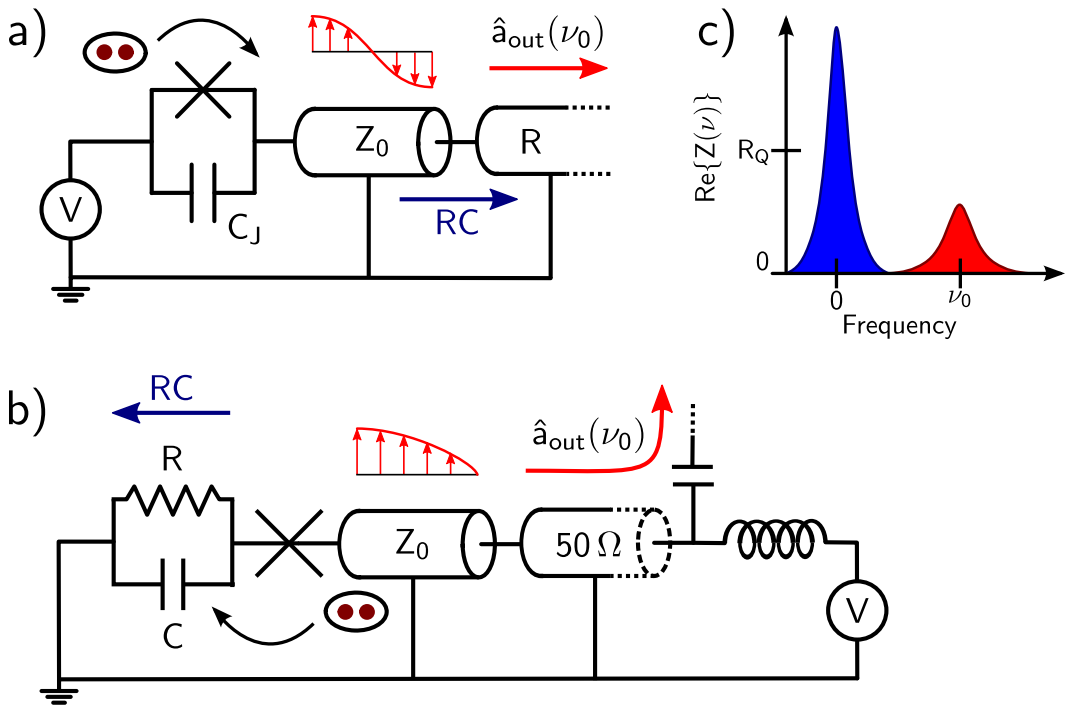

Figure (5.4): a) Our sample as described by [36]. Transmission lines are depicted as cylinders. This corresponds to the situation in Fig. 5.3, when $Z_1 = R \gg R_Q$ and $Z_0 < R$ leading to $\lambda/2$-type resonances in the segment closest to the junction. The voltage profile is shown schematically. Blue and red arrows indicate the direction of the discharging current and the outgoing high frequency photons. b) Representation of the actual experimental situation using the same schematic language. Here $Z_0 > 50\,\Omega$ leads to $\lambda/4$-type resonances. The voltage bias and high frequency response are separated by a bias tee and the capacitance of the junction is dominated by an external capacitor. c) The real part of the impedance seen by the junction is very similar in both cases and has two contributions: A peak around zero frequency (blue) with a height $> R_Q$ coming from the RC circuit and a high frequency Lorentzian (red) due to the resonator.

$$\mathrm{P}(E) \approx (1-p)P_{\mathrm{CB}}(E) + pP_{\mathrm{CB}}(E - h\nu_0), \tag{5.41}$$

where the factor $p \ll 1$ comes from the fact that the last term on the right-hand side originates from a second order process [2, 20, 36].

Another interesting prediction made in reference [36] is that bunching and anti-bunching can be achieved on the same sample by simply changing the voltage bias. This is illustrated in Fig. 5.6a, where the expected evolution of $g^{(2)}(\tau)$ at a temperature of 10 mK is shown as a function of τ for different values of $2eV$. Figure 5.6b shows $\mathrm{P}(E)$ as a function of the voltage bias energy $2eV$ in GHz. The colored arrows represent the respective voltage biases leading to the curves in Fig. 5.6a. When the junction is biased

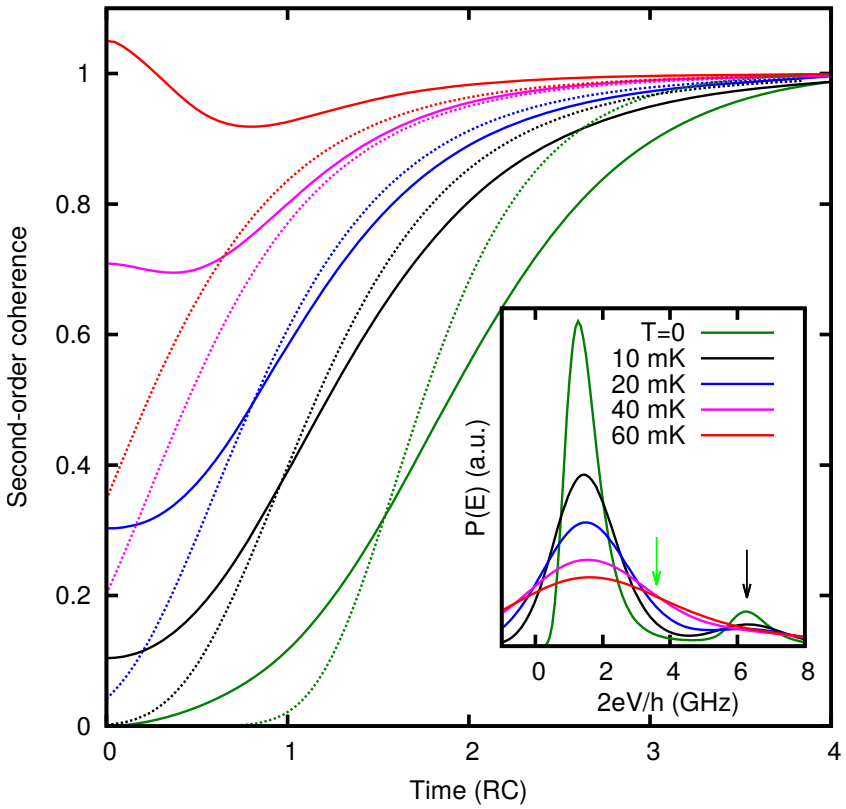

Figure (5.5): Solid (dotted) lines show the second order coherence function $g^{(2)}(\tau)$ as a function of τ in units of RC for the full numerical simulation (analytical approximation). Inset: P(E) *in arbitrary units as a function of the voltage bias at the junction in units of* GHz *for different temperatures. The black arrow indicates the voltage bias used for the results presented in the main figure and the green arrow shows how far the voltage drops immediately after an emission event (see Sec. 6.3.1).*

above the peak (blue, magenta and red arrows), the first tunneling event is likely to be followed by another one while the dropping voltage sweeps through the peak maximum. This leads to bunching in the output field. The black arrow indicates the optimal bias point at zero temperature. At finite temperature, however, noise leads to excursions on both sides of the peak and the depth of the anti-bunching dip is reduced. This is why the optimal bias point is slightly below the maximum of the peak (red arrow). Figure 5.6c displays a normalized 2D spectral density map of the emitted radiation as a function of bias energy and emission frequency (both in GHz). Colored arrows on the left correspond to the ones in Fig. 5.6b. The broadening of the peak along the voltage axis due to thermal fluctuations is clearly visible.

The results described above confirm our intuitive understanding of the system and predict stable anti-bunching at finite temperatures. Even though this treatment was carried out using E_J as a perturbation it includes all orders of the non-linear combinations of field

operators stemming from the tunneling Hamiltonian (5.11).

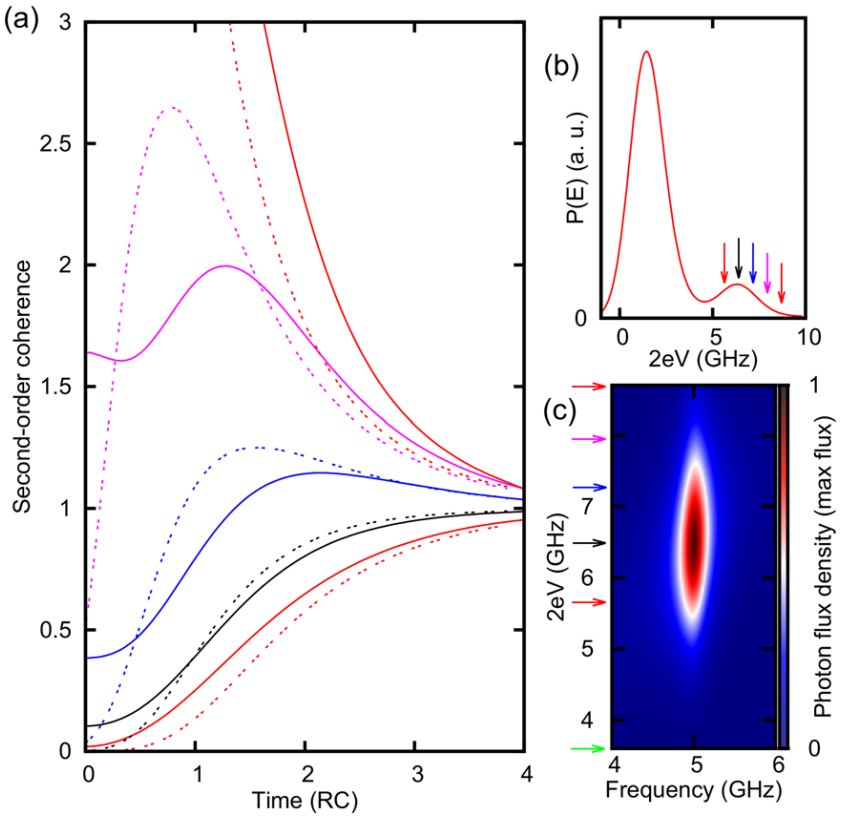

Figure (5.6): a) $g^{(2)}(\tau)$ as a function of τ in units of RC. Solid (dashed) lines correspond to the numerical (analytical) calculation. b) $P(E)$ at 10 mK. The arrows indicate the voltage biases corresponding to the curves in a). c) Normalized photon flux density as a function of voltage bias around the resonance frequency at 5 GHz.

Chapter 6

Photon emission through ICPT: Experimental results

6.1 Introduction

In this chapter, we will present the results obtained during several measurement campaigns on different samples in the course of this PhD work. The following two sections distinguish between devices where Cooper pairs tunnel independently as in reference [20], and others where an RC-circuit introduces correlations between tunneling events. Doing so, we follow the structure given by the preceding theoretical discussion (see Sec. 5.3). Of course, there is further variety within these classifications as we have measured samples with and without on-chip beam splitters (see Ch. 2) and with different resonator bandwidths. Nevertheless, the physics governing the emission statistics is the same within each of the two first mentioned categories and this is why we have chosen this organizational structure. All measurements presented in this chapter were performed on samples anchored to the base plate of our dilution refrigerator thermalized to its minimum temperature of $\approx 12\,\mathrm{mK}$. The exact parameters of each sample, with references to the corresponding figures, are given in appendix E.

6.2 Samples without RC-circuit: Independent Cooper pair tunneling

As mentioned above, this section focuses on samples where no RC-element is present. For most of the studied parameter range we can thus assume that Cooper pairs tunnel independently. We will first examine the power spectral density of the emitted photons and then take a look at their statistics.

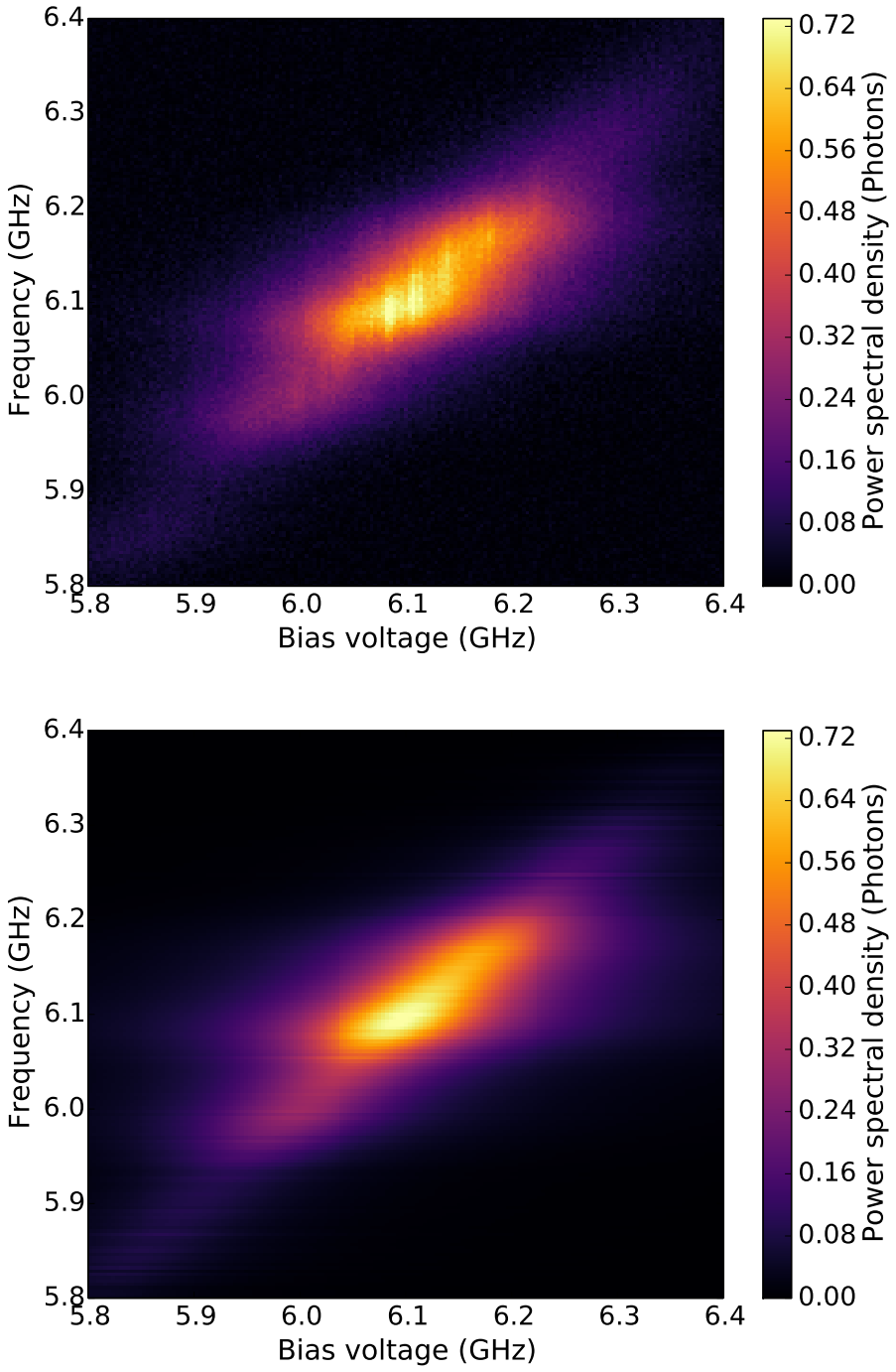

Figure (6.1): The experimental results (upper panel) and theoretical fit (lower panel) for the power spectral density emitted around the one photon peak at $2eV_1 = h\nu_0$. Both figures show the power spectral density emitted by the sample as a function of the applied voltage (converted to GHz*) and signal frequency.*

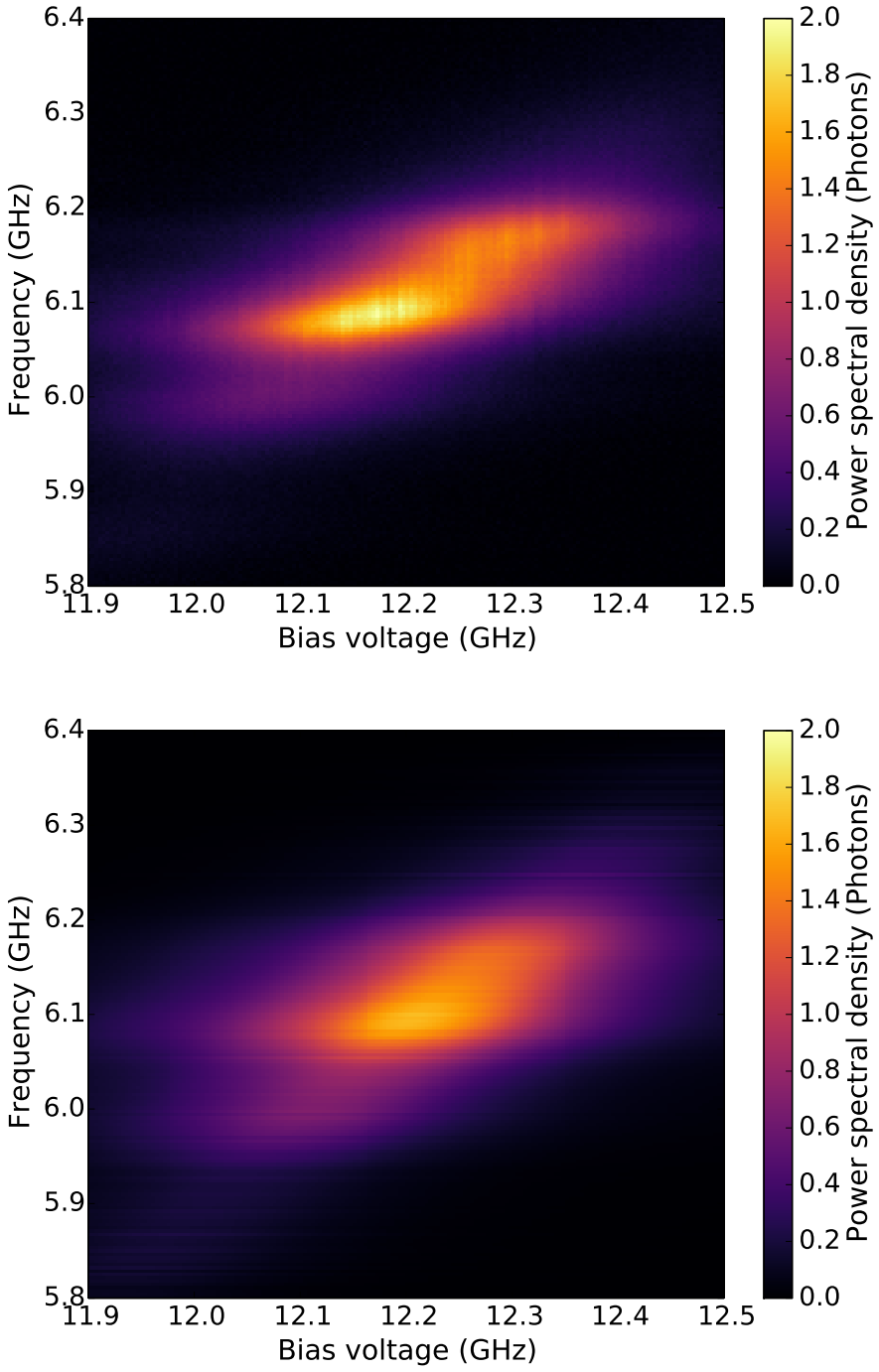

Figure (6.2): The experimental results (upper panel) and theoretical fit (lower panel) for the power spectral density emitted around the two photon peak at $2eV_2 = 2h\nu_0$. Both figures show the power spectral density emitted by the sample as a function of the applied voltage (converted to GHz*) and signal frequency.*

6.2.1 Power spectral density of the emitted radiation

The majority of this subsection presents data gathered on a sample of the on-chip beam splitter type (see Fig. 2.8) with a resonator designed to have a width of 175 MHz. We have mainly investigated the emission peaks around $2eV_1 = h\nu_0$ and $2eV_2 = 2h\nu_0$, where ν_0 is the resonance frequency of the fundamental resonator mode. Our main measurement results are shown in the upper panels of Figs. 6.1, for the first case, and 6.2 for the latter case. In both plots we show the power spectral density (PSD) in units of photons at the central frequency of the resonator. We have access to the output PSD of our sample through our calibration scheme enabling us to correct for the gain of our measurement chain (see Sec. 4.2.3). Then we divide the resulting power spectral density (in units of $\mathrm{W{\cdot}Hz^{-1}}$) by the energy of a photon at the measured frequency ($h\nu_0$). This quantity is shown as a function of the signal frequency and the bias voltage. To facilitate the interpretation of the data, the voltage axis is converted into frequency via the relation $\nu = 2eV/h$. This will be done consistently within this chapter. The value of the bias voltage at the sample is calculated from the applied voltage at room temperature using the known resistances of our voltage divider (see Sec. 4.3.3). Note that in both figures the frequency of the emitted radiation follows the voltage bias according to the relations given above.

Widths of the emission peaks and extraction of the environmental impedance

A slice through the PSD of the one photon peak along the voltage axis is plotted in the left panel of Fig. 6.3. It shows the photon emission measured at a single frequency point, while the bias voltage is swept. If there was no voltage noise, the only value of the bias voltage giving a signal would be exactly at $V_1 = h\nu_0/(2e)$. The finite width of this peak (≈ 160 MHz) is a measure of the fluctuations in the bias voltage at the sample. The width of the two photon peak in the right panel of the figure is slightly bigger at ≈ 230 MHz. This occurs, because at a given voltage bias the two emitted photons can compensate for each other in frequency within the bandwidth of the resonator. Then one photon is emitted at a slightly higher frequency compared to half the voltage bias and the other at a slightly lower one. This broadens the peak in addition to the effect of the voltage noise.

If the noise was much bigger than the resonator bandwidth, the complementary case where we look at a slice along the frequency axis at one fixed voltage, would give the shape of the impedance. This is not the case here. However, the actual form of the impedance seen by the junction can be extracted using the method presented in section 5.2.4. There we use the fact that the integration of a peak over voltage yields the form of the impedance times a factor depending only on the Josephson energy and fundamental constants. When both the one and two photon peaks are measured at the same (low) Josephson energy, we can extract the exact form of $\mathrm{Re}\{Z(\nu)\}$ from the ratio between both integrals. This has been done on an independent dataset and the resulting curve is presented in Fig. 6.4 as a function of frequency (solid red line). The resonance frequency is found to be around 6.1 GHz and the FWHM of the presented curve is indeed

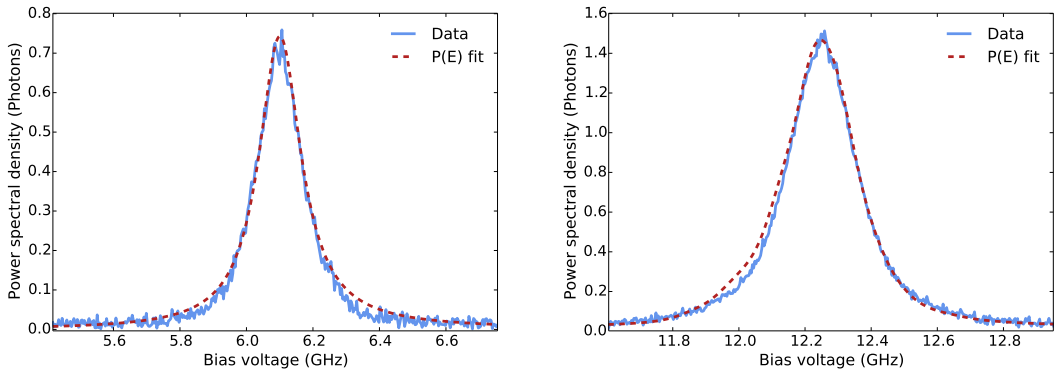

Figure (6.3): Slices through the power spectral density maps shown in Figs. 6.1 (left) and 6.2 (right) along the voltage axes. Both peaks are centered at $\approx 6.1\,\mathrm{GHz}$. *Solid blue (dashed red) lines show the experimental data (the theoretical simulation, see text).*

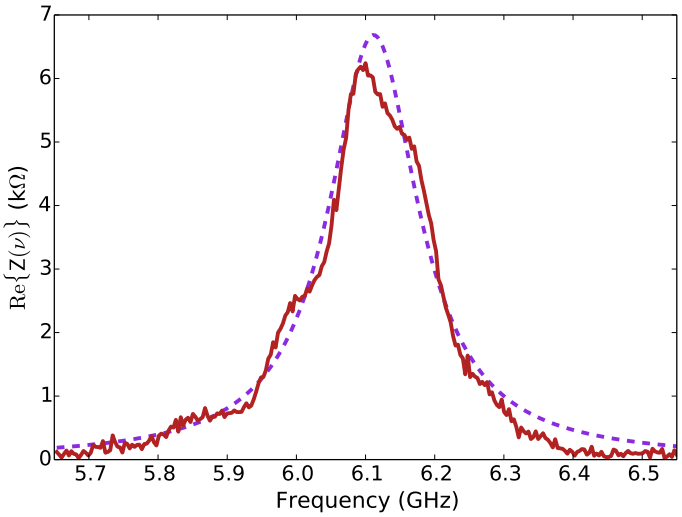

Figure (6.4): Solid red line: Real part of the environmental impedance seen by the junction. This was extracted from a dataset close to maximum frustration. We used this to predict the power spectral densities shown in the lower panels of Figs. 6.1 and 6.2. Dashed purple line: The expected real part of the impedance for this sample type shifted in frequency to $\approx 6.1\,\mathrm{GHz}$ *for comparison.*

$\approx 160\,\mathrm{MHz}$ corresponding rather well to the designed value. The dashed violet line in the figure shows the designed impedance for this type of sample when shifted to match the experimentally found resonance frequency. Such shifts of several hundred MHz occur regularly, in particular in materials with high kinetic inductance. One has to bear in mind that material and fabrication parameters such as square resistance or film thickness

can change over an entire wafer leading to fluctuations in the inductance of the coplanar waveguides and thus in the resonance frequency (see Chs. 1 and 2). Apart from the frequency shift, the actual impedance is slightly modulated, presumably by reflections in the measurement chain close to the sample. In spite of this, the areas under the curves are very similar and using Eq. (D.19) we find the characteristic impedances of 142 Ω and 154 Ω for the actual and designed curves respectively.

Theoretical fit of the data

Using the extracted impedance and the formalism developed in chapter 5 (Eq. (5.27)), we can fit the experimental power spectral densities for both peaks with an effective temperature T_{eff} and the Josephson energy E_{J} as free parameters. The first enters into the underlying P(E)-function, which we compute using the temperature dependent form derived in reference [18]. The result of this fit for the one photon peak is shown in the lower panel of Fig. 6.1. The best agreement with the data was achieved for a Josephson energy of 1.04 µeV and an effective temperature of 76.2 mK. For the two photon peak the best fit returns 7.01 µeV and 42.4 mK. For this measurement E_{J} was indeed readjusted to increase the signal. The computed PSD is shown in the lower panel of Fig. 6.2. Both temperatures should be interpreted as effective values describing the voltage noise at the junction. The difference in temperature is likely due to the second peak, which is already approaching the limit of validity of P(E)-theory. Here the resonator contains more than one photon on average making it narrower. Nevertheless, Fig. 6.3 shows the good agreement between measurement data (solid blue lines) and fit (dashed red line) at the center frequency of the resonator peak (≈ 6.1 GHz) for both peaks.
In order to verify the fitted values of E_{J} we can consider the maximum Josephson energy $E_{\text{J},0} \approx 25$ µeV, which has been determined from an independent measurement of the current voltage characteristic of the SQUID (not shown). This was done using the Ambegaokar-Baratoff relation as described in section 1.4.2 and calculating [56]:

$$E_{\text{J}}(\Phi) = E_{\text{J},0} |\cos(\pi\Phi/\Phi_0)| \tag{6.1}$$

Here, $\Phi_0 = h/(2e) \approx 2.07 \times 10^{-15}$ Wb is the magnetic flux quantum. In order to be able to evaluate this expression we need to know the value of the flux bias at the SQUID. This can be found directly by measuring the PSD on a given emission peak as a function of the current applied to the flux bias line. After sweeping the flux bias over several periods and observing the resulting oscillations in the PSD, one can straightforwardly extract the proportionality between applied current and flux as well as flux offset at the SQUID. Part of such a curve for the one photon peak is shown in Fig. 6.5, where the power spectral density has been integrated over the entire frequency range of our measurement to increase the signal to noise ratio.

With this calibration we can determine the flux bias of the two datasets. The one photon peak was recorded at a flux bias of $\Phi \approx -0.51\Phi_0$, while the two photon peak was measured at $\Phi \approx -0.61\Phi_0$, giving Josephson energies of 0.8 µeV and 8.5 µeV in good

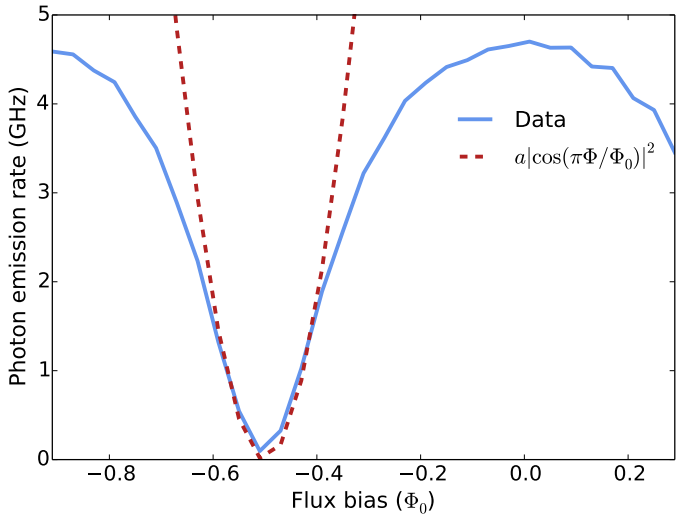

Figure (6.5): Solid blue line: The photon emission rate at the resonance condition of the one photon peak ($2eV_1 = h\nu_0$, voltage bias $\approx 6.12\,\mathrm{GHz}$) within the entire measurement bandwidth (from 5.65 GHz to 6.55 GHz) as a function of the calibrated flux bias in units of the flux quantum Φ_0. Dashed red line: The expected scaling of E_J^2 adjusted to fit the datapoints close to full frustration.

agreement with the fitted values. All axes depending on the flux bias of the SQUID in the experimental part of this PhD work will be given in units of the magnetic flux quantum Φ_0.
Additionally, Fig. 6.5 shows that at weak frustration, corresponding to large Josephson energies, the photon rate departs from the scaling with E_J^2 predicted by P(E)-theory. This is to be expected, since at one point E_J can no longer be considered a perturbation of the system Hamiltonian. The red dashed line shows the expression of E_J^2 for a balanced SQUID fitted to the data close to maximum frustration through scaling with an arbitrary factor a. This is meant to give a purely qualitative comparison between the expected and actual behavior. The very slight difference around maximum frustration, due to a finite value of the photon rate, can originate from a small imbalance between the two junctions in the SQUID.

6.2.2 Quartet and sextet peaks

A parenthetic, albeit notable, measurement result will be treated briefly in this subsection. At low voltage biases we observe weak peaks in the PSD of the emitted radiation, which do not follow the voltage bias in frequency according to the equation $2eV = h\nu$, but instead obey the relations $4eV = h\nu$ and $6eV = h\nu$. We interpret this as en effect where two or three Cooper pairs tunnel jointly, while emitting one photon. This is depicted in Fig. 6.6. Blue lines show the three equations mentioned above, where the voltages

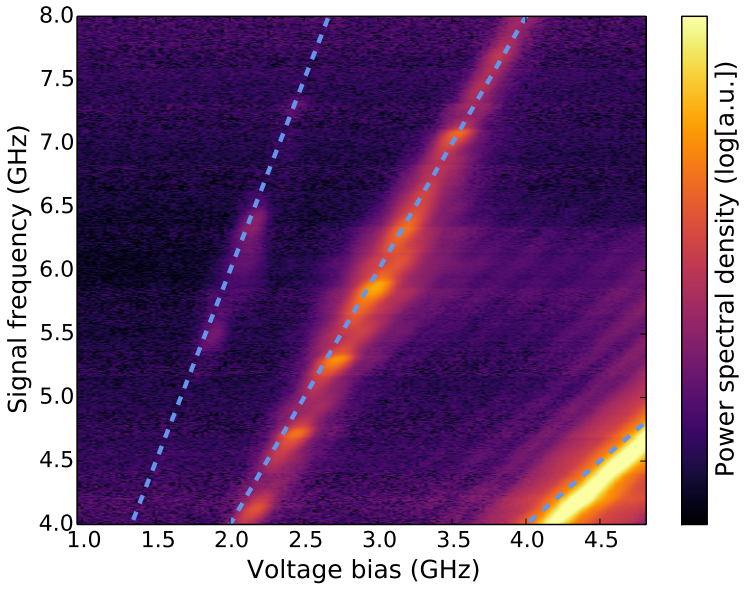

Figure (6.6): Power spectral density map on a logarithmic scale of arbitrary units (no calibration was performed during this measurement campaign) showing the quartet and sextet peaks. The blue lines show the predicted frequency evolution of the peaks with voltage.

have been converted into frequency, as before, using the known resistances of our voltage divider. The bright line in the lower right corner stems from the one photon peak and has a slope of ≈ 1 in the figure. Since this dataset has been recorded at very low frustration and thus high E_J the current due to the tunneling Cooper pairs becomes big enough to cause a considerable voltage drop over the bias circuit of our sample. This explains why the peak is shifted to higher values with respect to the dashed blue line of the prediction. The two other blue lines have slopes of 2 and 3, as expected for the processes described above, and agree well with the observed features.

6.2.3 Photon statistics

As stated before, the emission of photons in the case of the devices studied in this section is mainly based on independent Cooper pair tunneling events. In the previous section, we have shown that multiple CP can tunnel through the junction coherently, as is the case for the quartet and sextet processes. On the one and two photon peaks, however, we would expect two Cooper pairs traversing the junction to interact via the environment only for high emission rates of the order of the inverse resonator lifetime.
Concerning the expected statistics in this type of system, anti-bunching has been predicted for very high quality factors and characteristic impedances [33]. Nevertheless the samples at hand are in the limit where this possibility can be neglected. Strong bunching, on

the other hand, is expected for multi-photon emission processes. Intuitively, this can easily be understood by considering the Poisson statistics of the Cooper pair tunneling events. If one photon is generated per CP, it inherits its statistics and is neither bunched nor anti-bunched. If, on the other hand, multiple photons are emitted per Cooper pair, they will be bunched. This effect becomes more pronounced, when the time between the tunneling events becomes long compared to the resonator lifetime, as shown in section 5.3.1.

The results presented here, have been obtained from a different sample than the power spectral density measurements shown in section 6.2.1. The device measured here is the same as then one studied by Hofheinz *et al.* in reference [20]. Note that regardless of that, both samples are based on the same physics. Our measurements are summarized in Figs. 6.7 and 6.8. All data was taken with both the bias voltage and the frequency window centered on the maximum of the respective peak in the PSD. The calibration setup was not in place during this measurement campaign. Thus, the average occupation of the resonator $\langle n \rangle$ was calculated using the calibrated emission rates and the frustration dependence known from a prior measurement on the same sample. This leads to higher uncertainty in the photon number.

Figure 6.7 shows $g^{(2)}(\tau)$ for the one (two) photon peak as a dashed green (solid blue) line for an average photon number in the resonator of ≈ 0.5. While the peak at $2eV_1 = h\nu_0$, where one tunneling Cooper pair emits one photon, unsurprisingly shows the Poissonian statistics of independent events, the two photon process at $2eV_2 = 2h\nu_0$ exhibits clear bunching ($g^{(2)}(0) \approx 3.2$).

Figure 6.8 displays the values of $g^{(2)}(0)$ measured on the one (green dots) and two (blue dots) photon peaks as the frustration of the SQUID is sweeped. From right to left, as frustration increases, the emission rate and thus the resonator population decrease. As a result of this, the signal to noise ratio becomes more and more unfavorable leading to bigger uncertainty of the measured values. This could be at the origin of the one photon values slowly moving away from the expected Poisson statistics (black line). The tendency towards more bunched values could also be an indication that thermal noise plays a more dominant role in the emission process.

The statistics of the two photon process ($2eV_2 = 2h\nu_0$) show a different behavior. The curve steadily rises towards low resonator population numbers, approximately following the $1/(2\langle n \rangle)$-law derived in section 5.3.1. Here, measurement times were dynamically adjusted to keep the signal to noise ratio above a certain threshold. In spite of the fluctuations at low $\langle n \rangle$ we observe super-bunching with $g^{(2)}(0)$ values of the order of ≈ 100. Above $\langle n \rangle \approx 0.1$ the approximation $\langle n \rangle \ll 1$ starts to break down and the data points depart from the straight line given by Eq. (5.36).

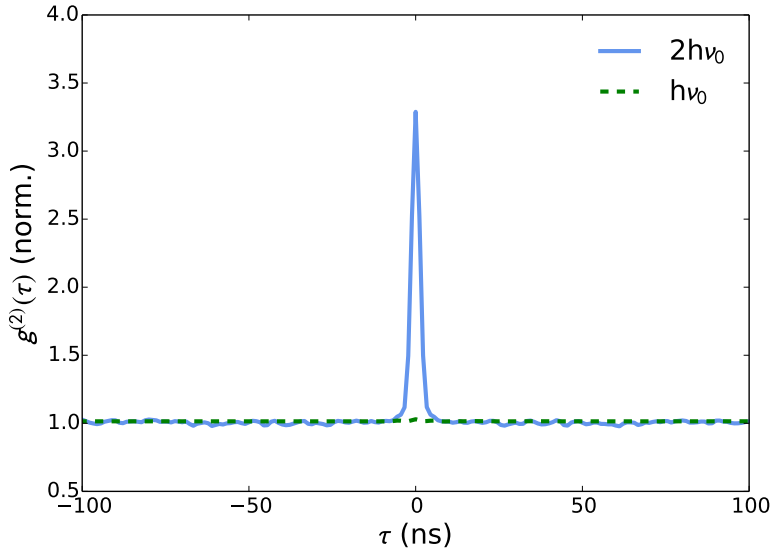

Figure (6.7): Dashed green (solid blue) lines show the second order correlations $g^{(2)}(\tau)$ for the one (two) photon peak at an average resonator population of $\langle n \rangle \approx 0.5$.

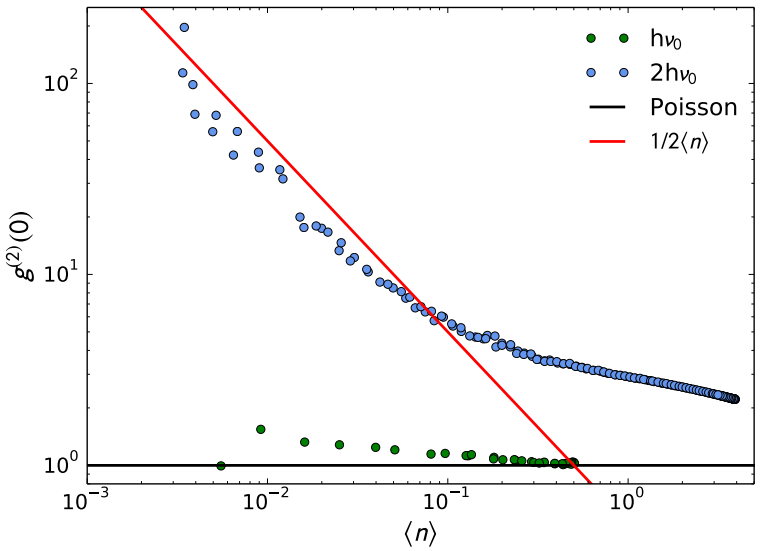

Figure (6.8): Second order correlations at zero time difference $g^{(2)}(0)$ for the one (green dots) and two (blue dots) photon peaks as a function of the estimated average photon population in the resonator. The black line shows the reference of independent emission (Poisson statistics) at $g^{(2)}(0) = 1$ and the red line corresponds to the simple scaling law for the two photon $g^{(2)}(0)$ at low emission rates given by Eq. (5.36).

6.3 Samples with RC-circuit: Correlated Cooper pair tunneling

The device investigated in this section is of the beam-splitter type. Like the sample studied in the preceding section, the resonator seen by the junction was designed to have $\nu_0 \approx 6.7\,\mathrm{GHz}$ with a full width at half maximum of $\approx 175\,\mathrm{MHz}$. The on-chip resistor is designed to be $\approx 21\,\mathrm{k\Omega}$ and the capacitance coming from the crossing of the flux bias line is estimated at $\approx 25\,\mathrm{fF}$ (see Sec. 2.6). From the current voltage characteristic of the SQUID, measured at 4.2 K (not shown), we have determined the normal resistance above the gap $R_\mathrm{N} \approx 220\,\mathrm{k\Omega}$, the gap voltage $2\Delta/e \approx 4.65\,\mathrm{mV}$ as well as the theoretical critical current at zero temperature $I_0 \approx 18.8\,\mathrm{nA}$ and the resulting maximal Josephson energy $E_\mathrm{J} \approx 37\,\mu\mathrm{eV}$.

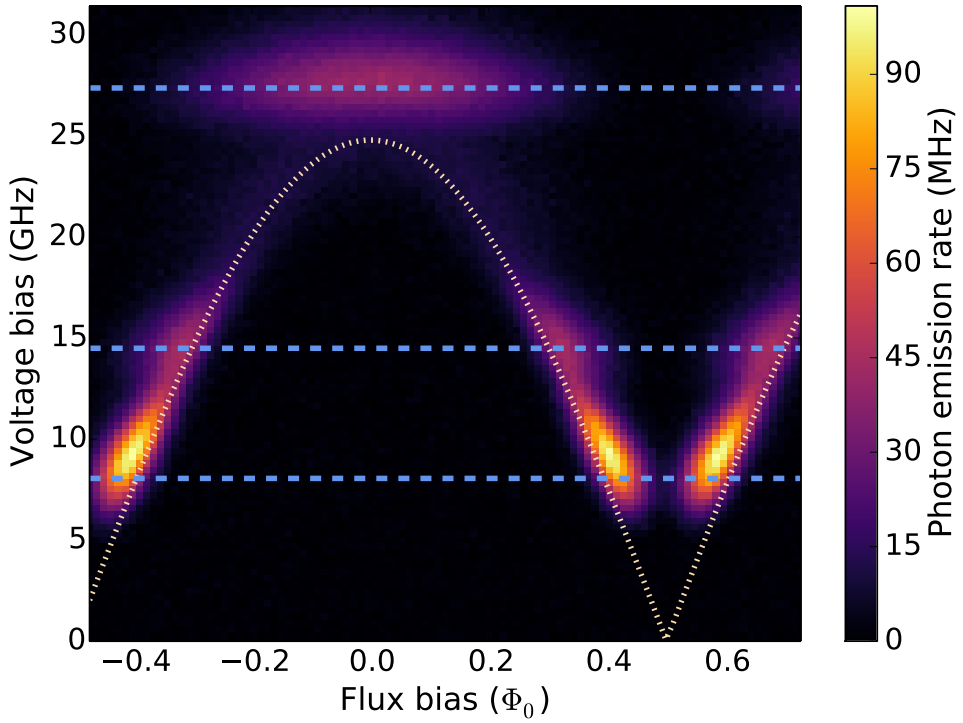

Figure (6.9): Calibrated photon emission rate (integrated from 6 GHz *to* 6.9 GHz*) as a function of the flux bias of the SQUID in units of the flux quantum* Φ_0 *and the applied voltage bias converted into* GHz*. The dashed blue lines show the expected values for the processes* $E_C + h\nu_0$*,* $E_C + 2h\nu_0$ *and* $E_C + h\nu_0 + h\nu_1$*, from small to high voltage biases. The dotted white line delimits the region where the system is on the current branch (see text for further details).*

6.3.1 Power spectral density of the emitted radiation

On this specific sample we have measured the power spectral density of the emitted radiation as a function of the SQUID frustration and the applied voltage. The values are again calibrated to units of photons emitted from the sample. Figure 6.9 shows the result integrated over the entire measurement bandwidth ($\approx 900\,\mathrm{MHz}$) giving a photon emission rate. Several prominent features are visible on the 2D-graph and will be analyzed in the following section. The origin of the dark region in the middle of the figure will equally be elucidated.

Analysis of the emission peaks

As described in the introduction and in chapter 5 we expect to see a peak in photon emission at bias voltages fulfilling the condition $2eV_1 = E_C + h\nu_0$, where $E_C = 2e^2/C$ is the charging energy of the island between the SQUID and the capacitor of the RC. To further investigate this, we consider Fig. 6.10 showing cuts through this 2D map along the voltage axis at different values of the flux threading the SQUID. We see the one photon peak evolve in voltage as we increase the Josephson energy, making it go along

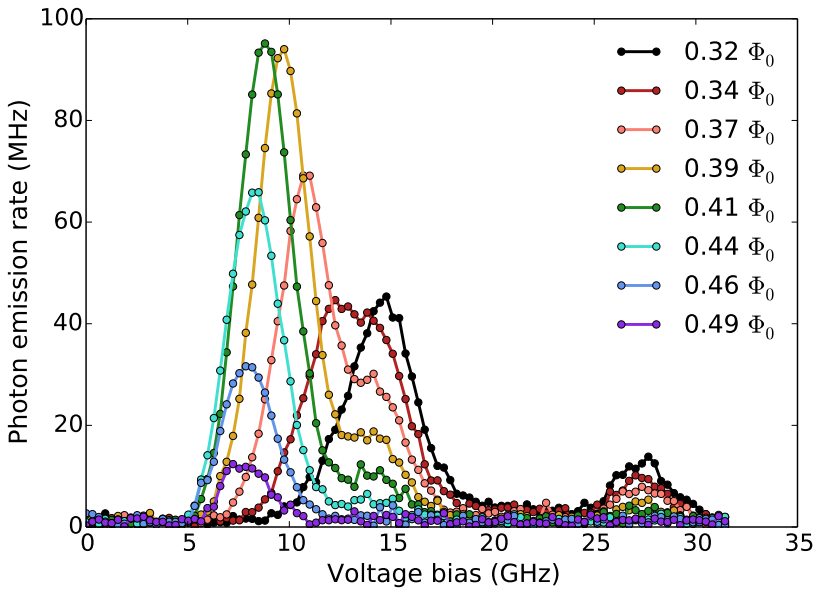

Figure (6.10): Cuts through the 2D-map of Fig. 6.9 along the voltage axis for different flux biases. As the frustration decreases, the one photon peak shifts upwards in voltage from initially 8 GHz. The two photon peak develops as a shoulder on the first peak around $0.44\Phi_0$ and slowly takes over at lower frustration. The peak emerging around 27.2 GHz is due to the combined emission of a photon into the first and second mode of the resonator. All peaks are offset by the charging energy (see text for further details).

the border of the dark region in Fig. 6.9. At high enough frustration (for $0.47\,\Phi_0$ and $0.49\,\Phi_0$) the peak stays at the same voltage bias of about 8.05 GHz and only evolves in magnitude.
We now focus on this peak and plot its PSD map as a function of voltage bias and frequency at the flux bias of $0.47\,\Phi_0$ (see Fig. 6.11). Now, we can integrate over the peak in voltage to get its profile in frequency as shown on the left side of Fig. 6.12. We derived in section 5.2.4 that this kind of integral gives the shape of the impedance seen by the junction. The resulting form is well described by a Lorentzian with a center frequency of $\nu_0 = 6.44\,\text{GHz}$ and a FWHM of 216 MHz. The right hand side of the figure displays the same peak integrated over frequency. It is possible to determine the charging energy $E_\text{C} = 2e^2/C$ and the effective temperature of the system by fitting this curve to the Gaussian predicted by Eq. (5.40). A Lorentzian fit is shown for comparison, but does not reproduce the behavior of the data as well as the Gaussian. We extract a value of 6.7 µeV (or 1.61 GHz) for the charging energy. This corresponds to an effective capacitance C_eff of 48 fF. We conclude that the stray capacitances of the island between the resistor and the junction almost double the designed value of 25 fF. The effective temperature T_eff is determined to be $\approx 28\,\text{mK}$. In spite of the increased capacitance we point out that this value of C_eff is almost identical to the one used in the theoretical description of our system in reference [36] (see Sec. 5.3.2), where clear anti-bunching of $g^{(2)}(0) \approx 0.5$ is predicted for this temperature.

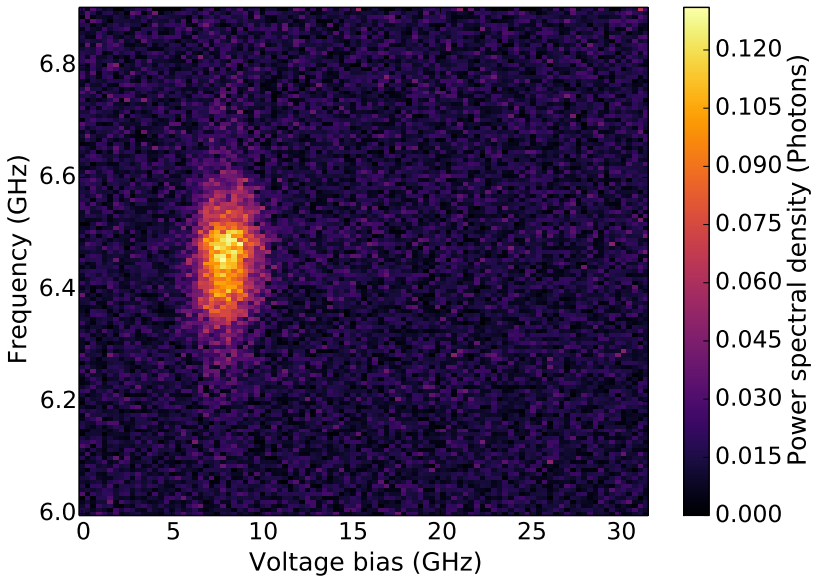

Figure (6.11): PSD map of the one photon peak at $2eV = E_C + h\nu_0$ for a flux bias of $0.47\,\Phi_0$. At this frustration no other emission processes are visible at any voltage bias.

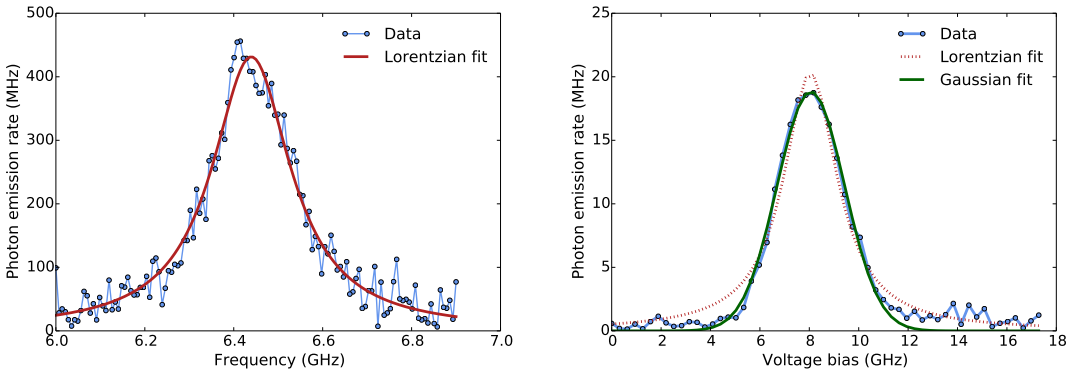

Figure (6.12): Left: Integral in voltage over the one photon peak in Fig. 6.11. The red curve is a Lorentzian fit giving a center frequency of $\nu_0 = 6.44\,\mathrm{GHz}$ *and a FWHM of* $216\,\mathrm{MHz}$*. Right: Integral in frequency over the same peak. The Gaussian fit according to Eq. (5.40) allows us to determine the effective capacitance* $(48\,\mathrm{fF})$ *and temperature* $(\approx 28\,\mathrm{mK})$ *of the RC.*

With these values we can predict the positions of two other features of similar magnitude at the energy balance conditions $2eV_2 = E_\mathrm{C} + 2h\nu_0 = 14.49\,\mathrm{GHz}$ and $2eV_3 = E_\mathrm{C} + h\nu_0 + h\nu_1 = 27.37\,\mathrm{GHz}$. The first corresponds to charging the island and simultaneously emitting two photons into the first mode of the resonator, while the latter includes the charging energy and emission of one photon each into the first (ν_0) and the second ($\nu_1 = 3\nu_0$) mode. For simplicity these features will henceforth be referred to as second and third peaks. Together with the one photon peak at $8.05\,\mathrm{GHz}$, these values are plotted as dashed blue lines in Fig. 6.9 and are in good agreement with the data. Since the ordinate of Fig. 6.9 is given by the total applied voltage, regions with considerable tunneling currents will be shifted to higher voltages just like in Fig. 6.6. On the maximum of the one photon peak the emission rate is $\approx 100\,\mathrm{MHz}$ leading to a current of $0.03\,\mathrm{nA}$. The voltage drop of $0.68\,\mu\mathrm{V}$ or $330\,\mathrm{MHz}$, caused by this, explains part of the difference between the dashed blue line and the actual position of the maximum. The emission rates on the other peaks are too low to generate notable voltage drops and corrections of the applied voltages are not necessary.
Finally, we can also investigate the other two peaks. It can be seen in Figs. 6.9 and 6.10 that the second peak slowly develops out of the first one, starting as a shoulder and taking over at low frustration. An integration of the peak over voltage at a coil bias of $0.32\,\Phi_0$ (not shown) returns similar values for the center-frequency ($6.44\,\mathrm{GHz}$) and FWHM ($230\,\mathrm{MHz}$) as for the one photon case. The third peak is of greater interest, since it is situated entirely outside of the region where no photon emission takes place. Integrating over voltage and averaging over several flux biases gives the detailed but arbitrarily scaled shape of the real part of the impedance seen by the junction. This is shown in the left-hand panel of Fig. 6.13. We would like to stress that in this case formula (5.2.4) still works, because the form of the extracted impedance is given around

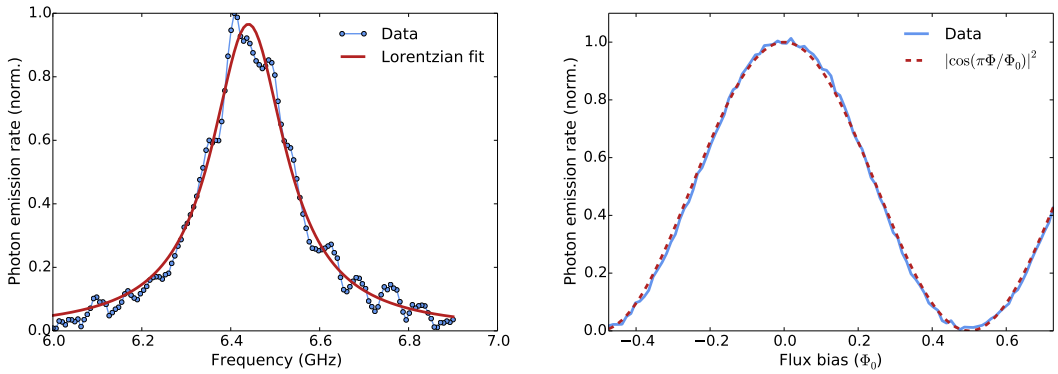

Figure (6.13): Left panel: Normalized form of $Re\{Z(\nu)\}$ around ν_0 extracted by integrating the third peak over voltage and averaging over several different SQUID frustrations. The data (blue) is fitted by a Lorentzian function (red) with $\nu_0 = 6.44\,\mathrm{GHz}$ and $FWHM = 202\,\mathrm{MHz}$. Right panel: Tunability of the Josephson energy with flux seen by integrating the third peak over voltage and frequency and subsequent normalization. The data points (blue) agree well with the expected flux dependency of $E_J^2 \propto |\cos(\pi\Phi/\Phi_0)|^2$ (dashed red).

the frequency of the observed radiation, while other impedances (such as the second mode at ν_1) are integrated out. The obtained resonance frequency (6.44 GHz) and FWHM (202 MHz) confirm the values found earlier on the other peaks.
We can also use the data gathered on the third peak to verify the dependence of the PSD on $E_J^2 \propto |\cos(\pi\Phi/\Phi_0)|^2$ and calibrate the flux axis. We do so by integrating the peak over frequency and voltage and plotting the result as a function of flux. The normalized curve given by this can be seen in the right panel of Fig. 6.13 (solid blue line) together with the expected flux dependence (dashed red line).

The dark region

In order to better understand what happens in the dark region of Fig. 6.9 we have tried to gain complementary information by measuring the transmission through the two RF ports with a vector network analyzer (VNA), while varying flux and voltage biases. This was done by sending the stimulus to the sample via the circulator of one of the amplifier chains (visible on the left side of Fig. 4.1) and then measuring the amplified response on the other channel.

As discussed in section 2.5, we expect the two RF ports to be decoupled on resonance, where the last $\lambda/4$ element between the node at point C in Fig. 2.2 and the SQUID acts as a stub [21]. Figure 6.14a gives a schematic representation of this effect. It only represents the parts of the on-chip beam splitter and bias tee relevant to the problem at hand. The vertical section corresponds to the two arms going down at 45° angles in Fig. 2.2 coupling point C to the RF ports. The resulting input impedance of an RF port

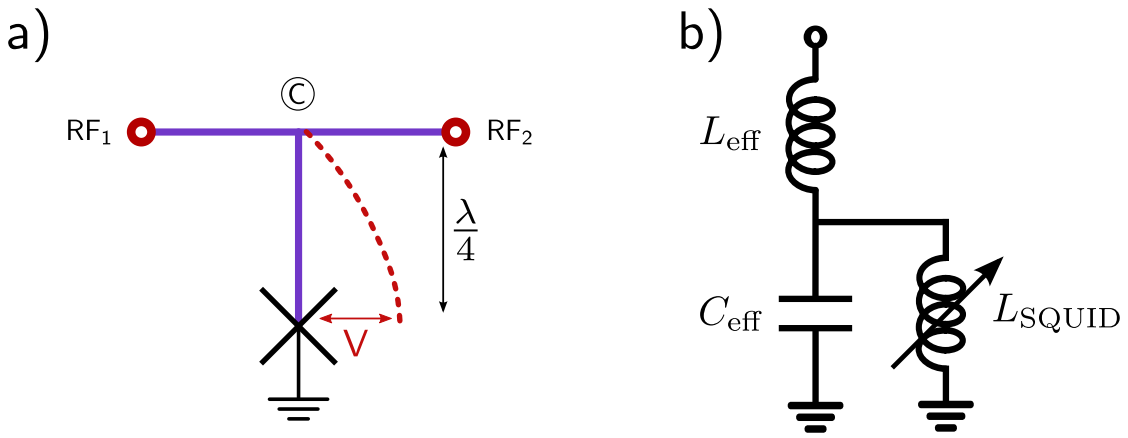

Figure (6.14): Model of the resonance observed in the VNA transmission measurements. a) Sketch of the relevant parts of the on-chip beam splitter from section 2.5. The point C is the same as indicated in Fig. 2.2. The $\lambda/4$ segment is labeled and the SQUID is represented by a cross. A dashed red line sketches the voltage profile at resonance. b) The lumped circuit element model of the $\lambda/4$-resonator and the SQUID consisting of the effective capacitance (C_{eff}) and inductance (L_{eff}) of the resonator as well as the tunable inductance of the SQUID (L_{SQUID}).

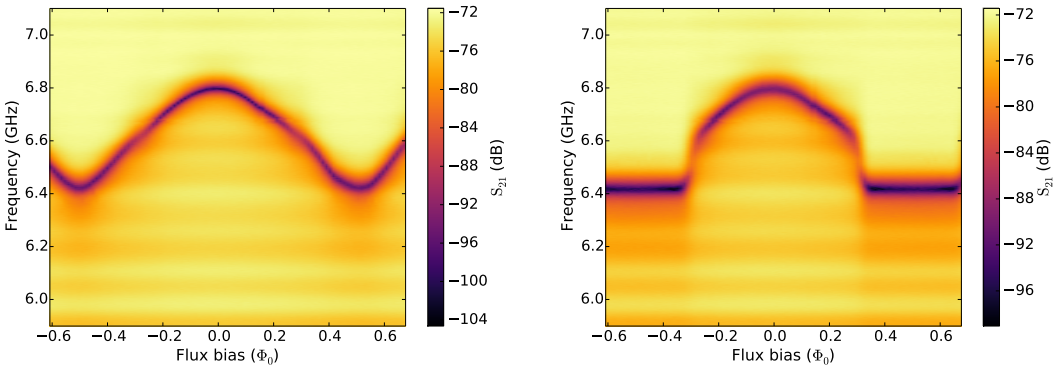

Figure (6.15): Left panel: Colormap of the frequency evolution of the anti-resonance found in the transmission between the two RF ports as function of the flux bias, when there is no applied voltage. Right panel: Same quantity when the voltage bias is at 14.5 GHz, corresponding to the two photon peak.

at point C is very low (of the order of $\approx 4\,\Omega$). As explained in section 2.5, this is done so that the RF ports dominate over the DC port at this point. A signal coming from one RF port, would normally couple well to the other one, but the stub leads to reflection of the incoming signals at frequencies where the open (the SQUID) is transformed to an impedance $< 4\,\Omega$. Hence, we expect to see a sharp dip in the transmission measurement, like the one shown in Fig. 2.6.
The result of such a measurement taken at voltage bias $V = 0$ is shown in the left panel of Fig. 6.15. It displays the transmission S-parameter of the device in dB as a function of flux bias and frequency. We clearly observe a dark line, corresponding to a dip in transmission, which is tuned in frequency with the frustration of the SQUID. This behavior can be understood by taking into account the Josephson inductance of the SQUID in the zero-voltage state:

$$L_{\mathrm{SQUID}} = \frac{\Phi_0}{2\pi I_{\mathrm{S}} \left|\cos\left(\frac{\pi\Phi}{\Phi_0}\right)\right|} \tag{6.2}$$

In this expression I_{S} is the critical current of the SQUID at finite temperature, Φ is the external applied flux and Φ_0 is the flux quantum. From Fig. 6.14a we can see that the SQUID is at the open end of the resonator, where the voltage is at its maximum, while the current is zero. This means that it is situated at the point of maximum impedance at resonance. This resonant circuit can be modeled by a series LC-circuit, since it produces a dip in the measured signal. The inductance coming from the SQUID shunts the effective capacitance to ground as shown in Fig. 6.14b. The anti-resonance in our measurement occurs at the frequency where the total impedance to ground of this effective circuit is zero:

$$\nu_0 = \sqrt{\frac{1}{L_{\mathrm{eff}} C_{\mathrm{eff}}} + \frac{1}{L_{\mathrm{SQUID}} C_{\mathrm{eff}}}} \tag{6.3}$$

This simple model, together with Eq. (6.2), illustrates why the resonance frequency is unaffected when L_{SQUID} tends towards infinity at maximum frustration ($\Phi = \Phi_0/2$). Then the total inductance will just stem from the effective inductance L_{eff} of the transmission line segment. However, when the frustration is decreased, the finite inductance of the SQUID contributes and the resonance frequency increases. This effect can be observed in the left panel of Fig. 6.15, where ν_0 goes from 6.44 GHz to a maximal value of ≈ 6.8 GHz at zero frustration.
The right panel shows what happens, when a finite voltage is applied to the junction. In the previous discussion the system was on the current branch of the junction IV-characteristic over the entire flux-bias range. Now, starting at a certain degree of frustration, the critical current of the SQUID $I_{\mathrm{S}}(\Phi)$ [56] has been suppressed to a level where the applied voltage becomes bigger than $RI_{\mathrm{S}}(\Phi)$; with R being the resistance of the RC circuit. Once this happens, a finite voltage drops over the junction, the system leaves the current branch and ν_0 lapses back to 6.44 GHz.
We propose a different, but equivalent, way of seeing this process by considering again

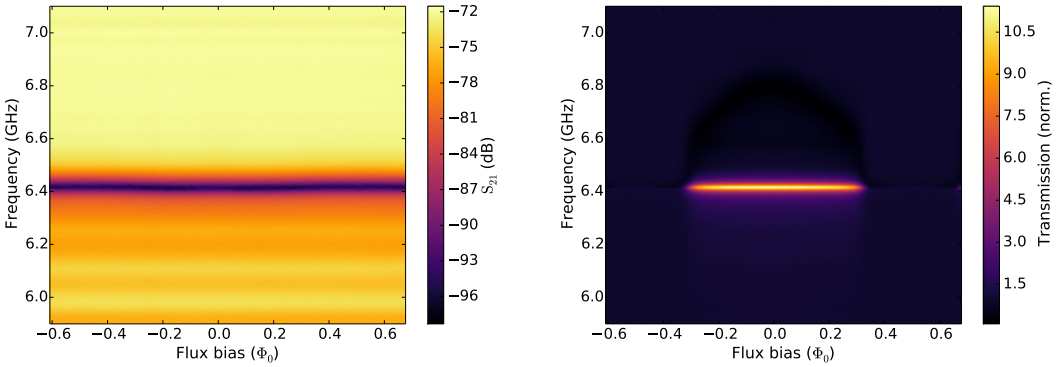

Figure (6.16): Left panel: Colormap of the frequency evolution of the anti-resonance found in the transmission between the two RF ports as function of the flux bias. Here the bias voltage is around 26.6 GHz*, which is situated on the third peak in Fig. 6.9. This anti-resonance is independent of the flux bias, indicating that the SQUID is always in the voltage state. Right panel: An example of how the normalization works. This is the map shown in the right panel of Fig. 6.15 divided by the left panel of this figure. The region where the resonance frequency is different from* 6.44 GHz *is greatly enhanced.*

the P(E)-function from the inset of Fig. 5.5. Two arrows are indicated in this figure. The black arrow corresponds to a voltage bias $2eV_1 = E_C + h\nu_0$ leading to photon emission and charging of the capacitor. This reduces the effective bias voltage at the junction by $2e/C$ to the value indicated by the green arrow. Now the system is on the $2eV_{RC} = E_C$ peak. At finite temperatures, this peak takes on high enough values at that voltage bias that a CP can tunnel just by exciting the RC-element leading to yet another voltage drop. In this fashion, the voltage does not regain the value necessary for emission of photons into the resonator at ν_0. In other words, the system gets trapped on the low frequency peak and further tunneling accompanied by voltage drops brings it to the current branch. In order to corroborate this view we want to highlight the parameter range where the SQUID is in the current state and the resonator is at a frequency different from 6.44 GHz. To do so, we divide each flux-frequency 2D map through the one presented in the left panel of Fig. 6.16. It was taken at high enough voltage (26.6 GHz) to never lapse back to the current branch. The right panel of the same figure displays the effect of this normalization on the spectrum from the right panel of Fig. 6.15. When integrating in frequency over this graph, the light region in the middle (where $\nu_0 \neq 6.44$ GHz) is greatly enhanced and the rest is normalized to one. After doing this to all datasets gathered for the different applied voltages we finally get Fig. 6.17. It shows exactly where in the voltage and flux parameter space, the system is on the current branch. Note that the value of I_S depends on the critical current at zero temperature, but is rescaled by thermal and quantum fluctuations [56]. Because of this, we can not easily calculate the resistance of the on-chip RC circuit from the data. Nevertheless, we can delimit the light region in this figure with a function $|\cos(\pi\Phi/\Phi_0)|$ rescaled to match its apex shown as a white

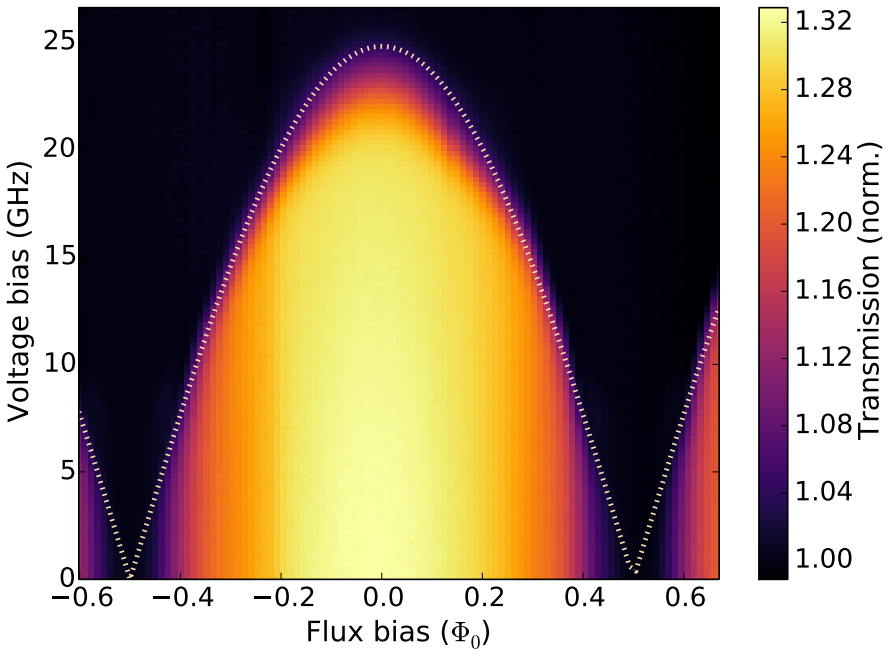

Figure (6.17): The result of the treatment performed on the data gathered with the VNA measurement. The light region indicates the parameter space in voltage and flux bias where the SQUID is in the current state. The white dotted curve is a function $|\cos(\pi\Phi/\Phi_0)|$*, rescaled so its apex matches the top of this region.*

dotted arch in Fig. 6.17. Finally, we can plot the same curve over Fig. 6.9. It coincides very well with the dark region where no photon emission occurs, further strengthening our interpretation of the phenomenon.

6.3.2 Photon statistics

As far as the photon statistics are concerned, our initial measurements on different locations in the parameter space of Fig. 6.9 have not revealed clear anti-bunching. We attribute this to the fact, that for the values of E_J enabling high emission rates (hence at weak frustration), the SQUID becomes trapped on the current branch, while for small emission rates the unfavorable evolution of the signal to noise ratio in the measurement of $g^{(2)}(\tau)$ (see Sec. 3.4.3) quickly becomes prohibitive. More specifically, for the latter case we reach the limit in measurement time where drifts in the system parameters compensate the advantage gained by further averaging. Another limiting effect is brought about by the very short RC-time of the system of the order of $\approx 1\,\mathrm{ns}$. We give a more detailed analysis of this effect towards the end of this chapter.
As a solution to this problem, we can periodically bring the SQUID to its maximum frustration point and back into the dark region of Fig. 6.9, where emission rates are in

principle high, while applying a voltage bias. When at full frustration, the system is forced onto the voltage branch by bringing the escaping current to zero. In the complementary picture, this suppresses the inelastic Cooper pair tunneling through the sample, which is proportional to E_J^2, thus eliminating the voltage drop over the resistor and reestablishing the voltage bias at the junction. Then, E_J is brought near its maximum and a photon is emitted immediately. Just afterwards, further emission is blocked by the effect of the charging energy and the subsequent lapse onto the current branch.
This technique is very promising, since it allows us to precisely control the emission rate. Through the pulsing, the system gains in complexity as illustrated by Fig. 6.18 presenting the altered power spectral density as a function of voltage bias and frequency. The data was recorded while pulsing the flux bias from maximum to minimum frustration with a rate of 120 MHz.

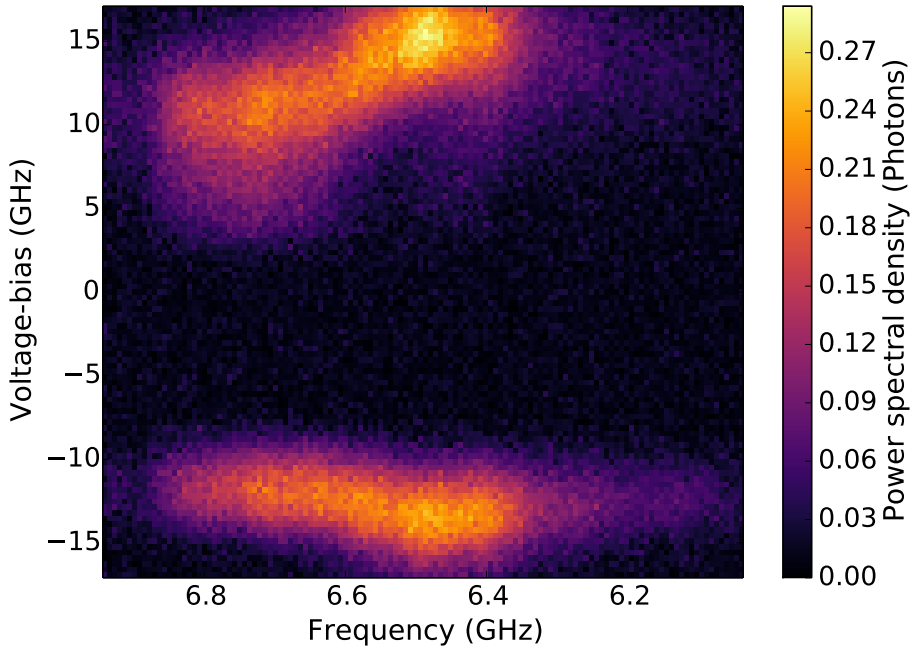

Figure (6.18): The altered power spectral density as a function of voltage and frequency when periodically changing the flux bias from maximum to minimum frustration using an approximate square pulse with a rate of 120 MHz.

Two effects can be observed here. On the one hand, whenever a photon is emitted into the resonator, the SQUID jumps to the current branch. As discussed in the previous section, this tunes the resonator frequency and, for sufficiently fast pulses, the photon leaks out only at the altered frequency. On the other hand, we observe a deformation of the peak along the voltage axis. It stretches to lower voltages on the positive side,

while being compressed on the negative side. This is due to the modulation of the voltage bias at the sample through the flux pulse. As was mentioned in section 2.6 and shown in Fig. 1.4, the on-chip flux bias line seconds as ground for the capacitance of the RC-element. This works well at DC, but for an AC current a voltage drops over the finite inductance of the line segment from the point under the capacitor to ground. Consequently, each flux pulse generates a voltage spike, which couples to the junction through the capacitance and modulates the voltage bias. This effect would concern positive and negative bias voltages alike, if it was not done in phase with the frustration pulse, which in turn is necessarily in phase with the emission of the photons we observe. In the dataset at hand, the current pulse went from positive values (full frustration) to negative values (maximum E_J), leading to a negative voltage spike behind the SQUID (as seen from the voltage source). This effectively increases the junction bias. The emission peaks are shifted towards smaller bias voltages, drawing the positive voltage peak down to lower values and pushing the negative peak to higher (more negative) values. The behavior of the respective high voltage sides of the peaks also depends on the emission into the two photon peak and higher peaks and can not be explained in this simple picture, which can in particular not account for the shape-asymmetry between positive and negative peaks.

In spite of these complications, this method allows us to circumvent the blockade of photon emission. We present here two $g^{(2)}(\tau)$ curves, measured with the same flux pulse as the PSD shown in Fig. 6.18. In both cases, the local oscillator frequency was chosen so that the measurement window was centered on an emission frequency of $\approx 6.75\,\mathrm{GHz}$. Under these conditions, we get clear anti-bunching in the emitted radiation when biasing the sample at a voltage corresponding to 5.8 GHz. Note that the value of the voltage bias is lower than the emission frequency, because of the effect of the flux pulse explained above. Figure 6.19 shows the obtained $\mathcal{G}^{(2)}(\tau)$ function presented as an emission rate in units of photons·ns^{-1}. This representation was chosen, because the standard normalization through division by $G^{(1)}(0)^2$, which is nothing but the average emitted power squared (see Eq. (3.9)), is not as informative in a pulsed experiment as in a free running one. In particular, it always normalizes $g^{(2)}(\tau)$, so that its average value is ≈ 1. Depending on the pulse frequency $g^{(2)}(\tau) = 1$ will then be situated somewhere at medium height of the peaks. Instead, we can integrate the peak in the calibrated power spectral density from Fig. 6.18 over frequency at the given voltage bias to get the photon emission rate. In this case we find $\approx 37\,\mathrm{MHz}$. Then we perform the standard normalization of $g^{(2)}(\tau)$, but multiply it with the extracted emission rate in photons·ns^{-1}. We call the obtained quantity $\mathcal{G}^{(2)}(\tau)$. With this normalization, the surface of each peak at times $\tau \neq 0$ corresponds to the number of photons contained in each pulse given by $37\,\mathrm{MHz}/120\,\mathrm{MHz} \approx 0.3$. The value of anti-bunching in a pulsed experiment is defined as the ratio between the residual value at $\tau = 0$ and the height of the peaks at $\tau \neq 0$. This ratio is ≈ 0.5 in the dataset at hand proving that our device can be used as a source of anti-bunched microwave light.

Moreover, we can alter the statistics of the emitted photons by simply changing the voltage bias. One example of this is shown in Fig. 6.20. Here we are using the exact same

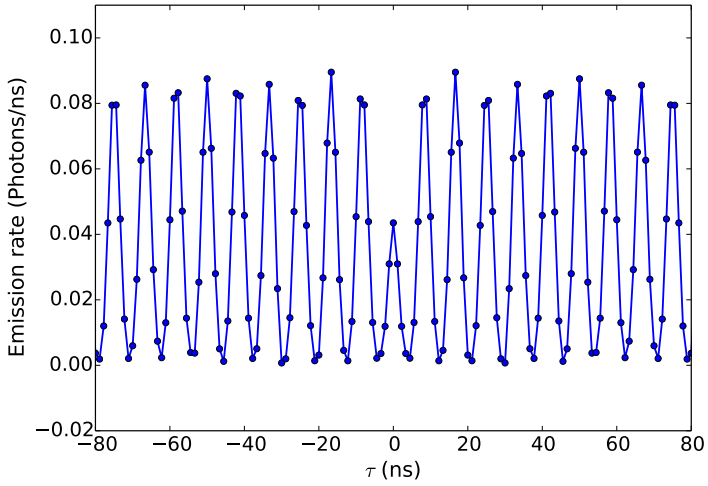

Figure (6.19): $\mathcal{G}^{(2)}(\tau)$ *normalized to give the emission rate in* photons·ns^{-1} *as a function of the time delay* τ *in* ns. *The data was taken at a voltage bias corresponding to* 5.8 GHz, *when periodically changing the flux bias from maximum to minimum frustration with a rate of* 120 MHz. *The measured photons are at a frequency of* 6.79 GHz. *Each peak at* $\tau \neq 0$ *contains* ≈ 0.3 *photons. The ratio between the height of the peak at* $\tau = 0$ *and the average height of the peaks at* $\tau \neq 0$ *is* ≈ 0.5, *showing clear anti-bunching.*

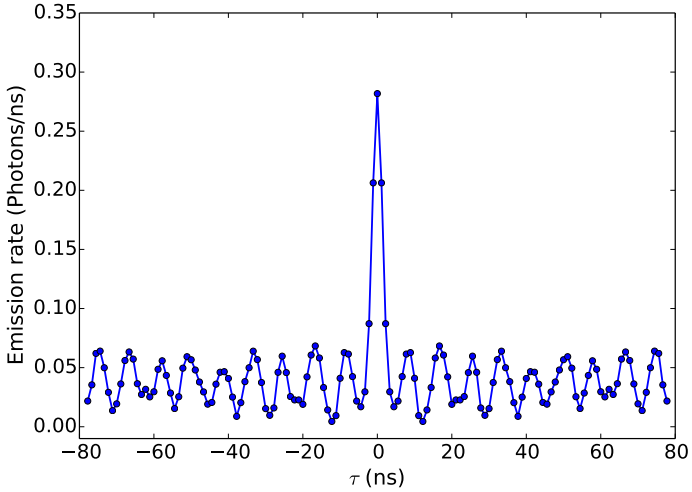

Figure (6.20): $\mathcal{G}^{(2)}(\tau)$ *normalized to give the emission rate in* photons·ns^{-1} *as a function of the time delay* τ *in* ns. *Apart from the voltage bias corresponding to* 12.6 GHz *the data was taken under the same conditions as in Fig. 6.19. Each peak at* $\tau \neq 0$ *contains* ≈ 0.3 *photons. Here, the ratio between the height of the peak at* $\tau = 0$ *and the average height of the peaks at* $\tau \neq 0$ *is* 4.72 *showing strong bunching.*

parameters as in the previous measurement with the exception of the voltage bias, which is now situated at 12.6 GHz. The resulting $\mathcal{G}^{(2)}(\tau)$ (normalized as previously) displays clear bunching of 4.72, with an emission rate of 34 MHz (again ≈ 0.3 photons peak).

6.3.3 Current measurements

The measurement of the current through the sample provides important complementary information to the photon emission spectrum. In particular, it allows us to calculate the exact value of the resistor in the RC-circuit. During the measurement campaign giving the results presented above, the transformer box (see Sec. 4.3.2) was not part of the setup, because it can introduce additional current noise. The measurements presented here were taken in an, at the time of the redaction of this manuscript, ongoing campaign on a slightly different sample. The device investigated here is designed to have a resonator with a FWHM of 700 MHz and an on-chip resistor of $\approx 43\,\mathrm{k}\Omega$.
The result of the current measurement as a function of bias voltage is given on the left-hand side of Fig. 6.21. Each curve is taken at a different flux bias, going from nearly full frustration (smallest current) to minimum frustration (largest current). The voltage axis is, as usual, given in units of GHz using the conversion $2eV/h = \nu$. The slope of the current branch at low frustration directly gives the resistance in series with the SQUID, which is entirely dominated by the resistor of the RC-circuit. From these curves we extract a value of $R = 34.5\,\mathrm{k}\Omega$. This is smaller than our original estimation, which was based on measurements of a comparable chromium thin film. The reason for this could be a reduction of the film resistance or a different residual resistivity ratio. The dashed green line in the figure shows $I = V/R$ confirming the extracted value.

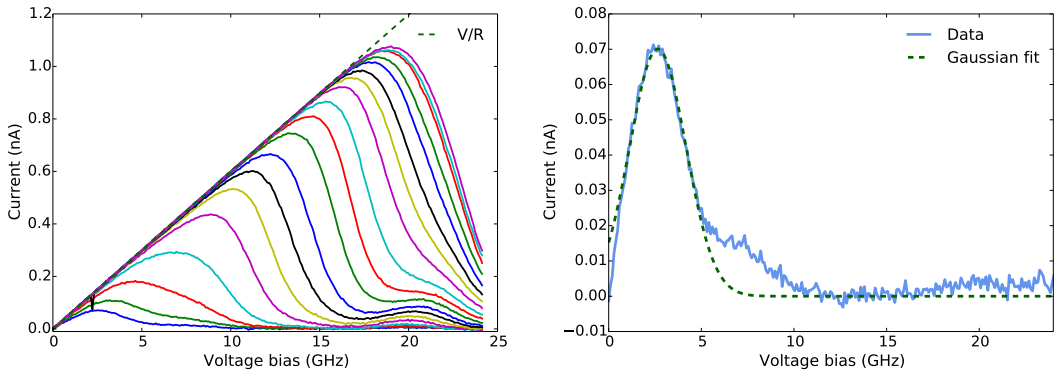

Figure (6.21): Left panel: Current through the sample in nA *as a function of bias voltage in* GHz. *The lowest curve is measured around maximum frustration ($\Phi \approx 0.5\,\Phi_0$) and the highest around minimum frustration ($\Phi \approx 0$). The dashed line shows the result of the fit of the RC resistance. Right panel: A current voltage characteristic of the sample close to full frustration (lowest curve in the left panel). The RC peak is fitted with the Gaussian function from Eq. (5.40).*

We can fit Eq. (5.40) to the low current curves, which are not yet noticeably affected by the voltage drop over the resistor and are more likely to be in the P(E)-limit. Doing so, we find the values of $\approx 29\,\mathrm{fF}$ for the total capacitance of the RC and $\approx 21\,\mathrm{mK}$ for its effective temperature. The charging energy associated with this capacitance is $\approx 11\,\mu\mathrm{eV}$ or $\approx 2.67\,\mathrm{GHz}$ when converted to frequency. The right panel of Fig. 6.21 shows an example of such a fit.
We interpret the two other visible features, namely the shoulder appearing out of the main peak and the peak around $\approx 20\,\mathrm{GHz}$, to the processes $E_\mathrm{C} + h\nu_0$ and $E_\mathrm{C} + h\nu_1$ respectively.

6.4 Single photon source: Analysis and perspectives

6.4.1 Free-running mode

As was mentioned above, no proof for anti-bunching in the free-running mode (without flux-pulsing and outside of the dark region) could be found. In this mode, our system has three characteristic rates being the inverse RC-time γ, the bandwidth of the resonator $\Delta\nu \approx 210\,\mathrm{MHz}$ and the photon emission rate $\Gamma \leq 20\,\mathrm{MHz}$. The latter value is taken from the integration over the one photon peak in Fig. 6.12. This very low rate is what makes it so difficult to measure anti-bunching. We can also give an approximate value for the RC-time using the extracted capacitance (48 fF) and correcting the designed R with the residual resistance ratio found on a similar sample in section 6.3.3 giving $R \approx 17\,\mathrm{k\Omega}$, $RC \approx 0.8\,\mathrm{ns}$ and $\gamma \approx 1.25\,\mathrm{GHz}$. Our measurement bandwidth is $BW = 900\,\mathrm{MHz} < \gamma$. This signifies that the only point in time on our $g^{(2)}(\tau)$ curves where we could possibly see the anti-bunching dip is at $\tau = 0$, since we can not resolve changes on the order of the RC-time and for time-scales longer than $RC = 1/\gamma$ the Poisson statistics of the much slower photon emission take over. Even worse, we average out the anti-bunching at $\tau = 0$ with the values at $\tau > 0$. To summarize, we find $\Gamma < \Delta\nu < BW < \gamma$. Contrary to this, the ideal situation in the free-running mode would be:

$$\gamma = \Gamma < \Delta\nu < BW \tag{6.4}$$

If this condition is fulfilled, the measurement bandwidth contains the resonator, which has an inverse lifetime bigger than the other rates in the system, meaning that it will at most contain one photon. The equality $\gamma = \Gamma$ signifies that the photon emission is purely controlled by the RC-time, as in our sketch in the introduction. We have designed and fabricated resonators with $\Delta\nu = 700\,\mathrm{MHz}$ and as is shown in section 6.2 (Fig. 6.5) and reference [20], values of $\Gamma = 500\,\mathrm{MHz}$ are achievable without leaving the domain of validity set by considering E_J as a perturbation. Consequently the conditions $\Gamma < \Delta\nu < BW$ are in principle easily achievable.
Now we turn towards the remaining condition $\gamma = \Gamma$. In order to have, for instance, $\gamma = 400\,\mathrm{MHz}$, considering the capacitance fixed at 48 fF, we would need a resistance of $\approx 52\,\mathrm{k\Omega}$. This comes, unfortunately, with the caveat of extending the range of the dark region, meaning that the measurable value of Γ is even more restricted. As was explained

earlier, this is due to the resulting increase of the RC-peak in the P(E)-function (at $2eV_{\mathrm{RC}} = E_{\mathrm{C}}$), or in the complementary picture, the change in the slope of the current branch making it even easier for the junction to jump away from voltage branch.
Unfortunately, the solutions to these problems are antagonistic. If we reduce R, the dark region in Fig. 6.9 would shrink and we could measure at higher photon emission rates. However, this would also lead to an even shorter RC-time. This is particularly detrimental, since we certainly would not like to increase C and thus decrease E_{C}, making the system more vulnerable to temperature and consequently further suppressing the anti-bunching effect. In spite of this grim prospect, there is a possible solution, which has the advantage of being part of this projects natural course, namely going to higher frequencies. From what was said above, we understand that increasing the distance $h\nu_0$ between the peaks at $2eV_{\mathrm{RC}} = E_{\mathrm{C}}$ and $2eV_1 = E_{\mathrm{C}} + h\nu_0$ can solve this problem. As soon as $h\nu_0/(2e)$ is much bigger than the voltage drop $\delta V = 2e/C$, which occurs immediately after an emission event, we expect the system to stay on the voltage branch even for high emission rates. Another possible solution is to increase the characteristic impedance of the resonator to a point where the height of the P(E)-function of the combined peak (at $2eV_1$) becomes comparable to its height at the RC-peak (at $2eV_{\mathrm{RC}}$). The result of this would be the same as in the solution mentioned just before, namely that the effective voltage bias needed to be at the maximum of the combined peak would increase. A third option is to augment the efficiency of our measurement setup, for instance by using quantum limited amplifiers. This would allow us to measure the anti-bunching signature at $\tau = 0$ for much smaller emission rates.

6.4.2 Pulsed mode

The minimum value of anti-bunching found while flux pulsing the sample was ≈ 0.5. As discussed earlier, the charging energy of the device ($C \approx 48\,\mathrm{fF}$ and $E_{\mathrm{C}} \approx 6.68\,\mu\mathrm{eV}$ or $1.6\,\mathrm{GHz}$) is almost the same as the one used for the calculations of Leppäkangas *et al.* in reference [36]. From their predictions shown in Fig. 5.5, we can see that at the extracted effective temperature ($\approx 27.8\,\mathrm{mK}$) one would indeed expect a value between 0.4 and 0.6. Operating the source in the pulsed mode is actually very promising, since it allows us to tune the emission rate *in situ*, effectively turning our system into an on-demand source of anti-bunched radiation. Moreover, in this case, the dark region works in our favor, since after each emission event the voltage drop rapidly moves the bias away from the one photon peak and onto the RC-peak suppressing further emission. The new quantities we have to consider are the flux pulse rate κ_{p} and the maximum instantaneous emission rate of the junction Γ_{max}. The latter should be understood as the instantaneous emission rate when bringing E_{J} to its peak value after full frustration. This is not directly experimentally accessible, because of the jump to the current branch following photon emission. Nevertheless, with the information gathered from the sample without RC-element; in particular from Fig. 6.5; we can safely estimate it to be able to reach $\Gamma_{\mathrm{max}} > 1\,\mathrm{GHz}$. It should however be noted, that in the case at hand we have to voltage bias the system far below the maximum point, because of the spurious modulation of the bias through the flux pulse. From the fact that each of our pulses only contains ≈ 0.3 photons,

we deduce that at the average applied voltage is small enough to give: $\Gamma_{\max} < \kappa_{\mathrm{p}}$. The ideal condition for the operation of the pulsed source would be:

$$\kappa_{\mathrm{p}} < \gamma < \Delta\nu < \Gamma_{\max} < BW \tag{6.5}$$

In this case, each pulse would leave the system enough time to emit one photon and then be blocked by the RC. Presumably the inverse RC-time γ is less important, because of the jump to the current branch. Nonetheless having $\gamma < \Gamma_{\max}$, could be useful, because it would slow down the system dynamics and thus reduce the heating of the resistor. Since $\Gamma_{\max}$ no longer limits the average emission rate of our source (this is done by κ_{p}), but only indicates how fast a photon is emitted once the system is brought to minimum frustration by the flux-pulse, we can exchange it with $\Delta\nu$. The resulting condition $\Delta\nu < \Gamma_{\max}$ would make the emitted photons indistinguishable. This is due to the fact that the length of an emitted photon in time is given by $1/\Delta\nu$. If the above condition is fulfilled, the jitter in photon emission times (of the order of $1/\Gamma_{\max}$) is negligible compared to their length.
Contrary to this ideal situation, we have $\Gamma_{\max} < \kappa_{\mathrm{p}} < \Delta\nu < BW < \gamma$. Luckily, decreasing γ, via an increase of R is no longer a problem, since the dark region now works in our favor. The restriction here is that the dark region should not become so wide that the noise on the flux pulse (which necessarily arrives slightly distorted at the sample) prevents us to efficiently frustrate the SQUID. This will set an upper limit to the resistance and naturally lead once more to the need for an increase of ν_0. Most importantly though, the rate $\Gamma_{\max}$ should be made more controllable by eliminating the parasitic coupling of the flux line to the bias voltage as discussed in the conclusion following this chapter.

Conclusion and outlook

In the final part of this manuscript, we want to quickly summarize the main results obtained during the course of this PhD work. This will be followed by a discussion of the feasibility of extending the frequency range of our light source to the THz regime and a more general outlook on other possible applications of photon emission through inelastic Cooper pair tunneling to practical devices.

The progress so far

In this project, we have developed a nano-fabrication process for very small ($0.022\,\mu m^2$) vertical NbN:MgO:NbN Josephson junctions using a self-aligned spacer technique. The obtained junctions show current voltage characteristics with low sub-gap currents (sub-gap resistance $\approx 100\times$ normal state resistance) and large gap voltages ($> 4.15\,mV$). We deposit the NbN:MgO:NbN films used for this ourselves, obtaining good quality tri-layers with a superconducting transition temperature of 15 K.
Building on this fabrication process, we have designed samples comprising superconducting interference devices, acting as flux-biasable Josephson junctions, which are embedded in different electromagnetic environments. The latter are engineered from combinations of coplanar wave guide transmission line segments allowing us to additionally implement a beam splitter and a bias tee on-chip.
We have built up an experimental setup for microwave photon correlation measurements starting from the installation and testing of the dilution refrigerator itself, through the wiring of the measurement chain to the implementation of the various calibration techniques and measurement scripts. In this dissertation, we have presented a detailed account of all the different spurious noise sources in our setup and how we correct for them.
We have participated in the development of a theoretical description of our samples, based on a model very close to the actual implementation of the device. This has led to the joint publication of reference [36] predicting anti-bunching over a wide temperature range. We have also developed a way of extracting the impedance seen by the junction only from power spectral density measurements.
Finally, we have shown our experimental results, beginning with samples without RC-elements. The environmental impedance was extracted with the method mentioned above and was used to simulate the expected power spectral densities for the one ($2eV_1 = h\nu_0$)

and two ($2eV_2 = 2h\nu_0$) photon emission peaks. Very good agreement with the obtained data was found. We then went on to investigate the second order correlation functions of the photons emitted on these peaks showing Poissonian and bunched statistics respectively. In particular, we have shown a divergence in the bunching obtained from the two photon process at low emission rates. This was predicted in a simple calculation shown in chapter 5.
The second part of chapter 6 was dedicated to the study of a sample with an RC-element. First, we performed a detailed analysis of the PSD obtained on this system as a function of the different parameters, using information gained through complementary measurements to explain the observed phenomena. Then, we demonstrated the operation of a bright (emission rate of $\approx 40\,\mathrm{MHz}$), on-demand source of anti-bunched ($g^{(1)}(0) \approx 0.5$) microwave photons. The chapter was ended with a detailed analysis of this source making suggestions for possible ameliorations.

Suggestions for a new design

Already in chapter 2, we have mentioned that the flux bias line is very robust in terms of its critical current. We could confirm, during our measurements, that we can sweep more than a hundred flux quanta through the SQUID without quenching the line and more than 10 without significantly heating the base-stage of the dilution refrigerator. Consequently, it would be largely sufficient to lead the current along one side of the SQUID only and not around it on three sides as is done in the present design (see Fig. 1.4). In this way the current does not flow under the capacitance of the RC-element and voltage and flux biases are decoupled.
Another suggestion concerns the nano-fabrication process for operating frequencies $< 60\,\mathrm{GHz}$. We have seen that the effective capacitance of the RC-element clearly dominates the capacitance of the Josephson junctions. In order to reduce the complexity of our nano-fabrication process we could eliminate the electron beam lithography (EBL) steps and replace them with deep-ultraviolet lithography (DUVL). By designing the Josephson junctions as the overlap between long but thin ($\approx 700\,\mathrm{nm}$) perpendicular lines, the high alignment precision of EBL becomes unnecessary. At this width DUVL is already rather precise, but could still lead to a slight imbalance in junction size. If the SQUID is slightly imbalanced, we will not be able to reduce E_J exactly to zero at full frustration (see App. D). We can counteract this by reducing the maximum critical current through an increase in the thickness of the tunnel barrier. This would, as an added benefit, also reduce the size of the dark region and the capacitance of the SQUID. One such SQUID, with a barrier thickness of $\approx 5\,\mathrm{nm}$ would have a capacitance of $\approx 17\,\mathrm{fF}$, which could be compensated for by reducing or eliminating the additional capacitance of the RC ($\approx 25\,\mathrm{fF}$). Note that this approach is limited in frequency, since it adds to the effective capacity of the transmission line resonator coupled to the SQUID decreasing its characteristic impedance $Z_0 = \sqrt{L/C} = 1/(\omega_0 C)$. On the other hand, the corresponding nano-fabrication process has already been developed during this thesis in order to produce test junctions and can be implemented easily and with very high yield.

Going to higher frequencies

When going to even higher frequencies the DUVL-fabrication approach described above is not applicable any more. In contrast to this, even at $\nu_0 = 1\,\mathrm{THz}$, the very small junction sizes we obtain with the EBL process ($C \approx 1\,\mathrm{fF}$) put the limit of Z_0 only at $160\,\Omega$. Naturally, the main issue at frequencies of the order of several hundred GHz or more will be to avoid spurious resonances on the chip and in the sample holder. At 1 THz the wavelength in vacuum is $\approx 300\,\mu\mathrm{m}$ and in our $50\,\Omega$ coplanar waveguides a $\lambda/2$ resonance would have the length of $\approx 40\,\mu\mathrm{m}$, which is smaller than the distance between two mass bridges. This particular problem can easily be remedied by decreasing this distance, but similar issues could occur on other parts of the chips. The solutions to these problems will have the found step by step by careful microwave engineering.
The increase in frequency would also have beneficial consequences, as was already touched upon. All peaks would move further apart in voltage, greatly reducing the impact of noise and the lapse onto the current branch as well as spurious two photon emissions should cease to happen. Note that the charging energy does not have to scale with ν_0, but only with $\Delta\nu$. Specifically, the capacitance still has to be small enough to make the voltage drop off the peak. For a reduced C_{eff} of 25 fF the voltage drop is 6 GHz and the peak should be no wider than $\Delta\nu \approx 3\,\mathrm{GHz}$. This will make the external quality factor ($Q_{\mathrm{e}} = \nu_0/\Delta\nu$) increase with frequency (≈ 330 at 1 THz). It is possible that the present values of the internal quality factor ($Q_{\mathrm{i}} \approx 7000$) will decrease at higher frequencies. These values were obtained on resonators etched into the entire trilayer and can probably be explained by dielectric losses in the MgO buffer layer, where the field densities of our CPWs are rather high. This could be avoided by fabricating the resonators without this buffer. The use of different substrates, such as single crystal MgO or Sapphire, which has a similar lattice constant, could also be envisioned.
Naturally, the main challenge will be to measure the photons produced at these high frequencies. Leading them out of the sample holder would prove extremely challenging. In this context, several other applications of the physics described in this work will be useful. Two of these, namely a frequency converter and a parametric amplifier, are currently being developed and will be very briefly described in the following section.

Other applications of this physics

The physics of inelastic Cooper pair tunneling also allows for processes involving photon absorption or combined absorption and emission at different frequencies. Two possible applications of this are frequency conversion and parametric amplification, which are described in Figs. 6.22 and 6.23. They would allow to translate THz photons to GHz photons or even amplify THz photons to GHz photons.

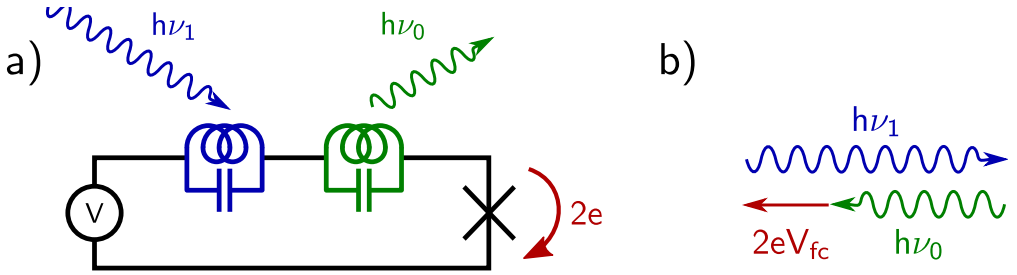

Figure (6.22): A voltage biased Josephson junction acting as a frequency converter. The environment seen by the junction consists of two resonators. The energy balance is set up so that $h\nu_1 = 2eV_{\rm fc} + h\nu_0$. An incoming photon at high frequency ν_1 provides enough energy for the Cooper pair to tunnel against the voltage bias, while emitting a photon at lower frequency ν_0.

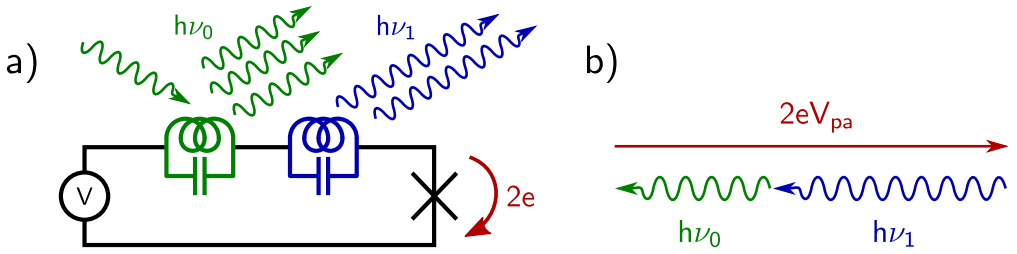

Figure (6.23): A voltage biased Josephson junction working as a parametric amplifier. As in the preceding case the environment is presenting two modes to the junction. Now the voltage bias is chosen to satisfy $2eV_{\rm pa} = h\nu_0 + h\nu_1$ and plays the role of the pump. An incoming photon at $h\nu_0$ leads to stimulated emission, while the second mode $h\nu_1$ acts as an idler.

Appendix A

Fabrication details

A.1 Sputtering parameters

Table A.1 shows the basic parameters used when sputtering the different materials and thin films mentioned in this thesis. Only the values used during deposition are given, the conditioning procedures are not detailed. Gas partial pressures are given in units of 1×10^{-4} mbar and times in seconds. RF-sputtering powers are given in W, whereas for DC-sputtering a current is given in A. An additional column specifies which of either sputtering modes is used. The parameter "Rotation" signifies that the substrate holder rotates during deposition leading to roughly seven times lower sputtering rates.

A.2 Etch recipes

Tables A.2, A.3, A.4, A.5 and A.6 describe the employed etch recipes. The flowrates for each gas are given in sccm and pressures are in units of mtorr. The power for generating the inductively coupled plasma (ICP) as well as the forward power (accelerating the ions towards the sample) are given in W. Times are given in seconds. EPD signifies that laser-reflectrometry is used to determine the duration of the etch. Numbers in parentheses are given whenever a different initial value of that parameter is used until the plasma has stabilized.

	Ar (10^{-4} mbar)	N_2 (10^{-4} mbar)	Power (W)	Time (s)	Rotation	Mode
Backsputtering	130		250	300-600	no	RF
MgO_{buffer}	125	10	550	70	no	RF
NbN_{inf}	150	20	4	54	no	DC
$MgO_{barrier}$	130		450	100	yes	RF
NbN_{sup}	150	20	4	22	no	DC
MgO_{SiN}	125	10	550	245	yes	RF
NbN_{top}	150	20	4	95	no	DC

Table (A.1): MgO_{buffer} corresponds to the buffer layer; the trilayer is made up of NbN_{inf}:$MgO_{barrier}$:NbN_{sup}, NbN_{top} stands for the topelectrode and MgO_{SiN} is the protective MgO layer sputtered onto the Si_3N_4 dielectric.

	SF_6 (sccm)	Ch_2F_2 (sccm)	Ar (sccm)	Pressure (mtorr)	ICP (W)	Forward (W)	Time (s)
NbN_{sup}	5	25	40	5(15)	500	70	120
$Overetch_{sup}$	10	10	40	20	500	20(50)	60
MgO	None	None	40	5	500	150	15
NbN_{inf}	5	25	40	5(15)	500	70	EPD
$Overetch_{inf}$	10	10	40	20	500	20(50)	45

Table (A.2): Procedure for etching the NbN(80 nm):MgO(4 nm):NbN(200 nm) trilayer. Each NbN layer is etched in two steps, a main step and an overetch step for better homogeneity. EPD stands for end point detection.

	SF_6 (sccm)	Ch_2F_2 (sccm)	Ar (sccm)	Pressure (mtorr)	ICP (W)	Forward (W)	Time (s)
MgO			100	5(15)	500	150	60
Pump							150
MgO			100	5(15)	500	150	20
Pump							150
MgO			100	5(15)	500	150	20
Pump							150
MgO			100	5(15)	500	150	20
Pump							150
MgO			100	5(15)	500	150	20
Pump							150
Si_3N_4	5	40	10	5(15)	700(600,500)	70(60,50)	EPD

Table (A.3): Procedure for etching the MgO(20 nm):Si_3N_4(500 nm) dielectric. Pumping steps are interlaced with the mechanical etch steps to allow for evacuation of the MgO residues from the chamber. The Si_3N_4 layer is etched using end point detection (EPD), but an over-etch of ≈ 5 seconds is added at the end. ICP and forward power are reduced to the next lower value in parentheses whenever the plasma has stabilized.

	SF_6 (sccm)	Ch_2F_2 (sccm)	Ar (sccm)	Pressure (mtorr)	ICP (W)	Forward (W)	Time (s)
NbN_{top}	5	25	40	5(15)	500	70	EPD
NbN_{sup}	5	25	40	5(15)	500	70	120
$Overetch_{sup}$	10	10	40	20	500	20(50)	60

*Table (A.4): Procedure for etching the NbN(*350 nm*) topelectrode as well as the* 200 nm *thick upper tier of the trilayer. An end point detection (EPD) is possible on the* NbN_{top} *layer. Afterwards calibrated time-etches are used.*

	O_2 (sccm)	Pressure (mtorr)	ICP (W)	Forward (W)	Time (s)
O_2 plasma	50	40	0	30	20

Table (A.5): Descumming plasma. This recipe is used to burn resist residues after development and to clean the wafer after resist removal.

	Ar (sccm)	Pressure (mtorr)	ICP (W)	Forward (W)	Time (s)
Ar plasma	40	5	500	150	32

*Table (A.6): This strongly forward-biased argon plasma is used to remove the Ti(*10 nm*):Pt(*60 nm*) hard-mask after the trilayer etch step.*

Appendix B

Transmission line theory

B.1 Waves on a lossless transmission line

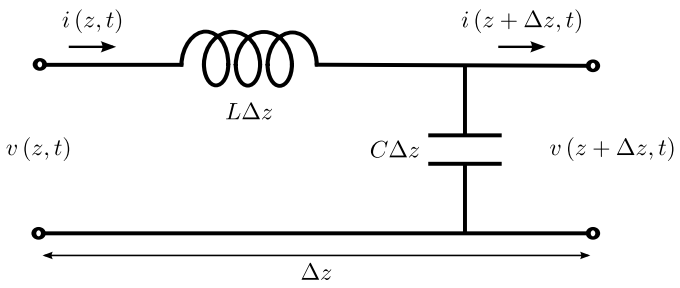

Figure (B.1): Piece of infinitesimal length of a lossless transmission line showing the series inductance and shunting capacitance of the element.

Figure B.1 shows a general phenomenological model for a lossless transmission line capable of supporting transverse electromagnetic (TEM) waves. The wave guide consists of two conductors which are subdivided into elements of infinitesimal length Δz. The voltage difference between the two wires before the element is $v(z,t)$ and the current along them is $i(z,t)$. Each section of length Δz has a series inductance per unit-length L and a shunting capacitance per unit-length C. This leads to a voltage difference $v(z+\Delta z,t)$ and a current $i(z+\Delta z,t)$ after the section. Kirchhoff's circuit laws for voltage and current give the two equations:

$$v(z,t) - \Delta z L \frac{\partial i(z,t)}{\partial t} - v(z+\Delta z,t) = 0 \tag{B.1}$$

$$i(z,t) - \Delta z C \frac{\partial v(z+\Delta z,t)}{\partial t} - i(z+\Delta z,t) = 0 \tag{B.2}$$

Reordering of the terms, dividing by Δz and performing $\lim_{\Delta z \to 0}$ leads to:

$$\frac{\partial v(z,t)}{\partial z} = -L \frac{\partial i(z,t)}{\partial t} \tag{B.3}$$

$$\frac{\partial i\left(z,t\right)}{\partial z}=-C\frac{\partial v\left(z,t\right)}{\partial t} \tag{B.4}$$

Phasor notation naturally leads to the ansatz $v\left(z,t\right)=\mathrm{Re}\{\sum_{\pm}\left|V_0^{\pm}\right|e^{j(\omega t\mp kz+\theta^{\pm})}\}=\mathrm{Re}\{V(z)e^{j(\omega t)}\}$, with:

$$V\left(z\right)=V_0^{+}e^{-j\beta z}+V_0^{-}e^{j\beta z} \tag{B.5}$$

$$I\left(z\right)=I_0^{+}e^{-j\beta z}+I_0^{-}e^{j\beta z} \tag{B.6}$$

This brings (B.3) and (B.4) into the form:

$$\frac{dV\left(z\right)}{dz}=-j\omega LI\left(z\right) \tag{B.7}$$

$$\frac{dI\left(z\right)}{dz}=-j\omega CV\left(z\right) \tag{B.8}$$

The general solution is a superposition of right and left moving traveling waves, where $\beta=\omega\sqrt{LC}$. $V_0^{\pm}=\left|V_0^{\pm}\right|e^{j\theta^{\pm}}$ as well as $I_0^{\pm}=\left|I_0^{\pm}\right|e^{j\theta^{\pm}}$ are complex amplitudes containing a magnitude and a phase factor.
Going back into time notation ($v\left(z,t\right)=\mathrm{Re}\{\left|V_0^{\pm}\right|e^{j(\omega t\mp\beta z+\theta^{\pm})}\}$), one readily extracts the wavelength as $\lambda=2\pi/\beta$ and the phase velocity $v_{\mathrm{p}}=\omega/\beta=1/\sqrt{LC}$.
Differentiating (B.5) with respect to z and comparing with (B.7) yields:

$$I\left(z\right)=\sqrt{\frac{C}{L}}V_0^{+}e^{-j\beta z}-\sqrt{\frac{C}{L}}V_0^{-}e^{j\beta z} \tag{B.9}$$

This leads to the definition of the characteristic impedance Z_0 relating the complex voltage and current amplitudes of the waves traveling on the transmission line as:

$$Z_0=\sqrt{\frac{L}{C}}=\frac{V_0^{+}}{I_0^{+}}=-\frac{V_0^{-}}{I_0^{-}} \tag{B.10}$$

B.2 The terminated lossless TL

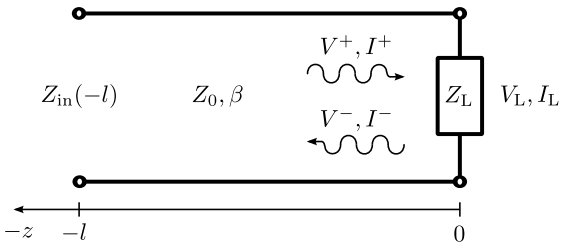

Figure (B.2): Incoming voltage waves will reflect off the load at the end of the transmission line if $Z_0 \neq Z_{\mathrm{L}}$.

Now consider a transmission line ending in a load with impedance Z_{L} as is shown in Fig. B.2. For an incoming wave $V(z) = V_0^+ e^{-j\beta z}$ going from left to right on the TL, the ratio between voltage and current is given by Z_0, but at $z = 0$ the boundary condition is $V_{\mathrm{L}}/I_{\mathrm{L}} = Z_{\mathrm{L}}$. This means that for $Z_0 \neq Z_{\mathrm{L}}$ a wave $V(z) = V_0^- e^{j\beta z}$ going into the opposite direction has to be reflected off the load. Using (B.5) and (B.9) we find:

$$Z_{\mathrm{L}} = \frac{V(0)}{I(0)} = \frac{V_0^+ + V_0^-}{V_0^+ - V_0^-} Z_0 \tag{B.11}$$

This expression can be rearranged in order to define the reflection coefficient Γ, giving the ratio between the reflected and incoming complex voltage amplitudes.

$$\Gamma = \frac{V_0^-}{V_0^+} = \frac{Z_{\mathrm{L}} - Z_0}{Z_{\mathrm{L}} + Z_0} \tag{B.12}$$

If $Z_{\mathrm{L}} = 0/\infty$, corresponding to a short/open load, $\Gamma = -1/+1$ and the reflection is total. In the case where $Z_{\mathrm{L}} = Z_0$, there is no reflection ($\Gamma = 0$) and the load is called "matched". Whenever $|\Gamma| \neq 1$ the voltage and current that are not reflected will dissipate in the load, leading to a steady power flow along the line. Of course, Z_{L} can also be a transmission line, terminated by its own characteristic impedance as is for instance the case with standard $50\,\Omega$ coaxial cables leading to an amplifier with a $50\,\Omega$ matched input impedance. Using Γ, Eqs. (B.5) and (B.9) can be expressed as:

$$V(z) = V_0^+ \left(e^{-j\beta z} + \Gamma e^{j\beta z} \right) \tag{B.13}$$

$$I(z) = \frac{V_0^+}{Z_0} \left(e^{-j\beta z} - \Gamma e^{j\beta z} \right) \tag{B.14}$$

This superposition of two waves propagating in opposite directions along the TL leads to standing waves in voltage and current. The impedance at each point of the line will depend on the ratio between these standing waves. Then, the expression for the input impedance seen at a point $z = -l$ is:

$$\begin{aligned} Z_{\mathrm{in}}(-l) = \frac{V(-l)}{I(-l)} &= \frac{e^{j\beta l} + \Gamma e^{-j\beta l}}{e^{j\beta l} - \Gamma e^{-j\beta l}} Z_0 \\ &= \frac{(Z_{\mathrm{L}} + Z_0) e^{j\beta l} + (Z_{\mathrm{L}} - Z_0) e^{-j\beta l}}{(Z_{\mathrm{L}} + Z_0) e^{j\beta l} - (Z_{\mathrm{L}} - Z_0) e^{-j\beta l}} Z_0 \\ &= \frac{Z_{\mathrm{L}} \cos(\beta l) + j Z_0 \sin(\beta l)}{Z_0 \cos(\beta l) + j Z_{\mathrm{L}} \sin(\beta l)} Z_0 \\ &= \frac{Z_{\mathrm{L}} + j Z_0 \tan(\beta l)}{Z_0 + j Z_{\mathrm{L}} \tan(\beta l)} Z_0 \end{aligned} \tag{B.15}$$

This result shows that the input impedance of a terminated lossless transmission line depends on the *distance* $-l$ from the load along the line and on the *frequency* of the wave (via $\beta = 2\pi/\lambda$).
A few special cases occur. Again, when the load is matched to the TL ($Z_0 = Z_L$) the impedance is constant for all frequencies ($Z_{in} = Z_0$). At $l = \lambda/2$, on the other hand, $Z_{in} = Z_L$, meaning that, when the frequency is such that the distance between the load and the position where the input impedance is evaluated is equal to $\lambda/2$, one recovers the load impedance. An even more interesting effect happens at $l = \lambda/4$:

$$Z_{in}\left(-\frac{\lambda}{4}\right) = \frac{Z_0^2}{Z_L} \tag{B.16}$$

This signifies that the input impedance, seen at a distance $\lambda/4$ from the load, is *inversely* proportional to the load impedance. In this way an open is transformed into a short and vice versa. This phenomenon plays a crucial role in the entire microwave-frequency design done during this PhD work.

B.3 The quarter-wave resonator

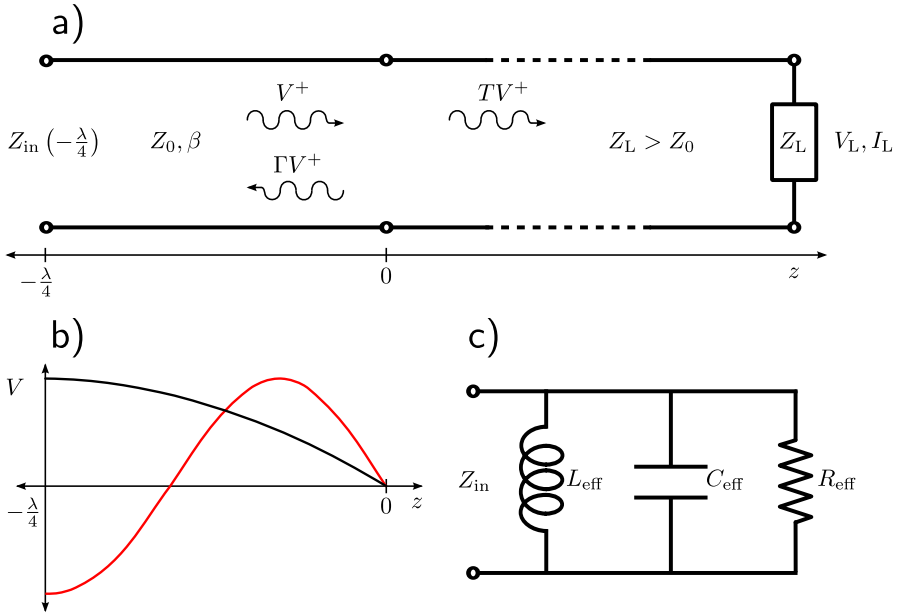

Figure (B.3): a) A transmission line segment with length $l = \lambda/4$ connected to a TL of impedance $Z_L < Z_0$ and terminated in a matched load. A voltage wave coming from the left can be reflected (Γ) or transmitted (T) at the interface. b) The voltage amplitude of the standing waves forming in the resonator as a function of the distance from the load impedance for the first (black) and second (red) modes. Here the ideal case where $Z_L = 0$ is shown. c) Schematic of the lumped element equivalent circuit.

In this section, we will use the framework of transmission line theory developed so far to explain why a TL of impedance Z_0 and length l, terminated with a load impedance $Z_\mathrm{L} < Z_0$ acts as a resonator. This can be understood intuitively by examining the limiting case shown in Fig. B.3b where the load is a short ($Z_\mathrm{L} = 0$). The voltage amplitude at the short has to be zero, which will lead to reflection of incoming waves as discussed above. The resulting standing wave has the same wavelength as its two constituents. Naturally, the voltage amplitude of the standing wave on the end where the resonator is excited is maximum. These boundary conditions lead to an infinite number of possible modes at frequencies $f_n = v_\mathrm{p}/\lambda_n$, where $(2n+1)\lambda_n/4 = l$ and $n \in \mathbb{N}$. As a simple analogy, one can imagine a length of rope tied to a fixed point. If agitated at the right frequency, the rope will form standing waves just like the voltage in a TEM transmission line. Even though this reasoning is carried out in terms of voltage, the same argument can be made in terms of current by inverting the values. On resonance, the current at the short has to be maximum and the current at the input at $z = -l$ is zero. One sees immediately that this leads to an infinite input impedance. Thus, the first mode of the quarter-wave resonator described here behaves like a parallel LC-resonator.
Here it should be noted that, in the case at hand, the source exciting the resonator on the left-hand side is the Josephson junction emitting photons. We are interested in measuring these photons, consequently we replace the short with a transmission line ($Z_\mathrm{L} < Z_0$) terminated by matched amplifiers. Clearly this entails that the quality factor of our resonator is no longer infinite as in the case of a perfect LC, since energy is now allowed to leak out. Albeit being lossless, this transmission line resonator can be assimilated to a parallel LCR, taking into account the dissipation happening in the amplifiers. This will be shown in the next section.

B.3.1 Quarter-wave resonator and parallel LCR

In the following, we derive expressions for the effective capacitance, inductance and resistance of a quarter-wave resonator coupled to an outgoing transmission line. To do so, it is useful to develop the input impedance of a parallel LCR (Fig. B.3) around $\omega_0 = 2\pi f_0 \approx \omega_0 + \delta\omega$, where $\delta\omega \ll \omega_0$.

$$Z_\mathrm{in} \approx \left(\frac{1}{R_\mathrm{eff}} + \frac{1}{jL_\mathrm{eff}(\omega_0 + \delta\omega)} + j(\omega_0 + \delta\omega)C_\mathrm{eff} \right)^{-1} \tag{B.17}$$

Using $\frac{1}{1+\frac{\delta\omega}{\omega_0}} \approx 1 - \frac{\delta\omega}{\omega_0}$ we find:

$$Z_\mathrm{in} \approx \left(\frac{1}{R_\mathrm{eff}} + 2j\delta\omega C_\mathrm{eff} \right)^{-1} \tag{B.18}$$

On the other hand, Eq. (B.15) giving the input impedance of a TL can be brought into the form:

$$Z_\mathrm{in} = \frac{-jZ_\mathrm{L}\cot(\beta l) + Z_0}{-jZ_0\cot(\beta l) + Z_\mathrm{L}} Z_0 \tag{B.19}$$

Again, we develop around ω_0 using $\beta \approx \omega_0/v_\mathrm{p} + \delta\omega/v_\mathrm{p}$. In the frequency range around ω_0 we approximate $l \approx \lambda/4 = \pi v_\mathrm{p}/(2\omega_0)$ and with

$$\cot(\beta l) = \cot\left(\frac{\pi}{2} + \frac{\pi\delta\omega}{2\omega_0}\right) = -\tan\left(\frac{\pi\delta\omega}{2\omega_0}\right) \approx -\frac{\pi\delta\omega}{2\omega_0} = -\delta,$$

we can write (B.19) as:

$$Z_\mathrm{in} \approx \frac{jZ_\mathrm{L}\delta + Z_0}{jZ_0\delta + Z_\mathrm{L}} Z_0 \tag{B.20}$$

Now, rationalizing the numerator and throwing away the higher order terms gives the final result:

$$Z_\mathrm{in} \approx \left(\frac{Z_\mathrm{L}}{Z_0^2} + j\frac{\pi\delta\omega}{2\omega_0 Z_0}\left(1 - \frac{Z_\mathrm{L}^2}{Z_0^2}\right)\right)^{-1} \tag{B.21}$$

Comparison with (B.18) allows us to find the effective capacitance, inductance and resistance of the quarter-wave resonator in terms of a parallel LCR circuit:

$$C_\mathrm{eff} = \frac{\pi}{4\omega_0 Z_0}\left(1 - \frac{Z_\mathrm{L}^2}{Z_0^2}\right) \tag{B.22}$$

$$L_\mathrm{eff} = \frac{1}{\omega_0^2 C_\mathrm{eff}} \tag{B.23}$$

$$R_\mathrm{eff} = \frac{Z_0^2}{Z_\mathrm{L}} \tag{B.24}$$

This entire calculation treats the loaded quarter-wave resonator as an LCR, where R_eff takes into account only the losses through Z_L. This approach is valid, because the external quality factors Q_e^TL of our TL resonators are, by design, always orders of magnitude smaller than the internal ones Q_i^{TL}. We can assume $Q_\mathrm{total}^\mathrm{TL} \approx Q_\mathrm{e}^\mathrm{TL} = Q^\mathrm{LCR}$. With this, we find:

$$Q_\mathrm{total}^\mathrm{TL} = \omega_0 R_\mathrm{eff} C_\mathrm{eff} = \frac{Z_0}{Z_\mathrm{L}} \tag{B.25}$$

For the uncoupled case ($Z_\mathrm{L} = 0$) we find the following expressions allowing us to easily convert between effective lumped element parameters (L_eff, C_eff) and transmission line values per unit length (L, C):

$$C_\mathrm{eff} = \frac{Cl}{2} \tag{B.26}$$

In the above equation l is the length of the transmission line segment acting as a resonator. With the expressions for the resonance frequency $f_0 = 1/(2\pi\sqrt{L_\mathrm{eff}C_\mathrm{eff}}) = v_\mathrm{p}/\lambda$, the phase velocity $v_\mathrm{p} = 1/\sqrt{LC}$ and $\lambda = 4l$ the effective inductance is found to be:

$$L_\mathrm{eff} = \frac{8Ll}{\pi^2} \tag{B.27}$$

The conversion between the effective characteristic impedance $Z_{\text{eff}} = \sqrt{L_{\text{eff}}/C_{\text{eff}}}$ of the resonator and the characteristic impedance $Z = \sqrt{L/C}$ of the TL is:

$$Z_{\text{eff}} = \frac{4}{\pi} Z \tag{B.28}$$

Finally, the resonance frequency of the quarter-wave resonator in terms of the transmission-line inductance and capacitance per unit-length is:

$$f_0 = \frac{1}{4l\sqrt{LC}} \tag{B.29}$$

B.4 Cascaded quarter-wave resonators

Figure B.4a shows a resonator made of several sections of transmission line with lengths $l = \lambda_0/4 = v_{\text{p}}/(4f_0)$ connected to a $50\,\Omega$ matched setup. Formula (B.15) can be used to first numerically calculate $Z'_{\text{in}}(\omega)$ for all frequencies. Then another iteration using $Z'_{\text{in}}(\omega)$ as the new load impedance gives $Z_{\text{in}}(\omega)$.
At resonance this simplifies to $Z'_{\text{in}}(\omega_0) = Z_1^2/50$ and $Z_{\text{in}}(\omega_0) = Z_0^2/Z'_{\text{in}}(\omega_0)$. For $Z_1 = 22\,\Omega$ and $Z_0 = 146\,\Omega$ we get $Z'_{\text{in}}(\omega_0) = 9.7\,\Omega$ and $Z_{\text{in}}(\omega_0) = 2.2\,\text{k}\Omega$. Since the development in the previous section has been carried out around $\omega = \omega_0$ this type of cascaded TL-resonator can still be approximated through an LCR-circuit by simply using $Z'_{\text{in}}(\omega_0)$ as the load impedance Z_{L} seen by the last section. In Fig. B.4b the real parts of the results of both calculations are shown for a resonance frequency of 6.7 GHz. Here the quality factor is $Q \approx 15$. The first mode is indeed well described by the approximation (red dotted line).
Finally, we can investigate how the parameters of such a resonator depend on the characteristic impedances of the different quarter-wave segments. The quality factor is adjusted through Z_1 via:

$$Q_{\text{total}}^{\text{TL}} = \frac{Z_{\text{L}} Z_0}{Z_1^2} \tag{B.30}$$

If we assume that $Z'_{\text{in}}(\omega)$ is almost flat around the resonance, the characteristic impedance is still approximately given by Eq. (B.28). Therefore, the characteristic impedance of the cascaded $\lambda/4$ resonator is controlled by Z_0 (the last segment), while the quality factor can be adjusted by changing Z_1.

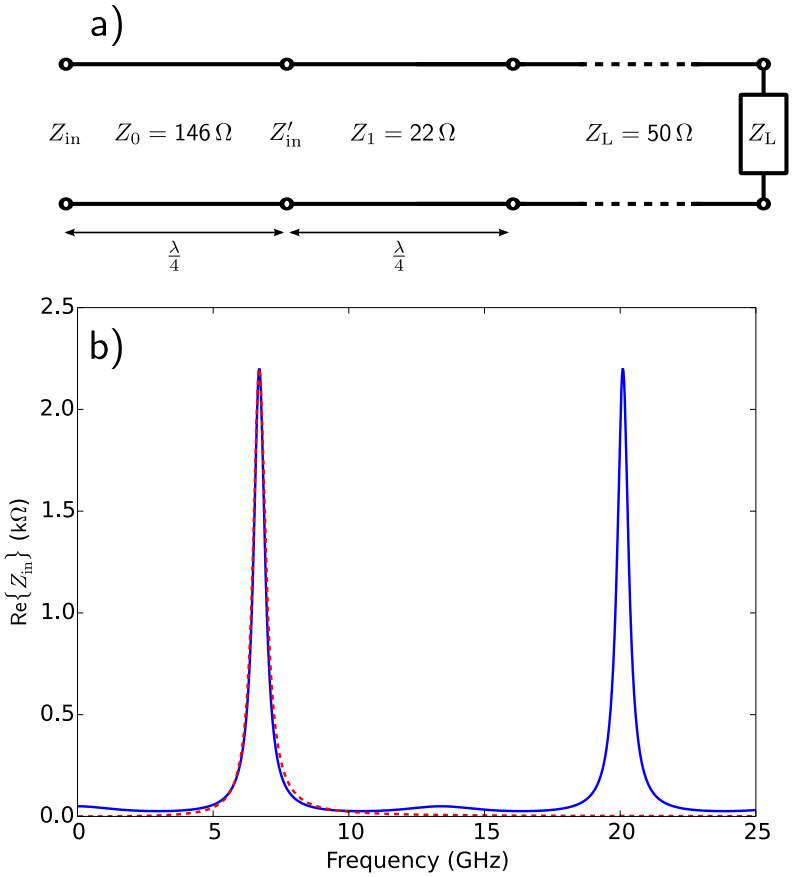

Figure (B.4): a) Two quarter-wave segments of transmission line with different characteristic impedance connected to a 50 Ω matched setup. b) The numerical result of the exact calculation for the given values (solid blue line) and the LCR approximation of the first mode (dotted red line).

Appendix C

Quadrature measurements and noise correlations

C.1 Quadrature measurements

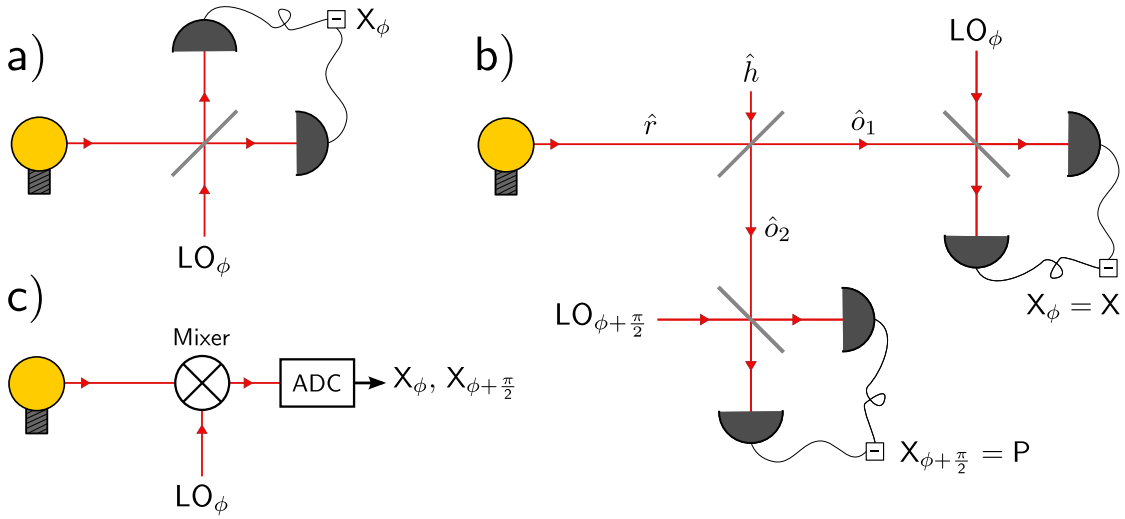

Figure (C.1): a) Measurement of a field quadrature in an optical frequency setup by mixing with a local oscillator (LO) and photon number detection b) Both quadratures can be measured, if the beam is mixed with another field (ideally in the vacuum state) on a beam splitter beforehand, since then the two resulting beams commute. c) In our case the signal is down-converted in frequency and the quadratures of the voltage are extracted numerically from the sampled values.

In the optical domain quadrature measurements are usually performed by mixing the light on a beam splitter with a signal of the same frequency (called local oscillator) providing a fixed phase reference (Fig. C.1a). The desired quantity is given by the

difference between the photon intensities on both outputs. This is often achieved by using the same oscillating field to excite the light source and to provide the local oscillator (homodyne detection [78]). If the output of the light source is split into two commuting fields, a different quadrature can be extracted from each beam without disturbing the other measurement. In practice, this is done by using two local oscillators (LO) with a relative phase difference of $\pi/2$.
At microwave frequencies, the same measurement can be performed using IQ (in-phase and quadrature) mixers. An IQ mixer is a standard microwave frequency device that splits an incoming signal and then mixes each output beam with a local oscillator (again with a relative phase shift $\pi/2$ between them). Afterwards, each voltage quadrature can be directly digitized, without performing a photon number measurement first.
Beam splitting always involves mixing with another mode, which will contribute some spurious signal. Figure C.1b shows the schematic representation of such a measurement. The input field is called $\hat{r}(t)$, the other mode $\hat{h}(t)$ and the two outputs of the 50/50 beam splitter $\hat{o}_{1,2}(t)$ are given by the standard relation (see Eq. (3.10)). The two field quadratures, each measured on one of the two output modes, are defined as in Eq. (3.4) giving:

$$\hat{X}(t) = \frac{\hat{o}_1(t) + \hat{o}_1^\dagger(t)}{\sqrt{2}} = \frac{1}{\sqrt{2}}\left(\hat{X}_r(t) + \hat{X}_h(t)\right) \tag{C.1}$$

$$\hat{P}(t) = -i\frac{\hat{o}_2(t) - \hat{o}_2^\dagger(t)}{\sqrt{2}} = \frac{1}{\sqrt{2}}\left(\hat{P}_r(t) - \hat{P}_h(t)\right) \tag{C.2}$$

Here $\hat{X}_{r,h}(t)$ and $\hat{P}_{r,h}(t)$ are the respective quadratures of the input fields. We can define a complex amplitude envelope $\hat{S}(t)$, which contains the field and a noise term:

$$\hat{S}(t) \equiv \hat{X}(t) + i\hat{P}(t) = \hat{r}(t) + \hat{h}^\dagger(t) \tag{C.3}$$

In our case, since our source is incoherent and addressed with a DC voltage bias, we do not perform homodyne detection. We use an external reference to down-convert the signal to an intermediate frequency (heterodyne detection) and extract both quadratures in post-processing (see Sec. 3.5 and Fig. C.1c). This means that our quadrature measurements do not involve beam splitters (not counting the one used to perform the second order correlation measurement). Nevertheless, we necessarily add noise in the process. This is caused by the fact that we mix our signal into either the positive or negative Nyquist band of our analog to digital converter (see Sec. 4.2.1). In the meantime, the other band still measures an "empty" frequency band. Instead of the vacuum fluctuations on the two beam splitters of the IQ-mixer, integrated over half the measurement bandwidth each, we measure the vacuum fluctuations integrated over the entire bandwidth in the unused Nyquist band. In terms of noise this approach is therefore equivalent.

C.2 Evaluation of the noise terms

As mentioned in section 3.4, the correlations of the complex envelopes contain the field correlations as well as noise terms. The goal of this section is to evaluate Eqs. (3.20) and (3.21) in more detail and to show that all noise contributions can be summarized and thus subtracted as discussed.
The first order cross-correlations of the complex envelopes are given by:

$$\begin{aligned}\Gamma^{(1)}_{\text{cross}}(t,t+\tau) &= \left\langle \hat{S}_c^\dagger(t)\,\hat{S}_d(t+\tau)\right\rangle \\ &= \sqrt{g_c g_d}\left[\left\langle \hat{c}^\dagger(t)\hat{d}(t+\tau)\right\rangle + \left\langle \hat{h}_d^\dagger(t+\tau)\hat{h}_c(t)\right\rangle\right]\end{aligned} \tag{C.4}$$

In this equation we have used that the fields $\hat{c}$, $\hat{d}^\dagger$, $\hat{h}_c$ and $\hat{h}_d^\dagger$ all commute and that noise and signal are uncorrelated (see assumptions and definitions made in Sec. 3.4.1). In the next step we go back to the field $\hat{b}(t) \propto \hat{a}(t)$, by taking into account the beam splitter:

$$\begin{aligned}\Gamma^{(1)}_{\text{cross}}(t,t+\tau) &= \sqrt{g_c g_d}\left[\frac{1}{2}\left\langle \hat{b}^\dagger(t)\hat{b}(t+\tau)\right\rangle - \frac{1}{2}\left\langle \hat{h}_{\text{BS}}^\dagger(t)\hat{h}_{\text{BS}}(t+\tau)\right\rangle + \left\langle \hat{h}_d^\dagger(t+\tau)\hat{h}_c(t)\right\rangle\right] \\ &= \sqrt{g_c g_d}\left[\frac{1}{2}G^{(1)}(t,t+\tau) - \frac{1}{2}G^{(1)}_{\text{BS}}(t,t+\tau) + G^{(1)}_{\text{x,n}}(t+\tau,t)\right]\end{aligned} \tag{C.5}$$

Again, we have used the assumptions made on the noise mode added on the beam splitter, notably that it is uncorrelated with the signal. The second line in the above equation simply establishes a naming convention. The two noise contributions can be condensed into one correlation and we find the result of Eq. (3.20) by defining:

$$G^{(1)}_{\text{x,noise}}(t+\tau,t) \equiv -\frac{1}{2}G^{(1)}_{\text{BS}}(t,t+\tau) + G^{(1)}_{\text{x,n}}(t+\tau,t) \tag{C.6}$$

Note the reversed time-ordering in the two terms on the right-hand side of the above equation.
Using the same rules as in (C.4) the second order correlation takes the form:

$$\begin{aligned}\Gamma^{(2)}_{\text{cross}}(t,t+\tau) &= \left\langle \hat{S}_c^\dagger(t)\,\hat{S}_c^\dagger(t+\tau)\,\hat{S}_d(t+\tau)\,\hat{S}_d(t)\right\rangle \\ &= g_c g_d\left[\left\langle \hat{c}^\dagger(t)\hat{c}^\dagger(t+\tau)\hat{d}(t+\tau)\hat{d}(t)\right\rangle + \left\langle \hat{c}^\dagger(t+\tau)\hat{d}(t)\hat{h}_d^\dagger(t+\tau)\hat{h}_c(t)\right\rangle\right. \\ &+ \left\langle \hat{c}^\dagger(t)\hat{d}(t)\hat{h}_d^\dagger(t+\tau)\hat{h}_c(t+\tau)\right\rangle + \left\langle \hat{c}^\dagger(t+\tau)\hat{d}(t+\tau)\hat{h}_d^\dagger(t)\hat{h}_c(t)\right\rangle \\ &\left.+ \left\langle \hat{c}^\dagger(t)\hat{d}(t+\tau)\hat{h}_d^\dagger(t)\hat{h}_c(t+\tau)\right\rangle + \left\langle \hat{h}_d^\dagger(t)\hat{h}_d^\dagger(t+\tau)\hat{h}_c(t+\tau)\hat{h}_c(t)\right\rangle\right]\end{aligned}$$

The first term on the right hand side of this equation can be written in terms of correlation functions $G^{(1)}(t_1,t_2)$ and $G^{(1)}_{\mathrm{BS}}(t_1,t_2)$ of the field $\hat{b}(t)$ and the noise on the beam splitter $\hat{h}_{\mathrm{BS}}(t)$ respectively:

$$\begin{aligned}\left\langle \hat{c}^\dagger(t)\hat{c}^\dagger(t+\tau)\hat{d}(t+\tau)\hat{d}(t)\right\rangle = \frac{1}{4}\Big[&G^{(2)}\left(t,t+\tau\right) - G^{(1)}\left(t,t+\tau\right)G^{(1)}_{\mathrm{BS}}\left(t+\tau,t\right)\\ &-G^{(1)}\left(t,t\right)G^{(1)}_{\mathrm{BS}}\left(t+\tau,t+\tau\right) - G^{(1)}\left(t+\tau,t+\tau\right)G^{(1)}_{\mathrm{BS}}\left(t,t\right)\\ &-G^{(1)}\left(t+\tau,t\right)G^{(1)}_{\mathrm{BS}}\left(t,t+\tau\right) + G^{(2)}_{\mathrm{BS}}\left(t,t+\tau\right)\Big]\end{aligned} \tag{C.7}$$

Terms 2 to 5 also contain correlations $G^{(1)}_{\mathrm{x,n}}(t_1,t_2)$ of the noise modes $\hat{h}_c(t)$ and $\hat{h}_d(t)$ after the beam splitter. The second term, for instance, can be rewritten as:

$$\begin{aligned}\left\langle \hat{c}^\dagger(t+\tau)\hat{d}(t)\hat{h}^\dagger_d(t+\tau)\hat{h}_c(t)\right\rangle = \frac{1}{2}\Big[&G^{(1)}\left(t+\tau,t\right)G^{(1)}_{\mathrm{x,n}}\left(t+\tau,t\right)\\ &-\left\langle \hat{h}^\dagger_{\mathrm{BS}}(t)\hat{h}_{\mathrm{BS}}(t+\tau)\hat{h}^\dagger_d(t+\tau)\hat{h}_c(t)\right\rangle\Big]\end{aligned} \tag{C.8}$$

The first term on the right-hand side of (C.8) and the second-to-last term in (C.7) combine to give:

$$\begin{aligned}&G^{(1)}\left(t+\tau,t\right)\left[-\frac{1}{2}G^{(1)}_{\mathrm{BS}}\left(t,t+\tau\right) + G^{(1)}_{\mathrm{x,n}}\left(t+\tau,t\right)\right]\\ &= G^{(1)}\left(t+\tau,t\right)G^{(1)}_{\mathrm{x,noise}}\left(t+\tau,t\right)\end{aligned} \tag{C.9}$$

The last term on the right-hand side of (C.8) is a second order cross correlation function between the different noise sources. All the terms of the form $\langle\hat{c}^\dagger\hat{d}\hat{h}^\dagger_d\hat{h}_c\rangle$ yield these two types of contributions. The first kind can be reduced to products of $G^{(1)}$ and $G^{(1)}_{\mathrm{x,noise}}$ correlators, while the second kind can be regrouped with the sixth term in the original $\Gamma^{(2)}_{\mathrm{cross}}\left(t,t+\tau\right)$ given by $\langle\hat{h}^\dagger_d(t)\hat{h}^\dagger_d(t+\tau)\hat{h}_c(t+\tau)\hat{h}_c(t)\rangle$ to give a general second order noise correlation $G^{(2)}_{\mathrm{x,noise}}\left(t,t+\tau\right)$, which is independent of the signal. With this, $\Gamma^{(2)}_{\mathrm{cross}}\left(t,t+\tau\right)$ takes the form shown in Eq. (3.21).

Appendix D

Auxiliary calculations

D.1 Critical current of an unbalanced SQUID

Here we give the derivation of the critical current of an unbalanced SQUID in presence of a magnetic field. The magnetic flux Φ threading the superconducting loop of the SQUID is linked to the phase differences φ_1 and φ_2 across the junctions via the relation [56]:

$$\varphi_1 - \varphi_2 = \frac{2\pi\Phi}{\Phi_0} \,(\text{mod } 2\pi) \tag{D.1}$$

Rewriting $\varphi_{1,2} = \varphi \pm \pi\Phi/\Phi_0$, and using the DC Josephson relation for each of the junctions [56] as well as Kirchhoff's law, the total critical current of a SQUID is:

$$\begin{aligned} I_c^{\text{tot}} &= I_{c1} \sin\left(\varphi + \frac{\pi\Phi}{\Phi_0}\right) + I_{c2} \sin\left(\varphi - \frac{\pi\Phi}{\Phi_0}\right) \\ &= (I_{c1} + I_{c2}) \sin(\varphi) \cos\left(\frac{\pi\Phi}{\Phi_0}\right) + (I_{c1} - I_{c2}) \cos(\varphi) \sin\left(\frac{\pi\Phi}{\Phi_0}\right) \end{aligned} \tag{D.2}$$

Here $I_{c1,c2}$ are the critical currents of junctions 1 and 2 respectively. With $\Sigma = (I_{c1} + I_{c2})$ and $\Delta = (I_{c1} - I_{c2})$, as well as the relations $a\sin(x) + b\sin(x) = c\sin(x + \varphi")$ and $c = \sqrt{a^2 + b^2}$ we find:

$$I_c^{\text{tot}} = \sqrt{\left(\Sigma \cos\left(\frac{\pi\Phi}{\Phi_0}\right)\right)^2 + \left(\Delta \sin\left(\frac{\pi\Phi}{\Phi_0}\right)\right)^2} \sin(\varphi + \varphi") \tag{D.3}$$

The maximum possible value of the critical current through the SQUID is then:

$$\max\left(I_c^{\text{tot}}\right) = \sqrt{\left(\Sigma \cos\left(\frac{\pi\Phi}{\Phi_0}\right)\right)^2 + \left(\Delta \sin\left(\frac{\pi\Phi}{\Phi_0}\right)\right)^2} \tag{D.4}$$

At full frustration, $\pi\Phi/\Phi_0 = (2n+1)\pi/2$ and $\max(I_c^{\text{tot}}) = \Delta$, whereas at minimum frustration, $\pi\Phi/\Phi_0 = n\pi$ and $\max(I_c^{\text{tot}}) = \Sigma$.

In the simpler case of a balanced SQUID, where $I_{c1} = I_{c2} = I_c$ and $\Delta = 0$, this expression simplifies to:

$$\max\left(I_c^{\text{tot}}\right) = 2I_c \left|\cos\left(\frac{\pi\Phi}{\Phi_0}\right)\right| \tag{D.5}$$

D.2 Integral over the real part of a parallel RLC

The impedance of a parallel RLC circuit is given by:

$$Z(\omega) = \frac{1}{i\omega C + \frac{1}{i\omega L} + \frac{1}{R}} \tag{D.6}$$

With $1/\sqrt{LC} = \omega_0$ and $1/(RC) = \gamma$, the real part of this can be expressed as:

$$\text{Re}\{Z(\omega)\} = \frac{\gamma}{C}\frac{\omega^2}{\left(\omega^2 - i\gamma\omega - \omega_0^2\right)\left(\omega^2 + i\gamma\omega - \omega_0^2\right)} \tag{D.7}$$

Writing $\omega_d = \sqrt{-\gamma^2/4 + \omega_0^2}$ the poles of this rational function take the form:

$$\omega_{1,2} = \frac{i\gamma}{2} \pm \omega_d \qquad\qquad \omega_{3,4} = -\frac{i\gamma}{2} \pm \omega_d \tag{D.8}$$

Consequently, when performing a contour integral on the positive complex plane only the poles $\omega_{1,2}$ give a contribution and we can write, using the residue theorem:

$$\int_{-\infty}^{\infty} \text{Re}\{Z(\omega)\}\text{d}\omega = 2\pi i\left[\text{Res}(\omega_1) + \text{Res}(\omega_2)\right] \tag{D.9}$$

Where the residue of $\text{Re}\{Z(\omega)\}$ at the pole ω_n is defined as:

$$\text{Res}(\omega_n) = \lim_{\omega\to\omega_n}(\omega - \omega_n)\frac{\gamma\omega^2}{C(\omega-\omega_1)(\omega-\omega_2)(\omega-\omega_3)(\omega-\omega_4)} \tag{D.10}$$

This can be evaluated to yield the final expression used in chapter 5:

$$\int_{-\infty}^{\infty} \text{Re}\{Z(\omega)\}\text{d}\omega = \pi\omega_0 Z_{\text{eff}} \tag{D.11}$$

Equivalently, using frequency instead of pulsation, we can write:

$$\int_{0}^{\infty} \text{Re}\{Z(\nu)\}\text{d}\nu = \frac{\pi}{2}\nu_0 Z_{\text{eff}} \tag{D.12}$$

In the last two terms we have used the resonance frequency of the RLC given by $\nu_0 = 2\pi/\sqrt{LC}$ as well as its characteristic impedance $Z_{\text{eff}} = \sqrt{L/C}$. It is important to note that this definition of Z_{eff} is based on the effective capacitance and inductance of a lumped element parallel RLC circuit and thus differs from the characteristic impedance of a transmission line resonator.

D.3 The Minnhagen equation at finite temperature

In chapter 5 we use a form of the Minnhagen equation, with a temperature dependent factor and an integral going from $-\infty$ to ∞ that is not found explicitly in reference [2]. They define the function $\mathrm{P}(E)$ via a Fourier transform as:

$$\mathrm{P}(E) = \frac{1}{2\pi\hbar}\int_{-\infty}^{\infty} \mathrm{d}t e^{\mathrm{J}(t)} e^{i\frac{E}{\hbar}t} \tag{D.13}$$

The phase correlation function $\mathrm{J}(t)$ is defined by:

$$\mathrm{J}(t) = \langle(\varphi(t) - \varphi(0))\varphi(0)\rangle = 2\int_{-\infty}^{\infty} \frac{\mathrm{d}\omega}{\omega} r(\omega) \frac{e^{-i\omega t} - 1}{1 - e^{-\frac{\hbar\omega}{k_b T}}} \tag{D.14}$$

Here $r(\omega)$ is the dimensionless resistance $\mathrm{Re}(Z(\omega))/R_Q$, where R_Q is the superconducting resistance quantum. Equation (D.13) uses the following definition of the Fourier transform:

$$\begin{aligned} \tilde{f}(\omega) &= \mathrm{FT}\left[f(t)\right] = \frac{1}{2\pi}\int_{-\infty}^{\infty} \mathrm{d}t f(t) e^{i\omega t} \\ \tilde{f}(E) &= \frac{1}{\hbar}\mathrm{FT}\left[f(t)\right] = \frac{1}{2\pi\hbar}\int_{-\infty}^{\infty} \mathrm{d}t f(t) e^{i\omega t} \end{aligned} \tag{D.15}$$

We calculate the time derivative of the exponential of the phase correlation function:

$$\frac{\mathrm{d}}{\mathrm{d}t} e^{\mathrm{J}(t)} = -2i e^{\mathrm{J}(t)} \int_{-\infty}^{\infty} \mathrm{d}\omega \frac{r(\omega)}{1 - e^{-\frac{\hbar\omega}{k_b T}}} e^{-i\omega t} \tag{D.16}$$

Using the above definitions we can calculate the Fourier transform of both sides of the above equation:

$$\frac{1}{\hbar}\mathrm{FT}\left[\frac{\mathrm{d}}{\mathrm{d}t} e^{\mathrm{J}(t)}\right] = -\frac{2i}{\hbar}\mathrm{FT}\left[e^{\mathrm{J}(t)}\mathrm{FT}^{-1}\left[\frac{r(\omega)}{1 - e^{-\frac{\hbar\omega}{k_b T}}}\right]\right] \tag{D.17}$$

Again, taking into account the definitions (D.15) the Fourier transform of a time derivative is given by $\mathrm{FT}[\dot{f}(t)/\hbar] = -iE\tilde{f}(\omega)$ allowing us to write:

$$-iE\mathrm{P}(E) = -\frac{2i}{\hbar}\mathrm{FT}\left[e^{\mathrm{J}(t)}\right] * \left(\frac{r(\frac{E}{\hbar})}{1 - e^{-\frac{E}{k_b T}}}\right) \tag{D.18}$$

Here we have used $*$ to denote a convolution product. Finally, we get the expression used in Eq. (5.32):

$$\mathrm{P}(E) = \frac{2}{E}\int_{-\infty}^{\infty} \mathrm{d}E' \frac{r(\frac{E'}{\hbar})}{1 - e^{-\frac{E'}{k_b T}}} \mathrm{P}(E - E') \tag{D.19}$$

The Minnhagen equation (5.15) is found from the above expression by going to the limit $T = 0$. This turns the Bose factor into a Heaviside step function, thus allowing us

to restrict the lower bound of the integral to zero. In a similar fashion it limits the upper bound to E, because, at zero temperature, tunneling against the voltage bias becomes impossible and $P(E < 0) = 0$.

Appendix E

Sample parameters

The following table lists different parameters of the samples that gave the results of chapter 6. $E_{\mathrm{J}}^{\mathrm{max}}$ is the maximum Josephson energy extracted from the current voltage characteristic using the Ambegaokar-Baratoff formula. $2\Delta/e$ is the gap voltage. R_{N} is the normal resistance of the SQUID. $R_{\square}$ is the square resistance of the NbN:MgO:NbN trilayer on the individual chip. R_{RC} is the estimated actual value of the on-chip resistor. $\Delta\nu$ is the designed resonator width. Junction size gives the surface of one Josephson junction in the SQUID. On-chip BS indicates if the sample contains an on-chip bias tee and beam splitter (see Sec. 2.5). Figures gives the references of the data plots concerning the sample. The first three samples were made out of NbN:MgO:NbN trilayers using the fabrication process described in chapter 1. The last sample is the one from reference [20] and uses aluminum as a superconductor.

	B104-H7b	B104-F7b	B104-C7b	Hofheinz *et al.* [20]
$E_{\mathrm{J}}^{\max}$	25 µeV	37 µeV	36 µeV	35 µeV
$2\Delta/e$	4.3 mV	4.65 mV	4.8 mV	0.4 mV
R_{N}	300 kΩ	220 kΩ	230 kΩ	17.9 kΩ
$R_{\square}$	8.9 Ω	7.5 Ω	5.3 Ω	-
R_{RC}	None	≈ 17 kΩ	≈ 34.5 kΩ	None
$\Delta\nu$	175 MHz	175 MHz	700 MHz	700 MHz
Junction size	0.022 µm^2	0.022 µm^2	0.022 µm^2	≈ 0.01 µm^2
On-chip BS	Yes	Yes	Yes	No
Figures	6.1,6.2,6.3, 6.4,6.5	6.9,6.10,6.11, 6.12,6.13,6.15, 6.16,6.17,6.18, 6.19,6.20	6.21	6.6,6.7,6.8

Bibliography

[1] K. K. Likharev. "Correlated discrete transfer of single electrons in ultrasmall tunnel junctions". *IBM J. Res. Dev.* 32.1 (1988), pp. 144–158.
DOI: 10.1147/rd.321.0144.

Cited on pages 1–3

[2] G.-L. Ingold and Y. V. Nazarov. "Charge tunneling rates in ultrasmall junctions". *Single charge tunneling*. Ed. by M. H. Devoret and H. Grabert. New York: Plenum Press, 1992.
DOI: 10.1007/978-1-4757-2166-9.

Cited on pages 1, 2, 4, 5, 11, 73, 76, 77, 80, 85, 86, 137

[3] C. A. Neugebauer and M. B. Webb. "Electrical conduction mechanism in ultrathin, evaporated metal films". *J. Appl. Phys.* 33.1 (1962), pp. 74–82.
DOI: 10.1063/1.1728531.

Cited on pages 1–3

[4] A. Blais, R. S. Huang, A. Wallraff, S. M. Girvin, and R. J. Schoelkopf. "Cavity quantum electrodynamics for superconducting electrical circuits: An architecture for quantum computation". *Phys. Rev. A* 69.6 (2004), p. 062320.
DOI: 10.1103/PhysRevA.69.062320.

Cited on pages 1, 44, 83

[5] A. Wallraff, D. I. Schuster, A. Blais, L. Frunzio, R.-S. Huang, J. Majer, S. Kumar, S. M. Girvin, and R. J. Schoelkopf. "Strong coupling of a single photon to a superconducting qubit using circuit quantum electrodynamics." *Nature* 431.7005 (2004), pp. 162–167.
DOI: 10.1038/nature02851.

Cited on page 1

[6] Y. Nakamura, Y. A. Pashkin, and J. S. Tsai. "Coherent control of macroscopic quantum states in a single-Cooper-pair box". *Nature* 398 (1999), pp. 786–788.
DOI: 10.1038/19718. arXiv: 9904003 [cond-mat].

Cited on page 1

[7] D. I. Schuster, A. A. Houck, J. A. Schreier, A. Wallraff, J. M. Gambetta, A. Blais, L. Frunzio, J. Majer, B. Johnson, M. H. Devoret, S. M. Girvin, and R. J. Schoelkopf. "Resolving photon number states in a superconducting circuit." *Nature* 445.7127 (2007), pp. 515–518.
DOI: 10.1038/nature05461.

Cited on pages 1, 44

[8] M. Hofheinz, H Wang, M Ansmann, R. C. Bialczak, E. Lucero, M Neeley, a. D. O'Connell, D Sank, J Wenner, J. M. Martinis, and a. N. Cleland. "Synthesizing arbitrary quantum states in a superconducting resonator." *Nature* 459.7246 (2009), pp. 546–549.
DOI: 10.1038/nature08005.

Cited on page 1

[9] M. Göppl, A. Fragner, M. Baur, R. Bianchetti, S. Filipp, J. M. Fink, P. J. Leek, G. Puebla, L. Steffen, and A. Wallraff. "Coplanar waveguide resonators for circuit quantum electrodynamics". *J. Appl. Phys.* 104.11 (2008), p. 113904.
DOI: 10.1063/1.3010859. arXiv: 0807.4094.

Cited on page 1

[10] Z. Leghtas, S. Touzard, I. M. Pop, A. Kou, B. Vlastakis, A. Petrenko, K. M. Sliwa, A. Narla, S. Shankar, M. J. Hatridge, M. Reagor, L. Frunzio, R. J. Schoelkopf, M. Mirrahimi, and M. H. Devoret. "Confining the state of light to a quantum manifold by engineered two-photon loss". *Science* 347.6224 (2015), pp. 853–857.
DOI: 10.1126/science.aaa2085.

Cited on page 1

[11] H. R. Zeller and I. Giaever. "Tunneling, zero-bias anomalies, and small superconductors". *Phys. Rev.* 181.2 (1969), pp. 789–799.
DOI: 10.1103/PhysRev.181.789.

Cited on pages 2, 3

[12] T. A. Fulton and G. J. Dolan. "Observation of single-electron charging effects in small tunnel junctions". *Phys. Rev. Lett.* 59.1 (1987), pp. 109–112.
DOI: 10.1103/PhysRevLett.59.109.

Cited on page 2

[13] L. J. Geerligs, V. F. Anderegg, C. A. van der Jeugd, J. Romijn, and J. E Mooij. "Influence of dissipation on the Coulomb blockade in small tunnel junctions". *Europhys. Lett.* 10.1 (2007), pp. 79–85.
DOI: 10.1209/0295-5075/10/1/014.

Cited on page 2

[14] P. Delsing, K. K. Likharev, L. S. Kuzmin, and T. Claeson. "Effect of high-frequency electrodynamic environment on the single-electron tunneling in ultrasmall junctions". *Phys. Rev. Lett.* 63.11 (1989), pp. 1180–1183.
DOI: 10.1103/PhysRevLett.63.1180.

Cited on pages 2, 4

[15] M. H. Devoret, D. Esteve, H. Grabert, G.-L. Ingold, H. Pothier, and C. Urbina. "Effect of the electromagnetic environment on the Coulomb blockade in ultrasmall tunnel junctions". *Phys. Rev. Lett.* 64 (15 1990), pp. 1824–1827.
DOI: 10.1103/PhysRevLett.64.1824.

Cited on pages 2, 5, 73

[16] D. Averin, Y. Nazarov, and A. Odintsov. "Incoherent tunneling of the cooper pairs and magnetic flux quanta in ultrasmall Josephson junctions". *Phys. B Condens. Matter* 165-166 (1990), pp. 945–946.
DOI: 10.1016/S0921-4526(09)80058-6.

Cited on page 2

[17] S. Girvin, L. Glazman, M. Jonson, D. Penn, and M. Stiles. "Quantum fluctuations and the single-junction Coulomb blockade". *Phys. Rev. Lett.* 64.26 (1990), pp. 3183–3186.
DOI: 10.1103/PhysRevLett.64.3183.
Cited on pages 2, 5

[18] G.-L Ingold and H. Grabert. "Finite-Temperature Current-Voltage Characteristics of Ultrasmall Tunnel Junctions". *Europhys. Lett.* 14.4 (2007), pp. 371–376.
DOI: 10.1209/0295-5075/14/4/015.
Cited on pages 2, 73, 77, 94

[19] T. Holst, D. Esteve, C. Urbina, and M. Devoret. "Effect of a transmission line resonator on a small capacitance tunnel junction". *Phys. Rev. Lett.* 73.25 (1994), pp. 3455–3458.
DOI: 10.1103/PhysRevLett.73.3455.
Cited on pages 3, 4, 9, 73, 80

[20] M. Hofheinz, F. Portier, Q. Baudouin, P. Joyez, D. Vion, P. Bertet, P. Roche, and D. Esteve. "Bright side of the Coulomb blockade". *Phys. Rev. Lett.* 106.21 (2011), p. 217005.
DOI: 10.1103/PhysRevLett.106.217005. arXiv: 1102.0131.
Cited on pages 5, 6, 25, 73, 77, 80, 84, 86, 89, 97, 112, 139, 140

[21] D. M. Pozar. *Microwave engineering, 4th edition*. Wiley Global Education, 2011.
Cited on pages 6, 22, 26, 27, 35, 103

[22] Y. A. Pashkin, H. Im, J. Leppäkangas, T. F. Li, O. Astafiev, A. A. Abdumalikov, E. Thuneberg, and J. S. Tsai. "Charge transport through ultrasmall single and double Josephson junctions coupled to resonant modes of the electromagnetic environment". *Phys. Rev. B* 83.2 (2011), p. 020502.
DOI: 10.1103/PhysRevB.83.020502. arXiv: 1010.3617.
Cited on page 7

[23] J. Basset, H. Bouchiat, and R. Deblock. "Emission and absorption quantum noise measurement with an on-chip resonant circuit". *Phys. Rev. Lett.* 105.16 (2010), p. 166801.
DOI: 10.1103/PhysRevLett.105.166801. arXiv: 1006.0892.
Cited on pages 7, 9

[24] M. P. Da Silva, D. Bozyigit, A. Wallraff, and A. Blais. "Schemes for the observation of photon correlation functions in circuit QED with linear detectors". *Phys. Rev. A* 82.4 (2010), p. 43804.
DOI: 10.1103/PhysRevA.82.043804. arXiv: 1004.3987.
Cited on pages 7, 10, 44, 46–49

[25] A. A. Houck, D. I. Schuster, J. M. Gambetta, J. A. Schreier, B. R. Johnson, J. M. Chow, L. Frunzio, J. Majer, M. H. Devoret, S. M. Girvin, and R. J. Schoelkopf. "Generating single microwave photons in a circuit." *Nature* 449.7160 (2007), pp. 328–331.

DOI: 10.1038/nature06126.

Cited on page 8

[26] D. Bozyigit, C. Lang, L. Steffen, J. M. Fink, M. Baur, R. Bianchetti, P. J. Leek, S. Filipp, M. P. da Silva, A. Blais, and A. Wallraff. "Measurements of the correlation function of a microwave frequency single photon source". *Nat. Phys.* 7.2 (2010), pp. 154–158.
DOI: 10.1038/NPHYS1845.

Cited on page 8

[27] Y. Yin, Y. Chen, D. Sank, P. J. J. O'Malley, T. C. White, R. Barends, J. Kelly, E. Lucero, M. Mariantoni, a. Megrant, C. Neill, a. Vainsencher, J. Wenner, A. N. Korotkov, a. N. Cleland, and J. M. Martinis. "Catch and release of microwave photon states". *Phys. Rev. Lett.* 110.10 (2013), p. 107001.
DOI: 10.1103/PhysRevLett.110.107001. arXiv: 1208.2950.

Cited on page 8

[28] I. C. Hoi, C. M. Wilson, G. Johansson, J. Lindkvist, B. Peropadre, T. Palomaki, and P. Delsing. "Microwave quantum optics with an artificial atom in one-dimensional open space". *New J. Phys.* 15.2 (2013), p. 025011.
DOI: 10.1088/1367-2630/15/2/025011.

Cited on page 8

[29] M. D. Eisaman, J. Fan, A. Migdall, and S. V. Polyakov. "Invited review article: Single-photon sources and detectors." *Rev. Sci. Instrum.* 82.7 (2011), p. 071101.
DOI: 10.1063/1.3610677.

Cited on pages 8, 46

[30] M. D. Birowosuto, H. Sumikura, S. Matsuo, H. Taniyama, P. J. van Veldhoven, R. Nötzel, and M. Notomi. "Fast Purcell-enhanced single photon source in 1,550-nm telecom band from a resonant quantum dot-cavity coupling". *Sci. Rep.* 2 (2012).
DOI: 10.1038/srep00321. arXiv: 1203.6171.

Cited on page 8

[31] B. Roche, E. Dupont-Ferrier, B. Voisin, M. Cobian, X. Jehl, R. Wacquez, M. Vinet, Y. M. Niquet, and M. Sanquer. "Detection of a large valley-orbit splitting in silicon with two-donor spectroscopy". *Phys. Rev. Lett.* 108.20 (2012), p. 206812.
DOI: 10.1103/PhysRevLett.108.206812.

Cited on page 8

[32] C. Padurariu, F. Hassler, and Y. V. Nazarov. "Statistics of radiation at Josephson parametric resonance". *Phys. Rev. B* 86.5 (2012), p. 054514.
DOI: 10.1103/PhysRevB.86.054514.

Cited on pages 9, 73, 82

[33] V. Gramich, B. Kubala, S. Rohrer, and J. Ankerhold. "From Coulomb-blockade to nonlinear quantum dynamics in a superconducting circuit with a resonator". *Phys. Rev. Lett.* 111.24 (2013), p. 247002.

DOI: 10.1103/PhysRevLett.111.247002.

Cited on pages 9, 73, 82, 96

[34] J. Leppäkangas, G. Johansson, M. Marthaler, and M. Fogelström. "Nonclassical photon pair production in a voltage-biased Josephson junction". *Phys. Rev. Lett.* 110 (2013), p. 267004.
DOI: 10.1103/PhysRevLett.110.267004.

Cited on pages 9, 82, 83

[35] A. D. Armour, M. P. Blencowe, E. Brahimi, and A. J. Rimberg. "Universal quantum fluctuations of a cavity mode driven by a Josephson junction". *Phys. Rev. Lett.* 111.24 (2013), p. 247001.
DOI: 10.1103/PhysRevLett.111.247001. arXiv: 1307.2498.

Cited on pages 9, 73, 82

[36] J. Leppäkangas, M. Fogelström, A. Grimm, M. Hofheinz, M. Marthaler, and G. Johansson. "Antibunched photons from inelastic Cooper-pair tunneling". *Phys. Rev. Lett.* 115.2 (2015), p. 027004.
DOI: 10.1103/PhysRevLett.115.027004.

Cited on pages 9, 11, 73, 83, 84, 86, 101, 113, 115

[37] O. Parlavecchio. "Dynamical Coulomb blockade: From electronic fluctuations to quantum microwaves." PhD thesis. Université Pierre et Marie Curie, 2014.

Cited on page 9

[38] A. D. Armour, B. Kubala, and J. Ankerhold. "Josephson photonics with a two-mode superconducting circuit". *Phys. Rev. B* 91.18 (2015), p. 184508.
DOI: 10.1103/PhysRevB.91.184508.

Cited on page 9

[39] M. Trif and P. Simon. "Photon cross-correlations emitted by a Josephson junction in two microwave cavities". *Phys. Rev. B* 92.1 (2015), p. 014503.
DOI: 10.1103/PhysRevB.92.014503.

Cited on page 9

[40] F. Chen, J. Li, A. D. Armour, E. Brahimi, J. Stettenheim, A. J. Sirois, R. W. Simmonds, M. P. Blencowe, and A. J. Rimberg. "Realization of a single-Cooper-pair Josephson laser". *Phys. Rev. B* 90 (2014), p. 020506.
DOI: 10.1103/PhysRevB.90.020506. arXiv: 1311.2042.

Cited on page 9

[41] L. Bretheau, Ç. Girit, H. Pothier, D. Esteve, and C. Urbina. "Exciting Andreev pairs in a superconducting atomic contact." *Nature* 499.7458 (2013), pp. 312–315.
DOI: 10.1038/nature12315. arXiv: 1305.4091.

Cited on page 9

[42] L. Bretheau, Ç. Girit, M. Houzet, H. Pothier, D. Esteve, and C. Urbina. "Theory of microwave spectroscopy of Andreev bound states with a Josephson junction". *Phys. Rev. B* 90 (13 2014), p. 134506.
DOI: 10.1103/PhysRevB.90.134506.

Cited on page 9

[43] L. Bretheau, Ç. Girit, L. Tosi, M. Goffman, P. Joyez, H. Pothier, D. Esteve, and C. Urbina. "Superconducting quantum point contacts". *Comptes Rendus Phys.* 13.1 (2012), pp. 89–100.
DOI: 10.1016/j.crhy.2011.12.006. arXiv: 1201.4739.

Cited on page 9

[44] L. Bretheau. "Localized excitations in superconducting atomic contacts : probing the Andreev doublet". PhD thesis. Ecole Polytechnique Paris, 2013.

Cited on page 9

[45] S. Dambach, B. Kubala, V. Gramich, and J. Ankerhold. "Time-resolved statistics of non-classical light in Josephson photonics" (2015). arXiv: 1506.05626.

Cited on page 9

[46] F. Lecocq, I. M. Pop, Z. Peng, I. Matei, T. Crozes, T. Fournier, C. Naud, W. Guichard, and O. Buisson. "Junction fabrication by shadow evaporation without a suspended bridge." *Nanotechnology* 22.31 (2011), p. 315302.
DOI: 10.1088/0957-4484/22/31/315302. arXiv: 1101.4576.

Cited on page 13

[47] G. J. Dolan. "Offset masks for lift-off photoprocessing". *Appl. Phys. Lett.* 31.5 (1977), pp. 337–339.
DOI: 10.1063/1.89690.

Cited on page 13

[48] A. Shoji, F. Shinoki, S. Kosaka, M. Aoyagi, and H. Hayakawa. "New fabrication process for Josephson tunnel junctions with (niobium nitride,niobium) double-layered electrodes". *Appl.Phys.Lett.* 41 (1982), p. 1097.
DOI: 10.1063/1.93378.

Cited on page 13

[49] V. Larrey, J. C. Villégier, M. Salez, F. Miletto-Granozio, and A. Karpov. "Processing and characterization of high Jc NbN superconducting tunnel junctions for THz analog circuits and RSFQ". *IEEE Trans. Appl. Supercond.* 9.2 (1999), pp. 3216–3219.
DOI: 10.1109/77.783713.

Cited on page 13

[50] V. Larrey. "Etude et réalistation de jonctions SIS à base de nitrure de niobium et d'une barrière tunnel adaptée permettant la montée aux fréquences THz des instruments hétérodynes." PhD thesis. Université Paris VI, 1998.

Cited on pages 13, 15

[51] T. Yamashita, S. Kitahara, Y. Onodera, Y. Goto, and T. Aso. "Upper critical field of superconducting NbN films". *J. Appl. Phys.* 43.11 (1972), pp. 4749–4751.
DOI: 10.1063/1.1661001.
Cited on page 20

[52] H. C. Jones. "Some properties of granular thin films of high-field superconductors". *Appl. Phys. Lett.* 27.8 (1975), pp. 471–473.
DOI: 10.1063/1.88532.
Cited on page 20

[53] M. Ashkin, J. R. Gavaler, J. Greggi, and M. Decroux. "The upper critical field of NbN films. II". *J. Appl. Phys.* 55.4 (1984), pp. 1044–1048.
DOI: 10.1063/1.333185.
Cited on page 20

[54] M. P. Mathur, D. W. Deis, and J. R. Gavaler. "Lower critical field measurements in NbN bulk and thin films". *J. Appl. Phys.* 43.7 (1972), pp. 3158–3161.
DOI: 10.1063/1.1661678.
Cited on page 20

[55] D. Sam-Giao, S. Pouget, C. Bougerol, E. Monroy, A. Grimm, S. Jebari, M. Hofheinz, J.-M. Gérard, and V. Zwiller. "High-quality NbN nanofilms on a GaN/AlN heterostructure". *AIP Adv.* 4.10 (2014), p. 107123.
DOI: 10.1063/1.4898327.
Cited on page 20

[56] M. Tinkham. *Introduction to superconductivity, 2nd edition.* Dover Books on Physics. Dover Publications, 2004.
Cited on pages 21, 22, 26, 75, 76, 83, 94, 105, 106, 135

[57] R. L. Kautz. "Picosecond pulses on superconducting striplines". *J. Appl. Phys.* 49.1 (1978), pp. 308–314.
DOI: 10.1063/1.324387.
Cited on page 21

[58] T. Van Duzer and C. Turner. *Principles of superconductive devices and circuits.* Elsevier, 1981.
Cited on page 21

[59] R. Barends. "Photon-detecting superconducting resonators". PhD thesis. TU Delft, 2009.
Cited on page 21

[60] D. C. Mattis and J. Bardeen. "Theory of the anomalous skin effect in normal and superconducting metals". *Phys. Rev.* 111.2 (1958), pp. 412–417.
DOI: 10.1103/PhysRev.111.412.
Cited on page 21

[61] A. Kawakami, Z. Wang, and S. Miki. "Fabrication and characterization of epitaxial NbN/MgO/NbN Josephson tunnel junctions". *J. Appl. Phys.* 90.9 (2001), pp. 4796–4799.
DOI: 10.1063/1.1409583.

Cited on pages 21, 22

[62] L. Longobardi, D. Massarotti, G. Rotoli, D. Stornaiuolo, G. Papari, A. Kawakami, G. Piero Pepe, A. Barone, and F. Tafuri. "Quantum crossover in moderately damped epitaxial NbN/MgO/NbN junctions with low critical current density". *Appl. Phys. Lett.* 99.6 (2011), p. 062510.
DOI: 10.1063/1.3624471. arXiv: arXiv:1111.5091v1.

Cited on page 22

[63] A. Shoji, M. Aoyagi, S. Kosaka, F. Shinoki, and H. Hayakawa. "Niobium nitride Josephson tunnel junctions with magnesium oxide barriers". *Appl. Phys. Lett.* 46.11 (1985), pp. 1098–1100.
DOI: 10.1063/1.95774.

Cited on page 22

[64] B. D. Hunt, H. G. LeDuc, S. R. Cypher, J. A. Stern, and A. Judas. "NbN/MgO/NbN edge-geometry tunnel junctions". *Appl. Phys. Lett.* 55.1 (1989), pp. 81–83.
DOI: 10.1063/1.101760.

Cited on page 22

[65] E. Dumur. "A V-shape superconducting artificial atom for circuit quantum electrodynamics". PhD thesis. Université de Grenoble, 2015.

Cited on page 23

[66] J. Gao. "The physics of superconducting microwave resonators". PhD thesis. Caltec, 2008.

Cited on page 29

[67] N. W. Ashcroft and D. N. Mermin. *Physique des solides*. Vol. 26. 1. EDP Sciences, 2002, pp. 42–50.

Cited on page 37

[68] F. C. Wellstood, C. Urbina, and J. Clarke. "Hot-electron effects in metals". *Phys. Rev. B* 49.9 (1994), pp. 5942–5955.
DOI: 10.1103/PhysRevB.49.5942.

Cited on pages 37, 38

[69] G. V. Samsonov. *Handbook of the physicochemical properties of the elements: Trans. from Russian*. Plenum, 1968.

Cited on page 37

[70] B. Huard, H. Pothier, D. Esteve, and K. E. Nagaev. "Electron heating in metallic resistors at sub-Kelvin temperature". *Phys. Rev. B* 76.16 (2007), p. 165426.
DOI: 10.1103/PhysRevB.76.165426. arXiv: 0708.3935.

Cited on page 38

[71] F. Giazotto, T. T. Heikkilä, A. Luukanen, A. M. Savin, and J. P. Pekola. "Opportunities for mesoscopics in thermometry and refrigeration: Physics and applications". *Rev. Mod. Phys.* 78.1 (2006), pp. 217–274.
DOI: 10.1103/RevModPhys.78.217.
Cited on page 38

[72] A. Steinbach, J. Martinis, and M. H. Devoret. "Observation of hot-electron shot noise in a metallic resistor". *Phys. Rev. Lett.* 76.20 (1996), pp. 3806–3809.
DOI: 10.1103/PhysRevLett.76.3806.
Cited on page 38

[73] M. H. Devoret. "Quantum fluctuations in electrical circuits". *Les Houches Sess. LXIII, Quantum Fluctuations*. Ed. by S. Reynaud, E. Giacobino, and J. Zinn-Justin. Amsterdam: North-Holland/Elsevier, 1995, pp. 351–386.
Cited on pages 43, 75

[74] L. S. Bishop. "Circuit quantum electrodynamics". PhD thesis. Yale University, 2010. arXiv: 1007.3520.
Cited on pages 43, 75

[75] B. Peropadre, J. Lindkvist, and I. C. Hoi. "Scattering of coherent states on a single artificial atom". *New J. Phys.* (2013), p. 035009.
DOI: 10.1088/1367-2630/15/3/035009. arXiv: arXiv:1210.2264v1.
Cited on page 44

[76] D. Walls and G. Milburn. *Quantum Optics, 2nd Edition*. Springer, 2008.
Cited on pages 44, 46, 47, 82, 84

[77] C. Eichler, D. Bozyigit, and A. Wallraff. "Characterizing quantum microwave radiation and its entanglement with superconducting qubits using linear detectors". *Phys. Rev. A - At. Mol. Opt. Phys.* 86.3 (2012), p. 32106.
DOI: 10.1103/PhysRevA.86.032106. arXiv: arXiv:1206.3405v1.
Cited on page 46

[78] S. Haroche and J. Raimond. *Exploring the quantum: atoms, cavities, and photons*. Oxford Graduate Texts. OUP Oxford, 2006.
Cited on pages 47, 82, 132

[79] C. M. Caves. "Quantum limits on noise in linear amplifiers". *Phys. Rev. D* 26 (8 1982), pp. 1817–1839.
DOI: 10.1103/PhysRevD.26.1817.
Cited on page 48

[80] D. H. Slichter, O. Naaman, and I. Siddiqi. "Millikelvin thermal and electrical performance of lossy transmission line filters". *Appl. Phys. Lett.* 94.19 (2009), p. 192508.
DOI: 10.1063/1.3133362. arXiv: 0903.1895.
Cited on page 66

[81] J. Leppäkangas, G. Johansson, M. Marthaler, and M. Fogelström. "Input-output description of microwave radiation in the dynamical Coulomb blockade". *New J. Phys.* 16.1 (2014), p. 15015.
DOI: 10.1088/1367-2630/16/1/015015. arXiv: arXiv:1309.3646v2.
Cited on pages 73, 83, 84

[82] P. Minnhagen. "Exact numerical solutions of a Nozieres-de Dominicis-type model problem". *Phys. Lett. A* 56.4 (1976), pp. 327–329.
DOI: 10.1016/0375-9601(76)90327-3.
Cited on page 77

[83] M. Marthaler, Y. Utsumi, D. S. Golubev, A. Shnirman, and G. Schön. "Lasing without inversion in circuit quantum electrodynamics". *Phys. Rev. Lett.* 107.9 (2011), p. 093901.
DOI: 10.1103/PhysRevLett.107.093901. arXiv: 1012.3557.
Cited on page 82

[84] P. Jung, S. Butz, M. Marthaler, M. V. Fistul, J. Leppäkangas, V. P. Koshelets, and A. V. Ustinov. "Multistability and switching in a superconducting metamaterial." *Nat. Commun.* (2014), p. 3730.
DOI: 10.1038/ncomms4730.
Cited on page 83

[85] M. Wallquist, V. S. Shumeiko, and G. Wendin. "Selective coupling of superconducting charge qubits mediated by a tunable stripline cavity". *Phys. Rev. B* 74 (22 2006), p. 224506.
DOI: 10.1103/PhysRevB.74.224506.
Cited on page 83